Design, modelling and testing of high heat flux components for fusion devices

Maria Lorena Richiusa

St Catherine's College

University of Oxford

Thesis submitted for the degree of

Doctor of Philosophy

Trinity 2023

This storm too shall pass.

To myself.

To my freedom.

To the power of choices.

To the fun driving research.

To the beauty of discoveries.

To the extraordinary capabilities of the human being.

To the countless possibilities that are about to open up.

Acknowledgements

I have carried out this research project while holding an Engineering Grant from EUROfusion during my employment at UKAEA, while also actively participating in the latest JET experimental campaign. Although the specifics of my Grant activities (carried out while being seconded to various institutions such as ENEA in Frascati, CEA in Cadarache, KIT in Karlsruhe, IPP in Garching) are not explicitly outlined in this thesis, the knowledge I have gained greatly informs the content of the work. The DPhil journey has fostered extensive international collaborations, which I believe will remain invaluable in my career.

I want to thank my two supervisors, Professor Peter Ireland from the University of Oxford and Dr. Zsolt Vizvary from UKAEA, for their invaluable insights and unwavering support during this research endeavor. Special thanks also go to Dr. Jack Nicholas, whose advisory role during my initial year at the Oxford Thermofluids Institute was invaluable.

Within UKAEA, I am grateful to Martin O'Brien for his instrumental support with the EUROfusion Grant and DPhil applications, Dr. Mike Porton (former JET Chief Engineer) for his decisive actions, and Jayne Moulster for her exceptional coordination efforts while I juggled responsibilities across multiple institutions.

I would like to express my appreciation to the Ukrainian researchers Igor Garkusha, Vadym Makhlaj, and Stanislav Herashchenko for their contribution to this work, particularly their assistance in providing data from the Ukrainian facility QSPA Kh-50, before running dedicated experiments. Regrettably, changes in international circumstances since early 2022 have halted our collaboration.

Special recognition is due to key individuals who facilitated the successful execution of the melting experiments in GLADIS. I extend my gratitude to Henri Greuner, the

scientific supervisor of the facility, as well as Dr. Jan Coenen and Dr. Sebastijan Brezinsek, leaders of the EUROfusion Plasma–Wall Interaction and Exhaust Work Package, for their pivotal roles in overcoming challenges, including those arising from uncertainties following Brexit.

Anna Widdowson's expertise in erosion provided invaluable insights for post–processing, which laid the groundwork for collaboration with the UKAEA's MRF. I thank Dr. Ed Eardley, the MRF scientific manager, for securing grants to support the post–processing activities and guiding me through sample preparation.

The University of Oxford Materials Department played a crucial role in post–processing imaging. I express my gratitude to Dr. Colin Johnston, manager of the Oxford Materials Characterization Service, for granting access to the Begbroke laboratory, and to Chris Salter for sharing his expertise in optical microscopy and material morphology. Special thanks also go to Dr. Andrew Lui for his invaluable feedback on imaging and Prof. David Armstrong for his interest in interpreting the results.

I am also grateful to Prof. Bruce Finlayson and Dr. Matt McLelland from Lawrence Livermore National Laboratory for their insightful contributions and engaging discussions on the workflow of melting experiments.

The conclusion of the EUROfusion Grant has led me to take on the role of leading the EU–DEMO Limiter System Design since June 2022. Within the DEMO Central Team, I extend my gratitude to Dr. Francesco Maviglia and Dr. Antonino Cardella for their feedback during the EUROfusion Grant. I also thank Dr. Gabriella Pautasso for sharing her expertise on plasma disruptions, and Dr. Mattia Siccinio for the engaging conversations around various plasma physics topics. Additionally, I express my gratitude to Dr. Emilia Genangeli and Armin Scherber for their insights on intellectual property matters, as well as to the University of Oxford Innovation Department for their support in safeguarding my student status rights.

In conclusion, I am deeply grateful to all who have supported me on this journey, whether for a brief period or from afar, enabling me to fully immerse myself in this enriching experience.

Abstract

The commercial feasibility of fusion energy requires advanced technological research, needed for withstanding more extreme conditions than fission or aerospace applications. One of the areas needing viable solution is the handling of high heat fluxes experienced by the wall surrounding the plasma, especially during off–normal transients. In such cases, the plasma can touch the wall, releasing up to GigaJoules of energy in milliseconds, which leads to surface degradation due to melting and vaporization. The wall protection strategy adopted for the EU–DEMO tokamak relies on sacrificial protruding panels, called limiters, devoted to deal with plasma–wall contact events following both normal and accidental transients. Limiters can be damaged, provided that their active cooling system preserves its integrity under any circumstances. Therefore, the limiter design requires any armour phase change to be considered, since it affects the cooling system design and integrity.

This research encompasses the limiter integrated design workflow under high heat flux and strong electro–magnetic loads due to disruptive events, with specific focus on tackling the heat transfer in solid components undergoing phase change through the development of an engineering methodology. The main steps of the research are here highlighted.

Given the initial assessment of plasma magnetic configurations during off–normal events, the limiter's plasma facing surface is designed and shaped accordingly, with the aim of spreading the energy deposited over as large a surface area as possible, avoiding edge–localized hot spots. The shaping is then verified and adapted to the different plasma magnetic configuration of the longest normal operation under heat load estimates by means of field line tracing codes.

Efforts towards heat transfer modelling in presence of phase change bring the author to the development of 3D–TARTIFL&TTE (**T**hermal **A**nalysis fo**R** **T**racking

Inter**F**aces under me**L**ting**&**vaporiza**T**ion–induced plasma **T**ransient **E**vents), implemented through COMSOL Multiphysics. It is an engineering model tracking the solid–to–liquid moving boundary within one single domain, while gas kinetics governs the amount of material removed by vaporization. The vapour domain is not modelled. The material removal due to the evaporative mass flux is modelled by means of moving mesh frames which push the recessive liquid interface backwards according to gas kinetics–driven boundary conditions. The melt pool is not removed during the transient. Mass balance considerations drive the liquid–to–vapour interface velocity.

The approach is benchmarked against Quasi–Stationary Plasma Accelerator (QSPA kh-50, Kharkov, Ukraine) data, and dedicated melting experiments run in Garching LArge DIvertor Sample test facility (GLADIS, Garching, Germany). In either cases, the code shows the capability to predicting surface temperature, absorbed energy, and melt layer thickness, paving the way for its use within the engineering design workflow of metallic plasma–facing components.

The application of 3D–TARTIFL&TTE to a tungsten monoblock armour leads to a preferred chosen thickness of 20 mm, as a conservative preliminary value to be checked under pressure and temperature values calculated at the cooling system outlet.

The first concept of the integrated design of the upper limiter is also presented. It is equipped with a sliced structural box which breaks down the eddy current paths and, hence, reduces the electro–mechanical loads acting on it. Built on static–structural and energy balance hand calculations based on, respectively, preliminary electro–magnetic and neutronic loads, the performance of the integrated design will be verified in a future work against electro–magnetic, neutronic, thermal–hydraulic load combination. The outcome is expected to be used as reference for future limiter engineering designs.

Contents

List of Figures

List of Tables

Nomenclature

Acronyms

ALE	Arbitrary Lagrangian–Eulerian	
CCD	Charged–Coupled Device	
CHF	Critical heat flux	W m^{-2}
CQ	Current Quench	
DBTT	Ductile to Brittle Transition Temperature	°C
DPA	Displacement Per Atom	
DVDE	Downward Vertical Displacement Event	
EU–DEMO	European DEMOnstration fusion reactor	
FPY	Full Power Year	
FWHM	Full Width at Half Maximum	
FW	First Wall	
GLADIS	Garching Large Divertor Sample Test Facility	
HBMI	Heat Balance Integral Method	
HFGC	High Field Gap Closure	
HTC	Heat Transfer Coefficient	W m^{-2} K^{-1}
ICRH	Ion Cyclotron Resonance Heating	
IEEE	Institute of Electrical and Electronics Engineers	
IML	Inboard Midplane Limiter	
IPP	Max Plank Institute for Plasma Physics	
IR	Infrared thermography	
ISFNT	International Symposium on Fusion Nuclear Technology	
ITER	International Thermonuclear Experimental Reactor	

IVC	In–Vessel Component
IVVS	In–Vessel Viewing System
IWGL	Inner Wall Guard Limiter
JET	Joint European Torus
KL	Knudsen Layer
LAS	Leica Application Suite
LBSRP	Load Bearing Septum Replacement Plate
LCFS	Last Closed Flux Surface
LHCD	Lower Hybrid Current Drive
LHS	Left–Hand Side
MRF	Materials Research Facility
MSG	Manufacturing Support Group
NASP	Non–Active Sample Preparation
ODE	Ordinary Differential Equation
OLL	Outboard Lower Limiter
OML	Outboard Midplane Limiter
OPT	Outer Protection Tile
PDE	Partial Differential Equation
PFC	Plasma–Facing Component
PL	Poloidal Limiter
PWR	Pressurized Water Reactor
Pyro (1-2c)	Pyrometer (1-2Colour)
QSPA Kh-50	Quasi–Stationary Plasma Accelerator Kharkov-50
RAFM	Reduced Activation Ferritic Martensitic steel
RD	Rump–Down
RHS	Right–Hand Side
RU	Ramp–Up
SB	Shield Block
SOFE	Symposium on Fusion Engineering
SOFT	Symposium on Fusion Technology

SOF	Start–Of–Flat top
SOL	Scrape–Off Layer
SS	Stainless Steel
TARTIFL&TTE	**T**hermal **A**nalysis fo**R** **T**racking **I**nter**F**aces under me**L**ting **&** vapor-iza**T**ion–induced plasma **T**ransient **E**vents
TC, TC1, TC2	Thermocouple
TFC	Toroidal Field Coil
TQ	Thermal Quench
TZM	Ti–Zr–Mo alloy
UIWPT	Upper Inner Wall Protection Tile
UKAEA–CCFE	UK Atomic Energy Authority–Culham Centre for Fusion Energy
UL	Upper Limiter
UVDE	Upward Vertical Displacement Event
VV	Vacuum Vessel
Z	Atomic number

Symbols

A	Area	m^2
a	minor radius	m
a_0	Atomic radius	m
B	Dimensionless variable for phase change, $H_v/c_{p,s}(T_v - T_m)$	
b	Magnetic pitch, $\text{atan}(\lvert\vec{B}_\vartheta\rvert/\lvert\vec{B}_\varphi\rvert) \approx \lvert\vec{B}_\vartheta\rvert/\lvert\vec{B}\rvert$	
$\vec{B}$	Magnetic field	T
C	Dimensionless specific heat capacity, $c_{p,l}/c_{p,s}$	
c	Sound speed in matter, $\sqrt{\gamma RT/M}$	
C_f	Channel peaking factor	
C_l	Connection length,	m
c_p	Specific heat capacity	J kg^{-1} $°C^{-1}$
D	Cross–field diffusion coefficient	m^2 s^{-1}
d_h	Hydraulic diameter	m
E	Energy	J

eV	ElectronVolt	$1.6 \cdot 10^{-19}$ J
F	Force	N
f	Friction factor	
H	Latent heat	J kg^{-1}
H^*	Dimensionless latent heat, H_v/H_m	
HF	Heat flux	W m^{-2}
I	Current	A
J	Net particle flux	particles s^{-1} m^{-2}
j	Current density	A m^{-2}
K	Dimensionless thermal conductivity, k_l/ks	
k	Thermal conductivity	W m^{-1} $°C^{-1}$
k_B	Boltzmann constant	$1.380649 \cdot 10^{-23}$ J K^{-1}
k_{loc}	Localized pressure drop coefficient	
L	Slab width	m
M	Molar mass	kg mol^{-1}
m	Particle mass, M/N_A	kg ion^{-1}
$\dot{m}$	Evaporative mass flux	kg m^{-2} s^{-1}
$M_x,\ M_y,\ M_z$	Moments along the x, y, z directions	N m
Ma	Mach number, $v/c_{gas} = v\sqrt{M}/\sqrt{\gamma RT}$	
mfp	Mean free path, $k_B T/\sqrt{2}\pi\sigma_s^2 \cdot P$	m
N	Particle flux, $\int_t J(t)dt$	ion m^{-2}
n	Particle density, $k_B T/P = molN_A/V$	ion m^{-3}
$\vec{n}$	Surface normal	
N_A	Avogadro constant	$6.022 \cdot 10^{23}$ atom mol^{-1}
Nu	Nusselt number, $d_h HTC/k$	
P	Pressure	Pa
$\dot{P}$	Power	W
Π	Peaking factor for halo effect estimates, $\Pi \propto \Pi_\vartheta \cdot \Pi_\varphi$	
Pr	Prandtl number, $c_p\mu/k$	
Q	Fusion power amplification factor	

q	Safety factor, $a\|\vec{B}_\varphi\|/R_{major}\|\vec{B}_\vartheta\|$	
R	Dimensionless density, ϱ_l/ϱ_s	
R	Molar gas constant, $N_A k_B$	8.314 J $mol^{-1}K^{-1}$
r	Liquid–to–vapour moving interface	m
r′	Dimensionless liquid–vapour interface, r/L	
R_{major}	Major radius of the machine,	m
Re	Reynolds number, $\varrho v d_h/\mu$	
s	Solid–to–liquid moving interface	m
$< \sigma\ v >$	Average reactivity per unit of time and particle density	$m^3\ s^{-1}$
S_m	Allowable normal stress	MPa
S_y	Yielding stress	MPa
s′	Dimensionless solid–liquid interface, s/L	
St.Dev.	Standard deviation	mm
T	Temperature	°C
t	Time	s
t′	Dimensionless time variable (Fourier number), t/τ	
V	Volume	m^3
v	Velocity	m s^{-1}
w	Halo region width	
x	Spatial coordinate	m
x′	Dimensionless positional variable, x/L	
Z	Atomic number	

Subscripts

0	Initial value
1/2	Half axisymmetric system
∥	Parallel field
⊥	Perpendicular field
abs	Absorbed
ave	Average
c	Condensation

CQ	Current Quench	
DW	Darcy–Weisbach	
e	Electron	
gas	Gaseous phase	
h	Halo	
i	Ion	
in	Incoming, inlet	
IR	Infra–red	
l	Liquid	
load	Loading	
loc	Localized	
m	Melting	
max	Maximum	
mis	Misalignment	
nu	Nucleon	
op	Operational	
out	Outgoing, outlet	
(1 – 2c) Pyro	(1-2Colour) Pyrometer	
p, plasma	Plasma	
R	Re–condensation	
rad	Radiative	
s	Solid	
sat	Saturation	
sep	Separatrix	
setback	Edge recession	
SOF	Start–Of–Flat top	
surf, front	Surface, front face	
TC, TC1, TC2	Thermocouple	
TQ	Thermal Quench	
UTS	Ultimate Tensile Strength	MPa

v	Vapour	
w	Wall	

Greek letters

α	Thermal diffusivity, $k/\rho c_p$	$m^2\ s^{-1}$
β	Retro–diffusion coefficient	
δ	Distance between LCFL and FW, $x - R_{LCFS}$	m
δ	Distance between the LCFS and the PFC, $x - R_{LCFS}$	
ε	Surface roughness	m
η	Coefficient of particle evaporation and condensation	
Γ	Particle flux density, $nv_\perp$	particles $m^{-2}\ s^{-1}$
γ	Adiabatic index, c_p/c_v	
Λ	Luminosity function	$W\ m^3\ ion^{-1}$
λ	Power fall–off length	m
φ	Toroidal direction	
ρ	Density	$kg\ m^{-3}$
σ_B	Stefan–Boltzmann constant	$5.6704 \cdot 10^{-8}\ W\ m^{-2}\ K^{-4}$
$\sigma_{bending}$	Bending stress	MPa
σ_s	Microscopic cross–section of scattering	barn=$10^{-28}\ m^2$
τ	Characteristic time, L^2/α_s	s
τ_c	Collision time	s
τ_E	Energy confinement time	s
τ_r	Relaxation time	s
τ_{shear}	Shear stress	MPa
Θ	Dimensionless temperature, $(T - T_m)k_s/(HF \cdot L)$	
ϑ	Poloidal direction	
ε	Surface emissivity	

Chapter 1

Introduction

"Those who are not shocked when they first come across quantum theory cannot possibly have understood it."

Niels H.D. Bohr

This chapter begins with an overview of the fundamentals of fusion energy, highlighting the physical requirements needed for nuclear fusion to occur. It requires matter to be brought to its fourth state, i.e. plasma, with a carefully engineered physical system to enclose it in a confined space. Magnetic confinement is introduced for this purpose, with its plasma–wall interactions happening in the region between the confined plasma and the structures. These interactions are expected to become more extreme in future commercial fusion devices, especially during accidental events. This introduces the need for critical components to protect the surroundings against plasma–wall contact events. These protective components, referred to as limiters, are the main focus of the present work.

1.1 The principles of fusion energy

Fusion is a nuclear reaction which occurs when highly energetic positively charged light nuclei are brought close enough to fuse together into heavier nuclei. At this distance, the short–range nuclear force overcomes the long–range Coulombian repulsion, helping nuclei to collide by a quantum mechanical tunnelling effect [1]. This process releases a huge amount of energy,

although it requires very high temperatures and adequate particle density to be sustained for sufficient confinement time.

The fusion counterpart is fission, which occurs when heavier nuclei, such as $_{92}U^{235}$, split into lighter nuclei under neutron bombardment, releasing 200 MeV energy per atom.

The curve of binding energy per nucleon vs. atomic mass (Fig. 1.1) shows how fission and fusion processes release nuclear energy through two opposite mechanisms, which results in the formation of nuclides having mass close to the Fe mass, the stablest and most abundant element on Earth. This explains why heavier nuclei whose mass spectrum lies on the right–hand side (rhs) of the curve are prone to fission, whereas nuclei like $_1H^1$ and its isotopes ($_1D^2$, $_1T^3$) lying on the left–hand side (lhs) of it are prone to fusion.

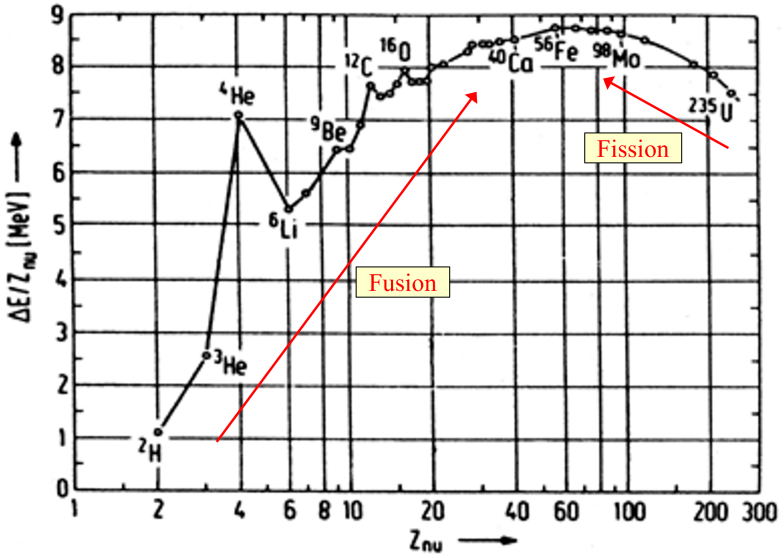

Fig. 1.1: Binding energy per nucleon vs. atomic mass (Z_{nu}) for different elements [2]. *Figure reproduced with permission from Springer Nature.*

Since fusion generates stabler nuclei with a higher value of binding energy among nucleons, the difference in energy or, equivalently, in mass [3] between reactant and product nuclei is released. It is then distributed as kinetic energy of the products in a quantity inversely proportional to their masses.

Possible fusion reaction fuels include $_1H^1$, $_1D^2$, $_1T^3$, $_2He^3$, $_3Li^6$ and $_4B^{11}$. As shown in Fig. 1.2, the most probable reaction at temperatures currently attainable in fusion devices (10 KeV≈100 million °C) is the D–T reaction, at least for the first generation of fusion power plants. At this temperature, all the particles are ionized and coexist in the state of plasma, which is a

macroscopically neutral gas.

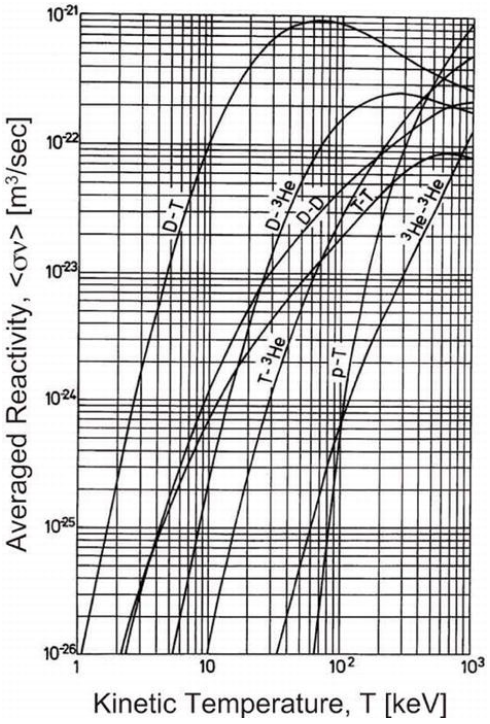

Fig. 1.2: Average reaction reactivity for different fusing fuels according to their kinetic temperature [4].

The D–T reaction (Eq. 1.1) produces a neutron and an alpha particle (known as "fusion ash"), plus 17.6 MeV of energy.

$$ {}_1\mathrm{D}^2 +_1 \mathrm{T}^3 \rightarrow {}_2\mathrm{He}^4 +_0 \mathrm{n}^1 + 17.6 \ \mathrm{MeV} \tag{1.1} $$

Only 20% of the reaction energy is carried by alpha particles and contributes to the plasma self–heating, while 80% is carried away by neutrons. Some neutrons escape, while others interact with the surrounding structure, where they deposit their energy. Their kinetic energy is converted in thermal energy of the coolant which is used in a power cycle to produce electricity. Neutron interaction with structural atoms can cause radioactivity, as well as structural damage.

The D–T reaction exploits an abundant fuel on Earth, since D can be extracted from seawater while T can be bred from Li^6 by absorbing fusion neutrons. Li^6 is also widely available in the Earth's crust.

The energy released by a fusion reaction is much larger than that generated by chemical reactions because the binding energy that holds the nucleons together greatly exceeds the elec-

tronic linkage energy present in atoms. Furthermore, the energy per nucleon released by the D–T reaction is greater than that released by U^{235} fission (17.6 MeV/5≫200 MeV/236). This makes fusion a high energy density source, without long–term radioactive nucleus production. Fusion is also inherently safe as there is no danger for chain reactions. In fact, a burning plasma is difficult to start and maintain, and it can only occur under strict operational conditions, outside of which the plasma naturally terminates losing its energy.

The commercial viability of fusion for electricity production is doable if the power ratio (Q, see Eq. 1.2) is much greater than unity, i.e. the net thermal power output produced by fusion reactions is at least 20 times higher than the thermal power input required to increase the kinetic energy of the plasma.

$$Q = \frac{\text{fusion power}}{\text{plasma heating power}} \tag{1.2}$$

A successful fusion plasma, indeed, requires that the fusion power compensates the energy losses by providing the necessary heating for keeping the plasma burning. This is known as *ignition* and it is the ideal self–sufficiency condition every fusion power device should aim for. For a D–T plasma, ignition is reached when the triple product of ion density (n), plasma temperature (T) and energy confinement time (τ_E) satisfies the Lawson criterion in 1.3 [3]:

$$n\,T\tau_E \geq 3 \cdot 10^{21}\ \mathrm{m^{-3}\ keV\ s} \tag{1.3}$$

For a typical ion density value of $10^{20}\ \mathrm{m^{-3}}$, and temperature value of 10 keV, the criterion requires a confinement time equal to or greater than 3 seconds.

1.2 The magnetic confinement inside a Tokamak

For an energetically viable fusion process, the reactants must not contact the walls of any confinement device for a sufficient time. Among the different approaches explored (i.e. gravitational, electrostatic, inertial confinements) for holding a burning plasma [1, 3], the magnetic confinement is the most promising one for steady–state operation. Its basic idea is to use toroidally–closed magnetic field configurations for trapping charged particle's motion along

magnetic lines of forces.

The magnetic confinement is currently used in two different machine configurations of tokamaks and stellarators [5]. Thanks to their engineering axisymmetry and modularity, tokamaks are the most well understood and developed magnetic configurations despite plasma current–driven instabilities and disruptions, while stellarators are considered as a backup program [6] for their inherent plasma stability, which is only attained by means of a complex engineering design. The word *tokamak* comes from a Russian acronym that stands for "toroidal chamber with magnetic coils". A tokamak is essentially a low pressure discharge tube bent in a closed doughnut–shaped domain, where the helicoidal magnetic field $\vec{B}$ (Fig. 1.3a and Fig. 1.3b) results from the combination of the poloidal $\vec{B}_\vartheta$ induced by the plasma current with the toroidal $\vec{B}_\varphi$ induced by external toroidal magnets. The toroidal plasma current (I_p), which is also used as plasma resistive heating, is mainly generated according to the transformer principle: a central solenoid acting as primary winding changes the magnetic flux that links with the toroidal plasma (Fig. 1.3a). Even though small, $\vec{B}_\vartheta$ is essential in the helicoidal configuration of $\vec{B}$, as it gives stability by opposing the effect of charge separation caused by the $\vec{B}_\varphi$ radial gradient ($|\vec{B}_\varphi| \approx 1/R_{major}$, being stronger at the machine centre and weaker outwards). External poloidal field coils are responsible for the plasma shaping and position control.

$|\vec{B}_\varphi| \gg |\vec{B}_\vartheta|$, $\vec{B}$ has a very shallow pitch angle ($b = \mathrm{atan}(|\vec{B}_\vartheta|/|\vec{B}_\varphi|) \approx |\vec{B}_\vartheta|/|\vec{B}| \approx 0.2$) [7], with each magnetic field line lying on the nested toroidal flux surfaces (Fig. 1.3a). Most magnetic lines never close on themselves after an entire toroidal turn, and therefore the lines cover ergodically the magnetic surfaces. The *safety factor* in Eq. 1.4 defines the number of toroidal turns required for $\vec{B}$ to make one poloidal transit. R_{major} and a are the major and minor radii of the machine, respectively.

$$q \approx \frac{a}{R_{major}} \cdot \frac{|\vec{B}_\varphi|}{|\vec{B}_\vartheta|} \tag{1.4}$$

Among the magnetic field lines, the so called *separatrix* (Fig. 1.3b), or *Last Closed Flux Surface* (LCFS), defines the separation between two domains: the *plasma core* where closed field lines trap the charged particles, and the *Scrape–Off Layer* (SOL) where field lines intersect the plasma–facing components (PFCs) [3]. Plasma–wall interactions occur in the SOL.

Another region of interest is the *plasma edge*, developed within the plasma core domain

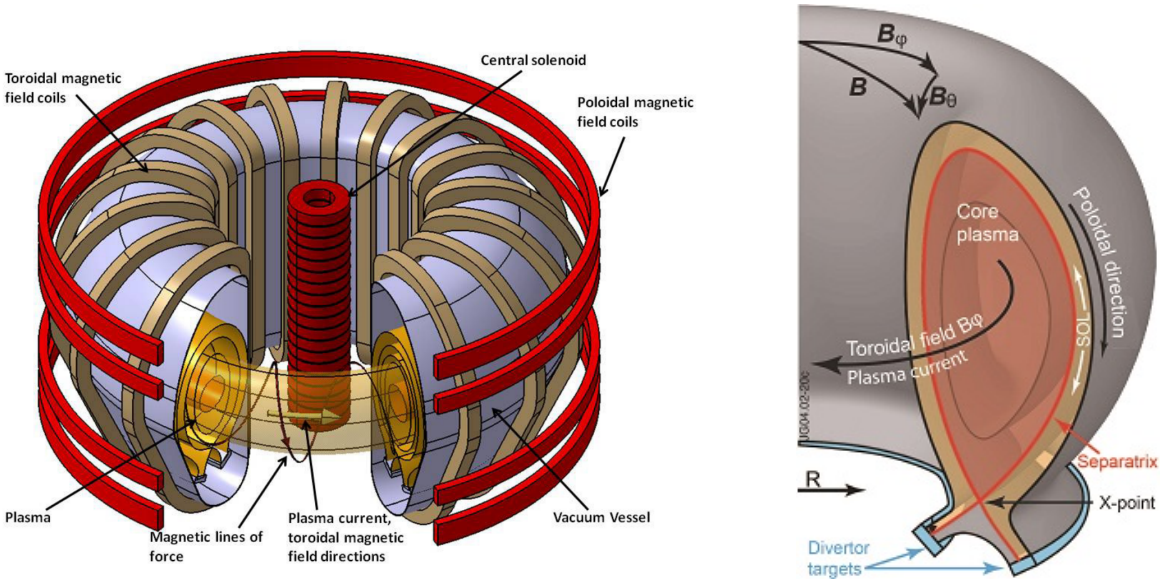

(a) (b)

Fig. 1.3: (a) Schematic of a tokamak [1] (*Figure reproduced with permission by the IAEA*); (b) Poloidal–radial section of an elongated plasma inside the main chamber of a tokamak [8] (*Figure attributed to Bruce Lipschultz and UKAEA graphics office, and used with permission*).

in proximity of the separatrix, Fig. 1.3b, where a strong pressure gradient is established if the plasma is heated above a threshold value. This pedestal, acting as a barrier to particle transport, characterizes the high–confinement regime (H–mode), in contrast to the low–confinement regime (L–mode) [9]. What determines the confinement regime is ultimately the amount of heating power received by the plasma or, more precisely, the power carried by charged particles crossing the LCFS. Albeit no first principle criterion exists to quantify such threshold power, various empirical scaling have been proposed in the past. The most commonly employed is the so–called Martin Scaling [10].

1.2.1 Roadmap towards commercial fusion power plants

The demonstration of the scientific feasibility of the fusion reaction on Earth has already been achieved by the world's largest tokamak, the Joint European Torus (JET), built in the 80's in Culham (UK). In 1997, JET produced 16 MW of transient fusion power with Q close to break–even (Q = 0.62) [11]. With its ITER–like wall, JET is, for the time being, the only device able to operate with D–T [12], therefore its experimental results support the next device along the fusion roadmap, i.e. the International Thermonuclear Experimental Reactor (ITER), currently under

construction in Cadarache (France). ITER is meant to demonstrate the engineering feasibility of large–scale tokamaks, with the goal of producing 500 MW thermal power over 400 seconds, achieving Q = 10. Furthermore, ITER is expected to test different concepts of tritium breeding modules in support of the next DEMOnstrations fusion power reactor (EU–DEMO), whose aim is instead to prove the commercial feasibility of fusion for electricity production with a closed self–sufficient fuel cycle [6]. While JET and DEMO are mainly European projects, ITER is classified as the biggest international joint experiment involving Europe, China, India, Japan, Korea, Russia and the United States.

1.3 Limiters in Tokamaks

The fraction of the total plasma input power (typically coming from ohmic, auxiliary heating and fusion alphas), which is not radiated arrives at PFCs by means of energetic particles. Synergic and multi–scale plasma–surface interactions occur in the SOL during normal operation (Fig. 1.4), which create a big challenge for plasma–facing materials. From the plasma side, energetic ions near the PFC can be neutralized, neutrals can then be ionised, giving electrons the ability to penetrate into the material. This enhances the recycling phenomena in proximity of the surface. Furthermore, in the region immediately close to the PFC, the SOL is characterized by an electrostatic and magnetic sheath produced by an accumulation of positively–charged particles attracted by the negative potential of the metallic structure. Although this potential sheath mediates the plasma–material interactions, there is a strong exchange between plasma and PFCs: the latter acts as a sink for both charged particles and power, while particles re–emitted from the PFC surface return to the plasma [7].

While most of the multi–scale radiation damage processes and kinetics are known, quantitative details regarding these interactions remain to be established, especially during plasma–wall contacts. Broadly speaking, the main wall's innermost layer (i.e. first wall, FW) experiences the interaction with plasma energy and particles, whose dynamics are more pronounced on either PFCs protruding from the main wall (i.e. limiters) or directly exposed to open field lines (i.e. divertor), which act as particle sink. A schematic of these two components is shown, respectively, in Fig. 1.5a and Fig. 1.5b. Both the limiter and divertor are included to protect the main wall

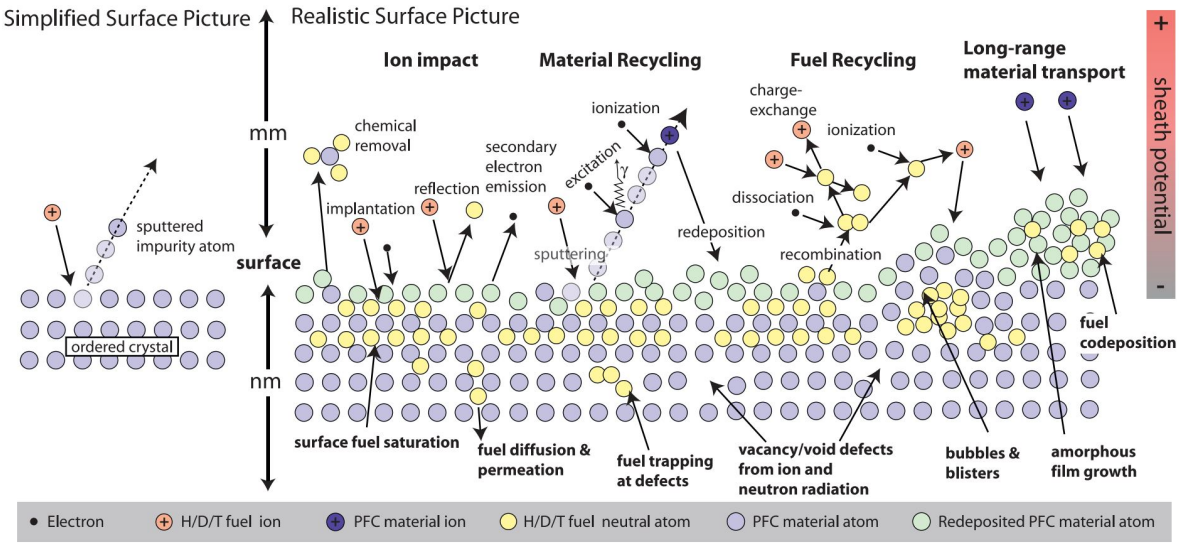

Fig. 1.4: Synergistic and dynamic multi–scale plasma–wall interactions occurring at the material surface in a tokamak environment [13]. *Figure used with permission of Springer Nature, from [13]; permission conveyed through Copyright Clearance Center, Inc.*

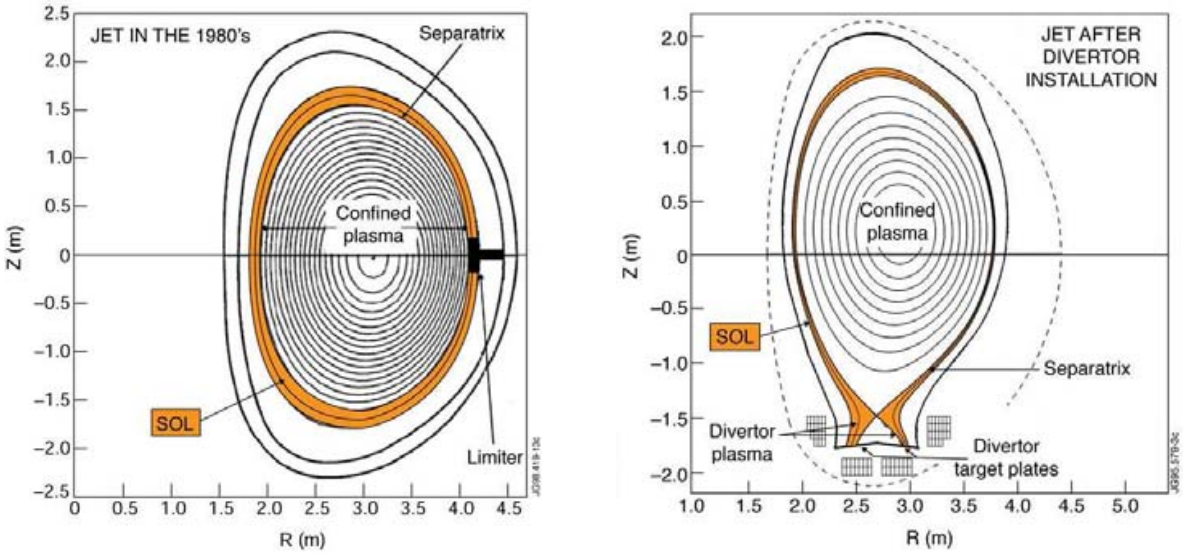

(a) (b)

Fig. 1.5: Poloidal–radial cross sections of: (a) limiter plasma magnetic configuration; (b) divertor plasma magnetic configuration of the Joint European Torus [12].

against excessive particle energy deposition, although their interaction with the plasma occurs under different conditions. In the first generation of tokamaks, the circular plasma is "limited" as its LCFS is defined by the contact with the most protruding PFC, hence the name *limiter*. However, in such configurations, a considerable amount of impurities are released into the

plasma due to erosion of the limiter material sputtered under charged particle bombardment, which unavoidably increases the plasma radiative losses. This effect is mitigated by a change in the plasma configuration, which becomes elongated and delimited by a LCFS with a null value of $|\vec{B}_\vartheta|$ at the X–point. The plasma elongated configuration is achieved with the introduction of additional poloidal field coils. No contact point between main wall and separatrix is present, except below the X–point where the divertor is required for exhausting the particle energy flowing along the open magnetic field lines of the SOL. Hence, the divertor is subjected to high heat flux during steady–state operation.

As the plasma volume and the complexity of the machine increased, the new "diverted" configurations overcome the main issues of the "limited" plasma, being more efficient in energy confinement and plasma impurity control [1]. Most tokamaks use a diverted configuration which enables the H–mode; however, typical plasma scenarios foresee limited plasma configuration phases during both normal operation transients (i.e. ramp–up and ramp–down) and off–normal transients (i.e. disruptions). With a diverted plasma, limiters do not shape the plasma. They are used instead for protecting the wall against potential contact with the plasma, which could damage the structure following any release of energy in small timescales. Unlike the divertor, limiters experience transient heat loads whose magnitude strongly depends on the energy content of the plasma touching them.

In principle, limiters can take any of the geometrical shape illustrated schematically in Fig. 1.6. The poloidal circular ring (Fig. 1.6a) and the continuous toroidal rail (Fig. 1.6c) represent the easiest limiter concepts behind the assumption of, respectively, toroidal and poloidal plasma symmetry. The connection length (C_l), i.e. the distance along $\vec{B}$ that a particle has to travel through the SOL before striking the limiter again is $C_l = 2\pi R$ for a poloidal ring and $C_l = 2\pi Rq$ for a toroidal rail, R being the major radius of the machine. It follows that any protruding object with a limited extent both in poloidal and toroidal directions (Fig. 1.6b) has a particularly large C_l, since almost none of the field lines close on themselves. Particles also eventually strike the inserted limiter, whilst mapping out the entire flux surface they lie on outside the LCFS. In JET (Fig. 1.7), there are several inertially–cooled poloidal limiters running from the top towards the divertor region. ITER, instead, will use a *wall–limiter*, i.e. a wall designed to withstand any plasma–wall contacts that might arise, and hence made of in–vessel tiles requiring high alignment

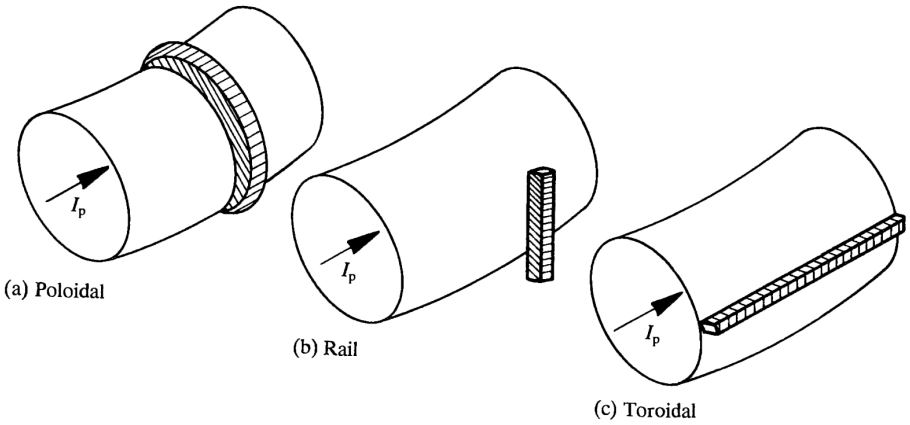

Fig. 1.6: Sketch of the three limiter geometry types: a) Poloidal Limiter; b) Rail Limiter; c) Toroidal Limiter [3]. *Figure reproduced with permission of the Oxford Publishing Limited through PLSclear.*

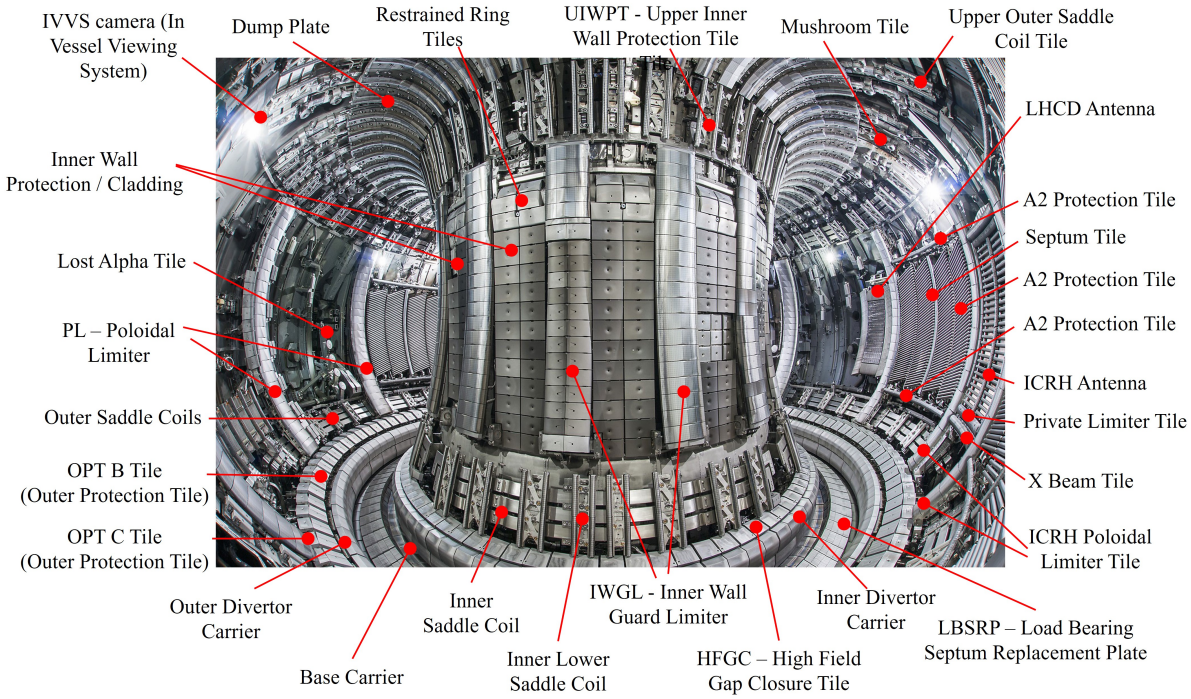

Fig. 1.7: JET in–vessel component overview [14].

precision and very small gaps between them.

The commercial feasibility of fusion with inherent tritium breeding self–sufficiency relies on maximising the in–vessel area of the breeding blanket, while protecting it using the minimum number of protection systems against plasma–wall contacts. This is the reason why discrete limiters are foreseen in DEMO as protections against disruptions, while ensuring the minimum impact on the tritium breeding ratio, i.e. the ratio between the bred and the burnt tritium.

1.3.1 DPhil research aim and thesis content

The main aim of this study is to define an engineering design workflow for high heat flux components for fusion devices. The work builds up both understanding and predictive modelling capabilities established by the author for phenomena occurring at the component plasma–facing surface. The main focus is the essential limiter technology within the in–vessel components of the EU–DEMO tokamak, although the application of the research findings goes beyond just DEMO. In fact, the TARTIFL&ETTE approach (explained below) developed by the author can be applied to any solid component undergoing high heat flux, regardless of the application field.

In a future power generation tokamak, limiters are essential to protect the main wall against energy depositions following any normal and off–normal plasma–wall contacts. Although the limiter concept can be understood from the theoretical standpoint, at the time of writing, no practical applications satisfying the DEMO requirements exist among the worldwide experimental devices. The need for some predictive engineering tools supporting the designer in the engineering design phase of a PFC leads the author to identify the main key phenomena and the way those could be tackled from an engineering perspective.

The content of the thesis is organized as follows. A general overview of fusion principles is followed by a literature review dealing with issues encountered on the way towards the identification of the research gap (Ch. 2). The content of Chapter 2 is referenced throughout the thesis.

The limiter design workflow is described in Ch. 3 with the definition of the PFC limiter design, followed by charged particle heat load calculations, based on field line tracing approach. The estimated maximum heat load during disruptions leads the author to investigate how the heat transfer in the presence of phase change could help evaluate the minimum required armour thickness to protect the cooling system integrity during such disruptive transients, which is one of the most crucial requirements for limiters. No such justification is found in literature for designing actively cooled PFCs, therefore this research gap is tackled by investigating other research fields (aerospace, applied maths, food and chemical industry). Treating the heat transfer in solids undergoing phase change as a *multi–phase moving boundary problem* (Ch. 3), the Matlab®–based TARTIFL&TTE (**T**hermal **A**nalysis fo**R** **T**racking **I**nter**F**aces under me**L**ting **&** vaporiza**T**ion–induced plasma **T**ransient **E**vents) software is developed and implemented by

the author for a basic understanding on how to tackle it, starting from 1D domains under uniform heat flux and constant material properties. The author then takes a step forward by developing the 3D–TARTIFL&TTE, which is a COMSOL Multiphysics® implementation for 3D domains and including more complex physics for realistically capturing the vaporization phase and its related material removal (Ch. 4).

Although TARTIFL&TTE is satisfactorily benchmarked against the only computational example found in literature, the significant contribution of this thesis is the 3D–TARTIFL&TTE, whose validation is supported by (a) semi–experimental data previously generated in the QSPA facility (Quasi–Stationary Plasma Accelerator Kharkov-50, Ukraine) – unfortunately no longer available due to the changed international circumstances since February 2022 – and by (b) data generated by a dedicated melting experiment campaign run in the GLADIS facility (Garching Large Divertor Sample Test Facility, Germany). The experimental apparatus is described in Ch. 5, together with the benckmark results.

Finally, in Ch. 6, the integrated design of the Upper Limiter is described. On a conceptual basis, the EU–DEMO limiter is made up of a refractory PFC directly exposed to the plasma, which is supported by a shield block (SB) made of water and steel. The latter is fastened directly to the vacuum vessel (VV). Both the PFC and SB are actively cooled by dedicated cooling systems, as described in Ch. 6.

Overall, the principal accomplishments in this DPhil research work include:

1. The determination of a whole engineering design workflow for a component undergoing high heat flux, resulting in the first example of integrated engineering design of the EU–DEMO Upper Limiter;

2. Identification of the working conditions for the design of a limiter PFC under a set of plasma magnetic configurations, followed by field line tracing code heat load calculations on PFCs;

3. The development of an engineering approach for modelling heat transfer in solids undergoing phase changes. This approach, implemented as a 3D model in COMSOL Multiphysics®, is able to capture the energy contributions involved in phase changes under high heat flux, and is proposed as a predictive tool to estimate the minimum and safest PFC armour

thickness during the engineering design phase;

4. Development of a novel methodology for measuring the depth of molten thickness in materials undergoing phase change, and benchmark it against the molten layer depth modelled by 3D–TARTIFL&TTE;

5. The integrated design of a limiter equipped with an alternative SB layout concept reducing the electro–magnetic effects.

As a result of this work, the following four papers are presented by the author, co–authored by Professor Peter Ireland and Dr. Zsolt Vizvary, and referenced throughout the text.

1. *Rationale Behind EU–DEMO Limiter's Plasma–Facing Component Design Under Material Phase Change*, published in Institute of Electrical and Electronics Engineers (IEEE) Transactions on Plasma Science, `https://doi.org/10.1109/TPS.2022.3169232`.

    - The paper was presented at the 2021 Symposium on Fusion Engineering (SOFE), and includes the Ch. 3 findings, i.e. the mathematical approach of TARTIFL&TTE and its computational benchmark. It is referenced throughout the text in [15].

2. *Advances in material phase change modelling approach for EU–DEMO limiter's plasma–facing components*, published in Fusion Engineering and Design, ISSN 0920-3796, `https://doi.org/10.1016/j.fusengdes.2023.113477`.

    - The paper was presented at the 32$^{\text{nd}}$ Symposium on Fusion Technology (SOFT–32), and includes the Ch. 4 findings, i.e. the 3D–TARTIFL&TTE implemented by the author in COMSOL, together with the benchmark against semi–experimental data generated from high heat flux QSPA facility. It also includes the UL PFC design in §6.2. It is referenced throughout the text in [16].

3. *High heat flux tests in support of the 3D computational modelling of melting for the EU–DEMO first wall limiters*, published in IEEE Transactions on Plasma Science, `https://doi.org/10.1109/TPS.2024.3375642`.

    - The paper was presented at the 2023 SOFE, and describes the 3D–TARTIFL&TTE benchmark against melting experimental data generated by the GLADIS facility (Ch. 5). It is referenced throughout the text in [17].

4. *The Integrated Engineering Design Concept of the Upper Limiter within the EU–DEMO LIMITER System*, published in Fusion Engineering and Design, ISSN 0920-3796, `https://doi.org/10.1016/j.fusengdes.2024.114329`.

    - The paper was presented at the 15$^{\text{th}}$ International Symposium on Fusion Nuclear Technology (ISFNT-15). It includes the UL integrated conceptual design equipped with a sliced SB, as conceived and developed by the author, followed by the assessment workflow (i.e. electro–magnetic, neutronic, thermal–hydraulic and thermal–structural assessments in support of the design choices), which is performed by a specialized group of analysts led by the author as EU–DEMO Limiter System Design Lead on behalf of the EUROfusion Demo Central Team (Ch. 6). It is referenced throughout the text in [18].

Chapter 2

Literature review

"Fusion will be ready when society needs it."

Lev Artsimovich

This chapter gives an overview on the current EU–DEMO design baseline, and its protection strategy which relies on the presence of limiters. The limiter location is based on predictions made on plasma–wall contacts following some of the foreseen deviations from the plasma equilibrium, which lead to disruptive events. This analysis builds on a description of the field line tracing approach for PFC surface heat load calculations due to charged particles. Disruption–induced heat loads are expected to be high enough to erode the metallic armour and cause phase changes. Reports of how heat transfers in solid undergoing phase changes are identified in literature, and gaps related to this field are also found and discussed.

2.1 The European DEMOnstration fusion power plant

The EU–DEMO bridges a gap in the European roadmap towards fusion electricity. It is expected to become operational after ITER, paving the way to the first–of–a–kind commercial power plant. DEMO's unique requirements [19] are: high coolant temperatures for efficient power conversion, structural materials operating in high neutron fluence environment, availability maximization, fuel self–sufficiency (i.e. closed fuel cycle).

The EU–DEMO is designed to produce 500 MW electric power from 2000 MW fusion power

during a 2 hours pulse [20]. In order to achieve a closed fuel cycle, different tritium breeding blanket concepts are currently under investigation [21]. They contain breeding material, enriched with Li^6, which is expected to cover more than 80% of the total surface exposed to the neutron flux for tritium breeding enhancement.

DEMO is currently in its conceptual design phase. The latest EU DEMO 2017 baseline foresees a DEMO torus with $R_{major} = 9$ m (and a minor radius equal to a = 2.9 m) [22], modularly subdivided in 16 sectors of 22.5°, each of them being enclosed between two toroidal field coils [23]. Every sector is equipped with upper and equatorial ports permitting the installation and maintenance of in–vessel components (IVC) [24].

In addition, every sector is subdivided into three outboard and two inboard segments, where the breeding blanket is enclosed. Every segment's FW is covered by a thin refractory W armour, to protect the blanket from excessive heating while minimizing the attenuation of the neutron flux into the tritium breeding zone. The steady state heat flux the present FW technology can cope with is limited to 1-2 MW m^{-2} [25]. DEMO foresees a lower single null divertor configuration for particle and power exhaust.

The DEMO breeding blanket is a complex and expensive system. The adopted DEMO protection strategy foresees the use of sacrificial protruding limiters, whose aim is to prevent any plasma–wall contacts from happening during the full plasma operation. Segments, limiters and divertor are directly attached to the VV, which is the containment ensuring a high degree of vacuum for plasma to occur. A 22.5° DEMO sector overview is shown in Fig. 2.1, where the different kinds of limiters, i.e. UL, OML, OLL, and IML, are introduced in §2.1.1.

VV, toroidal and poloidal field coils are enclosed in a cryostat enabling superconductive coils to be deployed for generating high $|\vec{B}|$ (4.89 T at the machine centre [22]).

2.1.1 Limiters in DEMO

A plasma pulse is a sequence of events that include: a *ramp–up* (RU) phase, going from the plasma creation (in limited configuration, whose magnetic snapshot is captured in Fig. 2.2a) to its burning state; a *flat top* phase, when the plasma current maintains its reference value while the plasma burns (plasma in diverted configuration, with a magnetic configuration in Fig. 2.2b); a *ramp–down* (RD) phase, i.e. when the plasma cools down and disappears. Although

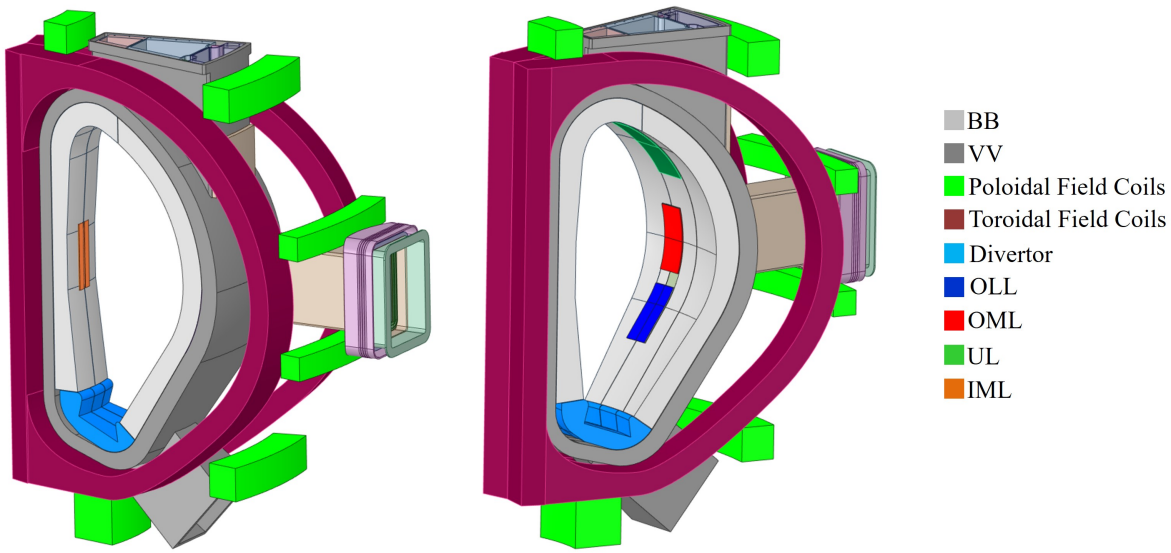

Fig. 2.1: Highlight of 22.5° DEMO sector main components [26].

the plasma is subjected to little variations during flat top, it is here assumed that the plasma magnetic configuration at the start–of–flat top (SOF) is representative of the entire flat top phase. The DEMO SOF foresees a single–null plasma shape whose separatrix is kept 225 mm away from the wall at the outer midplane [23, 27].

The plasma pulse evolution is usually simulated by a finite number of magnetic configurations computed by equilibrium codes that determine the plasma shape and position (i.e. the poloidal magnetic flux surfaces) in force balance with the magnetic field, given the configuration of the external coil currents. As a result of these simulations, plasma magnetic equilibrium snapshots like the ones in Fig. 2.2 are generated.

Although elongated plasmas enhance the fusion performance of a tokamak, they are vertically unstable, and therefore require an active stabilization system. Several factors cause the plasma to lose its stability and disrupt, i.e. a) plasma control system technical issues, b) plasma perturbations beyond controllable limits, c) plasma impurity concentration above the stability level. A disruption is a sudden loss of magnetic confinement, resulting in a release of plasma energy onto the surrounding structures [28]. It can evolve in different ways based on the displacement and velocity of the plasma magnetic axis position and on how fast the plasma energy decreases. A disruption is usually characterized by a plasma thermal quench (TQ), followed by a linear current decay from its nominal value to zero (current quench, CQ). When a plasma–terminating

disruption is initiated by an upward or downward vertical displacement of the plasma beyond its nominal position, then followed by TQ and CQ well after the plasma becomes limited, the off–normal transient is classified, respectively, as Upward or Downward Vertical Displacement Event (referred to as, respectively, UVDE and DVDE) [28]. Without any mitigation strategy in place, in fact, the worst–case scenario develops when the fully–energetic plasma loses its vertical stability, starts drifting vertically until it hits the wall and transitions towards a limited configuration, cooling down while releasing energy and current into the structure. Because motion into a limiting surface converts currents on closed field lines to current on open field lines (SOL) [28], a fraction of I_p (known as a halo current, I_h) can also flow through the wall. VDEs, and VDE–generated loads, will be taken as reference off–normal events for limiter design purposes. The magnetic snapshots of the plasma during UVDE and DVDE TQ phases are reported, respectively, in Fig. 2.2c and Fig. 2.2.

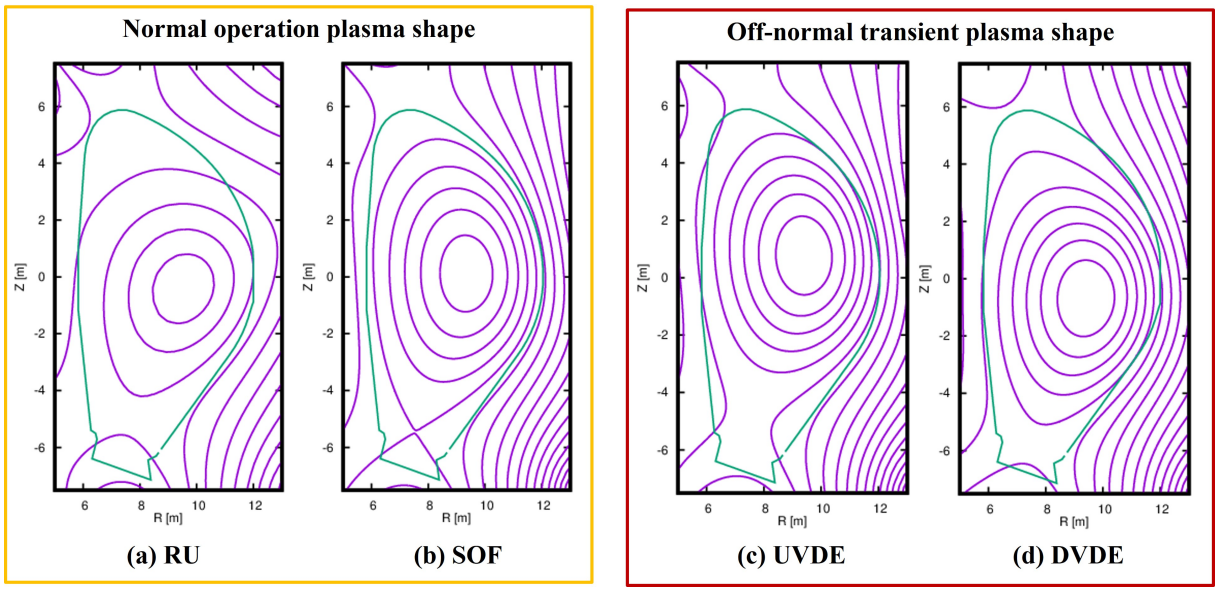

Fig. 2.2: Plasma magnetic snapshots during both normal operation and accidental transients.

Together with disruption mitigation strategies, special counteractions are needed to prevent the plasma from touching the wall during both normal and disruptive events in high–power tokamaks. Unlike the existing experimental tokamaks, which work without tritium and with lower plasma power levels, DEMO cannot operate safely with a bare tritium–breeding wall [29] as any plasma perturbation could push the plasma boundary towards the wall, causing severe damage. Therefore, as anticipated in §1.3, protruding protection panels – named limiters –

will be used for constraining the plasma boundaries. Limiters do not play any role in plasma stability. They are only meant to face plasma–wall impacts following unmitigated perturbations. Four different kinds of limiters are required to adequately protect the FW [30, 31] (see Fig. 2.3) against the plasma–wall contacts identified in Fig. 2.2. Every limiter's plasma–facing surface design is based on some assumptions on plasma parameters like $\dot{P}_{SOL}$ and λ, whose definition will be given in §2.2.1:

- Outboard Midplane Limiter (OML, 4 in the 360° torus) providing protection during plasma RU/RD normal operation transients, and located at the outboard midplane. Plasma parameters assumed as design criteria are: $\dot{P}_{SOL}$=3.5 MW deposited over 35 sec, with λ=6 mm;

- Outboard Lower Limiter (OLL, 4 in total) to protect against accidental DVDEs. Plasma parameters during TQ are: $\dot{P}_{SOL}$=325 GW released in 4 msec; λ=7 mm. Plasma parameters during CQ are: $\dot{P}_{SOL}$=10 MW over 200 msec; λ=10-30 mm.

- Upper Limiter (UL, 8 in total) to protect against UVDEs. Plasma parameters during TQ are: $\dot{P}_{SOL}$=325 GW in 4 msec, λ=7 mm. Plasma parameters during CQ are: $\dot{P}_{SOL}$=10 MW in 200 msec; λ=10-30 mm.

- Inboard Midplane Limiter (IML, 4 in total) designed to protect against other transient events such as H–L transitions (i.e. going from high to low plasma performances). Plasma parameters assumed as design criteria are: $\dot{P}_{SOL}$=30 MW in 5 sec, λ=2-4 mm.

2.2 DEMO plasma–wall interaction challenges

Plasma–facing materials are selected to cope with high heat flux under neutron irradiation while minimizing the influx of impurities in the plasma, the tritium trapping, and their neutron activation level. The DEMO baseline structural material selected is EUROFER97, a Reduced Activation Ferritic Martensitic (RAFM) steel produced by replacing high-activation elements (i.e. Mo, Nb) with lower–activation ones (i.e. W, Ta) [32]. This makes its low long–term activation compatible with radioactive waste minimization, and increases its mechanical properties under irradiation–induced damage as a result of its superior creep and swelling resistance under

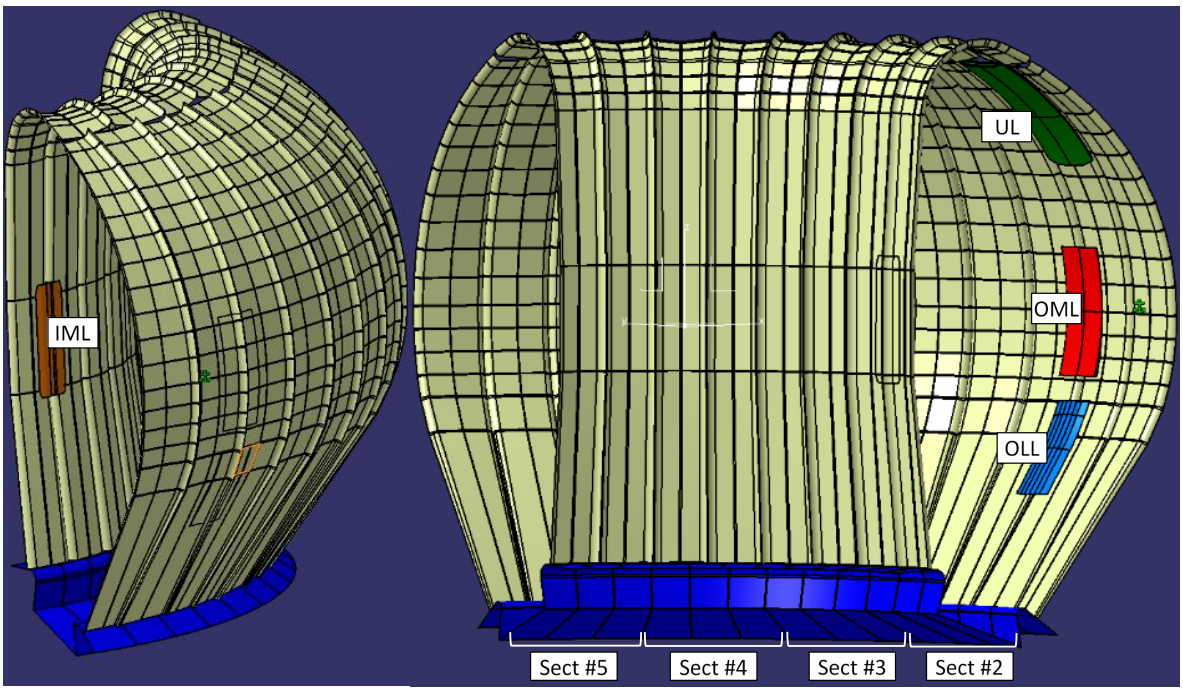

Fig. 2.3: 90° DEMO inboard (lhs) and outboard (rhs) FW equipped with limiters [27].

neutron fluence. However, it constrains the blanket service temperature window to between 350°C and 550°C. Its low thermal conductivity poses an intrinsic limit on the T_{max} it can withstand, above which creep rupture experiments show a change in its most likely deformation mechanism. T_{max} limits the tolerable peak heat flux value to 1-2 MW m^{-2} during flat top [25].

The most serious risk comes from the minimum operational temperature it can experience to avoid brittle failure caused by irradiation embrittlement or creep–fatigue effect combination [33]. Under irradiation, the EUROFER97 ductile–to–brittle transition temperature (DBTT) shifts from 0 to 200°C, below which the steel loses its ductile property and suddenly becomes brittle. The DBTT increase is also affected by He production under neutron irradiation, therefore the safe operation of the blanket should only be guaranteed if irradiated above 330°C [34].

For protecting the structural EUROFER from plasma exposure, a thin layer of W is chosen as plasma–facing armour. W advantages are that it has the highest melting point ($\approx$ 3450°C), low activation under neutron fluence, good thermal–mechanical properties, low sputtering erosion and low tritium retention and co–deposition with respect to other common plasma–facing materials [34, 35], such as Be, C, Mo, and liquid metals (Sn, Li) requiring further investigations.

IVCs experience both surface and bulk damages. The PFC is subjected to surface erosion due to both chemical and physical sputtering. While physical sputtering is a yield–energy

mechanism caused by energetic ions (H, D, T, and plasma impurities) impinging on PFCs, chemical sputtering leads to the breaking of chemical bonds by a moderate kinetic energy if the incident particle spends enough time between atoms [13]. The eroded material can be ionised, neutralized, transported and re–deposited in different areas where T can be trapped, hence affecting the T inventory. Low and medium–Z materials (Be, C, Fe) show unacceptably higher erosion rates than W (1-5 mm FPY^{-1} against 0.1 mm FPY^{-1}) [35]. Furthermore, the 14 MeV-peaked neutron flux interacts with the bulk material producing either vacancies in the lattice due to atom dislocations (i.e. dpa), or transmutation elements following neutron absorption. A typical example is He production, which can accumulate into interstitial gaps causing local swelling. Under neutronic irradiation, graphite shows a reduction of its thermal conductivity and anisotropic swelling. Mo has similar material properties as W but it produces long term activation isotopes, which are unwanted in a fusion reactor [34]. Disadvantages of W are its brittle behaviour even under no irradiation (DBTT$\approx$ 800°C), ion/neutron–induced ultra–structure changes and thermal fatigue behaviour under pulsed heat loads. Preliminary evaluations on alternatives to W have selected materials that have a similar response to W (e.g. Ta, Hf) [36], for which it is accepted that further investigation is needed.

As far as the W PFC heat sink is concerned, Cu alloys are the recommended materials due to the high Cu thermal conductivity. The most serious issue for them is related to the rapid loss of ductility under irradiation at temperatures below 180°C, therefore the operating temperature of the alloys used in DEMO should be kept above 200°C. For some alloys, i.e. CuCrZr, the decrease in strength under irradiation occurring above 250°C limits the upper temperature for engineering structural applications to 350°C, for doses up to $\approx$5 dpa [34].

The normal operation challenges, by themselves, degrade the material mechanical properties of IVCs, consequently reducing their lifetime. These interactions become more complex during off–normal events caused by confinement instabilities, when the fully energetic plasma starts moving from its equilibrium position until it touches the wall. Although the dynamics of any plasma–wall impact depends on the energy flux and the target material, a general trend can be described [37]. During the plasma–wall first touch, the energy carried by plasma ions and electrons is released into the component, which heats up eventually reaching its melting point. If the incoming energy is high enough, vaporization occurs on the front face of the liquid layer.

This is usually a surface effect, as the diffusion length for the duration of the contact $\sqrt{\alpha t}$ is much less than the characteristic length of the component. If well confined, the neutral vapour starts expanding into vacuum along the surface normal direction, while absorbing an increasing fraction of the incoming flux carried by plasma particles coming across the vapour cloud (due to different processes such as ionization, free electron excitation, elastic and inelastic scattering slowing down). The vapour cloud energy content will eventually be isotropically re–radiated as soft X–rays, thus reducing the amount of energy reaching the condensed front surface [38]. This very complex phenomenon is referred to as *vapour shielding*, and its understanding requires an interdisciplinary approach involving heat transfer in a target in the presence of phase changes, conjugated with fluid mechanics and gas dynamics, while self–consistently tracking the vapour–to–liquid interface. The damage of the PFC due to a disruption strongly depends on the different concomitant interactions between plasma and vaporized particles in presence of a magnetic field. So far, uncertainties related to both plasma physics and material behaviour under irradiation make difficult and critical the engineering modelling of the PFC surface damage during its design phase, which has attempted to be addressed through a campaign of experiments limited by the availability of both highly energetic plasma sources and achievable power density levels in different devices.

2.2.1 P_{SOL} and its distribution across the SOL

Predicting how the torus wall is heated during both normal operation and transient events is crucial for designing PFCs. However, the prediction of SOL dynamics during off–normal events is not well understood yet, and experiments on existing devices have been commissioned to explore these phenomena. Currently, predictions about the physics of future devices like DEMO are made through theoretical modelling approaches (e.g. integrated physics simulations) or empirical extrapolations from existing tokamaks (e.g. JET). Both approaches rely on experiments for validation and correlation, respectively. The use of predictive tools developed and validated for existing machines can help to model tokamak physical phenomena that can be scaled to DEMO. Tools for calculating the plasma shape evolution during transient are used for computing the power density on the wall using software that traces the charged particle trajectories in a 3D system, and calculate the related heat load on PFCs. These loads, together with the plasma

radiated power modelled through other numerical tools, give an estimate of the heat load total magnitude to be used for assessing the PFC structural behaviour [27, 31].

The plasma core loses its energy by two main phenomena: radiative and energy transport losses. The radiative losses include line radiation due to impurities, synchrotron radiation due to particle motion in a magnetic field, and Bremsstrahlung radiation due to Coulomb collisions. Transport losses refer to energetic particles escaping the plasma core by conduction along and diffusion across field lines. Consideration of these two mechanisms, shows that the motion parallel to field lines prevails over the cross–field diffusion, as the component of the particle velocity parallel to the magnetic field is close to the plasma sound speed ($v_{\parallel} \approx c_s \approx \sqrt{\frac{k_B \cdot (T_i + T_e)}{m_i}} \approx 10^5$ m s^{-1}, where c_s is calculated at the typical ion edge temperature $T_i \approx T_e = 100$ eV) [7], which is many orders of magnitude larger than the perpendicular one, $v_{\perp}$. A rough estimate of $v_{\perp}$ can be obtained by using the Fick's law for describing the particles diffusive motion across field lines. The particle flux density Γ [particles m^{-2} s^{-1}] can be expressed through Eq. 2.1, where n is the volumetric particle density [particles m^{-3}] and v is the particle bulk velocity [m s^{-1}].

$$\Gamma \equiv n v_{\perp} = -D_{\perp} \frac{dn}{dx} \approx -D_{\perp} \frac{n}{l_{\perp}} \tag{2.1}$$

Assuming the empirical cross–field diffusion coefficient is equal to $D_{\perp} \approx 1$ m^{2}s^{-1} [7], and the characteristic radial scale length of particles is equal to $l_{\perp} \approx \sqrt{\frac{D_{\perp} C_l}{c_s}} \approx 1$ cm, with $C_l = 100$ m for example, it follows that $v_{\perp} \approx 100$ m s^{-1}. The very large ratio $v_{\parallel}/v_{\perp}$ justifies the approximation of neglecting the cross–field transport, and also explains why the SOL is a thin radial layer, whose thickness might reach the order of centimeters [7]. Although the radiative losses in future devices are expected to be bigger than the particle losses along magnetic field lines [27], the radiated power is uniformly deposited over a large surface, and this does not pose any challenge to the PFC design. On the contrary, the energy carried by charged particles can generate hot spots which could overcome the engineering limits, thus requiring a suitable PFC engineering solution [27].

As far as the plasma power fluxes during DEMO normal operation are concerned, the current assumptions foresee a total alpha particle and auxiliary heating power equal to $\dot{P} = 450$ MW, of which $\dot{P}_{rad,core} \approx 300$ MW is radiated in the core and reaches the FW, whereas $\dot{P}_{sep} = 154$ MW, conservatively amplified by 1.5 times (231 MW), crosses the separatrix. $\dot{P}_{sep}$ is distributed

into three different channels, according to the following assumptions [27, 31]: $\dot{P}_{rad,LCFS} = 40\%\dot{P}_{sep}$ is radiated in the SOL, $\dot{P}_{near-SOL} = 30\%\dot{P}_{sep}$ directly flows onto the divertor surface through charged particles, while $\dot{P}_{far-SOL} = 30\%\dot{P}_{sep}$ is carried directly by charged particles to divertor and wall. $\dot{P}_{near-SOL}$ and $P_{far-SOL}$ are assumed to decay exponentially with two different values of fall–off lengths, namely $\lambda_{near-SOL}$ and $\lambda_{far-SOL}$, respectively. While the $\dot{P}_{near-SOL}$ parallel conduction exponential decay has been experimentally observed in existing devices [39], the $P_{far-SOL}$ decay is built on a conservative assumption of taking into account a very large perpendicular diffusion of particles far from the LCFS, which then affects the distribution of power deposited onto the wall [27]. The parameters of interest for this research work, especially for the limiter design, shaping, and heat load calculation, are $\dot{P}_{far-SOL}$ and $\lambda_{far-SOL}$, which will be hereinafter referred to as $\dot{P}_{SOL}$ and λ, respectively, unless differently specified.

As anticipated before, $\dot{P}_{SOL}$ is assumed to decrease exponentially across the distance δ between LCFS and wall by a characteristic fall-off length (λ) calculated at the mid–plane of the machine. λ is the far–SOL width carrying particles and power to the PFCs, and it is determined by the ratio of the transport coefficient perpendicular to magnetic field lines to the one parallel to them. Therefore, assuming that the power decay in the SOL is described by a single exponential function, the power deposition on a surface of normal $\vec{n}$ due to charged particles is calculated as in Eq. 2.2 [7, 40], where the sign "%" indicates the fraction of $\dot{P}_{SOL}$ directed towards the inner and outer targets, usually chosen to be 1/2 or 2/3 for the outboard targets. All the parameters at the denominator are calculated at the equatorial midplane.

$$HF = \frac{\%\dot{P}_{SOL}}{2\pi \cdot R_{LCFS} \cdot \lambda \cdot B_{\vartheta}} \vec{B} \cdot \vec{n} \cdot e^{-\frac{\delta}{\lambda}} \tag{2.2}$$

2.2.1.1 3D Field line tracing approach for surface heat load calculations

The pure parallel particle transport can be modelled by means of field line tracing codes such as SMARDDA [40] (or, equivalently, PFCflux [41]) for generating charged particles power deposition mapping (Eq. 2.2) on 3D PFC surface geometries.

Developed at UKAEA Culham Centre for Fusion Energy (UKAEA–CCFE), its acronym comes from SMART+DDA, with SMART=Spatial Measure for Accelerated Ray Tracing and DDA=Digital Differential Analyser [40]. The rationale behind the SMARDDA code entails

starting from a triangulated surface model. The magnetic field lines are then tracked backwards from every geometry cell centre. Each magnetic field line is approximated as a set of straight short segments, each of which is tested for intersection with the triangulated shadowing PFCs until a maximum distance (C_l) of the magnetic field line is spanned. In case the magnetic field line crosses the midplane – defined by the plasma centre coordinates of the scenario analysed – before hitting the shadowing geometry, the starting cell is considered wetted by the plasma, and the power "flows" from the midplane along flux tubes to the starting PFC cell position. Otherwise, if the magnetic field line hits any shadowing PFC before crossing the midplane, the starting position is considered shadowed by the intersected surface. The power deposition calculation is based on a simple flux–tube model: the magnetic field lines are followed until they intersect the geometry, and the power deposited (Eq. 2.2) is kept constant through the flux tube connecting the physical surface to the tokamak midplane [40].

One limitation to the backward field line tracing approach is related to the magnitude of the heat load calculated on the wetted area when plasma limited equilibria are analysed, and this effect is amplified in presence of discrete protruding components, like the limiters. As the power deposition value is related to the number of times the field line passes through the midplane before striking the wall, the heat flux pattern could be different whether the magnetic field line is allowed to cross the midplane several times after the first time. This uncertainty contributes to affect the missing power balance, i.e. the integrated power density at the end of every run ($\dot{P}_{output}$) is not always equal to the input power $\dot{P}_{SOL}$. In order to negate the missing power, the HF values are rescaled according to Eq. 2.3 in [42].

$$HF_{rescaled} = \frac{\dot{P}_{output}}{\dot{P}_{SOL}} \cdot HF \tag{2.3}$$

2.3 Heat transfer problems in solid components undergoing phase changes

Plasma loss of confinement events (e.g. VDEs) can bring the plasma to hit the metallic wall, releasing its energy content in a short time interval. During this timescale, the coolant does not play any role in mitigating the heat load, which is dissipated through the material thermal

inertia. As a consequence, the struck component is subjected to melting and surface erosion due to intense vaporization and liquid splashing, probably due to magneto–hydrodynamic instabilities. This leads to the potential structural failure of the component due to steep temperature gradient with high thermally–induced deformations. The importance of predicting the PFC surface damage following an interaction between highly energetic plasma and metallic structure is crucial for preventing high heat flux values from reaching the coolant channels, causing the tube wall burnout.

2.3.1 The Stefan Problem

The investigation of the heat transfer in solids involving a phase change falls within the class of Stefan problems [43, 44], named after the physicist Josef Stefan who first investigated the ice–water phase transition. This kind of problem is characterized by interfaces between different phases whose positions are not known in advance, being themselves part of the solution. Usually, a moving inter–phase is associated with time–dependent heat conduction problems described by the Fourier equations (Eq. 2.4 and Eq. 2.5), a set of initial and boundary conditions, and two additional conditions to be satisfied at the interface between phases. The first condition constrains the temperature to be at the phase change value (Eq. 2.6), whereas the second imposes the energy balance known as *Stefan condition* (Eq. 2.7). The solution describes the time–and–space temperature variation in all the phases and the evolution of the moving boundaries between them.

The Stefan condition (Eq. 2.7) can be intuitively determined by a graphical energy balance across an infinitesimal thickness of solid material undergoing phase change, under the assumption of phase–wise constant thermal properties and no difference in density between phases. Considering the 1D heat transfer process within a solid slab depicted in Fig. 2.4, if the heat flux causes the slab to melt, a moving boundary at s(t) separating the liquid and the solid phases appears during the process. If the inter–phase moves by ds in a time interval dt, the amount of energy per unit area $\rho H_m ds$ is absorbed through melting. The energy involved into the phase change is provided by the difference between the heat conducted in the solid into the elemental slab and that conducted into the liquid phase. According to Eq. 2.7, the rate of change of latent heat equals the jump in heat flux across the interface. The continuity of the heat flux across

the interface can be satisfied only if either no phase change occurs ($H_m = 0$) or the inter–phase does not move ($ds = 0$).

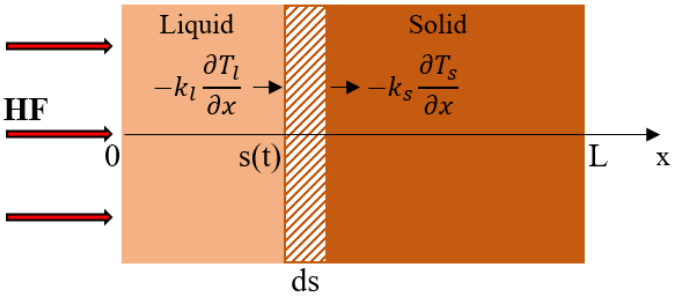

Fig. 2.4: Graphical visualization of the Stefan condition.

$$\rho c_{p,l} \frac{\partial T_l}{\partial t} = k_l \frac{\partial^2 T_l}{\partial x^2} \qquad \text{at } 0 \leq x \leq s(t) \tag{2.4}$$

$$\rho c_{p,s} \frac{\partial T_s}{\partial t} = k_s \frac{\partial^2 T_s}{\partial x^2} \qquad \text{at } s(t) \leq x \leq L \tag{2.5}$$

$$T(s(t), t) = T_m \qquad \text{at } x = s(t) \tag{2.6}$$

$$\rho H_m \frac{ds}{dt} = -k_l \frac{\partial T_l}{\partial x} + k_s \frac{\partial T_s}{\partial x} \qquad \text{at } x = s(t) \tag{2.7}$$

For two–phase moving boundary problems, the Stefan condition makes the partial differential equation (PDE) system strongly non–linear as the time and spatial variation of the boundary inherently depends on the temperature evolution.

These problems are common in different research areas of science and technology, i.e. casting solidification processes, food freezing, environmental engineering, ablation of missile skins under aerodynamic heating. Unfortunately, due to the non-linearity of the problem, exact analytical solutions are limited to single moving boundary problems where one of the two phases stays at the phase change temperature. This simplifies the problem since the Fourier equation resolution is only required in one phase [45]. Another example of one–phase Stefan problem is represented by ablation, which is a mechanism used as heat removal for structures facing huge heat fluxes. In this case, the solid material is ablated by an external flow, and this brings the inter–phase to be directly exposed to the ablative heat load following the material removal, for which no temperature evolution has to be modelled. Exhaustive solutions of the Stefan–like problems can

be found in [43]. For multiple moving boundary problems requiring the temperature distribution to be found in all the phases, the solution has to be found numerically [45].

2.3.2 Assumptions behind the multi–phase moving boundary problem

The heat conduction in solids undergoing material phase change involves lots of physical factors on which assumptions are made for simplifying the resolution of the problem. Among all the resources available in literature, the most common assumptions behind a more general multi–phase moving boundary problem are:

1. The heat is considered to be isotropically transferred through the solid body by pure conduction, neglecting other phenomena such as convection and radiation;

2. The thermal–physical properties of the different phases are considered constant within each phase and, sometimes, assumed the same among different phases;

3. Most of the problems considers the same density value of both liquid and solid phases. This means neglecting any effect due to volume variation during the phase change and, therefore, assuming that the energy balance affects only the body enthalpy, neglecting the contribution of the mechanical energy. Considering two different values of density for liquid and solid phases increases the complexity of the problem, and this will be described later (§2.3.2.1);

4. Latent heat is assumed to be constant and absorbed (or released) at a constant phase–change temperature;

5. Most problems assume a planar and sharp interface with zero thickness between phases, which always stays at the phase–change temperature. This is realistic for pure metals, whereas phase changes in alloys occur over a temperature range, with an intermediate "mushy" region as inter–phase.

2.3.2.1 Impact of density variation during melting

The assumptions in §2.3.2 introduce some simplification within an inherently complicated problem. According to V. Alexiades in [46], the most "unreasonable" among these assumptions

is the assumption of the same density for both liquid and solid phases, neglecting any movement of the liquid, which can introduce significant changes into the mathematical formulation of the problem. As an example, the assumption $\rho_l \leq \rho_s$ means that the liquid phase expands and pushes the solid with a uniform speed $v = v(t)$. Although the density change has the minimal thermal effect when the volume change is accommodated by the bulk movement of the existing phase, the only conservation of the thermal energy is not sufficient to determine the evolution of the system which must now satisfy the equations of mass, momentum and total energy. The change in density effectively forces the fluid motion, consequently introducing an advection term in the Fourier equation and a kinetic contribution into the Stefan condition. The macroscopic effect of the (advection) kinetic energy is to slow down the melting process, reducing the energy available for the phase change. Under this assumption, Eq. 2.4 remains the same while both the conductive and convective fluxes due to the motion of the solid (Eq. 2.8) are considered in the new Fourier equation for the solid phase (Eq. 2.9):

$$HF_s(x,t) = -k_s \frac{\partial T_s}{\partial x} + \rho_s c_{p,s}(T_s(x,t) - T_m)v(t) \tag{2.8}$$

$$\rho_s c_{p,s}\left(\frac{\partial T_s}{\partial t} + \frac{\partial T_s}{\partial x}v(t)\right) = k_s \frac{\partial^2 T_s}{\partial x^2} \tag{2.9}$$

The additional requirement related to the mass conservation through the interface gives the relation between $v(t)$ and the interface velocity:

$$\rho_s v(t) = (\rho_s - \rho_l)\frac{ds}{dt} \tag{2.10}$$

As far as the Stefan condition to be imposed at the inter–phase is concerned, the energy balance must take into account the total energy of the system, which has now both thermal and mechanical contributions due to the kinetic energy of the liquid motion. Therefore, at the inter–phase, the Stefan condition becomes Eq. 2.11 [47].

$$\rho_l H_m \frac{ds}{dt} + \frac{\rho_l}{2}\left(1 - \left(\frac{\rho_l}{\rho_s}\right)^2\right)\left(\frac{ds}{dt}\right)^3 = -k_l \frac{\partial T_l}{\partial x} + k_s \frac{\partial T_s}{\partial x} \tag{2.11}$$

The contribution of the kinetic energy in Eq. 2.11 could be neglected only after retaining the density difference in the term representing the motion of the outer boundary, i.e. using $(\rho_s - \rho_l)$

in place of ρ_l on the lhs term [47].

2.3.3 Boundary immobilization technique for Stefan condition non–linearity

Different numerical techniques have to be adopted to overcome the difficulty of solving a system of coupled differential equations within moving domains. Three methods are investigated among the ones available in literature.

Goodman and Shea [48] develop an approximate methodology (Heat Balance Integral Method, HBIM) that transforms the system of PDEs in ODEs (Ordinary Differential Equations) by integrating every energy balance contribution in space, so that the only variable left to solve is time. This requires deep analytical manipulation and the result depends on the initial assumption made upon the polynomial function describing the spatial temperature distribution. In addition, the presence of floating boundaries complicates the resolution of the system, which has some singularities when the phase change starts.

The second approach analysed is developed by Landau [49], and also used by Murray and Landis [50]. This method overcomes the difficulty related to the moving domains by means of a coordinate system transformation, based on the definition of spatial variables (one for each phase) depending on the moving interface position. Although the transformation introduces a convective term inside the classical Fourier equation governing the heat transfer in every phase, it has the advantage that all the spatial domains are now fixed between [0, 1] and their related spatial discretization takes into account the motion of the interface (i.e. the nodal points are actual positions of the interface at every time interval). Consequently, any of the numerical methods developed to solve systems of PDEs in fixed spatial domains can be applied to the problem. Considering similar moving boundary problems faced in solute diffusion–controlled processes [51] and food freezing applications [52], the Landau approach appears to offer the simplest way to solve the multi–phase moving boundary problems.

The third more complex and more computationally demanding Arbitrary Lagrangian–Eulerian formulation (ALE) is usually adopted by specialized software for solving fluid – solid interface problems in domains involving moving boundaries. The ALE method combines the advantages of the two classical kinematic descriptions, i.e. the Lagrangian one used in structural mechanics and the Eulerian one used in fluid–dynamics and electromagnetism.

In the Lagrangian method, PDEs are formulated in the *material frame*, which is fixed to the material and moves with it as it deforms. The Eulerian formulation is instead used for studying the physical state of fluids in fixed points in space (i.e. *spatial frame*), for which tracking the state of individual material particles is difficult. Through coordinate transformation, it is possible to transform the physical equations from the material frame to the spatial frame or vice versa [53].

The Lagrangian formulations cannot deal with large deformations without generating large element distortion, whereas the Eulerian formulation cannot handle moving interfaces or domains. The ALE formulation introduces another grid, referred to as *mesh frame*, whose dependencies with the other frames can be explicitly defined. The nodes of the *mesh frame* can be moved with the continuum following the Lagrangian approach, or held fixed as in the Eulerian system, or moved in arbitrarily specified ways. Both the material and the spatial frames are mapped into the *mesh frame* by means of mathematical equations, which allow the Lagrangian and Eulerian equations to be transformed and solved into the *mesh frame* [53].

In fluid–structure interaction involving moving boundary interfaces, the mechanical displacements represents the relationship between material and spatial frames, and the ALE method establishes additional relationships in the *moving mesh* or *deformed geometry* to describe the apparent displacements and shapes of mesh elements of the spatial frame, in order to take into account the change in the Eulerian domain boundary caused by mechanical deformations. The *deformed geometry* needs additional boundary condition at interfaces between Lagrangian and Eulerian domains, for feeding the structural deformations back into the spatial frame displacement of the *deformed geometry*. The ALE method can also be used with any other interfaces, useful for simulating boundary deformation under mass removal or deposition [53].

Because of the ALE freedom in arbitrarily moving the computational mesh domain without the need for the mesh movement to follow the material, greater distortions of the continuum can be handled than would be allowed by a purely Lagrangian method, with more resolution than that afforded by a purely Eulerian approach. The arbitrary motion of the mesh allows the problem to be solved on a fixed reference domain. Suitable boundary conditions are used for the interfaces [54, 53].

2.4 On the kinetics of evaporation

The first attempt towards evaporation rate estimate has started with Hertz in 1882 [55], followed by Knudsen [56] and Langmuir [57, 58], and since then it has been subjected to continuous improvements driven by its practical importance.

According to classical thermodynamics, vapour and liquid phases co–existing under equilibrium conditions are characterized by values of temperature and pressure which are continuous functions across their interface. In particular, temperature and pressure have the same value in both the phases, and no net particle flux is observed from one phase to another. The kinetics of evaporation becomes important when mass transfer occurs between condensed and gas phases under non–equilibrium conditions. In this case, the evaporation is said to be intense because the molecules do not follow any Maxwellian distribution function, which is typical of equilibrium problems, but they rather move with a thermal velocity that could reach sonic values. Intense surface evaporation is essentially a non–equilibrium interface process which should be described by the kinetic theory of gases.

Examples of intense phase change include evaporation of a liquid in vacuum, selective laser melting, laser ablation applications, simulation of space shuttle airflow during re–entry, etc. The Hertz–Knudsen–Langmuir formula (Eq. 2.12) is widely used for calculating the net molecular flux (J) at the interface between condensed and gas phases, based on the assumptions that particles with mass m_i do not interact with each other but move freely between collisions. They are emitted with a Maxwellian distribution function of velocity, with temperature and pressure values corresponding to the condensed phase temperature and related equilibrium vapour pressure [37, 59]. The net evaporative particle flux depends on the difference between the vapour pressure (P_{sat}) of the substance at its surface temperature (T_s) and the ambient pressure (P_c) exerted on the liquid surface. The saturation vapour pressure is related to the local surface temperature through the Clausius–Clapeyron law (Eq. 2.13), which depends on the ambient pressure (P_{amb}), latent heat of vaporization (H_v), particle mass (m_i), boiling temperature (T_v), T_s and the Boltzmann constant k_B. The maximum value of $J(T_s)$ is reached in vacuum ($P_c = 0$). Eq. 2.12 comes from considerations based only on mass conservation and, since it does not take into account bulk velocity effects in the dynamics of vaporization, it misses the physical coupling between vapour and liquid phases [60, 61]. Despite this, it remains the most widely used boundary

condition for evaporative particle flux evaluations.

$$J(T_s) = J_v^{sat}(T_s) - J_c(T_c) = \frac{\eta_v P_{sat}(T_s)}{\sqrt{2 m_i k_B T_s}} - \frac{\eta_c P_c(T_c)}{\sqrt{2 m_i k_B T_c}} \tag{2.12}$$

$$P_{sat}(T_s) = P_{amb}\ e^{\left(\frac{m_i H_v}{k_B T_v}\left(1 - \frac{T_v}{T_s}\right)\right)} \tag{2.13}$$

In order to take into account the discrepancy between actual and maximum predictable particle flux, two coefficients for evaporation (η_v) and condensation (η_c) are introduced by Knudsen. In the literature it is extensively assumed that $\eta_v = \eta_c = 1$ [62], which is valid during equilibrium conditions or weak evaporation.

The resolution of the gas kinetics problem with a Boltzmann distribution helps bridge this gap, highlighting that strong evaporation problems – especially with metal targets – are characterized by a sharp inter–phase boundary, and a transient non–equilibrium layer between the evaporating surface and the external continuum flow referred to as Knudsen Layer (KL), whose spatial extension is of the order of a few molecular mean free path (mfp). The KL expands with increasing bulk gas velocity away from the surface, where a new equilibrium condition is reached. Therefore, the KL has a sharp discontinuity in momentum, energy and mass balance equations, and the velocity distribution function differs from the equilibrium one [63, 64]. The degree of non–equilibrium (i.e. the intensity of evaporation) is described by the Mach number (Ma) on the KL outer boundary [64, 65]. Under irradiation in vacuum or with a low counter–pressure environment, evaporation occurs with a sonic velocity (Ma = 1), meaning that the particle flux through the KL boundary is the highest, the process takes place under the strongest non–equilibrium and the behaviour of the condensed phase is not affected by the vapour state. On the contrary, subsonic evaporation occurs when the counter–pressure exerted by the gas environment or the previously vaporized particles cannot be neglected, and the state of condensed and vapour phases are interrelated [59, 66]. While some authors have calculated the evaporative flux based only on the condensed phase state [37], others like Ytreus [65], Knight [67] and Anisimov [66] have solved the non–linear gas kinetic equations to calculate the net evaporative flux which is driven by values of temperature and pressure jumps across the KL.

In the following, a review of the relevant evaporative models found in literature are presented.

Although some of them do not directly find application in the following chapters, the author includes them within the literature selection because they have helped (a) build the knowledge background before approaching the problem and, most importantly, (b) reinforce the choices and assumptions behind the 3D–TARTIFL&TTE model (see Ch. 4), especially for the mass continuity boundary condition imposed at the liquid–to–vapour interface.

2.4.1 Intense evaporation models

Different approaches can be found in the literature for estimating the evaporative particle flux under intense evaporation. The two points to be addressed are the evaporation rate estimate and to what extent the KL discontinuity affects the boundary condition definition at the surface of the liquid phase. A brief summary of the most relevant ones for the aim of the present work is reported in the following.

2.4.1.1 Hassanein's modified kinetic theory phase change relationship

Starting from Eq. 2.12, Hassanein based his model in [62] upon the following considerations:

- J_v^{sat} represents the maximum collisionless evaporative flux under vacuum conditions, provided that the vapour expansion is high enough to keep a low vapour density;
- during plasma disruptions, intense vaporization occurs, hence the atom back–scattering cannot be neglected because of vapour density increase in front of the surface. It follows that $J = J_v^{sat}$ at the beginning of vaporization, while $J \leq J_v^{sat}$ thereafter due to recondensation caused by collisions between vapour and the previously vaporized substrate.

Based on Anisimov and Rakhmatulina's transport numerical studies on intense evaporation [66], the fraction of recondensed atoms will increase with time as the vapour density increases up to the asymptotic value $0.2J_v^{sat}$ which is reached after 20 collision times τ_c [s] (Eq. 2.14).

$$\frac{1}{\tau_c} = 16\sqrt{\pi} n_v a_0^2 \sqrt{\frac{k_B T_s}{m_i}} \tag{2.14}$$

πa_0^2 is the elastic scattering cross section of the vapour atoms, n_v the vapour density in front of the surface and m_i is the particle mass, i.e. the molar mass of the substance (M) divided

by the Avogadro constant (N_A). By considering the average Maxwellian velocity of the vapour cloud $\bar{v} = \sqrt{\frac{8k_B T}{\pi m_i}}$, the vapour density [ions m^{-3}] can be related to the particle flux [ions $s^{-1}m^{-2}$] through Eq. 2.15:, where $\frac{\bar{v}}{4}$ represents the average component of the stationary Maxwellian gas along the forward direction [62].

$$J_v^{sat}(t) = \frac{1}{4}\bar{v}n_v = n_v\sqrt{\frac{k_B T_s(t)}{2\pi m_i}} \tag{2.15}$$

Using the following approximation for the atomic volume [m^3 $atom^{-1}$] calculated through the elastic cross section:

$$\Omega = \frac{4}{3}\pi a_0^3 \tag{2.16}$$

Eq. 2.14 becomes:

$$\frac{1}{\tau_c} = 16\sqrt{2}\pi^{\frac{1}{3}}\left(\frac{3}{4}\Omega\right)^{\frac{2}{3}} J_v^{sat} \tag{2.17}$$

By defining τ_r as a relaxation time after which J_c reaches 98% of its asymptotic value, after $20\tau_c$

$$\tau_r = \frac{20\tau_c}{\ln 10} \approx 10\tau_c \tag{2.18}$$

it follows that the condensation flux can be expressed as Eq. 2.19, while the net flux follows Eq. 2.20:

$$J_c = 0.2J_v^{sat}\left(1 - e^{-\frac{t}{\tau_r}}\right) \tag{2.19}$$

$$J(t) = J_v^{sat}(t) - J_c(t) = J_v^{sat}\left(0.8 + 0.2e^{-\frac{t}{\tau_r}}\right) \tag{2.20}$$

Therefore, the evaporation flux is equal to $J(t) = J_v^{sat}(T_s)$ before vaporization begins, for then decreasing as in Eq. 2.20 afterwards. As τ_c can be considered a continuous function of $T_s(t)$, it will be a very large number before the intense evaporation begins, hence $J(t) \simeq J_v^{sat}(T_s(t))$ for $t \leq t_v$. The velocity of the receding surface is given by Eq. 2.21, whereas the evaporative heat flux estimate is calculated as Eq. 2.22:

$$\dot{r}(t) = \Omega J(t) \tag{2.21}$$

$$HF_v = J(t)m_i H_v \tag{2.22}$$

2.4.1.2 Evaporative heat flux estimate in additive manufacturing

In additive manufacturing, the need to accurately control the process has led to many studies on laser beam–matter interaction. This is the case of selective laser melting, also known as *laser beam melting*, where a computer–programmed laser is used as energy source for selectively melting successive layers of metal powder. Experimental and numerical work is dedicated to understanding the complex physical phenomena associated with this process. Under the laser energy the powder grains melt, bond together, wet the substrate, and create a melt pool. The strong temperature gradient stirs the melt pool. Finally, if the melt pool surface reaches the boiling temperature, it starts vaporizing and the related recoil pressure exerted on its surface is responsible for the "keyhole" formation, i.e. a trench surrounded by melt pool (see Fig. 2.5). The metal vapour is then ejected at speed close to the local sound speed, while interacting with the incoming laser. This process takes place under an inert argon environment. Aside from the

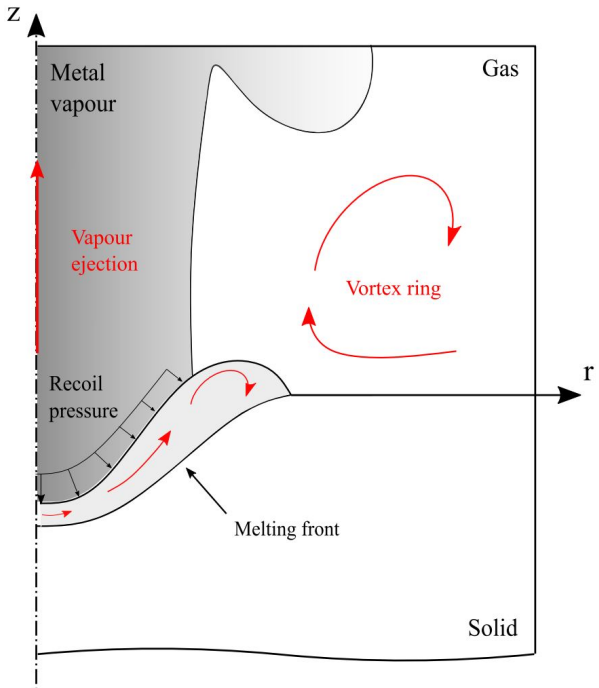

Fig. 2.5: Dynamics of laser–induced metal vaporisation [68]. *©IOP Publishing. Reproduced with permission. All rights reserved.*

physical domains associated with the different phases, in [69] the laser force is counterbalanced

by vaporization losses, convection within the liquid layer, and conduction within the condensed phase. The evaporative heat flux is expressed by using Eq. 2.23, where the evaporative mass flux is estimated by Eq. 2.24.

$$HF_v = \dot{m} H_v \tag{2.23}$$

$$\dot{m} = (1 - \beta_R)\sqrt{\frac{M}{2\pi RT}} P_{sat}(T) \tag{2.24}$$

Eq. 2.24 takes into account the back–scattering flux through β_R representing the fraction of evaporated particles which re–condensates after interacting with the surrounding gas. In the case of intense evaporation, $\beta_R \approx 0.18$ [70, 71]. P_{sat} is computed through Eq. 2.13. The normal velocities of the different phases are linked to the evaporative mass flux through their densities and the interface velocity (see Eq. 2.25).

$$\rho_v(\vec{v}_v \cdot \vec{n} - v_{int}) = \rho_l(\vec{v}_l \cdot \vec{n} - v_{int}) = \dot{m} \tag{2.25}$$

Based on findings from [69], Y.A. Mayi et al. have concluded that the evaporative flux should be revisited and modified with a more complex one taking into account the dynamic coupling between vapour and liquid. In [69] and [72], Y.A. Mayi et al. refer to Knight's studies on conservation of mass (Eq. 2.26) across the KL [67], to be used instead of Eq. 2.24,

$$\dot{m} = \sqrt{\frac{M}{2\pi RT_s}} P_{sat}(T) + \beta_R \sqrt{\frac{M}{2\pi RT_{KL}}} P_{sat}(T_{KL}) f(\Phi_{KL}) \tag{2.26}$$

where:

$$f(\Phi_{KL}) = \sqrt{\pi}\Phi_{KL}\, \mathrm{erfc}(\Phi_{KL}) - e^{-\Phi_{KL}^2} \tag{2.27}$$

$$\Phi_{KL} = \frac{u}{\sqrt{2RT}} = Ma_{KL}\sqrt{\frac{\gamma}{2}} \tag{2.28}$$

$$\gamma = \frac{c_p}{c_v} \tag{2.29}$$

Equation 2.30 between density and pressure is assumed valid:

$$\rho = \frac{M}{RT}P \tag{2.30}$$

All the variable values at the KL outer boundary are related to the surface variables through the following jump conditions (i.e. discontinuity in temperature and density) established by Knight after solving the conservation of mass, momentum and energy across the KL [67]:

$$\frac{T}{T_s} = \left[\sqrt{1+\pi\left(\frac{\Phi_{KL}}{2}\frac{\gamma-1}{\gamma+1}\right)^2} - \sqrt{\pi}\frac{\Phi_{KL}}{2}\frac{\gamma+1}{\gamma-1}\right]^2 \tag{2.31}$$

$$\frac{\rho}{\rho_s} = \sqrt{\frac{T_s}{T}}\left[\left(\Phi_{KL}^2+\frac{1}{2}\right)e^{\Phi_{KL}^2}\,\mathrm{erfc}(\Phi_{KL}) - \frac{\Phi_{KL}}{\sqrt{\pi}}\right] + \frac{1}{2}\frac{T_s}{T}\left[1-\sqrt{\pi}\Phi_{KL}e^{\Phi_{KL}^2}\,\mathrm{erfc}(\Phi_{KL})\right] \tag{2.32}$$

$$\beta_R = \left[\left(2\Phi_{KL}^2+1\right) - \Phi_{KL}\sqrt{\frac{\pi T_s}{T}}\right]e^{\Phi_{KL}^2}\frac{\rho_s}{\rho}\sqrt{\frac{T_s}{T}} \tag{2.33}$$

substituting for β_R from Eq. 2.33 in Eq. 2.26, Knight obtained the mass flow rate outside the KL [73]:

$$\rho v = \rho_s\sqrt{\frac{RT_s}{2\pi}}\left[1-\left(2\Phi_{KL}^2+1\right)\left(\sqrt{\pi}\Phi_{KL}e^{\Phi_{KL}^2}\,\mathrm{erfc}(\Phi_{KL})\right)\right] \tag{2.34}$$

Eq. 2.34 gives the fraction of the emitted mass flux that actually leaves the KL. It implicitly depends on the Ma_{KL}, which can be freely specified without violating conservation of mass, momentum, and energy across the KL, as its value is not determined by the analysis of the KL itself [67]. An estimate of the Ma_{KL} is possible, after modelling the gas domain and solving for its velocity in points far away from the vaporization front.

The energy balance and mass conservation at the vapour–liquid interface become, respectively, Eq. 2.35 and Eq. 2.36 [73].

$$\rho v H_v - k_l\frac{\partial T_l}{\partial x} = HF \tag{2.35}$$

$$\rho_l v_{int} = \rho v \tag{2.36}$$

The general non–linear theory predicts that non–equilibrium processes within the KL cannot drive the flow to greater than the sonic speed ($c_{gas} = \sqrt{\frac{\gamma RT}{M}}$) within the KL. If the external pressure is reduced (i.e. $P/P_{sat} < 1/5$), the remaining expansion must continue outside in the continuum flow [63, 66, 67, 74]. Knight's study is limited to $0 \leq Ma \leq 1$.

Similar jump conditions have been found by Ytrehus and Østmo in [63, 65], which relate the states at the interphase and external equilibrium in a similar way as the Rankine-Hugoniot equations relate the upstream and downstream of a shock wave [63].

Anisimov's work [70] is based on the assumption that with low flux densities the absorption of light by the vapour can be neglected, hence the expansion of the vapour occurs in a centered rarefaction wave. The obtained boundary conditions relate the values of the hydrodynamic variables outside of the KL with the metal surface temperature, by assuming a sonic vapour flow on the KL outer boundary, where temperature, density and pressure values approximates the critical values of $T_{KL} = 0.67T_s$, $n_{KL} = 0.31n_s$ and $P_{KL} = 4.81P_s$. Without solving the thermal problem in the condensed phase, the inclusion of the gas kinetics equations enables estimates of the surface temperature, velocity of the receding surface and recoil momentum through Eqs. 2.37, 2.38, 2.39, respectively.

$$m_i n_s(T_s)\sqrt{\frac{k_B T_s}{m_i}}\left(H_v + 2.2\frac{k_B T_s}{m_i}\right) = 3.1HF \tag{2.37}$$

$$v_{int} = \frac{HF}{\rho\left(H_v + 2.2\frac{k_B T_s}{m_i}\right)} \tag{2.38}$$

$$p = \frac{1.69 \cdot E_{abs}}{\sqrt{H_v}} \frac{\sqrt{\frac{k_B T_s}{m_i H_v}}}{1 + 2.2 \cdot \frac{k_B T_s}{m_i H_v}} \tag{2.39}$$

2.4.1.3 Evaporative heat flux estimate in electron–beam vaporization systems for metals

Electron–beam technology is becoming increasingly important in metal processing such as physical vapour deposition, welding, casting, and laser isotope separation. Electrostatically–accelerated beams of electrons provide high energy density on a metal target under vacuum. In a way similar to selective laser melting (Fig. 2.5), the metal flow is driven by thermally–induced gradients in density (buoyancy effect) and surface tension (Marangoni effect). At high vaporization rates, a trench forms at the liquid–vapour interface from the thrust of the departing vapour atoms.

When the beam impinges on the target surface, the kinetic energy of the accelerated electrons is converted into either heat or atomic excitation energy of the metal target. In practice, a considerable fraction (20%–35%, with a maximum of 50% for W [75]) of the incident electron beam is back–scattered, and this fraction increases with the material Z and the angle of incidence between beam and target surface. In addition, secondary processes produce X-rays, secondary electrons and thermionic electron emission at the beam incidence point. The energy absorbed by the target heats the material up to its melting and boiling point, while radiating to the cold surroundings [76]. The model developed in [77] imposes an evaporative heat flux boundary condition at the vapour–liquid interface which includes two different contributions: the latent heat and the translational kinetic contribution associated with the vapour flow (Eq. 2.40) [78]. The local evaporation flux $\dot{m}$ is calculated using the Hertz–Knudsen–Langmuir equation 2.24.

$$HF_v = \dot{m}\left(\frac{2RT}{M} + H_v\right) \tag{2.40}$$

The energy losses associated with secondary processes as “skip” or secondary electrons are included in the backscattered losses by taking the absorbed energy flux to be a fixed fraction of the incident beam flux [79]. There is no description of how the velocity of the receding surface is calculated in [77], therefore the author suggests it might be deduced from mass conservation consideration as in Eq. 2.41, which resembles the form of Eq. 2.38:

$$v_{int} = \frac{HF_v}{\rho_l\left(\frac{2RT}{M} + H_v\right)} \tag{2.41}$$

2.4.2 Vapour shielding dynamics

During intense evaporation events, it is thought that vapour shielding generally leads to a significant reduction of the evaporated material [37]. However, for refractory materials, vapour shielding's beneficial influence can also be seen in a reduction of the molten thickness. The insensitivity of the melt layer thickness to vapour shielding for low melting temperature materials is due to the melting preceding evaporation for a relatively long time. Furthermore, in a tokamak, the location of the intense evaporation site affects the vapour shielding effectiveness, as it is thought to work more in the divertor region than along the wall, where the field lines are almost parallel to the wall and vapour ions can be trapped and removed along field lines. Instead, in the divertor region, the better confined vapour can expand in front of the target for longer time before being swept off. For high–Z material targets (e.g. W), the vapour layer stays closer to the surface compared to low–Z material ones (e.g. C, B, Li, etc.). Although reduced from its original value, the net energy flux to the target surface (dominated now by vapour–generated photon radiation) is large enough to cause melting and further erosion of metallic components [80]. Vapour shielding is not a local phenomenon [81, 82] since vapour expansion will extend over a larger proportion of the wall than the original plasma–wall contact region, with the result of having a bigger area subjected to vapour cloud radiation than the plasma–wall contact footprint. The vapour shielding effect results in an intermittent phenomenon, with inherently difficult dynamics to resolve. Despite both the challenge of capturing its physics and the lack of experimental data, a few studies on vapour shielding effect modelling have been identified in literature. These will be briefly described in the following section.

2.4.2.1 Hassanein's [37] approximation of vapour shielding effects

Hassanein treated the energy deposition during a disruption as a surface phenomenon for which the average ion penetration range x_i in the condensed phase is short compared to the characteristic length of the problem. In stainless steel, $x_i = 7.5 \cdot 10^{-8}$ m [37, 62]. There is little information in the literature about transport mechanisms during disruptive events. The model is based on the following reasonable assumptions. Shielding is effective only when a sufficiently thick vapour layer is reached. This threshold value is defined as x_i. The vapour cloud, expanding as a sphere in front of the condensed phase, will interact continuously with

the incoming plasma particles, converting their unidirectional kinetic energy into isotropically–emitted radiative power. Hence, half of the incoming heat flux will be radiated back to the hotspot. Therefore, after the vaporization starts, the incoming heat flux can be approximated as it follows:

$$HF(t) = HF\left(1 - \frac{x(t)}{2x_i}\right) \qquad x(t) \leq x_i \tag{2.42}$$

$$HF(t) = \frac{HF}{2} \qquad x(t) > x_i \tag{2.43}$$

The heat absorbed by the vapour cloud and the subsequent reduction of the heat flux implies that the vapour is ionized, so that it may eventually be removed under the influence of the magnetic field lines resulting in a low vapour density in proximity with the target [37].

Experimental data for W in [83] shows that the maximum 250 eV–thermal energy D ion penetration range is $7 \cdot 10^{-10}$ m and that the maximum damage occurs at 20-30 nm, while the 3.5 MeV–thermal energy He ion penetration range is $6 \cdot 10^{-6}$ m, with a max damage occurring at $2 \cdot 10^{-6}$ m.

2.4.2.2 Russian experimental and numerical studies on vapour shielding

Linear steady–state and pulsed plasma accelerators are used to experimentally investigate the surface erosion of ITER divertor W monoblocks under high heat flux. Experiments carried out on W revealed that the melt motion is driven by plasma pressure when field lines strike the target perpendicularly (or in absence of magnetic field), while under tokamak–like conditions the melt motion is mainly driven by Lorentz forces arising from the interaction between $\vec{B}$ and thermoionically–induced currents (see §2.5), which drive the melt motion towards peripheral and colder areas of the target. It is also found that an energy threshold exists, at which the beginning of the intense evaporation is triggered, after which a secondary plasma arises and expands slowly along magnetic field lines.

Due to the difficulty of accurately simulating W radiation transport phenomena, three different models are proposed by D.I. Skovorodin et al. in [84] and reported in Table 2.1. All of these models assume that the shielding effect is proportional to the amount of vaporized material N_v, and their difference lies in the functional dependence of the heat flux HF_w reaching

the target surface of the ablated material. N_v is a function of the evaporation rate $J_v = J_0 e^{\frac{H_v}{T_s}}$. Therefore, the evaporated particle flux can be estimated, over the duration of the vaporization, as $N_v = \int_{t_v}^{t_f} J_v(t)dt$.

Models	HF_w
#1	$HF e^{-N_v \sigma_s}$
#2	$HF - \dot{P}_{rad,i} N_v$
#3	$HF - \frac{<Z>\Lambda_{rad}}{v_v t} N_v^2$

Table 2.1: Vapour shielding models [84].

In the first two models, σ_s is the effective collisional cross–section of the vapour, while $\dot{P}_{rad,i}$ is the power screened by the vapour shield per evaporated particle or, equivalently, the energy radiated by every particle. Hence, in the first two models, the heat flux attenuation is proportional to the radiation loss of each gaseous atom, whereas in practice the total power radiated by a vapour cloud of volume V can be expressed by using the "coronal equilibrium" (Eq. 2.44), which assumes the radiation losses $\dot{P}_{rad}$ to be proportional to the luminosity function (Λ_{rad}), the radiating ion and electron densities (n_i and n_e, respectively), and the average charge of the secondary plasma ions ($n_e \approx <Z> n_i$), by considering negligible the electron density of the incident plasma flow compared to the electrons generated by secondary ionization [84].

$$\dot{P}_{rad} = \dot{P}_{rad,i}\, n_i\, V = n_e\, \Lambda_{rad}\, n_i\, V = \Lambda_{rad}\ <Z>\ n_i^2\, V \tag{2.44}$$

In all the models, the vapour always has a low density, is transparent to the emitted radiation and it expands with a constant speed within a spherical volume ($V \approx v_v t = \sqrt{\frac{8 k_B T}{\pi m_i}} t$ can be considered valid in the 1D approximation).

The 1D numerical model set up in [84] and [85] is used against experimental data obtained by radiating W samples for 50 μs with HF values ranging from 1-20 MW m^{-2}. The stationary evaporation rate in vacuum is used for the estimate of the ablated material, $J_v(T_s) = \frac{8.167 \cdot 10^{34}}{\sqrt{T_s}} e^{-\frac{94670}{T_s}}$, and the Fourier equation is solved together with the boundary condition in Eq. 2.45:

$$k(T)\frac{\partial T_s}{\partial t} = -HF + n_e \Lambda_{rad} \int_{t_v}^{t_f} J_v(T_s)dt' \tag{2.45}$$

The main conclusions of the study in [84] are the following:

- When vaporization starts, the vapour shielding makes T_s decrease rapidly (see Fig. 2.6 for the HF = 20 MW m^{-2} case, with the appearance of vapour after 10 μs);
- For HF $\leq$ 8 GW m^{-2}, the T_s increase is not enough to enhance intense evaporation;
- Pulses with 8 $\leq$ HF $\leq$ 12 GW m^{-2} experience intense evaporation only at the end of the pulse time, therefore the shielding effect is not significant during the transient;
- For pulses with HF $\geq$ 12 GW m^{-2}, the intense evaporation reduces the incoming heat flux magnitude to 5 GW m^{-2}, although the shield formation time varies for different HF values.

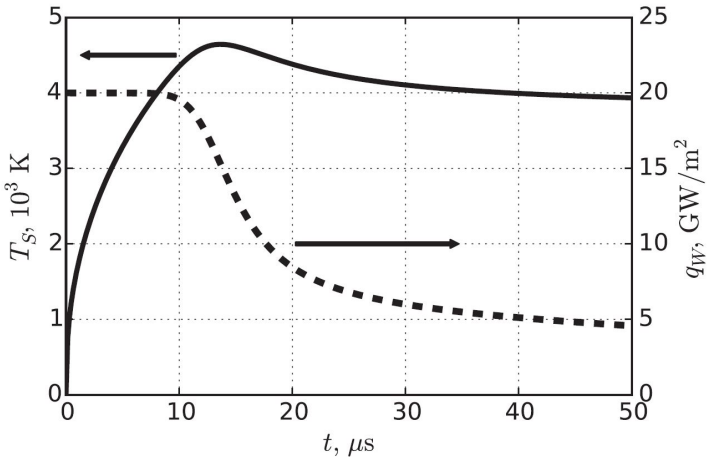

Fig. 2.6: Time evolution of T_s (solid line) and HF_w (dashed line) for a HF = 20 GW m^{-2} pulse [84]. *Figure reprinted from [84], with the permission of AIP Publishing.*

This experimental outcome highlights that vapour shielding can result in the saturation of the energy density absorbed by the target ($E_{abs,max}$), with the total energy density delivered by the plasma significantly larger than this value. The three models (Table 2.1) all give to the same asymptotic value [84] of the saturated energy absorbed by the target ($E_{abs,max}$) compared to the energy delivered by the plasma (see Fig. 2.7). The asymptotic value can be estimated by Eq. 2.46 as approximately [85].

$$E_{abs} = \int_0^{t_{pulse}} HF_{wall} dt \approx \sqrt{\pi \rho c_p k t_{pulse}} \, \frac{H_v}{2\ln(G)} \tag{2.46}$$

$$G = \sqrt{\frac{\pi c_p k J_0 \dot{P}_{rad,i}}{4 \cdot HF^3}}\ H_v \tag{2.47}$$

For t=50 μs, ln(G) ≈ 20 and $E_{abs,max} = 0.5$ MJ m^{-2} [86] (see Fig. 2.7). D.I. Skovorodin et

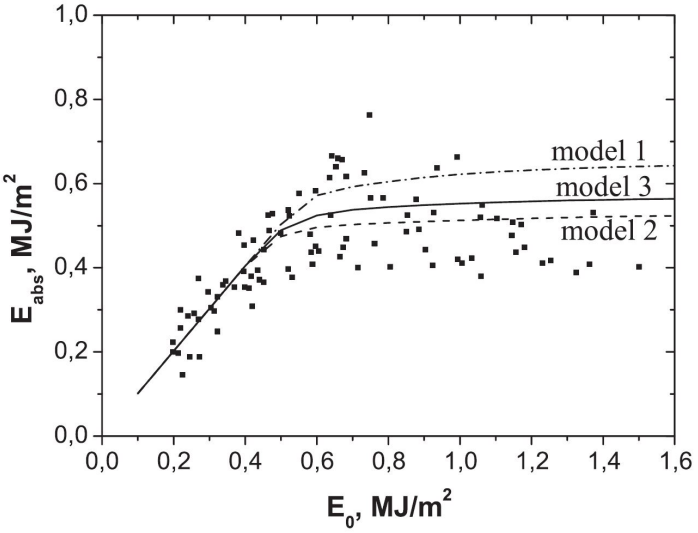

Fig. 2.7: E_{abs} estimates according to the models described in Table 2.1 and their benchmark against experimental data from the MK-200UG pulsed plasma gun in Troitsk (Russia) [84]. *Figure reprinted from [84], with the permission of AIP Publishing.*

al. in [84] interestingly highlighted that very similar results for E_{abs} were experimentally found for both C and W [86, 87] after reaching some evaporation threshold, despite their different radiation capabilities.

E_{abs} strongly depends on the thermodynamic properties of the material target, the heat pulse duration and evaporation energy, but with a week logarithmic dependence on $\dot{P}_{rad,i}$ and HF_w [84].

2.5 Melting experiments in existing tokamaks

Intentional and unintentional melting events are part of the experimental campaign for existing tokamaks. When intentional, their aim is mainly the investigation of the metal surface damage, and the consequences of the melt layer on plasma performances. Such studies have led researchers to the conclusion that any potential melt layer redistribution is mainly due to Lorentz forces $F_{j\times B} = \vec{j}_\perp \times \vec{B}$, resulting from the interaction between $\vec{B}$ and the current den-

sity generated by the thermionic electron emission at high temperatures. As a consequence of charge continuity, the replacement electrons from the bulk material move towards the hotter (molten) surface, replenishing the surface–emitted electrons. Gravity does not play a significant role, typically resulting in a force one order of magnitude lower than the Lorentz force, although gravity acts conjointly with plasma pressure, surface tension and Lorentz forces in non–refractory metals.

2.5.1 JET experiments with Be and W wall

At the end of the 2014 JET experimental campaign, melting events on both Be and bulk W tiles with a leading edge were observed after JET shutdown. While Be tiles had been subjected to repeated flash melting due to unmitigated disruptive events, the divertor W tiles had been installed for dedicated melting experiments in support of ITER [88].

Two trends are observed both in the outboard and inboard walls, as highlighted in Fig. 2.8a and Fig. 2.8b, respectively. On the high–field side (inboard wall), the melt layer is pushed radially outwards and upwards against gravity, while in the low–field side (outboard wall) the melt layer moves downwards. This evidence is explained by considering the Lorentz forces $\vec{j}_\perp \times \vec{B_\varphi}$ as main drivers of the melt motion. $j_\perp$ always flows across the melt layer (i.e. from the plasma to the wall) [88, 89], and could be either the current generated by secondary electron emission or the halo current flowing from the plasma through the tile during a VDE. The halo current density in JET has been estimated equal to 100 kA m^{-2} for $I_p = 1$ MA.

The divertor W melting experiments showed the same melt motion driven by $\vec{j}_\perp \times \vec{B}$, but the origin of $j_\perp$ in W has to be found in the thermally–emitted electron–generated current density of 1 MW m^{-2}, which was higher than the current density driving the Be layer ($j_{\perp,Be} = 60$ kA m^2). The current induced by thermally–emitted electrons at the Be melting layer generates a Lorentz force which is much lower in magnitude than the gravity force, therefore the upward motion of the Be liquid layer can be due to a combination of the Lorentz force arising from the secondary electron emission and forces induced by the plasma pressure [89]. It follows that with W, when $|\vec{B}| > 0.15$ T, the Lorentz forces overcome gravity if $j_{\perp,W} > 70$ kA m^2:

$$j_\perp > \frac{\rho g}{B_\varphi} \tag{2.48}$$

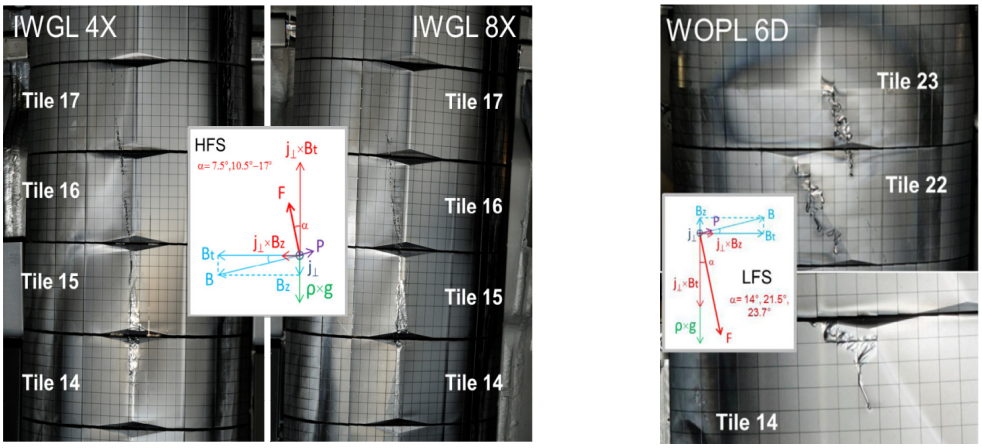

(a) (b)

Fig. 2.8: (a) Molten JET inner wall guard limiter force balance under JET discharge #83620; (b) Molten JET outer wall poloidal limiter force balance [89]. *©IOP Publishing. Reproduced with permission. All rights reserved.*

Further melting experiments in 2015, carried out in the JET divertor by exposing a sloped surface to open field lines, showed that where $\vec{B}$ intersects the surface at lower angles than in the case of the perpendicular impact on a leading edge (like in the 2014 JET divertor melting experiments), no runaway melt motion is observed, consistent with the hypothesis that the escape of thermionic electrons emitted from the melt zone is suppressed in sloped geometries [90].

2.5.1.1 TEXTOR experiments with W tiles

The same conclusions for W were arrived at from dedicated experiments carried out in the medium–sized TEXTOR tokamak [91] by installing three different types of bulk W test limiters: (a) 2 mm-thick W layer mounted on top of the graphite structure; (b) W castellated structure; (c) JET divertor–like bulk W tile. The first two tiles were mounted on the upper part of the main chamber, as opposed to the third one which was installed in the lower part. The melt motion and erosion are analysed under "steady–state conditions" and medium–to–high $|\vec{B}|$ (2.25-2.75 T) [90, 92]. The experiments showed that the molten W layer moves perpendicular to $\vec{B}$ due to its interaction with the thermo–electron emission current, and the resulting Lorentz force leads to the material redistribution without ejection of molten material into the plasma. In general, the molten layer is subjected to the action of the force exerted by plasma pressure (F_{plasma}),

Lorentz forces ($F_{j\times B}$), and the force exerted by the vapour (i.e. recoil pressure). In the TEXTOR experiments, for a maximum locally observed 1 mm–thick molten layer over an area A=2 cm^2, the following condition prevails $F_{gravity} < F_{plasma} < F_{j\times B}$ and, hence, $\varrho gAh < PA < j|\vec{B}|Ah$. The quantitative estimate for the pressure contributions related to the above three forces is the following: $P_{gravity} = 188$ N m^{-2}, $P_{plasma} = 200$ N m^{-2} and $P_{j\times B} = 2700$ N m^{-2} [**?**].

2.6 Key findings and research gaps identified by the author

1. Different aspects of the limiter design still have to be addressed in fusion research, with a few or no preceding examples available in literature. All the limiters designed so far are inertially cooled and meant to face a less energetic plasma than the one foreseen for DEMO. At present, no existing limiters are compatible with the DEMO conditions.

   Although limiters and divertors might be considered as two similar high heat flux systems sharing specific technological solutions, they have different loading conditions. In fact, the design of their plasma–facing surfaces follows different criteria dictated by the way the field lines strike the wall, as well as the nature of the heat load they have to withstand – the divertor is subjected to a steady state high heat flux whereas the limiter should not experience any significant heat load during normal operation but extremely high heat fluxes during short transients.

2. The limiter design should take into account the impact of the phase change on the cooling system integrity requirement. To the author's knowledge, the current literature does not include any predictive 3D finite element model used in fusion research design able to predict melting, re–solidification, vaporization, under the assumptions of no removal of the melt layer nor has the resulting deformed geometry been used for subsequent structural analyses. Previous investigations with 1D models have been carried out, but little or no information has been found to justify the PFC armour thickness.

   Many processes occurring at the PFC surface still need to be quantified, such as the experimental vapour shielding effect and the way it can be modelled. A predictive design tool should be able to model the physical phenomena taking part in a plasma–wall impact in a simplified way; to quantify the energetic contributions associated with them; to

give a realistic quantification of the energy absorbed by the condensed phase. A finite element predictive design tool would also help quantify the material skimming among the plasma–facing material candidates, and enable different design points and erosion evaluation studies for damaged components. It would also allow the designer to perform a mechanical assessment of the limiter, since the processes responsible for the energy decrease will be modelled by means of suitable boundary conditions, leaving the reshaped condensed domain able to be assessed. The inclusion of the physics underpinning the model would allow users to assess damage without the need for plasma physics information. The author has identified a clear need to deliver a PFC design workflow able to address all the engineering gaps.

Chapter 3

DEMO limiter PFC design and shaping under material phase change

"If you can't explain it simply, you don't understand it well enough."

Albert Einstein

As the most demanding requirement for limiters is protecting the first wall against any plasma impacts, the limiter design starts from its plasma–facing component front face, as described in §1.3.1. This chapter describes the rationale adopted by the author for the limiter shaping, designed in such a way to comply with both off–normal and normal operation plasma configurations. The estimate of the heat loads on both the newly designed limiters and first wall is explained, as well as the field line tracing approach used for it.

This is the beginning of the limiter engineering design workflow, where some boundaries driving the integrated design of such sacrificial components are fixed.

The findings in §3.1 and §3.3 of this chapter are published by the author in [15], co–authored with all the author's supervisors, i.e. Prof. P. Ireland, Dr. J. Nicholas, and Dr. Z. Vizvary.

3.1 Plasma–facing surface shaping

Any break in the continuity of the main wall causes the exposure of leading edges to open field lines in the SOL. It follows edge–localized hot spots due to charged particles power deposition

(see Fig. 3.1a). This effect is amplified by components protruding from the main wall (Fig. 3.1b), which define the plasma boundary (LCFS), and expose their side walls perpendicularly to magnetic field lines. Since the deposited power follows Eq. 2.2, they are subjected to the highest heat flux magnitude. Hence the need to have an accurate design and shaping of the surfaces directly exposed to plasma open field lines. The aim of the PFC shaping is two–fold, as it should spread the power carried by particles spiralling around magnetic field lines on a surface area as large as possible, while shadowing the edges of adjacent panels. Through a rooftop–shaped PFC (Fig. 3.1c), it is possible to achieve both goals, since the central ridge of one panel shadows a portion of the adjacent panel's surface by intercepting magnetic field lines. Although limiters

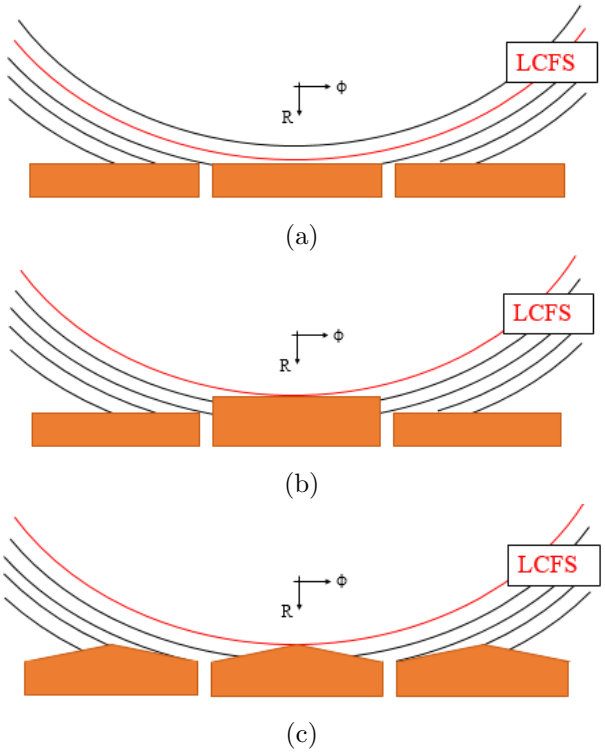

Fig. 3.1: Top–view sketch of the way SOL field lines strike the FW panels in presence of: (a) perfectly aligned flat tiles; (b) protruding components; (c) rooftop–shaped tiles.

should be primarily designed for facing transient thermal loads, in reality their design is required to be suitably and safely adapted to withstand steady–state heat loads, avoiding edge–localized peaks during the longest SOF. As a result of the different plasma magnetic configurations, finding a unique surface shaping that spreads the charged particle power as even as possible during both SOF and transients is not straightforward, since Eq. 2.2 describing the power distribution depends on the fall–off decay length λ. Therefore, the maximum value of the heat

flux (HF_{max}) moves from the center of the surface for smaller λ values, i.e. during disruptions, towards the edges for larger λ values – i.e. during SOF.

Each limiter front face has been designed by the author starting from a similar approach to the one used for designing the ITER FW [93, 94]. As the toroidal component of the magnetic field line is considerably larger than the poloidal one, the toroidal shaping has larger impact then the poloidal one. The ideal design would have a toroidally continuous wall without any gaps or misalignments but, in reality, toroidal gaps are necessary for handling the IVCs during installation. Despite its generalized validity, the attention is currently focused on finding the toroidal mid–plane profile with respect to a rectilinear coordinate system, whose origin lies in the centre of the PFC face. The toroidal (φ) and poloidal (ϑ) coordinates are aligned with the cylindrical global ones but tangential to the PFC surface at their origin, whereas the third coordinate (x) along which the distance between PFC and plasma is calculated is orthogonal to them, and points towards the surface. The following assumptions are made:

- The shape of the PFC surface can be approximated by the sum of poloidal $g(\vartheta)$ and toroidal $f(\varphi)$ shape functions like:

$$x_{surf}(\varphi, \vartheta) = f_{surf}(\varphi) + g_{surf}(\vartheta) \tag{3.1}$$

- The function describing the radial distance between the segment face and the LCFS is:

$$\delta(\varphi, \vartheta) = f(\varphi) + g(\vartheta) \tag{3.2}$$

$$f(\varphi) = f_{surf}(\varphi) + f_{LCFS}(\varphi)$$

$$g(\vartheta) = g_{surf}(\vartheta) + g_{LCFS}(\vartheta)$$

- The toroidal shape of the plasma can be considered to be circular with positive/negative curvature for the inboard/outboard segment (r_φ is the plasma toroidal radius of curvature at the mid–plane):

$$f_{LCFS}(\varphi) = \frac{\pm\varphi^2}{2r_\varphi} \tag{3.3}$$

- The poloidal shape of the plasma can be approximated with the following function (r_ϑ is

the plasma poloidal radius of curvature at the mid–plane):

$$g_{LCFS}(\vartheta) = \frac{-\vartheta^2}{2r_\vartheta} \tag{3.4}$$

- The toroidal profile of the PFC and the plasma are related according to:

$$f_{surf}(\varphi) = f(\varphi) - f_{LCFS}(\varphi) \tag{3.5}$$

As mentioned, assuming that the poloidal profile of the limiter follows the plasma profile, no additional poloidal shaping is required. This means that the analysis refers to the toroidal plane ($\vartheta_{edge} = 0$). The toroidal shape of the PFC is optimized if $f(\varphi)$ satisfies the following Cauchy problem [94]:

$$f(0) = 0 \tag{3.6}$$

$$e^{-\frac{f(\varphi)}{\lambda}} \cdot f'(\varphi) = C \tag{3.7}$$

The initial condition on $f(\varphi)$ (Eq. 3.6) imposes a null distance between plasma and PFC at the origin of the coordinate system (i.e. at the LCFS–limiter contact point in the graphs in Fig. 3.2), while Eq. 3.7 imposes a uniform constant power density value in all its toroidal profile. The solution gives a logarithmic shape of the toroidal profile as in Eq. 3.8, with a toroidal recession at the edges by the quantity defined by Δ^φ (Eq. 3.11) with respect to the LCFS:

$$f(\varphi) = -\lambda \cdot \ln\left(1 - \frac{C \cdot \varphi}{\lambda}\right) \tag{3.8}$$

$$C = \left(\frac{\lambda}{\Delta\varphi_{1/2}}\right) \cdot \left(1 - e^{\frac{-\Delta^\varphi_{setback}}{\lambda}}\right) \tag{3.9}$$

The minimum value of the toroidal setback to ensure shadowing and protection of the toroidal edges is:

$$\Delta^\varphi_{setback}(\vartheta_{edge}) = \Delta_{mis} + \frac{\left(\vartheta_{edge} + b \cdot \left(\Delta\varphi_{1/2} + \Delta_{gap}\right) - \vartheta^{centre}_{plasma}\right)^2 - \left(\vartheta_{edge} - \vartheta^{centre}_{plasma}\right)^2}{2 \cdot r_\vartheta} \tag{3.10}$$

where $\left(\vartheta_{\text{edge}} - \vartheta_{\text{plasma}}^{\text{centre}}\right)$ is the distance along the vertical axis of the machine between the edge and the plasma centre, and considers any vertical offset of the plasma centre from its nominal position. Therefore, the toroidal setback at the edges of each segment is:

$$\Delta^{\varphi} = \Delta^{\varphi}_{\text{setback}}(\vartheta_{\text{edge}}) + \text{f}_{\text{LCFS}}(\Delta\varphi_{1/2}) \tag{3.11}$$

If the setback value is small enough, the resulting "logarithmic profile" can be approximated by a piece–wise linear function giving a rooftop–shaped toroidal profile.

The iterative procedure followed by the author for limiter design and shaping is summarized below.

- Analytical approach: starting from the plasma scenario faced by every limiter, with its related $\dot{\text{P}}_{\text{SOL}}$ and λ parameters, the logarithmic shape resulting from the Cauchy problem resolution is calculated;
- Computational approach: using CAD modeler tools, the 3D limiter surface is designed and tested with SMARDDA (see §2.2.1.1) for calculating the power deposition on its surface during the related plasma scenario;
  - The constraint on mitigating the power deposition peaks below 1 MW m^{-2} during SOF leads to the introduction of chamfers close to the edges, which change the angle between $\vec{\text{B}}$ and $\vec{\text{n}}$. The new resulting profile is referred to as "2shape" profile.

All the resulting limiter profiles are shown in Fig. 3.2.

3.2 Surface heat load calculation by 3D field line tracing approach

Both plasma radiative and charged particle energy contribute to the power deposition on the FW. However, the former can be considered almost uniformly spread all over the wall, whereas the latter causes localized hot spots on PFCs. This is in fact the most critical contribution to manage.

SMARDDA and PFCflux were used by the author for calculating the heat flux pattern on PFCs for all the plasma scenarios foreseen for DEMO. This activity was performed by the author

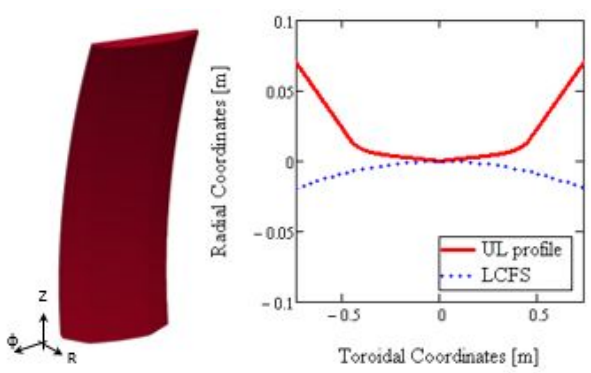

(a) UL PFC (lhs) and 2shape profile (rhs).

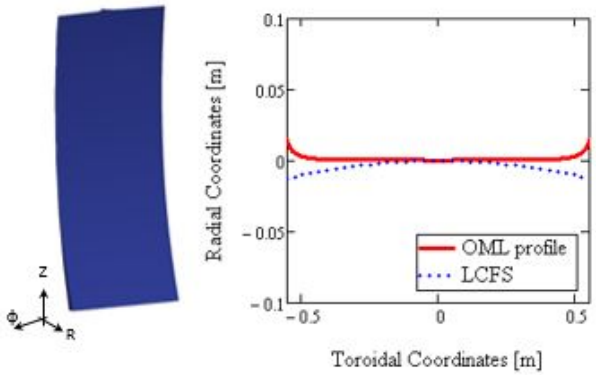

(b) OML PFC (lhs) and profile (rhs).

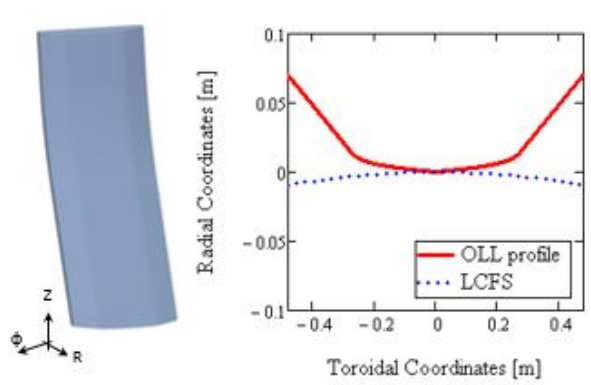

(c) OLL PFC (lhs) and 2shape profile (rhs).

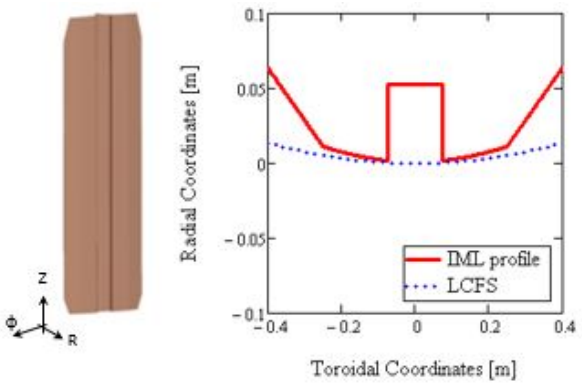

(d) IML PFC (lhs) and profile (rhs).

Fig. 3.2: Limiter's PFC shapes.

during her secondment to CEA Cadarache (France), in collaboration with French researchers and after an extensive benchmark between SMARDDA and PFCflux. The main required input parameters are:

1. The magnetic configuration developed for a plasma scenario.

   This is usually provided in EQDSK file format [95], which contains an array of rigorously organized numbers giving information on plasma physics and machine geometry at every point of the defined working grid. It includes I_p, R_{major}, the position of both the plasma magnetic axis and boundaries, the 2D poloidal–radial FW silhouette, the poloidal and radial distribution of the magnetic flux, the value of $\vec{B}$ at R_{major}, and the value of the plasma pressure. The plasma magnetic equilibrium is calculated by using a software describing the time evolution of a free plasma boundary and electromagnetic fields in axisymmetric toroidal configurations, therefore requires working with a 2D toroidal cross–section of

the tokamak as input geometry, like MaxFEA [96]. Fig. 3.3 shows a sequence of plasma magnetic configuration evolution snapshots during a simulated UVDE. This sequence was generated by the author as an exercise through MaxFEA during her 2 months secondment to ENEA Frascati (Rome). The plasma instability is triggered 4 ms after the plasma reaches the X–point formation due to a voltage variation imposed on the vertical control circuit. This action kicks the plasma upwards, and starts the plasma TQ, which brings the plasma towards a new limited configuration, while shrinking. At 9 ms, the plasma current quench is triggered, which accelerates the plasma volume reduction until it disappears at 500 ms.

2. Finite element model of the 3D geometry facing the plasma.

   The input geometry is represented by surface models that are discretized by using triangular meshes. The mesh should be as refined as needed by subsequent analyses using the obtained results, as the ray–tracing approach is sensitive to slight geometrical changes if the discretization does not approximate well enough any solid geometry curvature.

   The two pieces of software refer to two different kind of input geometries for the computation of the shadowing pattern:

   - The shadowed (or result) geometry where the power deposition is computed;
   - The shadowing geometry which can only intersect magnetic field lines and determines which areas of the shadowed geometry receives power (i.e. which regions of the shadowed geometry are wetted by the plasma);

3. $\dot{P}_{SOL}$ and λ values characterizing the power distribution across the SOL for that particular scenario.

In the following, the PFC power deposition patterns (due to charged particles) are reported for the main foreseen plasma magnetic snapshots.

- The RU equilibrium is shown in Fig. 2.2b. The plasma input parameters are: $\dot{P}_{SOL} = 3.5$ MW; $\lambda = 6$ mm. It is foreseen to last about 35-60 seconds. The plasma is meant to ramp–up on the outboard equatorial wall, where the OML has been located. The OML is designed for accommodating the plasma ramp–up heat loads, being this phase a planned

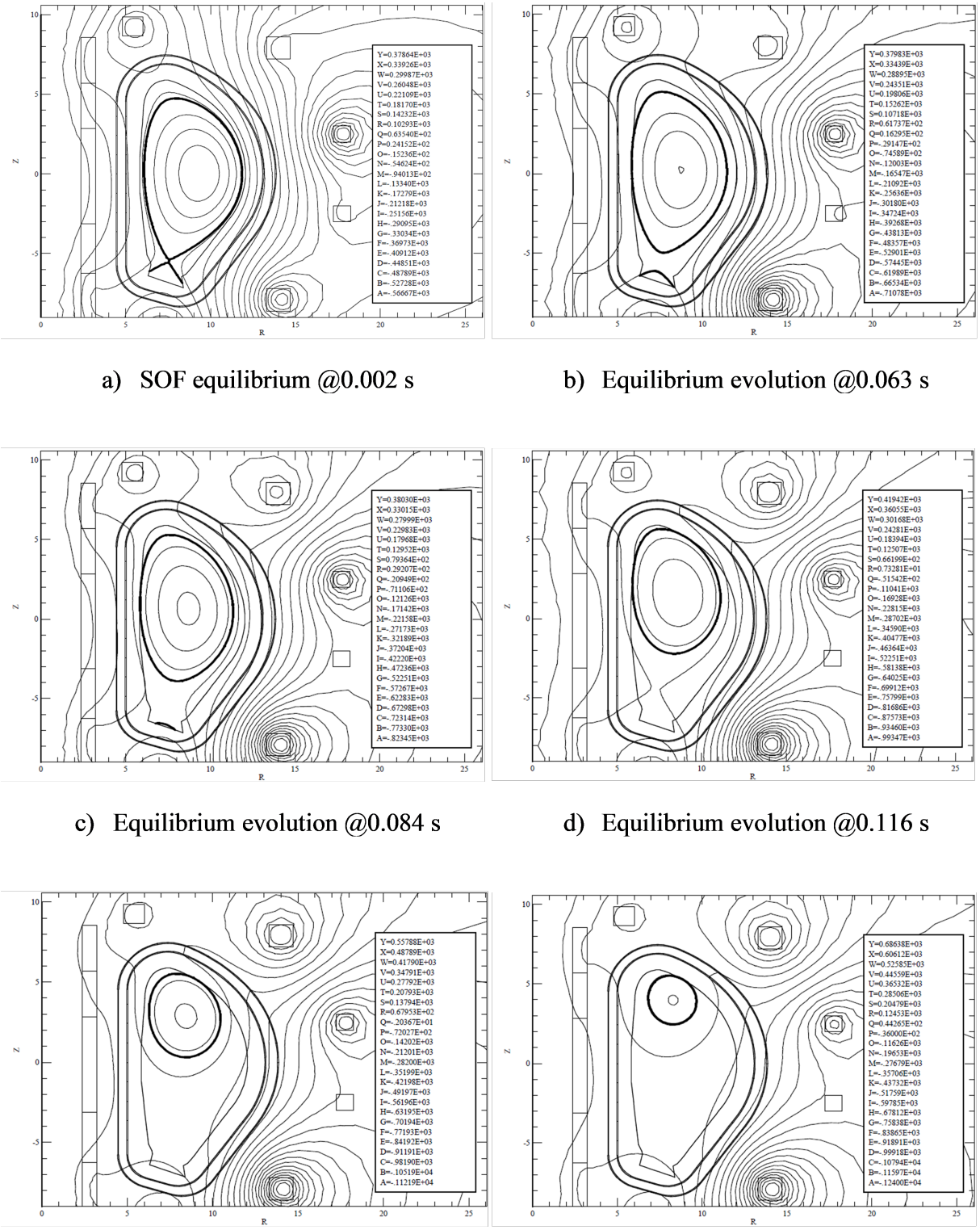

a) SOF equilibrium @0.002 s

b) Equilibrium evolution @0.063 s

c) Equilibrium evolution @0.084 s

d) Equilibrium evolution @0.116 s

e) Equilibrium evolution @0.141 s

f) Equilibrium evolution @0.164 s

Fig. 3.3: Example of a DEMO plasma boundary dynamic evolution during UVDE. Due to the MaxFEA software settings, the squared box appearing as a legend on the rhs cannot be removed nor modified.

normal transient happening before and after every discharge. Therefore, the maximum value of the power deposition is on the OML, whose power deposition pattern is shown in Fig. 3.4, while nothing is deposited in the rest of the wall (see Table 3.1). The power deposition pattern is symmetric every 90° due to the presence of limiters that break the toroidal symmetry of the wall. This is a general conclusion which stands for all the scenarios.

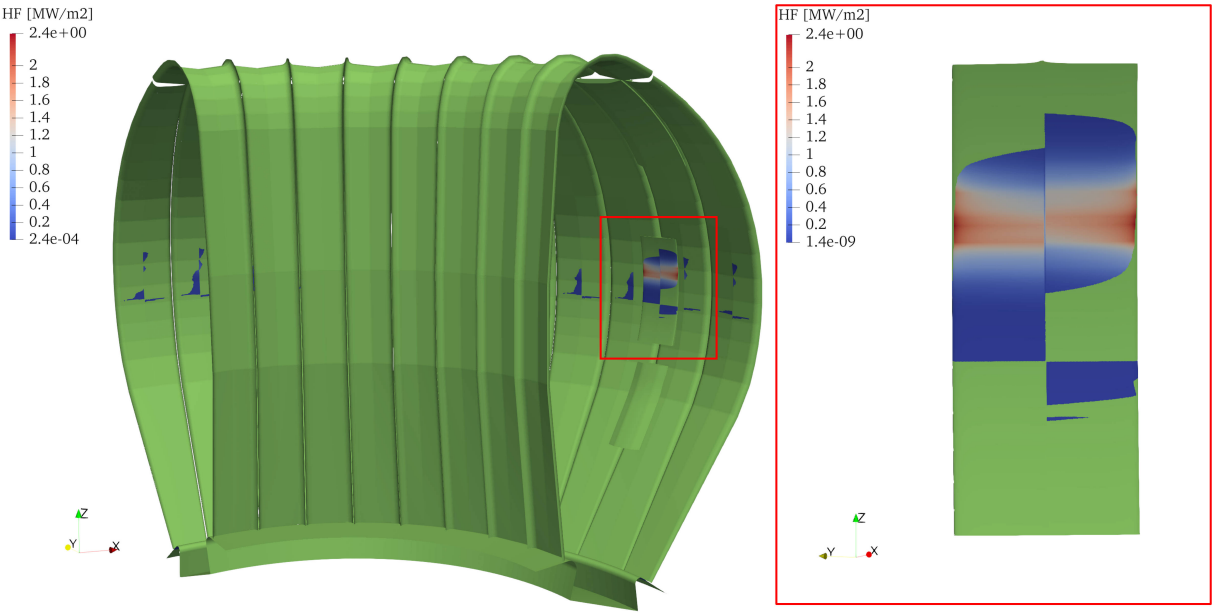

Fig. 3.4: Charged particle power deposition pattern on 90° DEMO FW sector during RU (lhs), with emphasis on the OML (rhs).

- The SOF equilibrium is shown in Fig. 2.2b. The plasma input parameters are: $\dot{P}_{SOL}$ = 69 MW; λ = 50 mm. This characterizes the flat top, during which the designed PFCs experience a maximum heat flux value below the engineering constraint (1-2 MW m^{-2}), as Table 3.1 shows. The SOF power deposition pattern generated by SMARDDA is shown in Fig. 3.5.

- The UVDE–TQ equilibrium is shown in Fig. 2.2c. The plasma input parameters are: $\dot{P}_{SOL}$ = 325 GW; λ = 7 mm. This is a 4 ms transient, followed by a 200 ms CQ where the heat load decreases to 2.52 MW m^{-2} on the UL. Since the most critical phase for PFC thermal loads is the TQ, the results are only related to this phase. The UL is the most affected component during such transients, whose related power distribution is shown in

	RU		SOF	
Component	HF_{max} [MW m^{-2}]	$\dot{P}$ [MW]	HF_{max} [MW m^{-2}]	$\dot{P}$ [MW]
FW	0.29	0.063	0.40	3.30
DIV	$\leq$0.001	$\leq$0.001	2.07	62.1
OML	2.37	0.81	0.53	0.14
OLL	0.000	0.000	0.09	0.07
IML	0.000	0.000	0.00	0.00
UL	0.000	0.000	0.82	3.30

Table 3.1: Maximum heat flux values and total power on PFCs during RU and SOF.

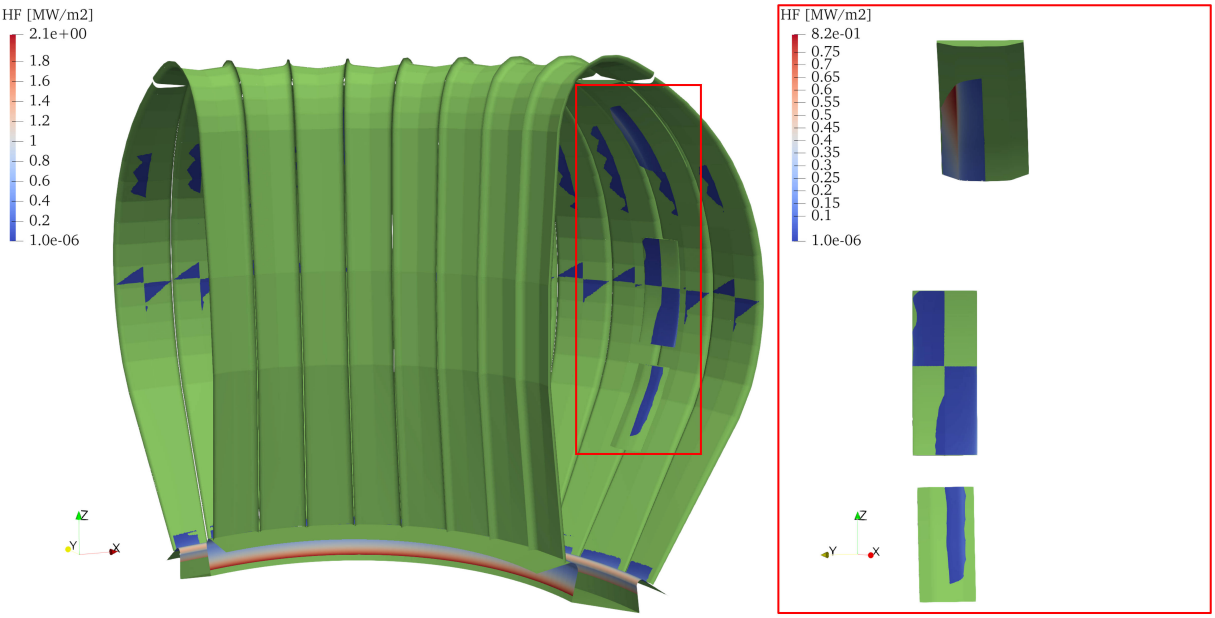

Fig. 3.5: Charged particle power deposition pattern on 90° DEMO FW sector during SOF, with emphasis on UL, OML and OLL (rhs).

Fig. 3.6, whereas the maximum heat load values on PFCs during UVDE–TQ are listed in Table 3.2.

- The DVDE–TQ equilibrium is shown in Fig. 2.2d. The plasma input parameters are: $\dot{P}_{SOL}$ = 325 GW; λ = 7 mm. This scenario is equivalent to the UVDE, but during the CQ the heat load on the OLL is negligible. Two different DVDE evolutions are foreseen from the physics point of view: the first one foresees a diverted plasma during the TQ, and most of the power is released into the divertor rather than the OLL, which experiences $HF_{max} \approx 5$ GW m^{-2}; the second case foresees a TQ phase in plasma limited configuration

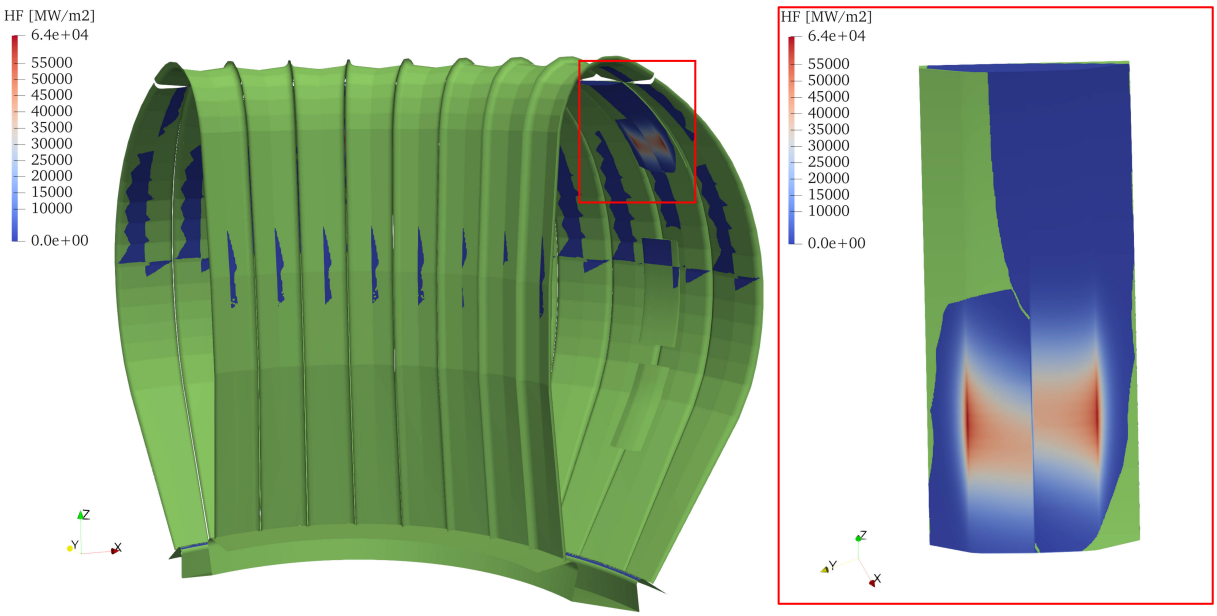

Fig. 3.6: Contour plot of the charged particle power deposition pattern on 90° DEMO FW sector during UVDE TQ, with emphasis on the UL (rhs).

while it touches the OLL. This is the most critical case for the OLL, and its heat flux could reach $HF_{max} \approx 300$ GW m^{-2}. The contour plot of the power deposited during UVDE–TQ is shown in Fig. 3.7 and Fig. 3.8 for, respectively, the two above–mentioned cases. The maximum heat load values on PFCs during DVDE–TQ are listed in Table 3.2.

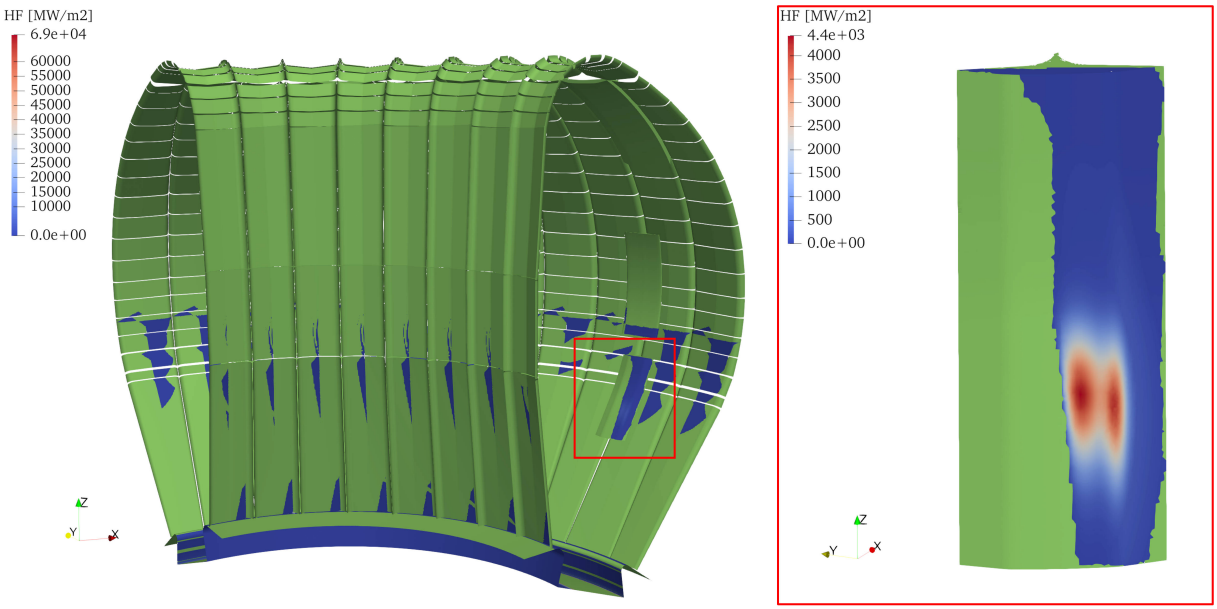

Fig. 3.7: Contour plot of the charged particle power deposition pattern on 90° DEMO FW sector during UVDE TQ – less critical case for OLL (rhs).

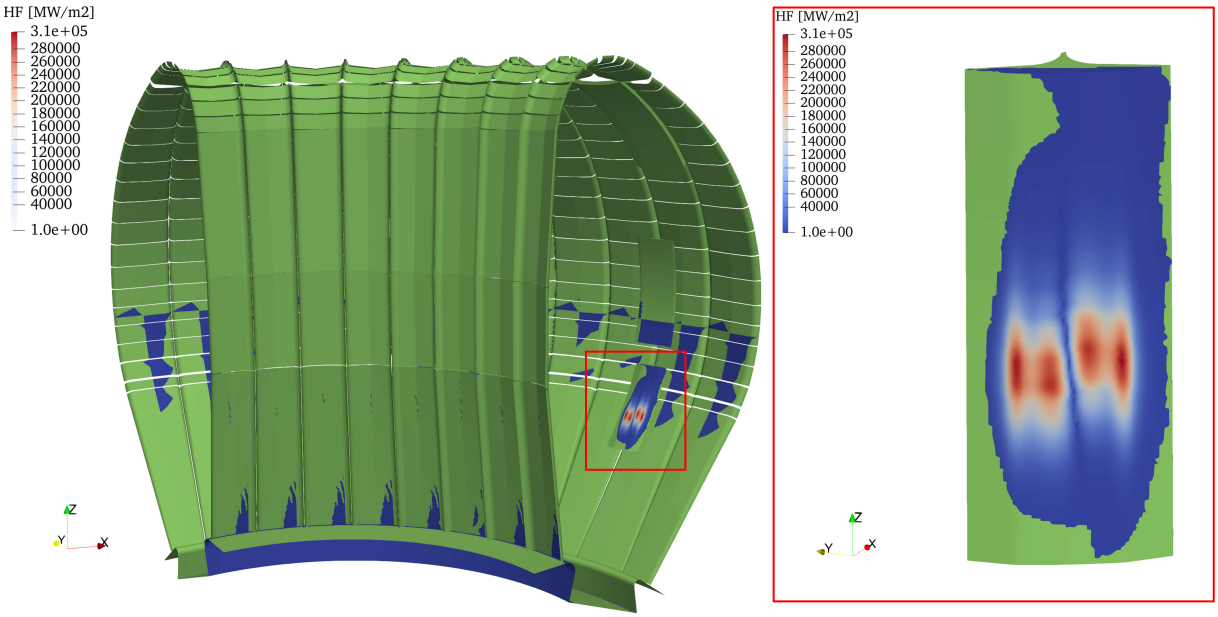

Fig. 3.8: Contour plot of the charged particle power deposition pattern on 90° DEMO FW sector during UVDE TQ – most critical case for OLL (rhs).

	UVDE		DVDE	
Component	HF_{max} [MW m^{-2}]	$\dot{P}$ [MW]	HF_{max} [MW m^{-2}]	$\dot{P}$ [MW]
FW	138	383.780	8.114	15.7
DIV	≤0.001	≤0.001	69425	322600
OML	≤0.001	≤0.001	0.769	0.165
OLL	≤0.001	≤0.001	4422.7 (300000[1])	2383
IML	≤0.001	≤0.001	0.842	0.106
UL	63568	324616	0.000	0.000

[1] Two different plasma evolution cases for DVDE are here used for heat load calculations. Both foresee the fully energetic plasma moving downwards. In one case, plasma becomes limited in proximity of the OLL, which is the only touched component and, hence, the most heavily loaded during the TQ ($HF_{max} \approx 300$ GW/m^2). In the other case, the plasma TQ occurs before the plasma becomes limited, therefore most of its energy is driven by the X–legs towards the divertor, which is indeed more loaded than the limiter ($HF_{max} \approx 5$ GW/m^2).

Table 3.2: Maximum heat flux values and total power deposited on PFCs during UVDE.

During unmitigated VDEs, the heat flux due to charged particles constitutes the predominant contribution to the PFC heat load, as opposed to the mitigated disruptions where impurities are injected into the plasma core to enhance its cooling through radiative emission, which therefore becomes dominant. It is expected to have a few unmitigated full power disruptive events, whose effects will then be mitigated by disruption avoidance and mitigation systems currently under study. As this work mostly considers SOF and unmit-

igated transients, the radiative contribution is neglected throughout this work. Due to the uncertainties on DVDEs, the reference transient is assumed to be the UVDE from now on, whereas the heat loads calculated under DVDEs are only used as exercise.

Fig. 3.9 summarizes the maximum heat flux values on limiters under the relevant plasma transient they are designed for, together with the power deposition time. Although these are the reference HF_{max} values on limiters, any change in physics assumptions and geometry will affect them.

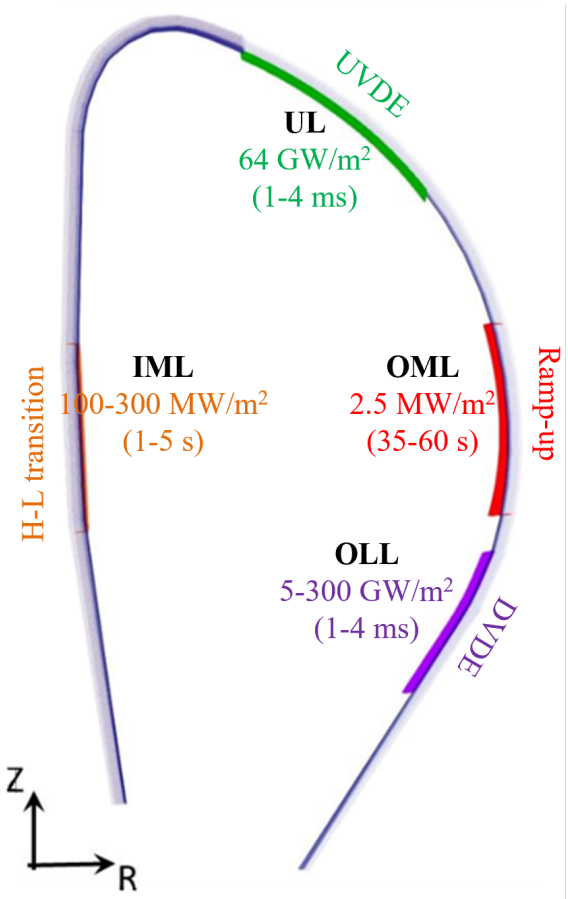

Fig. 3.9: Charged particles–induced HF_{max} values experienced by every limiter during the transient event it is designed to face.

3.3 Heat transfer in presence of phase change: multi–phase moving boundary model

Metallic PFCs are prone to phase change under heat flux magnitudes reported in Fig. 3.9, which are going to raise the temperature of the exposed surfaces up to the melting point and eventually, the boiling point.

The thermal inertia is an important property to consider when choosing a plasma–facing material as armour, within the range of material availability. The thermal response of W and its high–Z material alternatives (e.g. Ta, Hf, highlighted in [36]) is roughly compared in Fig. 3.10 under a DVDE–TQ energy release. By assuming that all the released energy is instantaneously absorbed by the PFC (i.e. the OLL, in this case), a few material candidates are quickly skimmed based on the molten and vaporized thickness estimates through Eq. 3.12, which takes into account the two contributions of sensible and latent heat of melting and vaporization. The results in Fig. 3.10 confirm the suitability of W over the chosen metals.

$$h = \frac{HF_{max}}{\rho \cdot (c_p(T_m - T_{op}) + H_m + H_v)} \tag{3.12}$$

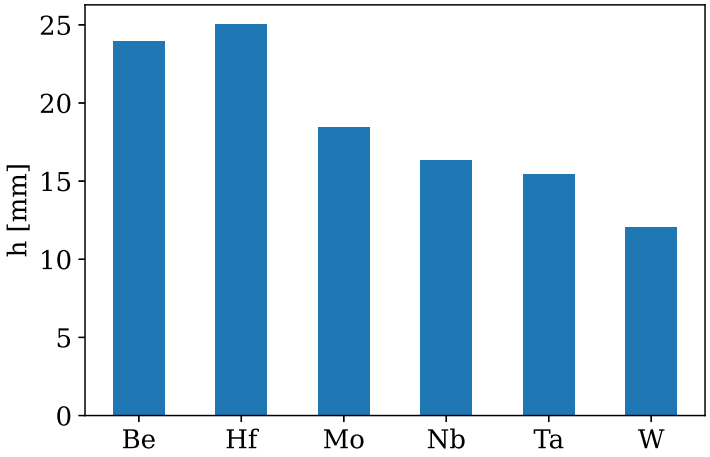

Fig. 3.10: Thickness of material undergoing melting and vaporization under $HF_{max} \approx 300$ GW m^{-2}, the worst–case scenario for the OLL during a DVDE.

Since this causes erosion and reduction of the PFC lifetime, the estimate of the "removed" amount of material should drive the design, and should be incorporated into the PFC finite element modelling and assessment. This becomes even more important when considering the

requirement of avoiding any water leakage inside the main chamber, under any circumstances. Hence, the study is here focused on developing a predictive engineering model which fulfils this goal.

As a starting point, the author needs to understand more about the approach to follow. The heat transfer in solids undergoing phase changes is conceived by the author as a three–stages process highlighted in Fig. 3.11. This leads the author to implementing a Matlab® thermal model tackling the multi–phase Stefan problem for a solid material subjected to a constant heat flux (HF) on one side ($x = 0$), and thermally insulated on the other side ($x = L$). The following assumptions are also made for further simplifying the problem:

- The heat transfer is one dimensional and occurs along the x–direction or along the sample thickness;
- The material thermal properties are assumed to be constant within each phase but differ from one phase to another;
- The temperature values at the interfaces are assumed constant and equal to the temperature of the phase changes;
- The solid is initially assumed to be at its isothermal temperature (T_{op});
- No temperature distribution in the vapour phase is calculated. The vapour phase is assumed to be removed, once it appears.

With the above assumptions in mind, each phase of Fig. 3.11 is analysed in detail in the following subsections.

3.3.1 Solid heating up – pre–melting stage: $0 \leq t \leq t_m$

This stage deals with the heating of the solid phase, initially at $T = T_{op} \leq T_m$. The governing equations are the following:

$$k_s \frac{\partial^2 T_s}{\partial x^2} = \rho_s c_{p,s} \frac{\partial T_s}{\partial t} \qquad \text{at } 0 < x < L \tag{3.13}$$

$$T = T_{op} \qquad \text{at } t = 0 \tag{3.14}$$

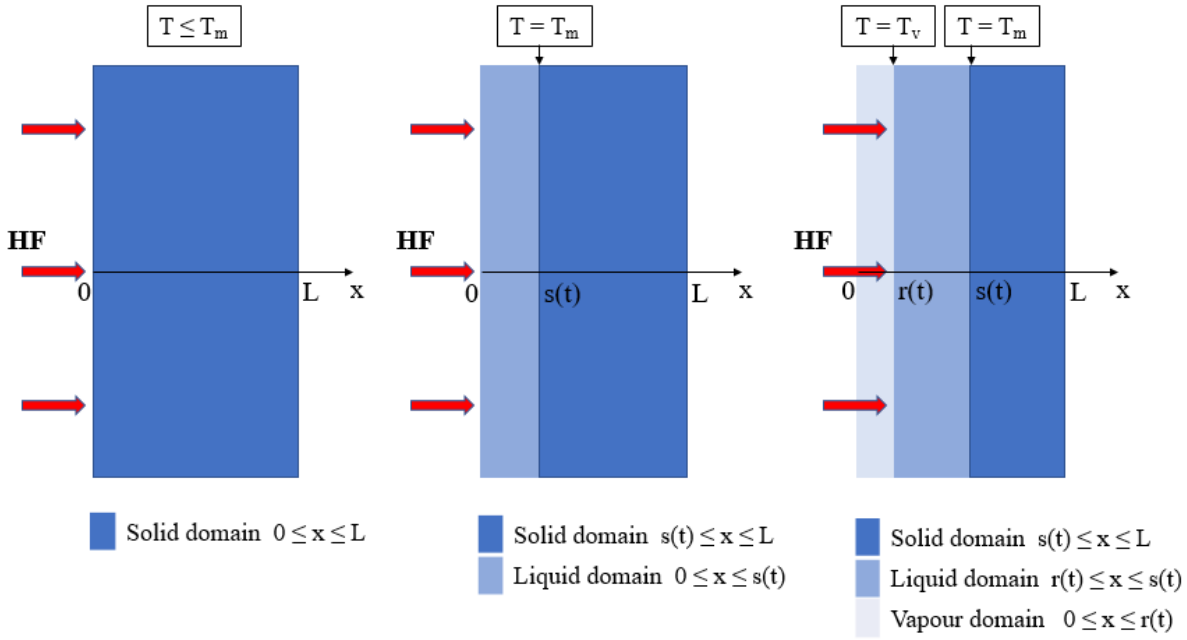

Fig. 3.11: Thermal model breakdown into the three main stages: heating phase (lhs), melting phase (center), and vaporization phase (rhs).

$$k_s \frac{\partial T_s}{\partial x} = -HF \qquad \text{at } x = 0 \tag{3.15}$$

$$k_s \frac{\partial T_s}{\partial x} = 0 \qquad \text{at } x = L \tag{3.16}$$

This stage ends at $t = t_m$, time instant when the surface temperature reaches the melting point of the material (T_m).

3.3.2 Melting stage: $t_m < t \leq t_v$

In this stage both the liquid and the solid phases coexist, and are separated by a moving interface located at $x = s(t)$. The initial distribution of temperature in the solid at $t = t_m$ comes from the previous stage (Eq. 3.20). At the interface, the Stefan condition holds (Eq. 3.22).

$$k_l \frac{\partial^2 T_l}{\partial x^2} = \rho_l c_{p,l} \frac{\partial T_l}{\partial t} \qquad \text{at } 0 < x < s(t) \tag{3.17}$$

$$k_s \frac{\partial^2 T_s}{\partial x^2} = \rho_s c_{p,s} \frac{\partial T_s}{\partial t} \qquad \text{at } s(t) < x < L \tag{3.18}$$

$$s = 0 \qquad \text{at } t = t_m \tag{3.19}$$

$$T_s = T(x, t_m) \qquad \text{at } t = t_m \tag{3.20}$$

$$k_l \frac{\partial T_l}{\partial x} = -HF \qquad \text{at } x = 0 \tag{3.21}$$

$$(\rho_s - \rho_l)^1 H_m \frac{ds}{dt} = -k_l \frac{\partial T_l}{\partial x} - \left(-k_s \frac{\partial T_s}{\partial x}\right) \qquad \text{at } x = s(t) \tag{3.22}$$

$$T_s = T_l = T_m \qquad \text{at } x = s(t) \tag{3.23}$$

The melting stage ends at $t = t_v$, time instant when the surface temperature reaches the boiling point of the material (T_v).

3.3.3 Vaporization stage: $t > t_v$

In this stage, a second moving interface separating the vapour from the liquid domain appears at $x = r(t)$. Consequently, another Stefan condition has to be satisfied at this interface (Eq. 3.30). The initial distributions of temperature in the solid and liquid phases come from the previous stage (Eq. 3.28, 3.29), as well as the position of the interface between the solid and liquid domains (Eq. 3.27).

The governing equations are therefore:

$$k_l \frac{\partial^2 T_l}{\partial x^2} = \rho_l c_{p,l} \frac{\partial T_l}{\partial t} \qquad \text{at } r(t) < x < s(t) \tag{3.24}$$

$$k_s \frac{\partial^2 T_s}{\partial x^2} = \rho_s c_{p,s} \frac{\partial T_s}{\partial t} \qquad \text{at } s(t) < x < L \tag{3.25}$$

$$r = 0 \qquad \text{at } t = t_v \tag{3.26}$$

$$s = s(t_v) \qquad \text{at } t = t_v \tag{3.27}$$

$$T_s = T(x, t_v) \qquad \text{at } t = t_v \tag{3.28}$$

$$T_l = T(x, t_v) \qquad \text{at } t = t_v \tag{3.29}$$

$$(\rho_s - \rho_l)^1 H_m \frac{ds}{dt} = -k_l \frac{\partial T_l}{\partial x} + k_s \frac{\partial T_s}{\partial x} \qquad \text{at } x = s(t) \tag{3.30}$$

[1] According to Eq. 2.10 in §2.3.2.1.

$$\rho_l H_v \frac{dr}{dt} = HF - \left(-k_l \frac{\partial T_l}{\partial x}\right) \qquad \text{at } x = r(t) \tag{3.31}$$

$$T_l = T_v \qquad \text{at } x = r(t) \tag{3.32}$$

$$T_s = T_l = T_m \qquad \text{at } x = s(t) \tag{3.33}$$

3.3.4 TARTIFL&TTE: a Matlab®–based thermal model

The resolution of the systems of equations described in the previous sections is carried out by means of the Matlab® built–in PDEPE algorithm [97], which solves 1D parabolic and elliptic PDEs in one spatial variable x and time t, together with initial and boundary conditions. It requires the PDE to be rewritten as in Eq. 3.34.

$$c\left(x, t, u, \frac{\partial u}{\partial t}\right)\frac{\partial u}{\partial t} = x^{-m}\frac{\partial}{\partial x}\left(x^m f\left(x, t, u, \frac{\partial u}{\partial x}\right)\right) + s\left(x, t, u, \frac{\partial u}{\partial x}\right) \tag{3.34}$$

Eq. 3.34 can be solved in different slab, cylindrical and spherical symmetric problems by imposing m=[0,1,2], respectively. On the rhs, $f\left(x, t, u, \frac{\partial u}{\partial x}\right)$ is a flux term, whereas $s\left(x, t, u, \frac{\partial u}{\partial x}\right)$ is the source term. The term $c\left(x, t, u, \frac{\partial u}{\partial x}\right)$ on the lhs represents the diagonal matrix coupling the partial derivatives with respect to time. The diagonal elements can be either zero (for elliptic equations) or positive (for parabolic equations). C, f, and s are output column vectors with as many elements as the number of equations. U is the temperature, x is the space vector, and t is the time vector.

The boundary conditions must be rewritten in the form of Robinson conditions (Eq. 3.35), which becomes a Dirichlet condition for $q = 0$ and a Neumann condition for $p = 0$.

$$p(x, t, u) + q(x, t) f\left(x, t, u, \frac{\partial u}{\partial x}\right) = 0 \tag{3.35}$$

Initial conditions, time and space vectors are defined separately. Other options such as absolute and relative solution tolerances, as well as condition on variable values can be also defined. The ODEs resulting from PDE discretization in space are integrated to obtain approximate solutions at the times specified by the time vector. The PDEPE algorithm returns values of the solution on mesh points defined by the spatial discretization vector. The chosen built–in solver

for the time integration of the resulting ODEs is the implicit *ode15s*.

The triggering condition on threshold temperature values are activated through the Matlab® Event Function, which allows the numerical integration to stop or continue after the condition is met. Two Event Functions are used here for triggering both the melting and vaporization phases by monitoring the surface temperature over time. After triggering any phase change, the system of equations are solved into a different coordinate system (see §3.4.1 for a description of the implemented immobilization technique), which overcomes the system non–linearities due to the dependence between position of the moving boundary and temperature. Furthermore, during the phase change, the system involves both PDEs and ODEs to be solved simultaneously. Since Matlab® does not have any built–in function for solving such systems, an open source finite element algorithm is adopted. This is part of the open source Matmol [98], a toolbox encompassing Matlab®–based method–of–lines (MOL) algorithms used for approximating the spatial operators of differential equations by means of finite differences, finite elements, finite volumes before performing the time integration of the resulting discrete equations with an ODE solver.

The thermal model's name TARTIFL&TTE stands for **T**hermal **A**nalysis fo**R** **T**racking **I**nter**F**aces under me**L**ting **&** vaporiza**T**ion–induced plasma **T**ransient **E**vents.

3.3.5 TARTIFL&TTE computational benchmark

The TARTIFL&TTE code is benchmarked against computational results found in literature [99, 100]. Two 1D problems are only found by the author in [100], respectively tackling (a) the collapse of a solid wall due to melting under constant heat flux on one side and insulation layer on the opposite side, and (b) the collapse of a solid slab under both melting and partial vaporization of the liquid layer, with the same boundary conditions as case (a). M. Zerroukat et al. in [100] compare different algorithms (finite elements, finite differences, boundary elements) for solving the same multi–phase moving boundary problem.

By using the same input data in (Table 3.3), the two problems are solved by TARTIFL&TTE. The benchmark between the "Reference results" in [100] and the modelled results shows a very good agreement, which is graphically reported in Fig. 3.12. It collects the main outputs related to Case (a) and Case (b) on the lhs and rhs, respectively. The plots include the time evolution

of the surface and mid–thickness temperatures, the inter–phase boundary tracking and their related velocities. Table 3.4 lists the time instants when phase change occur for both cases (a) and (b).

Input	Case (a)	Case (b)
L [m]	1	1
T_{ini} [°C]	27	27
T_m [°C]	638	1454
T_v [°C]	2480	3000
ρ [kg m^{-3}]	2.77	1
$c_{p,s}$ [J kg^{-1} K^{-1}]	1.041	4.944
$c_{p,l}$ [J kg^{-1} K^{-1}]	1.041	4.944
k_s [W m^{-1} K^{-1}]	1.73	0.259
k_l [W m^{-1} K^{-1}]	0.865	0.259
H_m [J kg^{-1}]	400	2160
H_v [J kg^{-1}]	10700	37200
HF[W m^{-1}]	2500	2500

Table 3.3: Multi-phase moving boundary problem input parameters [100] used for the computational benchmark.

The comparison between Fig. 3.12-a.3 and Fig. 3.12-b.3 shows that the velocity of the solid–to–liquid front decreases once vaporization starts, meaning that less heat is available to be conducted through the condensed phase.

The successful benchmark supports both the concept and implementation behind TARTIFL&TTE, although it tackles the phase changes as Stefan conditions and does not consider any physics behind intense vaporization yet. This aspect is addressed in Ch. 4.

	Reference values		Calculated values	
Time [s]	(a)	(b)	(a)	(b)
t_m	0.2322	0.32768	0.2341	0.3287
t_v		1.63439		1.6163

Table 3.4: Time instants triggering melting and boiling for Case (a) and Case (b).

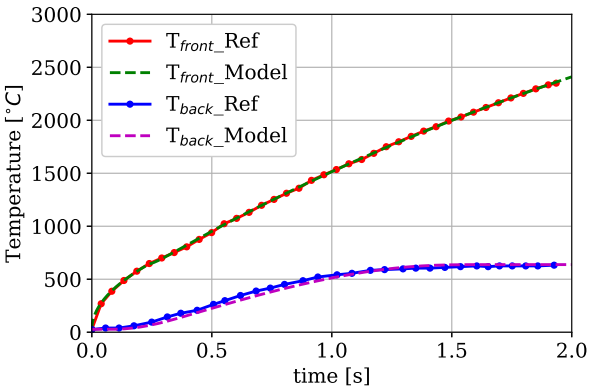

(a.1) Front and back surface T evolution.

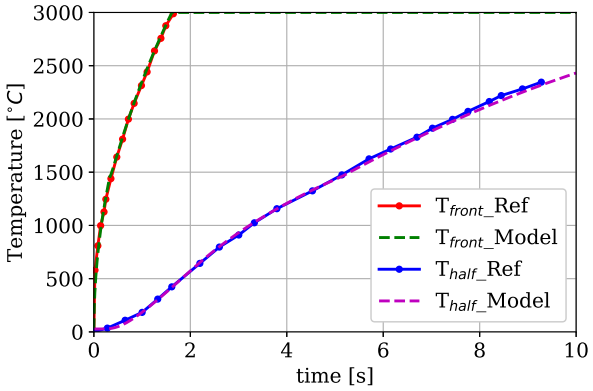

(b.1) Front and mid–thickness T evolution.

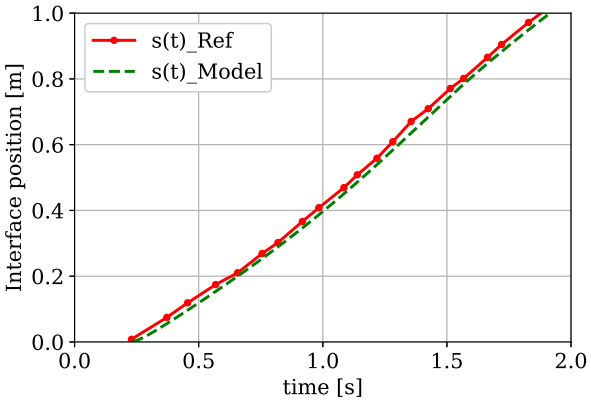

(a.3) Solid–to–liquid moving boundary interphase tracking.

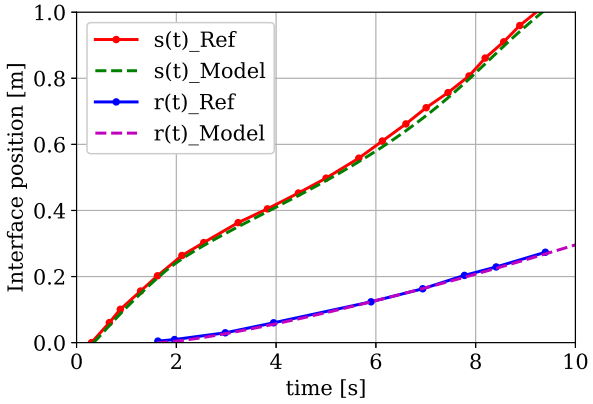

(b.3) Solid–to–liquid and liquid–to–vapour moving boundary interphase tracking.

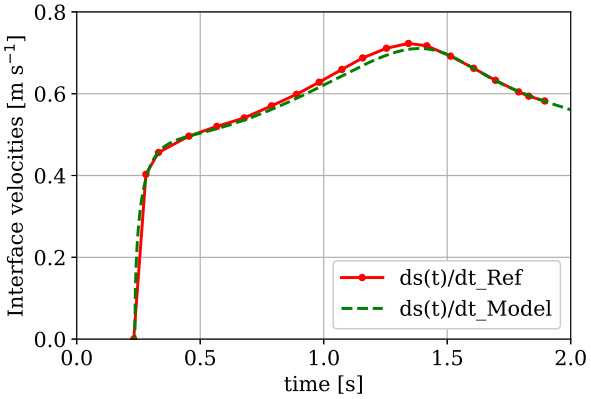

(a.2) Solid–to–liquid (s(t)) moving boundary interphase velocity.

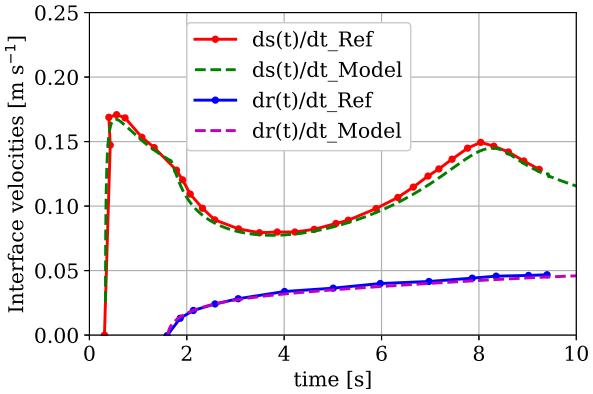

(b.2) Solid–to–liquid and liquid–to–vapour moving boundary interphase velocities.

Fig. 3.12: Multi–phase moving boundary problem computational benchmarks for Case (a) and Case (b).

3.3.5.1 Considerations on TARTIFL&TTE application to a W monoblock under UVDE

Although the thermal model needs further development, especially on capturing the vaporization phase, as a pure exercise it is here applied for an estimate of the W molten thickness under heat loads generated by UVDE (HF $\approx$ 70 GW m^{-2} for 4 ms). Such high heat flux causes an instantaneous rise of W surface temperature up to the melting point (3422° C in 0.42 μs), and eventually up to the boiling point (5660° C in 2 μs), producing a final melt and vapor thicknesses of, respectively, 4.5 and 4 mm. The same sudden temperature rise trend occurs under DVDE heat loads, although the huge amount of energy deposited on the surface brings it to melting in 0.06 μs and vaporization in less than 1 μs . At the end of the transient, the depth of the molten layer is ≈18 mm, of which ≈17 mm are vaporized. Under DVDE, the vapor thickness may seem unrealistic since vapor shielding effects are not here considered, and therefore the total incoming heat flux is solely absorbed by phase changes rather than shielded by the vapor layer, which would affect the energy balance. Therefore, the simulated cases are the worst case scenarios. Based on these preliminary results, TARTIFL&TTE predicts at least a 20 mm–thick W armor to face the critical plasma–surface impact during VDEs. However, these results might not be realistically catching the physics governing the intense evaporation under vacuum, due to gas kinetics not being taken into account in TARTIFL&TTE for describing the vaporization phase, which in its intense occurrence under vacuum conditions might not be well represented by a simple energy balance at the inter–phase. Despite this, the molten layer depth during UVDE appears to be of the same order of magnitude than the estimated molten thickness of ≈1100 μm in [31]. Hence, there is the need to validate the TARTIFL&TTE approach against experimental results.

Generally speaking, the TQ time scale is too short for letting the heat diffuse across the sample thickness, therefore the PFC outermost layers only faces the thermal wave by means of their material thermal inertia, leaving the rest of it at T = T_{op}. Provided that the molten thickness estimate is acceptable, this means that any cooling system located at least 20 mm far away from the PFC surface should be considered unperturbed by the disruptive event. The Landau transformation is an easy way of overcoming the more complicated Lagrangian—Eulerian approach to the moving boundary problems, which require more coding and computational ef-

forts. The computational benchmark at low power level is promising, and encourages a further development of the TARTIFL&TTE approach after a deep dive on how the vaporization affects the heat transfer on the condensed phase, and whether any vapor shielding effects should be considered in the total amount of energy diffused across it.

3.4 Non–dimensional TARTIFL&TTE

The dimensional variables identified as physically relevant for the problem are 17: $T - T_m$, $T_{op} - T_m$, $T_v - T_m$, t, x, L, s, r, HF, k_s, k_l, $c_{p,s}$, $c_{p,l}$, ρ_s, ρ_l, H_m, H_v.
According to the Buckingham–Pi theorem, if 5 is the number of fundamental dimensional variables required for describing the problem (i.e. temperature, time, length, mass and heat flux), the remaining ones can be expressed by a minimum number of dimensionless and independent "Pi groups", which in this specific case is equal to $17 - 5 = 12$. Assuming that the energy absorbed by the structure has the only effects of raising its temperature, the contribution of the mechanical energy can be neglected; therefore, the heat flux can be considered an independent variable for describing the system.

By choosing the dimensionless variable in 3.36 in place of the temperature, after multiplying by L both the left and right terms of Eq. 3.14 and indicating the thermal diffusivity as α_s, Eq. 3.14 can be rewritten as Eq. 3.37:

$$\Theta = \frac{(T - T_m)k_s}{HF \cdot L}, \tag{3.36}$$

$$L^2 \frac{\partial^2 \Theta_s}{\partial x^2} = \frac{L^2}{\alpha_s} \frac{\partial \Theta_s}{\partial t} \tag{3.37}$$

From Eq. 3.37, two dimensionless variables for position and time in 3.38 can be derived, leading to the complete dimensionless Eq. 3.39. The characteristic time scale t' is represented by the Fourier number (Fo), which gives information about the rate of diffused energy with respect to the rate of stored energy.

$$x' = \frac{x}{L}, \quad t' = t\frac{\alpha_s}{L^2} = \frac{t}{\tau} = Fo \tag{3.38}$$

$$\frac{\partial^2 \Theta_s}{\partial x'^2} = \frac{\partial \Theta_s}{\partial t'} \tag{3.39}$$

Carrying on with the scaling procedure, the complete set of identified Pi groups describing the system of governing equations are listed below:

$$\Theta = \frac{(T - T_m)k_s}{HF \cdot L}, \quad \Theta_{zero} = \frac{(T_{op} - T_m)k_s}{HF \cdot L}, \quad x' = \frac{x}{L}, \quad s' = \frac{s}{L}, \quad r' = \frac{r}{L}, \quad t' = \frac{t}{\tau}, \quad R = \frac{\rho_l}{\rho_s},$$

$$C = \frac{c_{p,l}}{c_{p,s}}, \quad K = \frac{k_l}{k_s}, \quad H^* = \frac{H_v}{H_m}, \quad {\Theta_v}^2 = \frac{(T_v - T_m)k_s}{HF \cdot L}, \quad B = \frac{H_v}{c_{p,s}(T_v - T_m)}.$$

By integrating the Pi groups into the dimensional system of equations, the new dimensionless equations governing the three stages of the process are as follows.

- **Heating up – pre–melting stage: $0 \leq t \leq t_m$**

$$\frac{\partial^2 \Theta_s}{\partial x'^2} = \frac{\partial \Theta_s}{\partial t'} \qquad \text{at } 0 < x' < 1 \tag{3.40}$$

$$\Theta_s = \Theta_{zero} \qquad \text{at } t' = 0 \tag{3.41}$$

$$\frac{\partial \Theta_s}{\partial x'} = -1 \qquad \text{at } x' = 0 \tag{3.42}$$

$$\frac{\partial \Theta_s}{\partial x'} = 0 \qquad \text{at } x' = 1 \tag{3.43}$$

- **Melting stage: $t_m < t \leq t_v$**

$$\frac{\partial^2 \Theta_l}{\partial x'^2} = \frac{R \cdot C}{K} \frac{\partial \Theta_l}{\partial t'} \qquad \text{at } 0 < x' < s' \tag{3.44}$$

$$\frac{\partial^2 \Theta_s}{\partial x'^2} = \frac{\partial \Theta_s}{\partial t'} \qquad \text{at } s' < x' < 1 \tag{3.45}$$

$$\frac{\partial \Theta_s}{\partial x'} = -\frac{1}{K} \qquad \text{at } x' = 0 \tag{3.46}$$

$$(\rho_s - \rho_l)\frac{H_m \alpha_s}{L^2}\frac{ds}{dt'} = -k_l \frac{HF}{k_s}\frac{\partial \Theta_l}{\partial x'} + k_s \frac{HF}{k_s}\frac{\partial \Theta_s}{\partial x'} \quad \Rightarrow$$

$$\rho_s \left(1 - \frac{\rho_l}{\rho_s}\right) \frac{H_v}{\rho_s c_{p,s}(T_v - T_m)} \frac{H_m}{H_v} \frac{k_s (T_v - T_m)}{HF \cdot L} \frac{d(\frac{s}{L})}{dt'} = -K \frac{\partial \Theta_l}{\partial x'} + \frac{\partial \Theta_s}{\partial x'} \quad \Rightarrow$$

[2] Θ_v and H^* appear in Eq. 3.47 after multiplying lhs and rhs terms by $(T_v - T_m)$ and H_v.

$$(1-\mathrm{R})\frac{\mathrm{B}\Theta_\mathrm{v}}{\mathrm{H}^*}\frac{\mathrm{ds}'}{\mathrm{dt}'} = -\mathrm{K}\frac{\partial\Theta_\mathrm{l}}{\partial \mathrm{x}'} + \frac{\partial\Theta_\mathrm{s}}{\partial \mathrm{x}'} \qquad \text{at } \mathrm{x}' = \mathrm{s}' \tag{3.47}$$

$$\Theta_\mathrm{s} = \Theta_\mathrm{l} = 0 \qquad \text{at } \mathrm{x}' = \mathrm{s}' \tag{3.48}$$

$$\frac{\partial\Theta_\mathrm{s}}{\partial \mathrm{x}'} = 0 \qquad \text{at } \mathrm{x}' = 1 \tag{3.49}$$

- **Vaporization stage: $\mathbf{t > t_v}$**

$$\Theta_\mathrm{v} = \frac{(\mathrm{T_v} - \mathrm{T_m})\mathrm{k_s}}{\mathrm{HF}\cdot\mathrm{L}} \qquad \text{at } 0 < \mathrm{x}' < \mathrm{r}' \tag{3.50}$$

$$\Theta_\mathrm{l} = \Theta_\mathrm{v} \qquad \text{at } \mathrm{x}' = \mathrm{r}' \tag{3.51}$$

$$\frac{\partial^2\Theta_\mathrm{l}}{\partial \mathrm{x}'^2} = \frac{\mathrm{c_{p,l}k_s}}{\mathrm{c_{p,s}k_l}}\frac{\partial\Theta_\mathrm{l}}{\partial \mathrm{t}'} \;\Rightarrow\; \frac{\partial^2\Theta_\mathrm{l}}{\partial \mathrm{x}'^2} = \varkappa\frac{\partial\Theta_\mathrm{l}}{\partial \mathrm{t}'} \qquad \text{at } \mathrm{r}' < \mathrm{x}' < \mathrm{s}' \tag{3.52}$$

$$\frac{\partial^2\Theta_\mathrm{s}}{\partial \mathrm{x}'^2} = \frac{\partial\Theta_\mathrm{s}}{\partial \mathrm{t}'} \qquad \text{at } \mathrm{s}' < \mathrm{x}' < 1 \tag{3.53}$$

$$\rho_\mathrm{l}\frac{\mathrm{H_v}\alpha_\mathrm{s}}{\mathrm{L}^2}\frac{\mathrm{dr}}{\mathrm{dt}'} = \mathrm{HF} + \mathrm{k_l}\frac{\mathrm{HF}}{\mathrm{k_s}}\frac{\partial\Theta_\mathrm{l}}{\partial \mathrm{x}'} \;\Rightarrow$$

$$\rho_\mathrm{l}\frac{(\mathrm{T_v} - \mathrm{T_m})\mathrm{k_s}}{\mathrm{HF}\cdot\mathrm{L}}\frac{\mathrm{H_v}}{\rho_\mathrm{s}\mathrm{c_{p,s}}(\mathrm{T_v} - \mathrm{T_m})}\frac{\mathrm{d}(\frac{\mathrm{r}}{\mathrm{L}})}{\mathrm{dt}'} = 1 + \mathrm{K}\frac{\partial\Theta_\mathrm{l}}{\partial \mathrm{x}'} \;\Rightarrow$$

$$\mathrm{RB}\Theta_\mathrm{v}\frac{\mathrm{dr}'}{\mathrm{dt}'} = 1 + \mathrm{K}\frac{\partial\Theta_\mathrm{l}}{\partial \mathrm{x}'} \qquad \text{at } \mathrm{x}' = \mathrm{r}' \tag{3.54}$$

$$(1-\mathrm{R})\frac{\mathrm{B}\Theta_\mathrm{v}}{\mathrm{H}^*}\frac{\mathrm{ds}'}{\mathrm{dt}'} = -\mathrm{K}\frac{\partial\Theta_\mathrm{l}}{\partial \mathrm{x}'} + \frac{\partial\Theta_\mathrm{s}}{\partial \mathrm{x}'} \qquad \text{at } \mathrm{x}' = \mathrm{s}' \tag{3.55}$$

$$\Theta_\mathrm{s} = \Theta_\mathrm{l} = 0 \qquad \text{at } \mathrm{x}' = \mathrm{s}' \tag{3.56}$$

$$\frac{\partial\Theta_\mathrm{s}}{\partial \mathrm{x}'} = 0 \qquad \text{at } \mathrm{x}' = 1 \tag{3.57}$$

3.4.1 Moving Boundary immobilization technique

The solution of the system of equations governing the pre–melting stage is straightforward as it requires the solution of the Fourier equation in the solid domain subjected to initial and boundary conditions. The problem becomes more complicated in presence of a phase change, i.e. during the melting and vaporization stages, when the appearance of a moving interface not known in advance becomes part of the solution. Therefore, two aspects have to be tackled in

the resolution of the system of equations during melting and vaporization stages:

- Fourier equations are solved in spatial domains with moving boundaries;
- The moving boundary evolution strongly depends on the temperature distribution of the different domains.

Taking into account moving boundary problems faced in freeze–drying [52] and solute concentration diffusion–controlled processes [51], the Landau approach [49] is adopted by the author for fixing the spatial extent of the different phase domains between [0,1], simplifying the resolution of the problem. This is based on a transformation of the coordinate system by defining the new positional variables in Table 3.5, which leads to the new system of equations in §3.4.1.1 and §3.4.1.2 for the melting and vaporization stages, respectively.

		Vapour	Liquid	Solid
Melting Stage	Domain		$0<x'<s'$	$s'<x'<1$
	Variables		$\xi = \frac{x'}{s'}$	$\eta = \frac{x'-s'}{1-s'}$
Vaporization Stage	Domain	$0<x'<r'$	$r'<x'<s'$	$s'<x'<1$
	Variables	$\zeta = \frac{x'}{r'}$	$\xi = \frac{x'-r'}{r'-s'}$	$\eta = \frac{x'-s'}{1-s'}$

Table 3.5: Spatial coordinates for boundary immobilization purposes.

3.4.1.1 Melting stage

By dropping the prime notation, the equations to be solved during the melting stage after the coordinate transformation become:

$$\frac{\partial \Theta_l}{\partial t} = \frac{K}{R \cdot C}\frac{1}{s^2}\frac{\partial^2 \Theta_l}{\partial \xi^2} + \frac{ds}{dt}\frac{\xi}{s}\frac{\partial \Theta_l}{\partial \xi} \qquad \text{at } 0 < \xi < 1 \tag{3.58}$$

$$\frac{\partial \Theta_s}{\partial t} = \frac{1}{(1-s)^2}\frac{\partial^2 \Theta_s}{\partial \eta^2} + \frac{ds}{dt}\left(\frac{1-\eta}{1-s}\right)\frac{\partial \Theta_s}{\partial \eta} \qquad \text{at } 0 < \eta < 1 \tag{3.59}$$

$$\frac{1}{s}\frac{\partial \Theta_l}{\partial \xi}\Big|_{\xi=0} = -\frac{1}{K} \tag{3.60}$$

$$(1-R)\frac{B_v \Theta_v}{H^*}\frac{ds}{dt} = -\frac{1}{1-s}\frac{\partial \Theta_s}{\partial \eta}\Big|_{\eta=0} + \frac{K}{s}\frac{\partial \Theta_l}{\partial \xi}\Big|_{\xi=1} \tag{3.61}$$

$$\Theta_s\Big|_{\eta=0} = \Theta_l\Big|_{\xi=1} = 0 \tag{3.62}$$

$$\frac{1}{1-s}\frac{\partial \Theta_s}{\partial \eta}\Big|_{\eta=1} = 0 \tag{3.63}$$

3.4.1.2 Vaporization stage

In the same way, the application of the coordinate transformation leads to the following system of equations during the vaporization stage:

$$\Theta = \Theta_v \qquad \text{at } 0 < \zeta < 1 \tag{3.64}$$

$$\Theta_v\Big|_{\zeta=1} = \Theta_l\Big|_{\xi=0} \tag{3.65}$$

$$\frac{\partial \Theta_l}{\partial t} = \frac{K}{R \cdot C(s-r)^2}\frac{\partial^2 \Theta_l}{\partial \xi^2} + \frac{\frac{dr}{dt} + \xi(\frac{ds}{dt} - \frac{dr}{dt})}{s-r}\frac{\partial \Theta_l}{\partial \xi} \qquad \text{at } 0 < \xi < 1 \tag{3.66}$$

$$\frac{\partial \Theta_s}{\partial t} = \frac{1}{(1-s)^2}\frac{\partial^2 \Theta_s}{\partial \eta^2} + \frac{ds}{dt}\left(\frac{1-\eta}{1-s}\right)\frac{\partial \Theta_s}{\partial \eta} \qquad \text{at } 0 < \eta < 1 \tag{3.67}$$

$$RB_v\Theta_v\frac{dr}{dt} = 1 + \frac{K}{s-r}\frac{\partial \Theta_l}{\partial \xi}\Big|_{\xi=0} \tag{3.68}$$

$$(1-R)\frac{B_v\Theta_v}{H^*}\frac{ds}{dt} = -\frac{1}{1-s}\frac{\partial \Theta_s}{\partial \eta}\Big|_{\eta=0} + \frac{K}{s-r}\frac{\partial \Theta_l}{\partial \xi}\Big|_{\xi=1} \tag{3.69}$$

$$\Theta_s\Big|_{\eta=0} = \Theta_l\Big|_{\xi=1} = 0 \tag{3.70}$$

$$\frac{1}{1-s}\frac{\partial \Theta_s}{\partial \eta}\Big|_{\eta=1} = 0 \tag{3.71}$$

3.4.1.3 Dimensionless model sensitivity analysis

The harsh conditions during VDEs might not be simulated in the current devices available worldwide. This opens up two possibilities on experiment planning towards validation, i.e. either choosing a different combination of lower power density and low melting point materials matching the same dimensionless parameters calculated for the reference case, or deploying one of the existing and available devices delivering the power density it can provide as a first step within a step–wise validation process. Although this last option will be the final author's choice (see Ch. 5), here the author briefly describes a sensitivity analysis carried in support of the first option, in order to identify which of the dimensionless parameters affect the output the most.

By considering a 1D 1 m-thick W slab facing HF = 300 GW m^{-2} on one side and insulated on the other, several analyses are run by altering one dimensionless parameter at a time (by a quantity listed in the second column of Table 3.6), while leaving all the others unchanged, in order to quantify the effect of each variation onto the output parameters. All the runs are carried out by keeping the same dimensionless total time $Fo(t_{end}) = 1.14 \cdot 10^{-7}$. From Table 3.6, the most affected output parameters are found to be the dimensionless times triggering melting and vaporization (Fo_m and Fo_v, respectively), and the dimensionless front face temperature at the end of the run (Θ_{front}). The dimensionless temperature at the beginning of the transient, i.e. Θ_{zero}, is found to be the most important variable affecting two (out of three) output parameters, Fo_m and Fo_v.

As already mentioned, the energy released by the plasma in 4 ms (transient duration) is absorbed by a thin layer of plasma–facing material, since the heat does not have enough time to reach the cooling system. The above–mentioned thickness of the material facing this fast transient is indicated as L in Fig. 3.13. By fixing L = 0.02 m, the relevant dimensionless parameter are reported in the second column of Table 3.7.

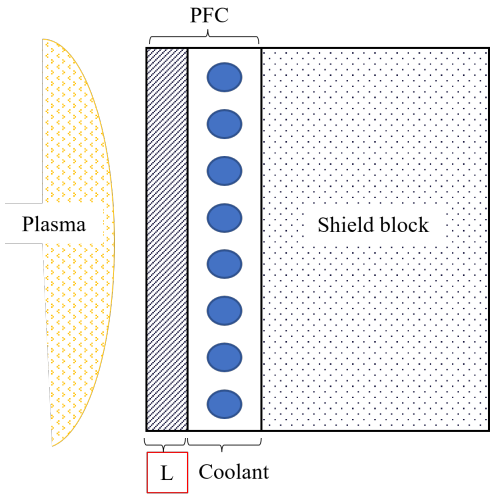

Fig. 3.13: Schematics of a limiter layout cross–section foreseeing a protruding material armour with a characteristic thickness L, to protect the cooling system underneath it.

Considering future potential experiments for validating the model, the $Fo(t_{end})$ and Θ_{zero} values in Table 3.7 can help scale the experimental equivalent conditions with respect to the worst–case scenario (i.e. using an equivalent combination of lower melting point materials and different heat flux conditions, whose values of Θ_{zero} and Fo match the related parameters for W

Dimensionless numbers	Ref. value	Variation	Fo_m	Fo_v	$\Theta_{front}(t = t_{end})$
$\Theta_{zero} = \frac{(T_{op}-T_m)\cdot k_s}{HF\cdot L}$	-1.01E-06	x 1	–	–	–
		x 0.85	15%	14%	–
		x 0.65	35%	33%	–
		x 0.45	55%	52%	–
$R = \frac{\rho_l}{\rho_s}$	0.8309	x 1	–	–	–
		x 0.85	–	1%	–
		x 0.65	–	2%	–
		x 0.45	–	3%	–
$K = \frac{k_l}{k_s}$	0.8479	x 1	–	–	–
		x 0.85	–	–	–
		x 0.65	–	–	–
		x 0.45	–	–	–
$C = \frac{c_{p,l}}{c_{p,s}}$	1.4685	x 1	–	–	–
		x 0.85	–	1%	–
		x 0.65	–	2%	–
		x 0.45	–	3%	–
$H^* = \frac{H_v}{H_m}$	16.3817	x 1	–	–	–
		x 0.85	–	–	–
		x 0.65	–	–	–
		x 0.45	–	–	–
$\Theta_v = \frac{(T_v-T_m)\cdot k_s}{HF\cdot L}$	7.50E-07	x 1	–	–	–
		x 0.85	–	5%	15%
		x 0.65	–	5%	35%
		x 0.45	–	5%	55%
$B = \frac{H_v}{c_{p,s}\cdot(T_v-T_m)}$	10.3157	x 1	–	–	–
		x 0.85	–	–	–
		x 0.65	–	–	–
		x 0.45	–	–	–

Table 3.6: Sensitivity analysis aiming at capturing the variation of the output parameters according to a prescribed variation of the input parameters.

in critical conditions). One way to scale up potential experiments is sketched in Fig. 3.14. Once the upper limits of the main variables involved in the thermal problem are set, like source power $\leq$ 10 kW, HF $\leq$ 0.1 MW m^{-2}, L $\leq$ 1 m, t $\geq$ 10 s, the choice of the material helps define the thermal diffusivity in Fo and the melting point in Θ_{zero}. T_{op} is the room temperature, therefore the thickness of the sample can be inversely calculated from Θ_{zero}, as well as the time duration of the experiment, calculated from Fo.

Variables	L=1 [m]	L=0.02 [m]
Fo(t=t_{end})	1.14E-07	2.84E-04
Θ_{zero}	-1.01E-06	-4.95E-05
Θ_{v}	7.50E-07	3.83E-05
R	8.31E-1	8.31E-1
K	8.48E-1	8.48E-1
C	1.47E0	1.47E+0
H*	1.64E+1	1.64E+1
B	1.03E+1	1.03E+1

Table 3.7: Dimensionless parameter values for a 1 m and 0.02 m-thick W slab.

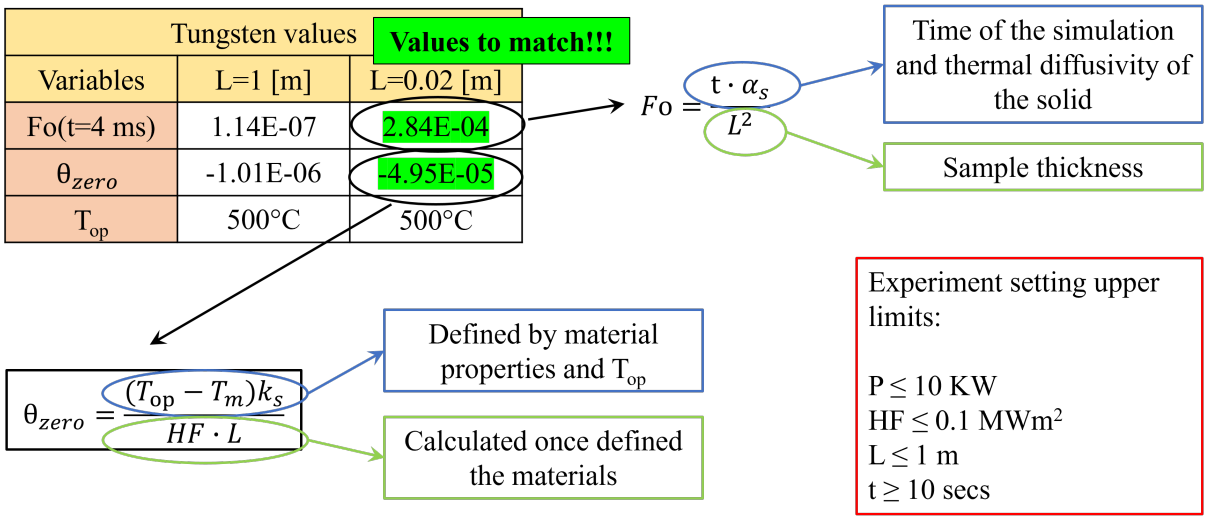

Fig. 3.14: Potential workflow for experimental setup scaling.

In conclusion, the TARTIFL&TTE analysis has been part of the author's initial experiment planning. The 1D model produces a strategy for tackling the heat transfer in presence of phase change and builds up an understanding on how this effect could be approached. However, its simplicity opens points to be addressed, since in reality the heat load on PFCs is hardly uniform, and the intense evaporation in vacuum is likely to affect the energy and mass balance. Since the coding becomes more and more convoluted, the focus is now looking for software helping with the implementation of the TARTIFL&TTE approach while allowing complexity to be added to the model, with the possibility to extend the analysis to 3D domains withstanding non–uniform HF. This allows the author to study the physics behind the phenomenon by moving the computational implementation of the mathematical model forward, after validating the TARTIFL&TTE approach.

Chapter 4

Multiphysics approach for heat transfer in presence of phase change in 3D geometries

"Essentially, all models are wrong, but some are useful."

George E.P. Box

The TARTIFL&TTE approach developed by the author is here described in its implementation through COMSOL Multiphysics®, therefore becoming 3D–TARTIFL&TTE. Although the approach is similar to TARTIFL&TTE, 3D–TARTIFL&TTE works on 3D geometries, and involves a more realistic way of computing the vaporization phase and its related mass removal from the condensed domain. This chapter focuses on 3D–TARTIFL&TTE description and its capability to predict the energy contributions involved during phase changes against existing experimental data.

The content of this chapter is published by the author in [16], co–authored with all the author's supervisors, i.e. Prof. P. Ireland, Dr. F. Maviglia, Dr. J. Nicholas, and Dr. Z. Vizvary.

4.1 Introduction

The way the multi–phase moving boundary problem is approached, and implemented in MATLAB®, leads to the creation of the TARTIFL&TTE (**T**hermal **A**nalysis fo**R** **T**racking

Inter**F**aces under me**L**ting **&** vaporiza**T**ion–induced plasma **T**ransient **E**vents) software. The energy balance behind this approach helps develop an understanding on the nature of this problem and the computational techniques to adopt. Although it requires improvements in the physics behind vaporization and the way it affects the energy balance, the computational implementation becomes more and more convoluted when going from 1D to more complex 3D geometries subjected to non–uniform heat flux. Since the methodology requires assessment, the aid of Multiphysics environments and software is sought as a step forward to equivalently reproduce the TARTIFL&TTE approach with both 2D/3D geometries and more complex physics. Therefore, the 3D–TARTIFL&TTE model implemented through COMSOL Multiphysics® is described hereafter, highlighting the main differences with TARTIFL&TTE.

Matlab® capability offers the built–in solver PDEPE for PDEs in one single spatial variable, with the possibility of solving two–space variable PDEs by means of the *PDE Toolbox*. The 3D upgraded version of *PDE Toolbox* is FEMLAB, developed by COMSOL Limited (Ltd) for solving PDEs numerically based on the finite element method. FEMLAB has later become COMSOL Multiphysics®, which is ultimately the commercial software chosen for this kinds of investigation.

COMSOL Multiphysics® is a general–purpose simulation software equipped with a user–friendly interface for CAD geometry handling. It offers both single–physics and multi–physics coupling among electromagnetism, structural mechanics, acoustics, fluid flow, heat transfer, and chemical engineering. It offers a Matlab–like environment where the user can input mathematical expressions describing a particular physical condition, which can depend on calculated variables, resulting in the software being relied upon to computationally solve the well–posed problem.

4.2 3D–TARTIFL&TTE

The TARTIFL&TTE stepwise approach of breaking down the heat transfer process in three phases, i.e. heat up, melting and vaporization, is replaced by a single transient thermal analysis. Any phase change is triggered and tackled within a single solid geometry domain, under the following assumptions:

1. Gravity effect can be neglected on melt pool of refractory materials in presence of strong

magnetic fields (based on findings in §2.5);

2. A single disruptive event might not be long and effective enough to completely remove the liquid layer from the melt pool (based on findings in §2.5.1). Therefore, the liquid layer always stays in place within the solid domain. This means that changes in tile shaping following local drifts of the melt mass towards the heated footprint neighbouring areas are neglected, together with any unavoidably alteration of the heat flux pattern with potential hot spots.

3. Although the scarcity of information on vapour shielding effects makes it difficult to model, there is no evidence yet that it works in reducing the incoming heat flux along any poloidal location of the wall, where the vapour cloud could be immediately ionized and removed along magnetic field lines. Therefore, a conservative approach of neglecting its effects might also be beneficial at this stage.

In the 3D–TARTIFL&TTE, the solid–to–liquid phase change is tracked within the solid domain by means of the *apparent heat capacity* formulation [101]. It describes and solves the thermal problem by using one energy balance equation (Eq. 4.1) that does not involve any latent heat. It assumes, instead, that the solid–to–liquid phase change occurs over the predefined temperature interval $T_m - \frac{\Delta T}{2}$ and $T_m + \frac{\Delta T}{2}$. The latent heat of fusion enters into the definition of *effective material properties* (see Eq. 4.2 for heat capacity, Eq. 4.4 for thermal conductivity and Eq. 4.5 for density definitions [101]), which are calculated from the temperature–dependent material property values assigned to every phase. The specific heat capacity is redefined as in Eq. 4.2, and encompasses the liquid and solid specific heat capacities plus the enthalpy ($\delta H = H_l - H_s = H_m$) required by the mass fraction α_m to change state. The transition is tracked by means of a temperature–dependent phase indicator Ω, whose value ranges between [0, 1]. Before melting, $\Omega_s = 1$ and $\Omega_l = 1 - \Omega_s = 0$, whereas $\Omega_s = 0$ and $\Omega_l = 1$ if only liquid phase is present. The mass fraction α_m ranges from [-1/2,+1/2] for, respectively, solid and liquid phases [101]. The position of the melting interface over time is tracked by means of linear projections adopted for integrating Ω_l within the volume of the geometric domain.

$$\frac{\partial H}{\partial t} = \frac{\partial H}{\partial T}\frac{\partial T}{\partial t} = c^A \frac{\partial T}{\partial t} = \boldsymbol{\nabla} \cdot (k^A \boldsymbol{\nabla}(T)) \tag{4.1}$$

$$c^A = \frac{1}{\rho^A}(\Omega_s \rho_s c_{p,s} + \Omega_l \rho_l c_{p,l}) + \delta H \frac{d\alpha_m}{dT} \tag{4.2}$$

$$\alpha_m = \frac{1}{2}\frac{\Omega_l \rho_l - \Omega_s \rho_s}{\rho^A} \tag{4.3}$$

$$k^A = \Omega_s k_s + \Omega_l k_l \tag{4.4}$$

$$\rho^A = \Omega_s \rho_s + \Omega_l \rho_l \tag{4.5}$$

In line with the TARTIFL&TTE approach, the vapour domain is not simulated. While TARTIFL&TTE removes the vapour phase once formed by leaving the surface at the fixed boiling temperature T_v, 3D–TARTIFL&TTE simulates the vaporization phase by means of boundary conditions imposed on the top surface of the liquid layer. The vapour phase contribution to the energy balance is calculated through the estimate of the evaporative mass flux departing from the liquid layer after reaching the boiling point. Only at that point the contribution of the evaporative heat flux does become high enough to decrease the incoming heat flux magnitude, without the need to impose a threshold boiling temperature value to trigger this phase change. Furthermore, in the 3D–TARTIFL&TTE the surface temperature is allowed to adjust its value in accordance with the saturation pressure, which affects the amount of the evaporative mass flux at every time instant. This affects, in turn, the surface temperature.

In summary, the heat flux absorbed by the domain (HF_{abs}) as sensible and latent heat of fusion results from a balance between the incoming space–and–time–varying heat flux (HF_{in}) and the outgoing energy contributions due to either evaporative (HF_v) and radiative (HF_{rad}) heat fluxes. As a result of this balance, the heat flux applied to the front face of the loaded component is computed as in Eq. 4.6. The evaporative heat and mass fluxes are evaluated by using the gas kinetics approach (Hertz–Knudsen–Langmuir law, Eq. 4.7), where the retro–diffusion coefficient $\beta_R = 0.18$ [70] accounts for the fraction of evaporated particles which re–condensates after interacting with the surrounding gas.

The radiative heat flux depends on the temperature–dependent surface emissivity (ε) and the Stefan–Bolzmann constant ($\sigma_B = 5.6704 \cdot 10^{-8}$ W m^{-2} K^{-4}).

$$HF_{abs} = HF_{in} - HF_v - HF_{rad} \tag{4.6}$$

$$HF_v = (1 - \beta_R)\sqrt{\frac{M}{2\pi RT}}P_{sat}(T)H_v = \dot{m}H_v \tag{4.7}$$

$$HF_{rad} = \varepsilon\sigma_B\left(T_{front}^4 - T_{amb}^4\right) \tag{4.8}$$

Another difference between the two models is how the phase change is computationally tackled. In the 3D–TARTIFL&TTE, the evaporative mass flux pushes the surface of the condensed domain back, which unavoidably deforms under mass loss. This recession is simulated by using the Lagrangian–Eulerian approach (ALE, already implemented in COMSOL Multiphysics®) with a deformed mesh domain whose front face recessive velocity (v_v, Eq. 4.9) is defined by imposing the mass continuity at the front face.

$$v_v = \frac{\dot{m}}{\rho_l} \tag{4.9}$$

For helping the software solve the computational problem, while avoiding the presence of distorted elements under a deforming domain, the velocity of the moving interface v_v is not imposed directly. It is instead used for calculating the equivalent deformation of every spatial point undergoing vaporization (see Eq. 4.10, with a damping factor d_a equal to 1 and a null mass coefficient $e_a = 0$). The spatial displacement is imposed as boundary condition through the definition of the boundary PDE in Eq. 4.10. The vapour–to–liquid interface is tracked by storing the average and maximum displacement values over time. A 2D sketch of the 3D domain subjected to phase change is shown in Fig. 4.1.

$$e_a\frac{\partial^2 x_v}{\partial t^2} + d_a\frac{\partial x_v}{\partial t} = v_v \tag{4.10}$$

4.2.1 Validation activity

The model needs to be validated for understanding its level of reliability under high heat flux. Since there is no data available in literature to be reproduced with high fidelity, either due to lack of clear input data, or due to the different purpose of the performed experiments, dedicated experiments are planned. Therefore, high heat flux source facilities are sought after.

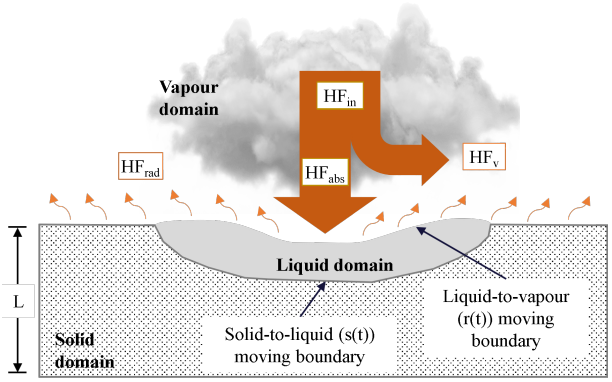

Fig. 4.1: 2D visual sketch of 3D–TARTIFL&TTE implementation. HF_{rad}, HF_v and any potential vapour shielding effects not yet modelled are responsible of decreasing the amount of energy absorbed by the domain as sensible and latent heat of fusion.

The two main facilities identified for supporting the validation activity are: QSPA Kh-50 (Ukraine), and GLADIS (Germany). The preliminary validation of the computational model is here based on data generated from past experiments run in QSPA (see §4.2.1.1). Unfortunately, due to the current international circumstances, QSPA is no longer available for running new dedicated experiments. The experimental campaign was instead performed in the GLADIS facility, whose description and results are presented in Ch. 5.

4.2.1.1 Benchmark against semi-experimental data from QSPA Kh-50

The Quasi–Stationary Plasma Accelerator (QSPA Kh-50) [102, 103, 104] is the largest world-wide plasma accelerator with unique plasma conditions. It is hosted by the Institute of Plasma Physics in Kharkov (Ukraine), and it can deliver an average heat flux of 4 GW m^{-2} over a 0.18 m-diameter footprint during a 0.25 ms pulse. It is used for loading samples devoted to vapour shielding investigations, although very little is available in terms of experimental output data, due to the lack of high–sensitivity diagnostics characterizing this facility. Before the facility became unavailable in early 2022, a mix of both experimental and computationally reconstructed data have been collected and provided by Ukrainian researchers [105, 106, 107, 108] to the author, which are here used for an assessment of the 3D–TARTIFL&TTE.

The provided data are related to shots where 5x5x1 cm^3 pure W samples are loaded for 0.25 ms with a 6 GW m^{-2}–peaked triangularly time–varying heat flux profile over a 3 cm-diameter footprint, which is defined by a Mo diaphragm with an aperture of 3 cm installed in front of the

W target to provide a clear–cut spot irradiated with uniform power density [105]. Among the measured data, i.e. plasma density, pressure, velocity, and integrated energy density absorbed by the target, only the last one is used in the present work. All the other output parameters indicated hereafter as "reference", such as the surface temperature evolution, heat flux and time evolution of the molten layer depth are inversely reconstructed in [105] and [107] by means of the PEGASUS-3D software [106]. The data on molten layer depth and vaporized thickness come from post–mortem analyses on loaded samples [108].

Two shots are here taken as reference (see Fig. 4.2a). Fig. 4.2b shows the W sample and its footprint subjected to the two triangularly–shaped heat flux evolutions, i.e. HF_1 and HF_2, respectively, plotted in Fig. 4.2a. $E_{abs_1} = 0.75$ MJ m^{-2} and $E_{abs_2} = 1.51$ MJ m^{-2} are, respectively, the integrated absorbed energy densities for the two shots. The rest of the provided

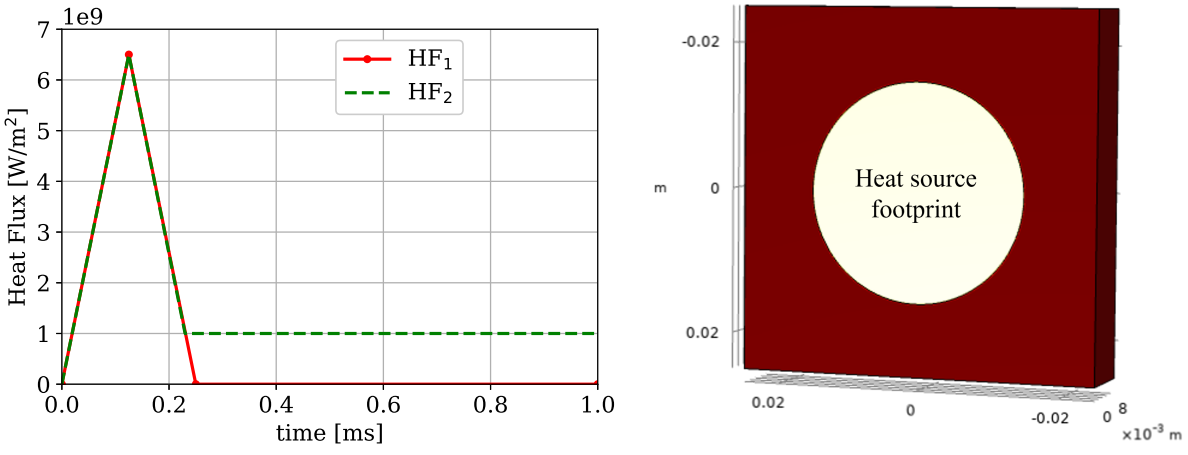

(a) (b)

Fig. 4.2: (a) Time-dependent heat flux values applied over the 3 cm-diameter footprint of the (b) W sample.

data is listed in Table 4.1, where they are compared with the related data calculated by 3D–TARTIFL&TTE. Fig. 4.3 compares the time evolution of the surface temperatures, whereas the molten layer depths are reported in Fig. 4.4. Fig. 4.5 and Fig. 4.6 plot other output parameters calculated by 3D–TARTIFL&TTE, such as the vapour interface, its velocity, the evaporative heat flux and the absorbed energy density over time. The material properties used for pure W are taken from [109].

The input heat flux is applied at every time step along the fixed plasma stream direction,

	Reference	Calculated	Error
HF_{max1}/HF_{max2} [GW m^{-2}]	6.0/6.0	6.5/ 6.5	8%
E_{abs1}/E_{abs2} [MJ m^{-2}]	0.75/1.51	0.81/1.57	8%/4%
t_m [ms]	0.13	0.14	8%
t_{solid} [ms]	0.23	0.21	9%
$T_{front,max}$ [K]	4089	4011	2%
Melt layer [μm/pulse]	6.6	5.7	14%

Table 4.1: QSPA Kh-50 data for validation provided by Ukrainian researchers [105, 107]

whose peak over time is increased by 0.5 MW m^{-2} to overcome the smoothing introduced by the boundary PDE used for imposing the deformation simulating the evaporative mass removal. The reference value of the integrated absorbed energy density is 1.51 MJ m^{-2}. The calculated

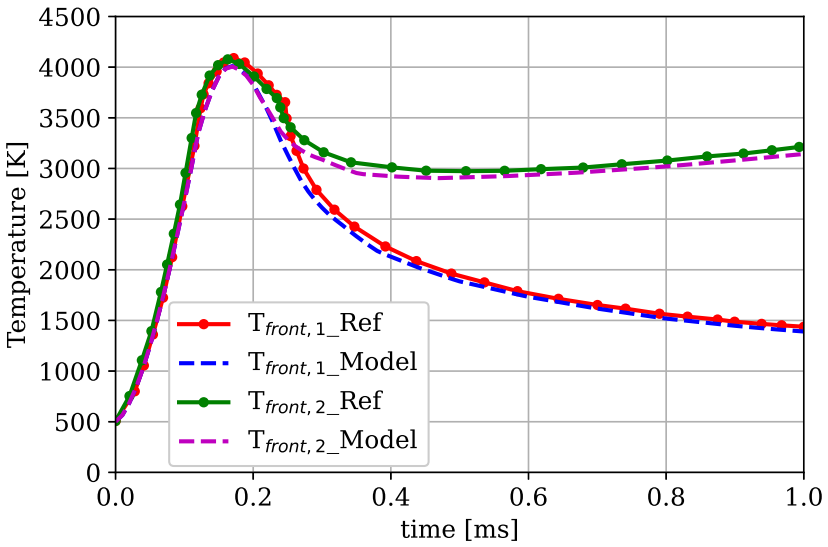

Fig. 4.3: Time evolution of the reference VS modelled surface temperatures under the applied HF_1 and HF_2 profiles.

one is 1.57 MJ m^{-2}, considering the increase of the maximum value of the input heat flux by 8%. In terms of molten and vaporized layer depths, indicated respectively as s(t) and r(t), the two heat flux profiles produce the same effect. 3D–TARTIFL&TTE starts experiencing melting ($T_{front} = T_m = 3695$K [109]) at 0.14 ms, while solidification is experienced at 0.21 ms. The reference data highlights that the melting layer starts appearing at 0.1 ms, and it solidifies at 0.23 ms. The maximum modelled molten layer depth is 5.7 μm against the reference 6.6 μm. This leads to a preliminary satisfactory conclusion on the 3D–TARTIFL&TTE approach, being

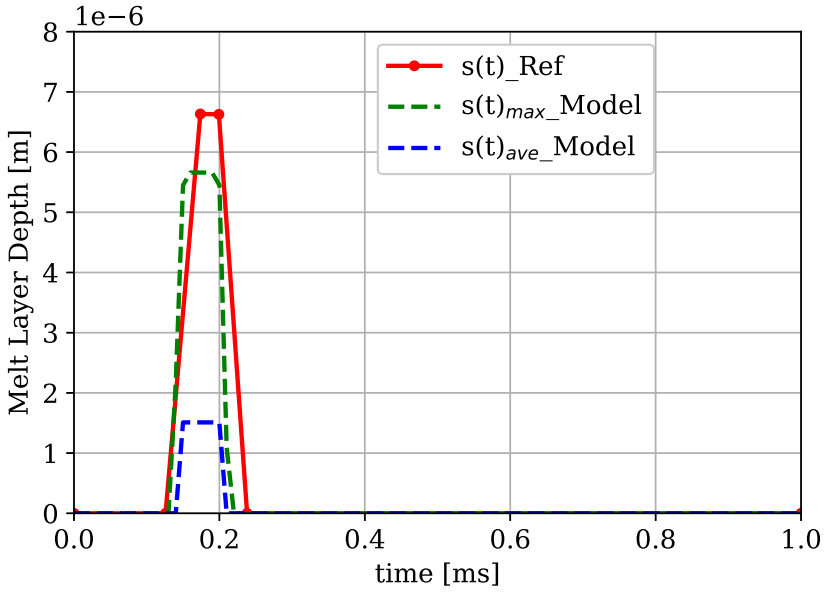

Fig. 4.4: Time evolution of the reference solid–to–liquid interface position VS the calculated one. Both the maximum and the average modelled values are here reported.

able to match the key–output parameters, i.e. surface temperature and melt layer depth, with a 3D domain undergoing non–uniform heat flux.

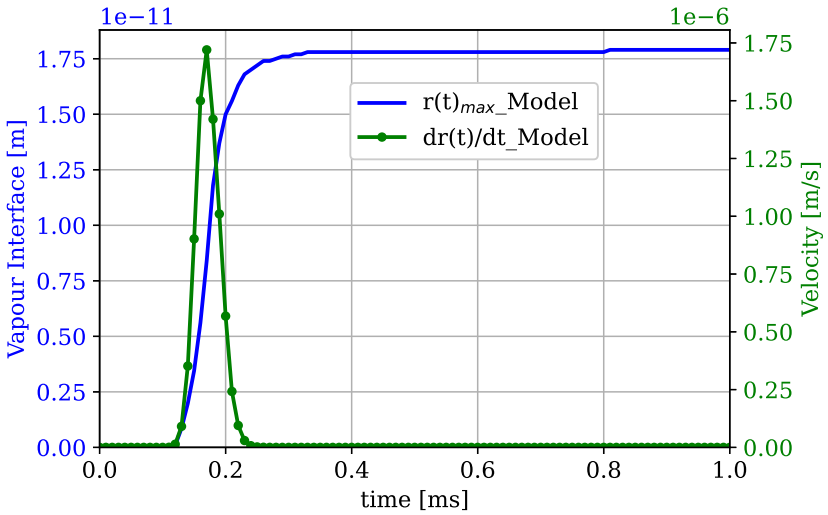

Fig. 4.5: Modelled vapour–to–liquid interface position over time and surface recession velocity due to vaporization.

As for the surface recession due to vaporization, the calculated maximum value of the surface deformation is 0.018 nm, meaning that vaporization is negligible ($T_{front} \ll T_v \approx 5800K$ [110]) and only a moderate evaporative mass flux leaves the surface. V.I. Tereshin et al. in [108]

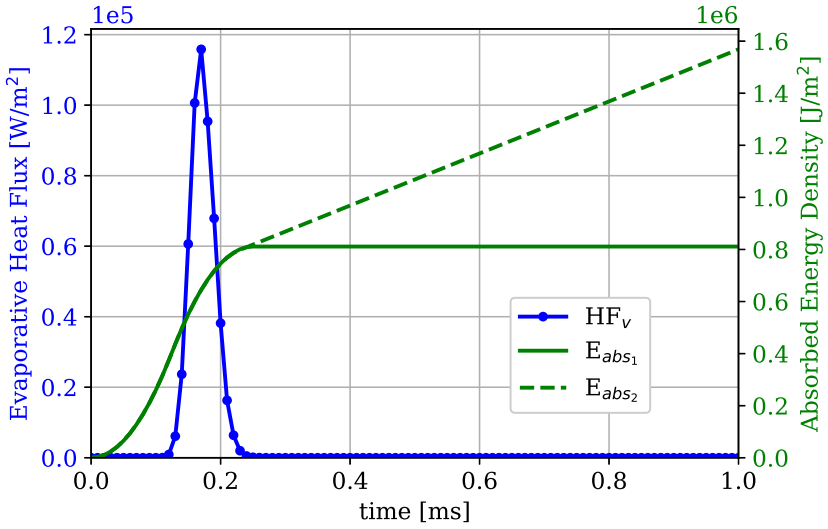

Fig. 4.6: Time evolution of the calculated HF_v and deposited energy density E_{abs}.

estimated the average erosion rate to be ≈30 nm/pulse for W samples subjected to repetitive QSPA pulses with 1.1 MJ m^{-2} energy density, which is 10 times less for pulses delivering 0.7 MJ m^{-2}. However, they underline that for initial pulses, the boiling is initiated on the surface by impurities, and only after 25 pulses it becomes a volumetric phenomenon which contributes to mass losses possibly due to intensification of evaporation and W splashing. Although 3D–TARTIFL&TTE can deal with vaporization, impurities effects, splashing and melt motion are not captured. Therefore, no unambiguous conclusion based on common assumptions can be here stated on the modelled vapour layer.

4.3 Results

The benchmark reported in §4.2.1.1 shows good agreement between the reference and modelled data, especially in terms of maximum surface temperature and melting interface depth. Although the molten layer always stays in place during the heating time, all the parameters agree well within 15% error. As for the vapour layer depth, no clear comparison can be established between the reference and the modelled data, due to the different conditions under which vaporization occurs both in experiments and computational modelling. This has to be added to the difficulty to reach experimental vaporization conditions well captured by diagnostics. If the evaporative erosion rate is assumed as reference value, one explanation to this discrepancy

might be related to the combined effects of heat flux acting on deforming mesh elements and the smoothing effect produced by the way the surface deformation is imposed through PDEs. This would explain why only the liquid–to–vapour interface tracking is affected, whereas the energy contribution is rightly captured as shown in Fig. 4.4. Three main points should be here argued: (a) the front face of the sample never reaches the boiling point (Fig. 4.3); (b) material impurity effects are not taken into account for the estimate of pure W melting and boiling points; (c) average erosion rate in [102] is based on vaporization strongly affected by impurities during the first shots of a series of repetitive pulses. Therefore, due to lack of solid basis on which establishing any comparison on the vapour layer, the author cannot draft any final conclusions on vapour layer yet, leaving the investigation of this aspect only after assessing the 3D–TARTIFL&TTE capability of correctly capturing the melt layer depth.

In conclusion, the first benchmark against QSPA data shows a good agreement on molten layer depth estimate, paving the way for its use within the engineering design workflow of metallic plasma–facing components. A stepwise validation activity is now foreseen to further support the benchmark of the 3D–TARTIFL&TTE approach and drive its way of approaching the phase changes, especially when they involve intense vaporization. Therefore, as a step forward, a dedicated campaign of melting experiments is foreseen in the GLADIS facility to support a further validation of the model. The results of this experimental validation is described in Ch. 5.

Chapter 5

Melting experiment campaign supporting the computational modelling

"Without data you are just another person with an opinion."

William Edwards Deming

The preceding chapters describe the TARTIFL&TTE approach for tackling the phase change occurrence when solid components are subjected to high heat fluxes. This chapter describes the 3D–TARTIFL&TTE benchmark against dedicated experimental results, whose primary aim is to test its capability of reliably predicting the molten layer depth. This chapter includes the description of the melting experiments hosted by the GLADIS facility, as well as the experimental results and the related benchmark activity.

The author acknowledges the support of the scientific supervisors of the GLADIS facility in preparing the beam source experimental setup and the diagnostic calibrations. Although they are briefly described by the author, these activities are not performed by the author and, hence, they are not part of this work.

The findings of this chapter are published by the author in [17], co–authored with the scientific supervisors of the GLADIS facility, i.e. H. Greuner and B. Boswirth, as well as the author's supervisors, i.e. Prof. P. Ireland and Dr. Z. Vizvary.

5.1 Experimental requirements

The experiments are conducted under the following requirements, dictated by the 3D–TARTIFL&TTE capability of reproducing them:

1. Measurable power density deposited at the sample front face;
2. Power density as uniform as possible onto the heated surface;
3. Well–defined initial and boundary conditions of the samples throughout the experiments;
4. Calibrated diagnostics for characterizing the samples throughout the experiments;
5. Exposure time to be long enough for ensuring the collection of data;
6. Melt layer always in place during the exposure time.

Although the facility and the experimental choices are driven to great extent by these requirements, the search for worldwide heat sources mostly depends upon their availability. As already introduced in Chapter 4, the GLADIS facility supported the melting experiments as a first validation stage.

5.2 GLADIS

The Garching Large Divertor Sample Test Facility (GLADIS) [111] is operated by the Max Plank Institute for Plasma Physics (IPP, Garching, Germany). The facility is firstly commissioned for providing high heat flux testing capability for highly loaded PFCs. Hence, it is mainly deployed for testing the candidate plasma–facing material behaviour under high heat flux, whose magnitude is typical of the divertor heat loads. Fig 5.1 gives an overview of the GLADIS main chamber and its auxiliary systems. The samples are introduced into the main chamber through the lateral guiding system, which is also equipped with a sample cooling system in–between pulses. The inlet temperature and pressure values can range, respectively, 20-230°C and 1-4 MPa.

GLADIS is equipped with two H neutral beam sources of 1 MW each, delivering heat fluxes in the range 5-45 MW m^{-2} over 0.001-45 s pulse length. The power density is spatially deposited

Fig. 5.1: Overview of the GLADIS test chamber.

onto the target with a Gaussian profile, peaked at the centre of the beam. The 150 mm FWHM of the neutral beam deposits more than 90% of the central power density within a 50 mm-diameter footprint [111].

Fig. 5.2 shows a top view of the experimental setup. Hydrogen atoms (in green) are ionized, accelerated under voltage up to 50 kV, neutralized and conveyed towards the target.

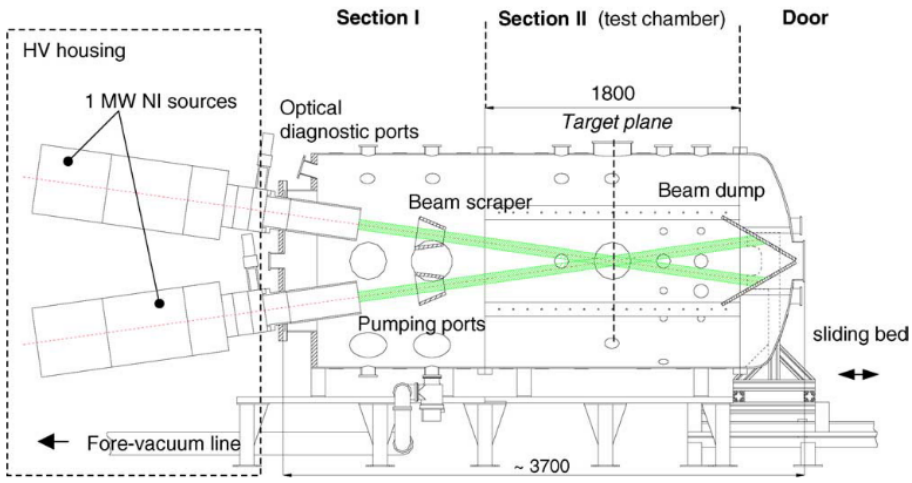

Fig. 5.2: GLADIS experimental setup top view [mm] [111].
Figure reprinted from [111], with permission from Elsevier.

Figure 5.3 gives an overview of the installed diagnostics, which make GLADIS one of the most well–characterized facilities within the worldwide fusion community. The different diagnostics are listed below.

- Charged–Coupled Device (CCD) camera for visual monitoring sitting on the ion source

flange;

- Calorimeter located at the top of the main chamber to measure the power density deposited onto the target. It consists of thermally insulated Cu plugs of known mass, mounted in a Cu bar located at a known distance from the beam. The calorimeter can be moved inside the vessel through a manipulator system;
- One colour and two colour pyrometers for single point surface temperature measurements, indicated respectively as 1c–Pyro [350-3500°C] and 2c–Pyro [500-1700°C];
- 200 Hz infra–red thermography (IR) camera for surface temperature mapping;
- Two N–type thermocouples (TCs) fixed at the back of the samples through springs for in–depth measurements of temperature up to 1700°C.

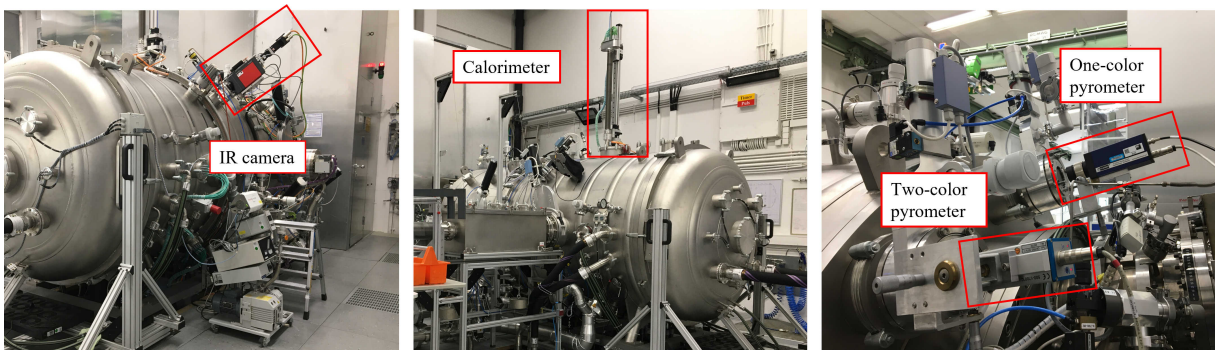

Fig. 5.3: Overview of GLADIS diagnostic system.

As opposed to electron beam, the neutral beam generates an almost homogeneous heating due to the complete absorption of the beam power onto the target surface. This is particularly useful for metallic components, where electron beams suffer from back–scattering and formation of secondary electrons on the target surface, which reduce the absorbed power by up to 50% of the input beam power [112]. Furthermore, electrons have a deeper penetration range than ions with the same kinetic energy, therefore the neutral beam is the preferred heat source for this first experimental campaign.

5.3 Definition of the experimental campaign

The validation of the modelled data is based on the comparison against the following measured parameters:

- Surface temperature evolution;
- Integrated energy density deposited onto the sample during the heating time;
- Position of the solid–to–liquid interface at the end of the transient.

The first two points are part of the non–destructive post–processing, since IR and pyros collect real–time temperature measurements over the shot duration. As far as the last comparison is concerned, no suitable diagnostics are found for tracking the solid–to–liquid interface position during the pulse. Therefore, a destructive post–processing is pursued at the end of the experimental campaign, aiming to sectioning the samples for cross–section analyses. The detection of the interface position between different material structures at microscopic level should give an indication on the depth of the molten layer at the end of the transient. The post mortem analysis also involves the weighting of the sample after the experimental campaign. Measurements of the mass loss are taken as comparison between every sample weight before and after the experiments.

5.3.1 Sample design and fabrication

The samples are shown in Fig. 5.4. They are 80x60x30 mm^3–sized bricks, whose technical

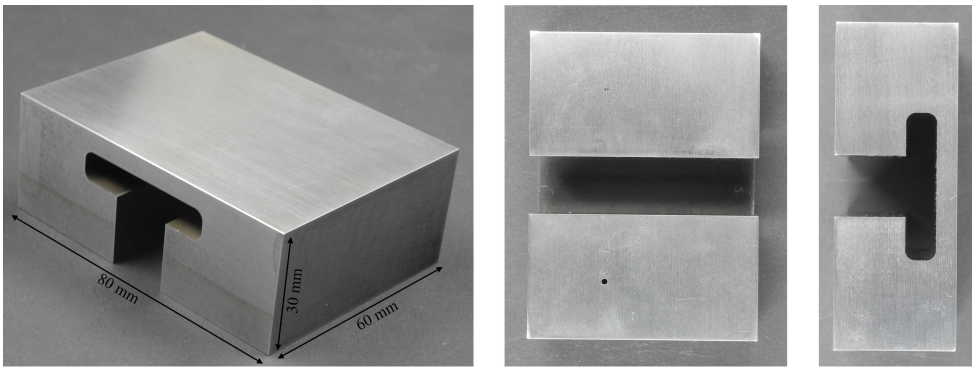

Fig. 5.4: Manufactured samples (3D and 2D sides).

specifications are shown in Fig. 5.5. They are designed compatibly with the T–shaped sliding

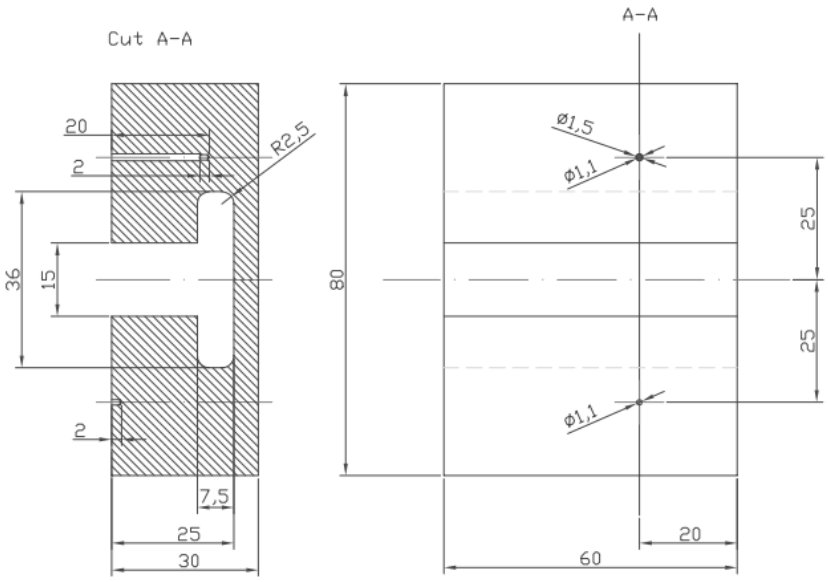

Fig. 5.5: Technical specification of the samples. All the measurements are in mm.

system holding them in place inside the main chamber of GLADIS, as shown in §5.3.2. Two TC holes are embedded into them to track the temperature evolution at two different depths, i.e. 20 mm and 2 mm, respectively, from the sample's back–surface. Fig. 5.6 highlights the described features.

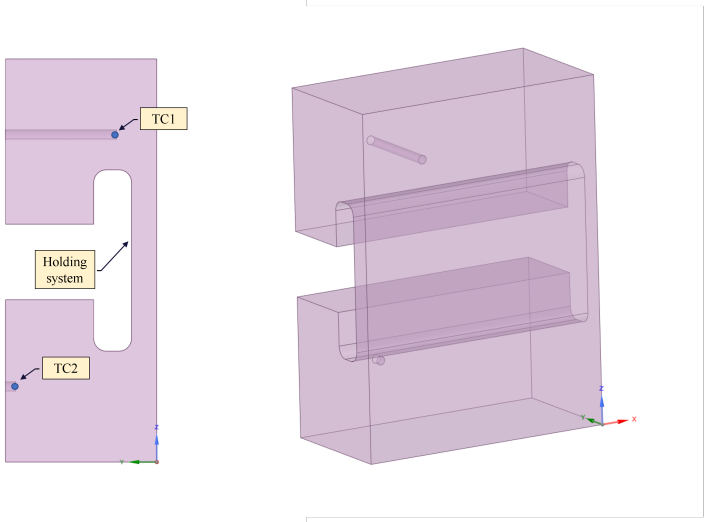

Fig. 5.6: Geometric model of the sample.

Samples are manufactured by the UK–based Formagrind Ltd [1] company, and then shipped to the IPP for experiments.

[1] `https://www.futurealloys.co.uk`

The three materials highlighted below are selected, based on both their relevance to fusion components and the possibility to broaden and diversify the data obtained from different materials in support of the benchmark. For every material, two samples are loaded for result repeatability. Table 5.1 reports chemical composition of the materials provided by the manufacturer.

- Titanium Zirconium Molybdenum (TZM) alloy (TZM–1 and TZM–2 samples), mostly containing Mo (99.42%) with a little percentage of Ti (0.5%) and Zr (0.08%). TZM has the same thermal behaviour as pure Mo but better mechanical properties, and its melting point is lower than W.
- Pure W (W–1 and W–2 samples): this is the targeted plasma–facing material for DEMO.
- Stainless Steel (SS) – grade 316 (SS–1 and SS–2 samples). SS has different material properties than Mo and W, and it will help diversify the experimental results against which to benchmark the model.

	Fe	Ni	Si	Ti	Zr	C	N	O	Mg	P	S	Cr	Ni	Mo	W
							weight %								
TZM	0.0020	0.0009	0.0010	0.52	0.079	0.011	0.0008	0.046						Balance	
W	0.008 max	0.005 max	0.007 max	0.013 max		0.006 max	0.003 max	0.002 max						0.013 max	Balance
SS316			0.41			0.014	0.042		1.75	0.032	0.025	16.85	10.10	2.04	

Table 5.1: Samples' material composition (weight%) provided by the manufacturer.

5.3.1.1 Material Properties

The thermophysical properties of W, TZM and SS are gathered by the author from the literature references listed below.

- TZM properties are taken from [113, 114, 115]. Due to the lack of available data and high concentration of Mo in TZM, the author uses bulk Mo thermophysical properties for this study.
- W data are taken from [109, 116, 117] and the NIST website[2].
- SS data are found in [116, 117, 118, 119].

[2] https://webbook.nist.gov

Temperature–dependent c_p, λ, ρ, and ε are plotted in Fig. 5.7, Fig. 5.8, Fig. 5.9, and Fig. 5.10, respectively.

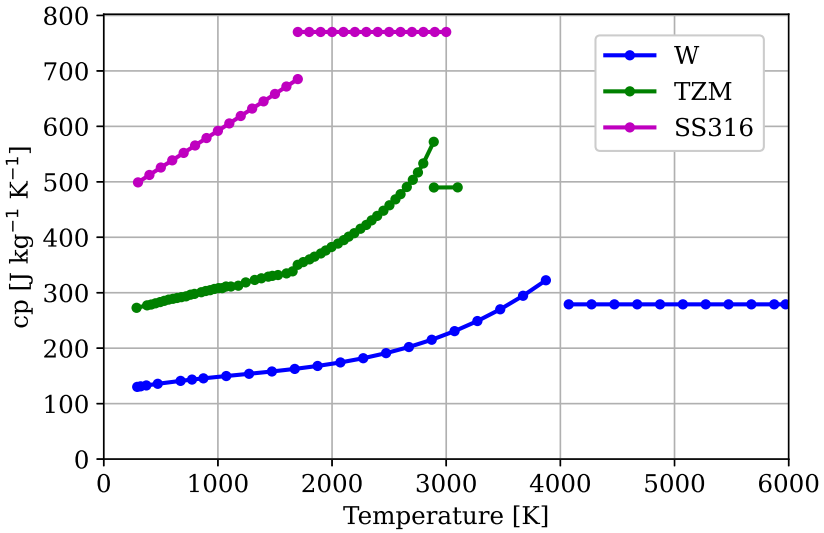

Fig. 5.7: Temperature–dependent specific heat capacities for W, TZM and SS316.

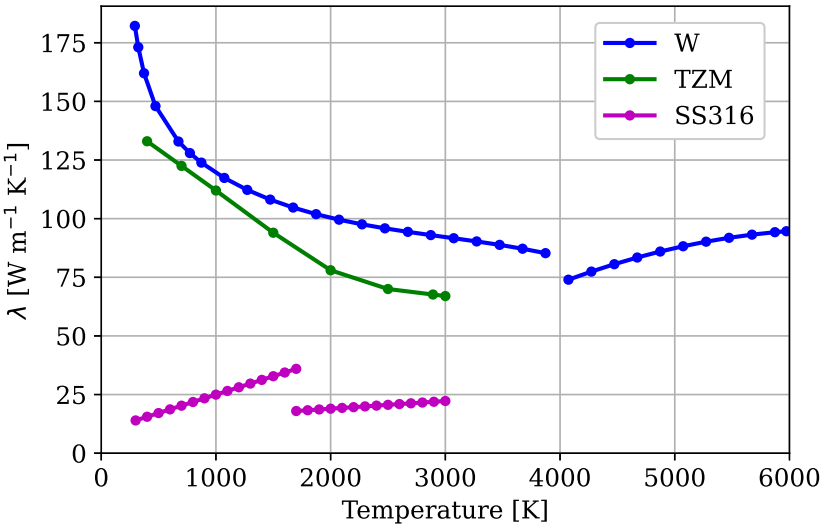

Fig. 5.8: Temperature–dependent thermal conductivities for W, TZM and SS316.

The vapour pressure of TZM, W and SS316 are driven by Eqs. 5.1, Eq. 5.2 and Eq. 5.3, respectively, and plotted in Fig. 5.11. For TZM, the Mo data is assumed to be valid.

$$\log P_v\ [\mathrm{Pa}] = 10^6 \cdot \left(5.147 - \frac{30500}{T[\mathrm{K}]}\right) \tag{5.1}$$

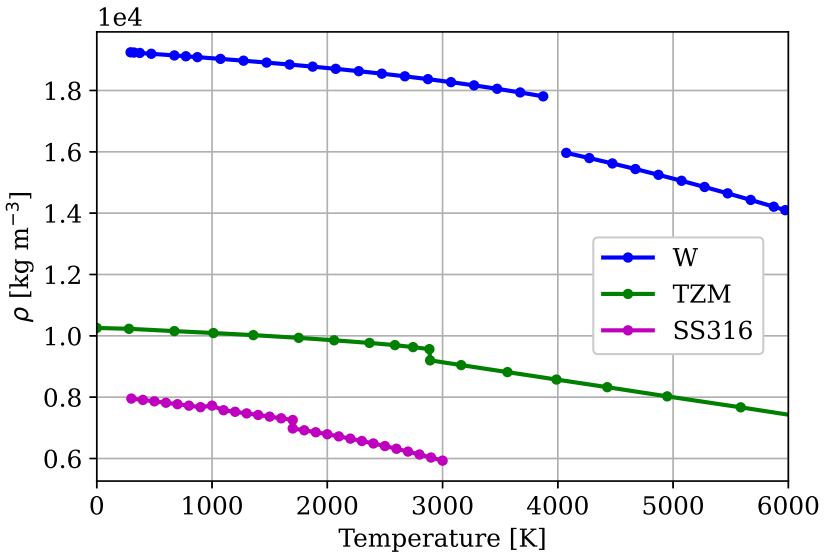

Fig. 5.9: Temperature–dependent densities for W, TZM and SS316.

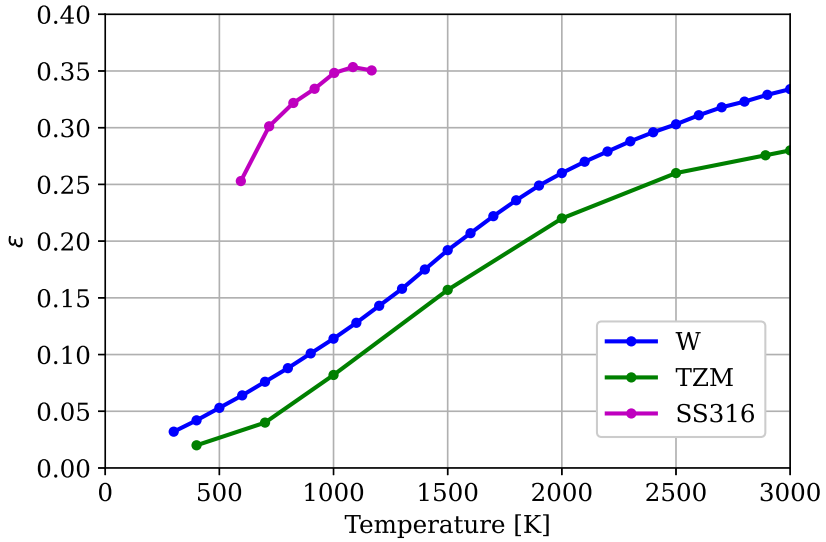

Fig. 5.10: Temperature–dependent emissivity values for W, TZM and SS316.

$$\mathrm{P_v\ [Pa]} = \exp\left\{26.19104 - \frac{8.39713 \cdot 10^4}{\mathrm{T[^\circ C]}}\right\} \tag{5.2}$$

$$\log \mathrm{P_v\ [Pa]} = 10^6 \cdot \left(5.237 - \frac{19100}{\mathrm{T[K]}}\right) \tag{5.3}$$

Table 5.2 summarizes the melting and boiling temperatures of TZM, W and SS316, as well

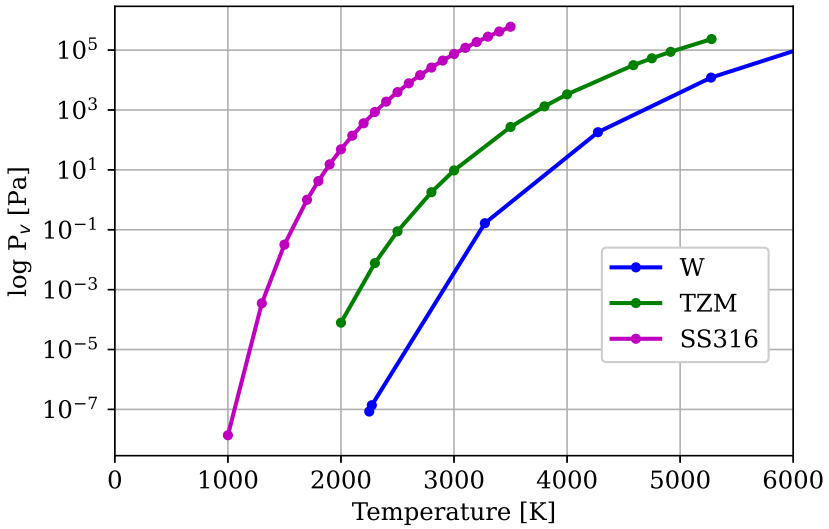

Fig. 5.11: Surface temperature–dependent P_v for W [116], TZM [117] and SS316 [117].

as the related latent heat of fusion and vaporization.

Material	T_m [K]	T_v [K]	H_m [Jkg^{-1}]	H_v [Jkg^{-1}]
W	3695	5900	273607	4629188[1]
TZM	2892	4983	390869	6149677
SS316	1700	3090	288889	7410636

[1] https://webbook.nist.gov/cgi/cbook.cgi?ID=C7440337&Units=SI&Mask=1#Thermo-Gas

Table 5.2: Phase change parameter values adopted for TZM, W, and SS316.

5.3.2 Experimental Methodology

Fig. 5.12 gives an overview of the sample installation before they are introduced into the main vacuum chamber. Samples are held in place by means of a T–shaped bar, which is tightly mounted onto an actively cooled Cu plate acting as heat sink. At the back of the sample, the two TCs are fixed by springs inside their dedicated machined holes.

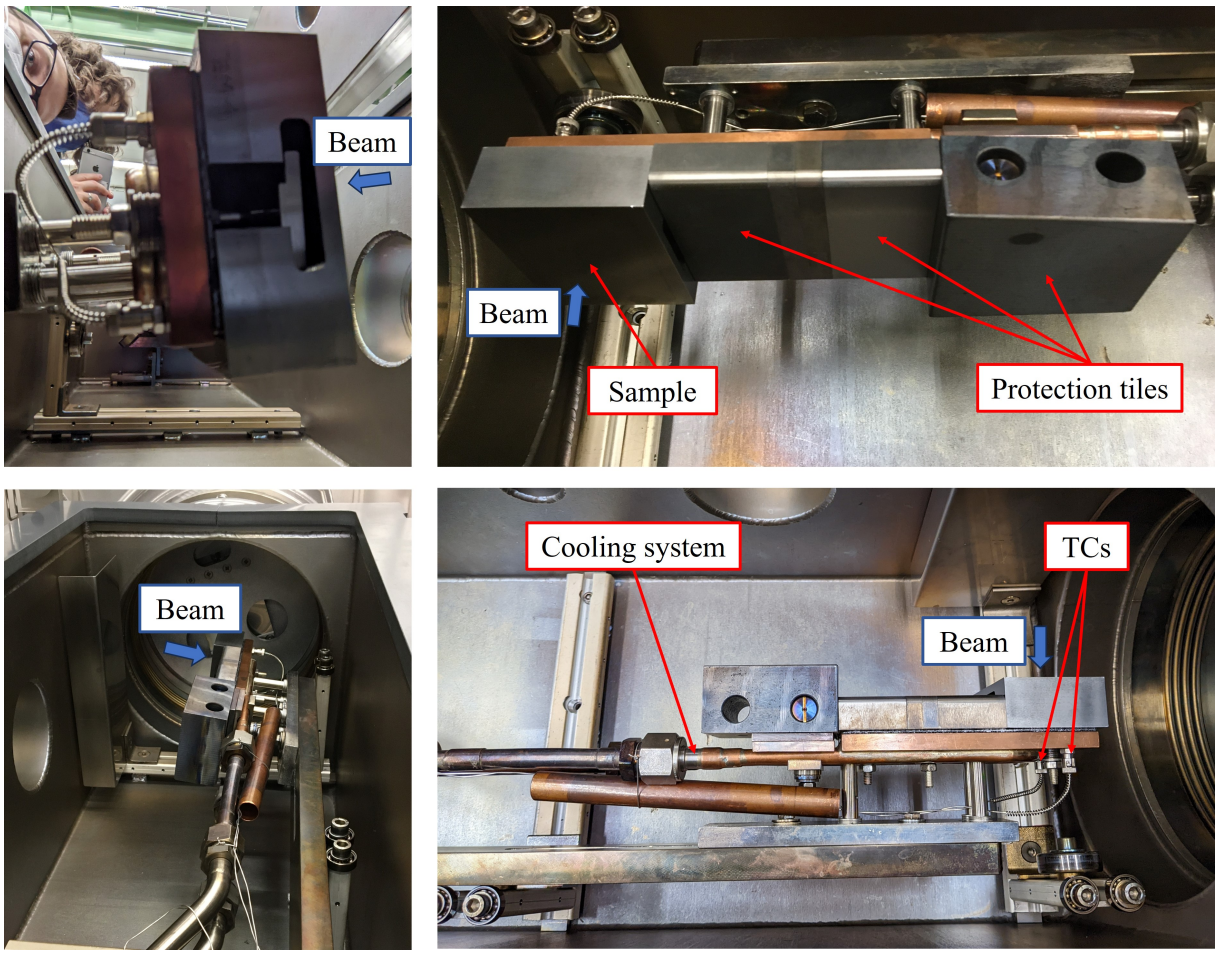

Fig. 5.12: Sample mounting and installation on the lateral guiding chamber.

After mounting the sample inside the lateral sliding guide (see Fig. 5.1), vacuum is created until the pressure reaches $P < 10^{-3}$ mbar. This pressure value triggers the opening of the shutter to the main vacuum chamber, where the sample is inserted. An automatic system deals with the alignment of the sample centre with the beam centre. Fig. 5.13 shows the sample inserted in the main chamber and ready for the shot.

Every sample is thermally loaded under a spatial Gaussian waveform of the heat flux, whose maximum values and standard deviations are listed in Table 5.3. For every sample, Table 5.3

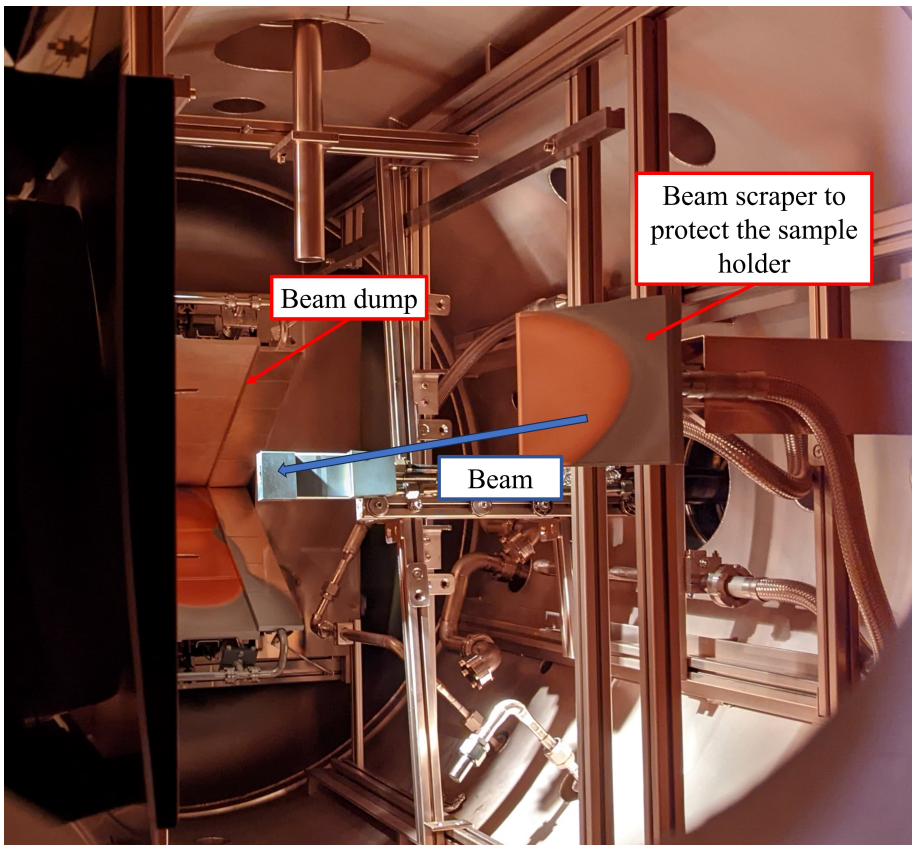

Fig. 5.13: Installation of the sample within the GLADIS main chamber.

reports the loading time, the time instants at which IR and 1c–Pyro trigger the beginning of the melting phase ($t_{m,IR}$ and $t_{m,pyro}$, respectively), and the initial temperature (T_0) calculated as the average value between the two TC measurements before the beam is switched on. Experiments are conducted under vacuum conditions.

Sample	HF_{max} [MWm^{-2}]	St.Dev. [mm]	Δt_{load} [s]	$t_{m,pyro}$ [s]	$t_{m,IR}$ [s]	T_0 [°C]
TZM–1	30	64.98	1.567	0.96	0.96	12
TZM–2			1.301	0.95	0.95	13
W–1	30	64.98	1.865	1.48	1.49	12
W–2			1.819	1.50	1.50	17
SS–1	10	64.64	1.875	1.61	1.61	19
SS–2			2.109	1.63	1.60	20

Table 5.3: Sample's maximum HF, Gaussian standard deviation and exposure time.

Since the experimental setup foresees a horizontal beam focused on a vertically–oriented target, gravity is likely to act on the molten layer that starts drifting down as soon as it appears.

To comply with the experimental requirement to always have the liquid layer in place during the heating time, the exposure time is calibrated accordingly, in such a way to heat each target up to its melting point. This helps prevent the complete loss of the liquid layer from the power deposition footprint under gravity action. This effect is strongly experienced during the first loaded TZM–1 sample, where the longest heating time increases the loss of liquid metal, due to both gravity and impact–generated instabilities before it even reaches the boiling point. Therefore, no attempts to reach vaporization is made.

Weight measurements are carried out in GLADIS by using a weighting balance with a sensitivity up to two decimal places. The bigger difference in weight between the two W samples

Sample	Weight [g] – pre–experiment	Weight [g] – post–experiment	Mass loss [g]
TZM–1	1090.53±0.3	1080.04±0.03	10.49±0.2
TZM–2	1089.17±0.04	1089.07±0.04	0.11±0.04
W–1	2123.57±0.03	2123.48±0.03	0.09±0.03
W–2	2136.49±0.03	2136.36±0.03	0.13±0.03
SS–1	891.15±0.04	891.10±0.04	0.05±0.04
SS–2	889.70±0.04	889.66±0.04	0.03±0.04

Table 5.4: Samples' weights and related mass losses before and after the experiments. The mass loss is calculated by comparison between the two sets of measurements.

is due to sample W–1 being delivered undersized. Unfortunately, samples are delivered with a poor documentation, lacking accurate data for their material properties as well.

5.4 Finite Element modelling

The finite element model of the sample tiles (Fig. 5.14) is generated from the geometrical model in Fig. 5.6. The same finite element model is built for all the samples, therefore a common overview is presented in this section. Quantitative values of both initial and loading conditions vary for the different samples, whose values are listed in §5.5.

The mesh is composed of 15907 linear hexahedral elements, linked through 18565 nodes. The variables the model solves for are temperature, mesh displacement and surface deformation. A mesh sensitivity analysis drives the mesh element size ensuring a smooth and continuous

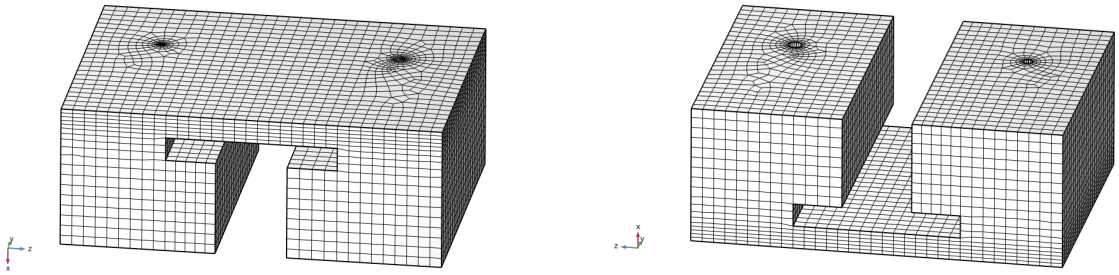

(a) (b)

Fig. 5.14: Finite element model of the sample tiles built in COMSOL.

transition in both the temperature profile between hottest and coldest areas (especially needed in presence of sharp boundaries between hot and cold domains, like the samples in §4.2.1.1) and the interface between liquid and solid domains. The element size goes down to ≈1 μm for capturing the extent of the molten layer depth. The material properties are described in §5.3.1.1, with initial condition values taken from Table 5.3. The Gaussian footprint of the heat flux is imposed on the top surface as in Fig. 5.15a. The tile cooling is simulated by a convective condition at the back of the sample, where water flows at T=20°C and provides an Heat Transfer Coefficient (HTC) equal to 2000 W m^{-2} K^{-1} (Fig. 5.15b), whereas the rest of the tile radiates energy towards the surroundings at 20°C (Fig. 5.15c), with emissivity values in §5.3.1.1 only valid during the heating phase. Once reaching the melting point, the front face goes through emissivity changes due to a modification in the surface morphology and finishing. The emissivity values (ε_m) listed in §5.5 under every sample's dedicated section are triggered by the melting temperature.

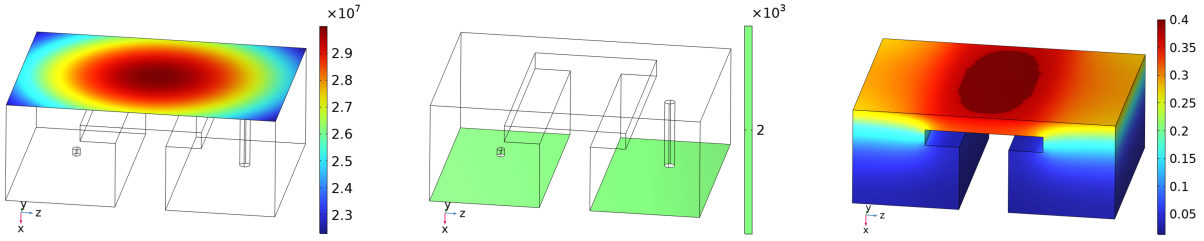

(a) Gaussian distribution of the heat flux [MW m^{-2}].

(b) Convective condition HTC value [W m^{-2} K^{-1}].

(c) T–dependent ε values for W.

Fig. 5.15: Overview of the boundary conditions defined in the finite element model.

The model is run within a deformed mesh domain, with material removal under evaporation and subsequent recession of the front face. §5.5 collects both the experimental and the

computational result obtained for every sample.

5.5 Results

This section gathers all the thermal results obtained through modelling, and benchmarked against the experimental ones. Therefore, the calculated data is labelled with the subscript *model* for distinguishing them from the experimental data, marked with the diagnostics they come from. Considerations and conclusions are instead provided by the author in §5.8 and §5.9.

5.5.1 TZM–1 – temperature data, imaging and computational benchmark

This section collects both the experimental and the modelled results for the TZM–1 sample. Fig. 5.16 reports a sequence of IR frames collected during the experiments. This is the first loaded sample, whose heating time is based on computational predictions of the melting point. As a result of heating the sample for slightly longer than its melting point, the shot is characterized by liquid droplets falling off the surface under both gravity and beam impact. The loss of material experienced by this sample is therefore bigger compared to the next shots, when the heating time is progressively reduced until only melting occurs. Fig. 5.17 shows an overview of the sample shape after the experiment. The loaded footprint is marked with solidified material, whereas the whole sample shows bending effects under such high thermal gradient.

The modelled maximum surface temperature is plotted in Fig. 5.18, together with experimental measurements from IR camera and pyros, as well as measurements collected by TCs at the back of the sample. The big uncertainty on the temperature measurements comes from the emissivity changes of the heated surface, due to its increased surface corrugation caused by melting.

Diagnostic calibration is not part of this work, as it is performed by researchers running the GLADIS facility. However, a few highlights on diagnostic measurements are mentioned by the author. The bifurcation between IR and 1c–Pyro temperature data beyond a certain threshold ($\approx 2000°C$) derives from the measurements at different radiative wavelenght. IR and pyros work with fixed emissivity values, which do not completely consider the change of emissivity depending on sample temperature and energy (i.e. radiative wavelenght). Therefore, for compensating

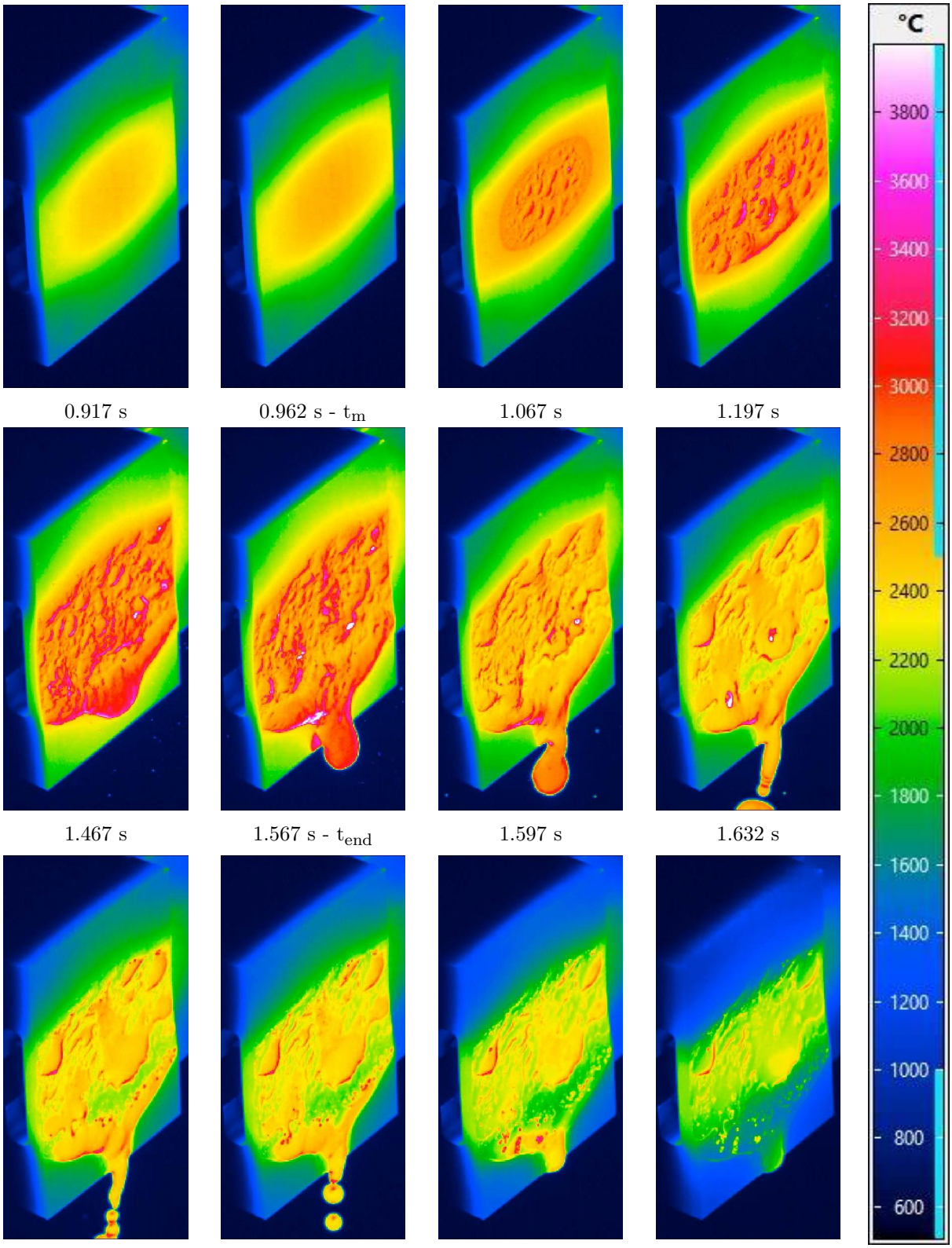

Fig. 5.16: TZM–1 IR frames.

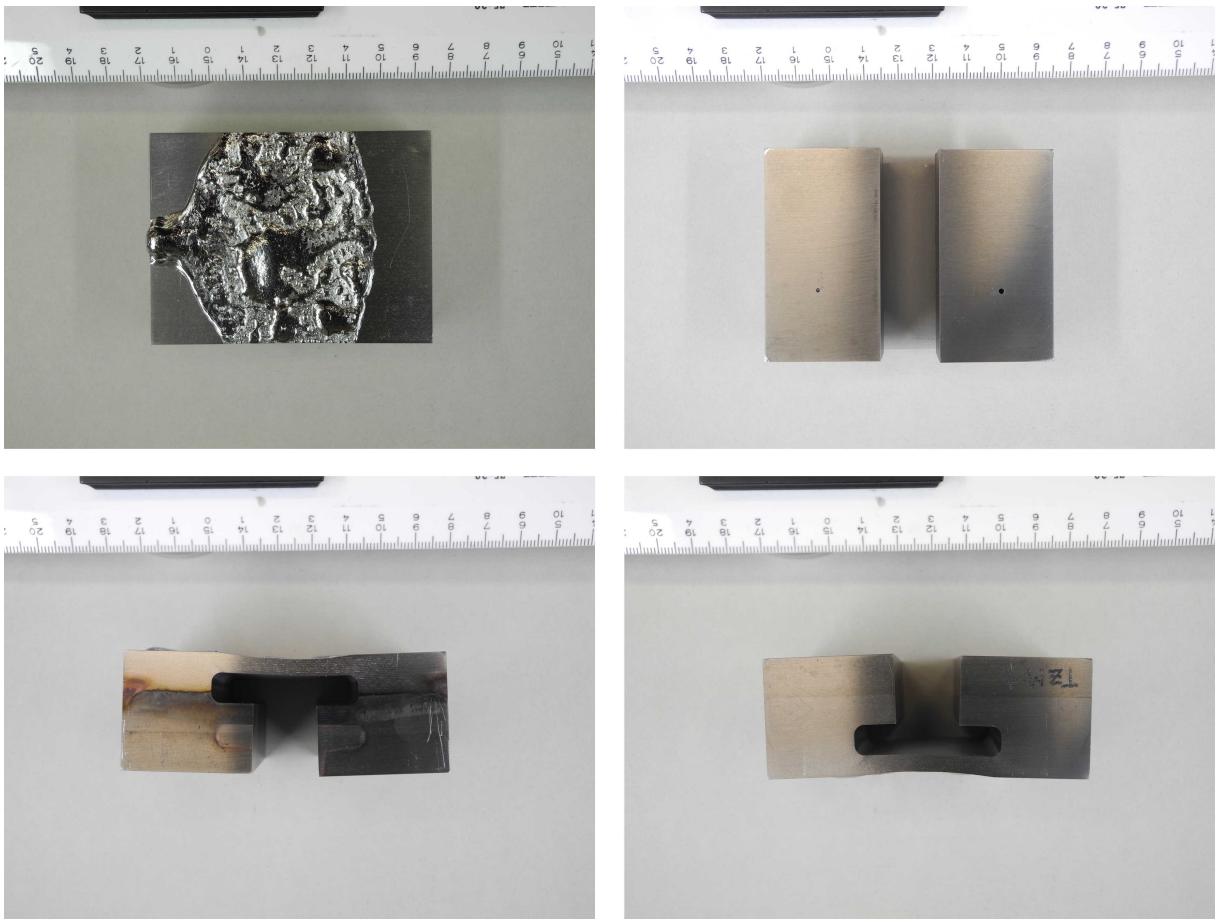

Fig. 5.17: TZM–1 sample at the end of the experiments.

this variation in surface emissivity following phase change, IR and 1c–Pyro temperature measurements are extrapolated by adjusting their emissivity values upon two certain data, i.e. the low temperature 2c–Pyro temperature value and, at high temperature, the sudden change of emissivity at melting corresponding to the well–known T_m. The 2c–Pyro is used for measuring the reference emissivity value at low temperature threshold (below 1700°C). This explains the mismatch between IR and 1c–Pyro data above 2000°C. The IR and 1c–Pyro experimental temperature extrapolation is valid for all the shots.

Both the 1c and 2c–Pyros can be used for temperature measurements up to 1700°C. This is the maximum temperature threshold of the 2c–Pyro, beyond which it becomes insensitive. It starts acquiring temperature values when the sample cools down to 1700°C, but at this point the captured temperature values are unreliable because affected by different values of surface emissivity due to phase change surface alterations. The gap in 2c–Pyro measurements is visible for any of the cyan curve in the plots below.

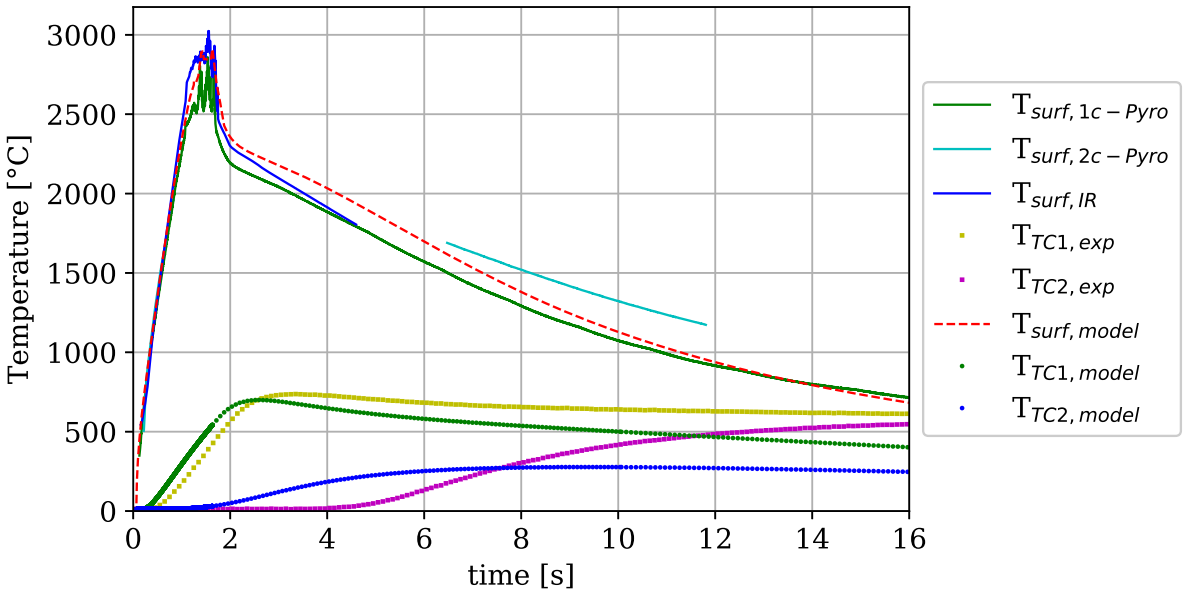

Fig. 5.18: TZM–1: Experimental VS modelled temperature evolutions.

Fig. 5.19 provides a snapshot of the temperature distribution and melt pool volume contour plot after the heating time. Table 5.5 collects the quantitative benchmark between the maximum

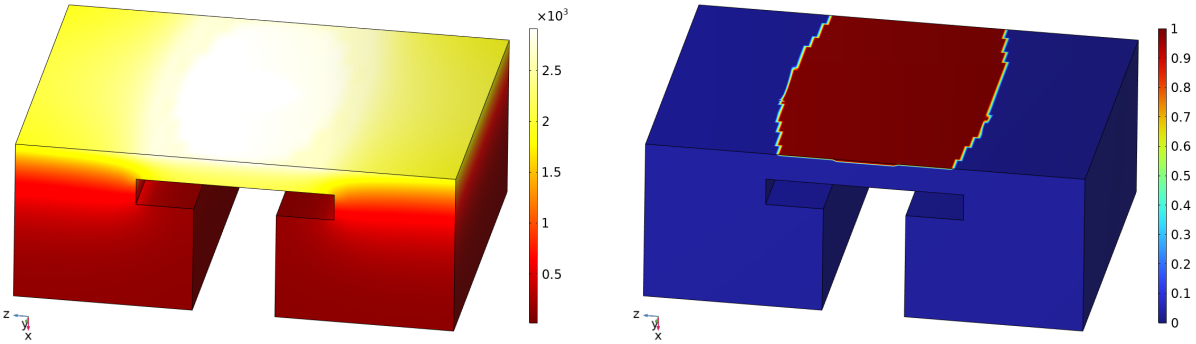

(a) Temperature field [°C].

(b) Melt pool within the solid domain (Ω_2).

Fig. 5.19: TZM–1 contour plots at the end of the heating time.

measured compared to modelled values of the main parameters of interest.

	TZM–1				
	EXP		**TARTIFL&TTE**	**Δ**	
	1c–Pyro	IR			
$\mathbf{t_m}$ **[s]**	0.96	0.96	1.11	16%	16%
$\mathbf{T_m}$ **[°C]**	2619	2619	2619	–	–
$\mathbf{T_0}$ **[°C]**	12	12	12	–	–
$\mathbf{HF_{max}}$ **[MW m^{-2}]**	30	30	30	–	–
Δt [s]	1.57	1.57	1.57	–	–
$\mathbf{T_{surf,max}}$ **[°C]**	2859	3024	2911	2%	4%
$\mathbf{TC1_{max}}$ **[°C]**	731		700	4%	
$\mathbf{TC2_{max}}$ **[°C]**	570		277	51%	
E_{abs} **[kJ]**	206		205	–	–
HTC [W m^{-2} K^{-1}]	2000		2000	–	–
ε_m	–	–	0.8	–	–
Mass loss [g]	10.49[1]		0.002[2]	–	–
Molten mass [g]	–		9.00	–	–
s(t) [m]	–		0.001	–	–
r(t) [m]	–		2.40E-07	–	–

[1] Mass loss weight.
[2] Evaporative mass loss.

Table 5.5: TZM–1 quantitative benchmark.

5.5.2 TZM–2 – temperature data, imaging and computational benchmark

This section focuses on the results related to the TZM–2 sample. Fig. 5.20 shows a collection of IR frames acquired during the shot, whereas Fig. 5.21 shows the sample shape after the experiments.

The modelled maximum surface temperature is plotted in Fig. 5.22, together with experimental measurements from IR camera and pyros, as well as measurements collected by the TC1. The TC2 measurements are missing from the plot due to a fault in the TC. Fig. 5.23 provides a snapshot of the temperature distribution and melt pool volume contour plots at the end of the heating time.

Table 5.6 collects the quantitative benchmark between the maximum measured compared to modelled values of the main parameters of interest.

	TZM–2				
	EXP		**TARTIFL&TTE**	**Δ**	
	1c–Pyro	IR			
$\mathbf{t_m}$ **[s]**	0.95	0.95	1.11	17%	17%
$\mathbf{T_m}$ **[°C]**	2619	2619	2619	–	–
$\mathbf{T_0}$ **[°C]**	13	13	13	–	–
$\mathbf{HF_{max}}$ **[MW m^{-2}]**	30	30	30	–	–
Δt [s]	1.30	1.30	1.30	–	–
$\mathbf{T_{surf,max}}$ **[°C]**	2631	3120	2680	2%	14%
$\mathbf{TC1_{max}}$ **[°C]**	627		603	4%	
$\mathbf{TC2_{max}}$ **[°C]**	No data		334	–	
E_{abs} **[kJ]**	171		170	–	
HTC [W m^{-2} K^{-1}]	2000		2000	–	–
ε_m	–	–	0.8	–	–
Mass loss [g]	0.11[1]		0.005[2]	–	–
Molten mass [g]	–		2.70	–	–
s(t) [m]	–		2.62E-04	–	–
r(t) [m]	–		4.60E-08	–	–

[1] Mass loss weight.
[2] Evaporative mass loss.

Table 5.6: TZM–2 quantitative benchmark.

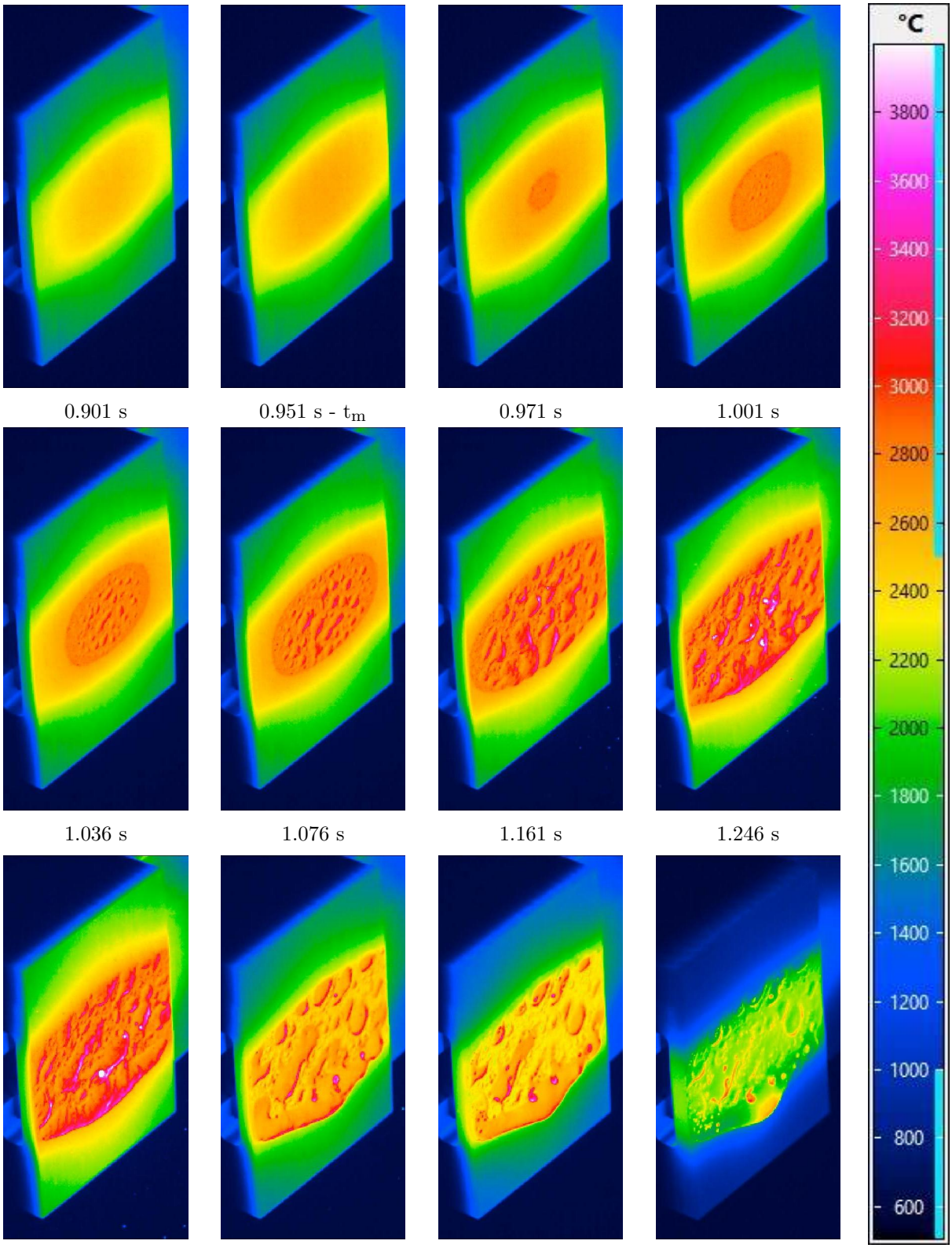

Fig. 5.20: TZM–2 IR frames.

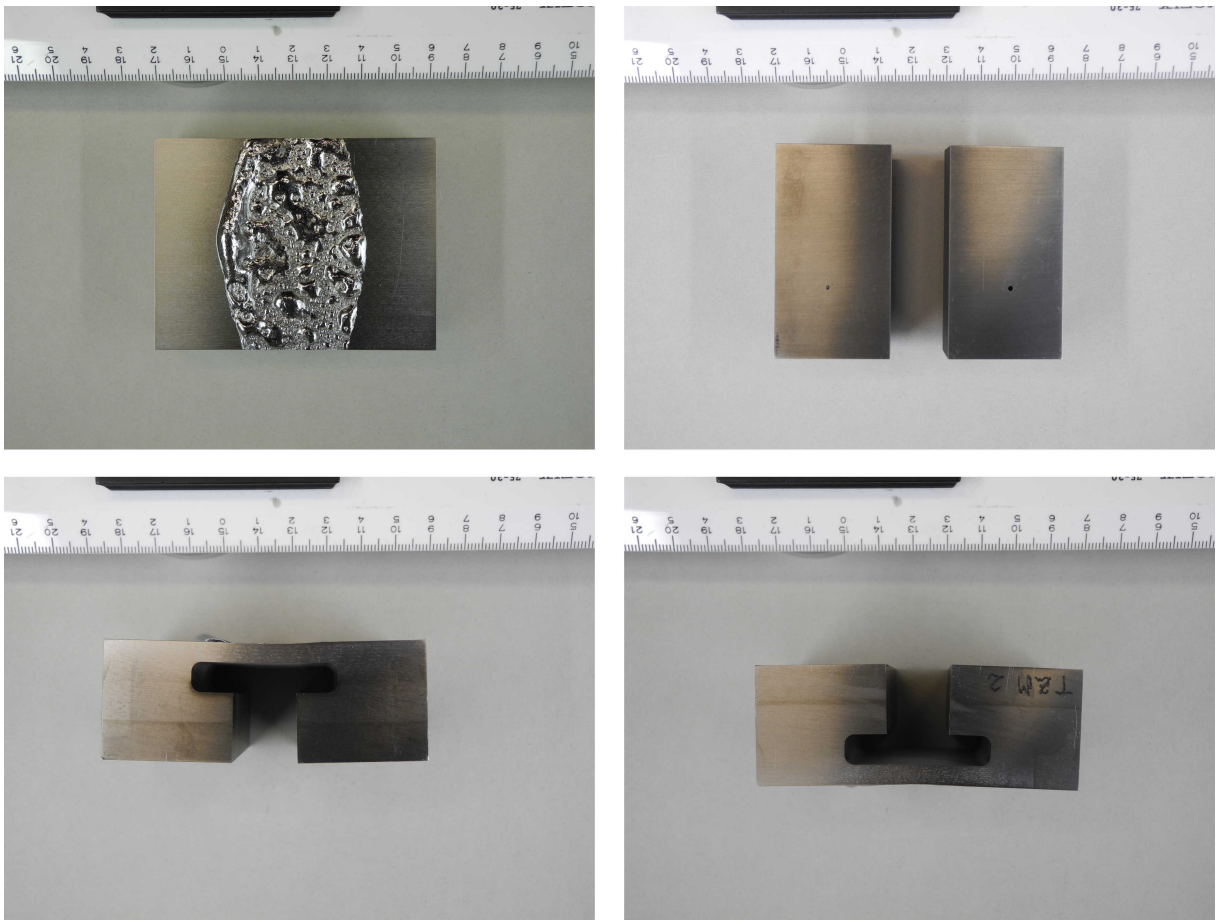

Fig. 5.21: TZM–2 sample at the end of the experiments.

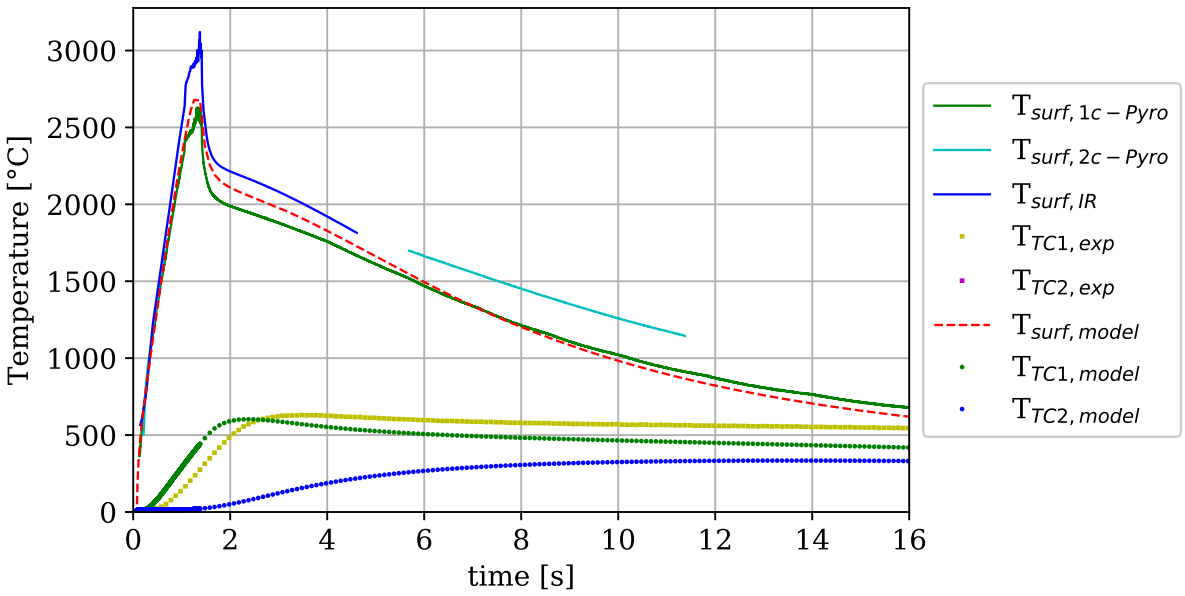

Fig. 5.22: TZM–2: Experimental VS modelled temperature evolutions.

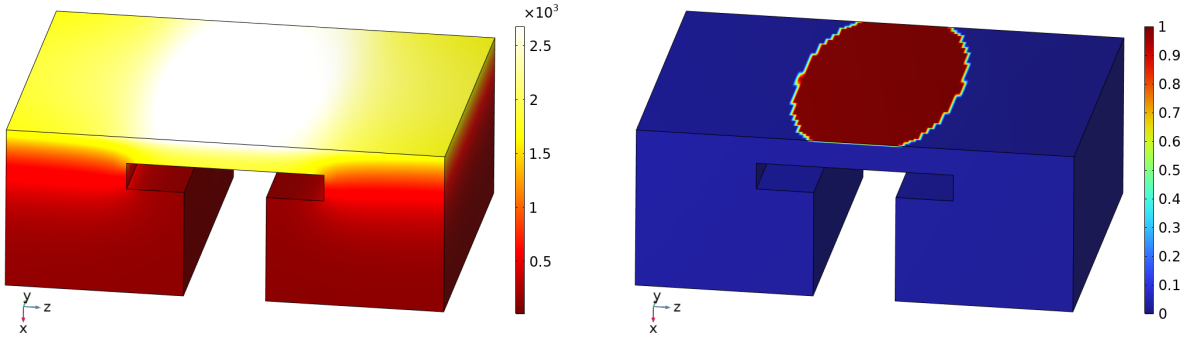

(a) Temperature field [°C]. (b) Melt pool (Ω_2).

Fig. 5.23: TZM–2 contour plots at the end of the heating time.

5.5.3 W–1 – temperature data, imaging and computational benchmark

This section collects the results related to the W–1 sample. Fig. 5.24 shows a selection of frames acquired by the IR cameras during the pulse. Unlike TZM and SS, both the W samples experience cracking damage as soon as they start heating up. However, the cracks do not cause the tile to fall apart. Although W is known for its brittle behaviour, it cannot be excluded that the cracking damage has started from the little TC holes machined at the back of the samples. Fig. 5.25 shows the tile shape at the end of the experiments.

The modelled maximum surface temperature is plotted in Fig. 5.26, together with all the experimental measurements from IR camera, pyros, and TCs. Fig. 5.27 provides a snapshot of the temperature and melt pool volume contour plots at the end of the heating time.

Table 5.7 collects the quantitative benchmark between the maximum measured compared to modelled values of the main parameters of interest.

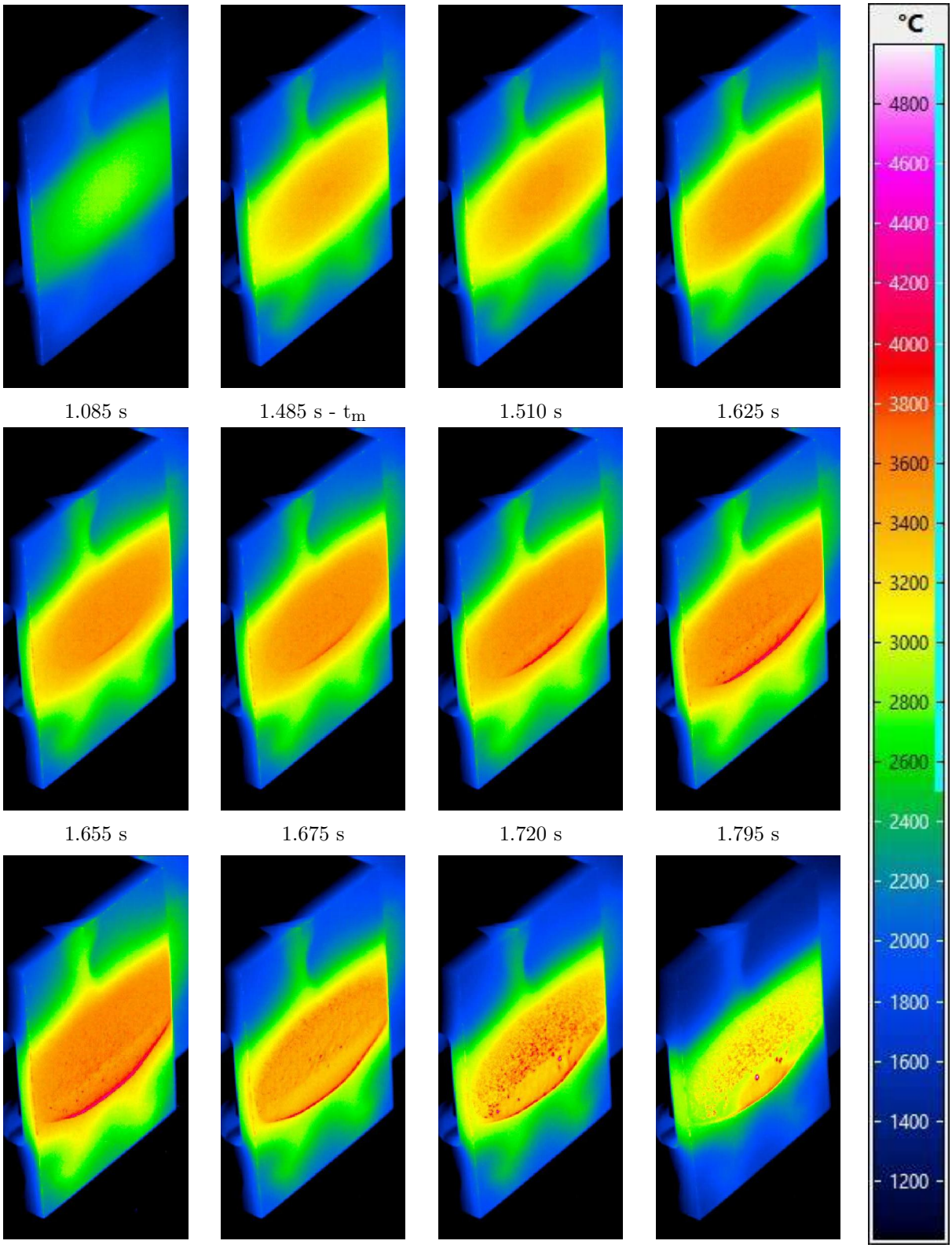

Fig. 5.24: W–1 IR frames.

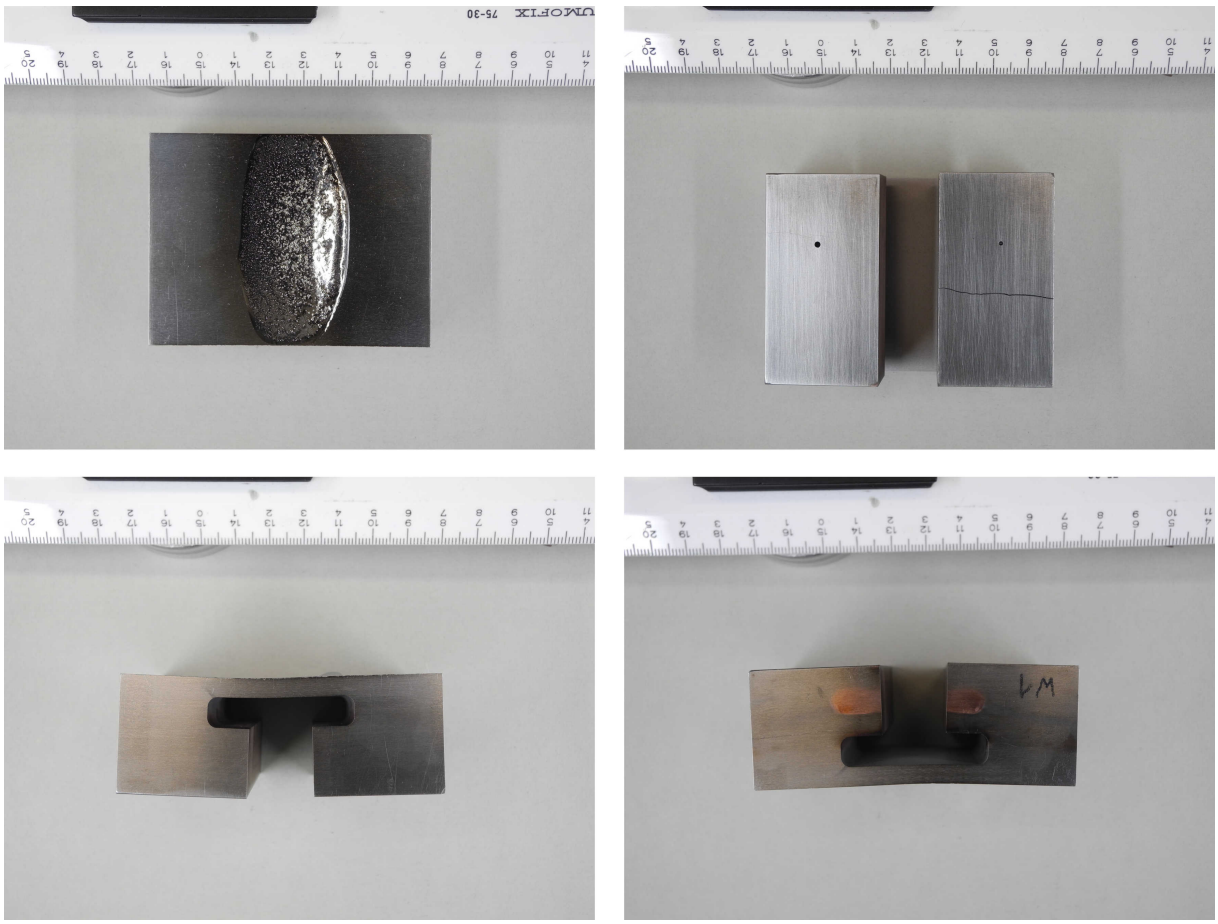

Fig. 5.25: W–1 sample at the end of the experiments.

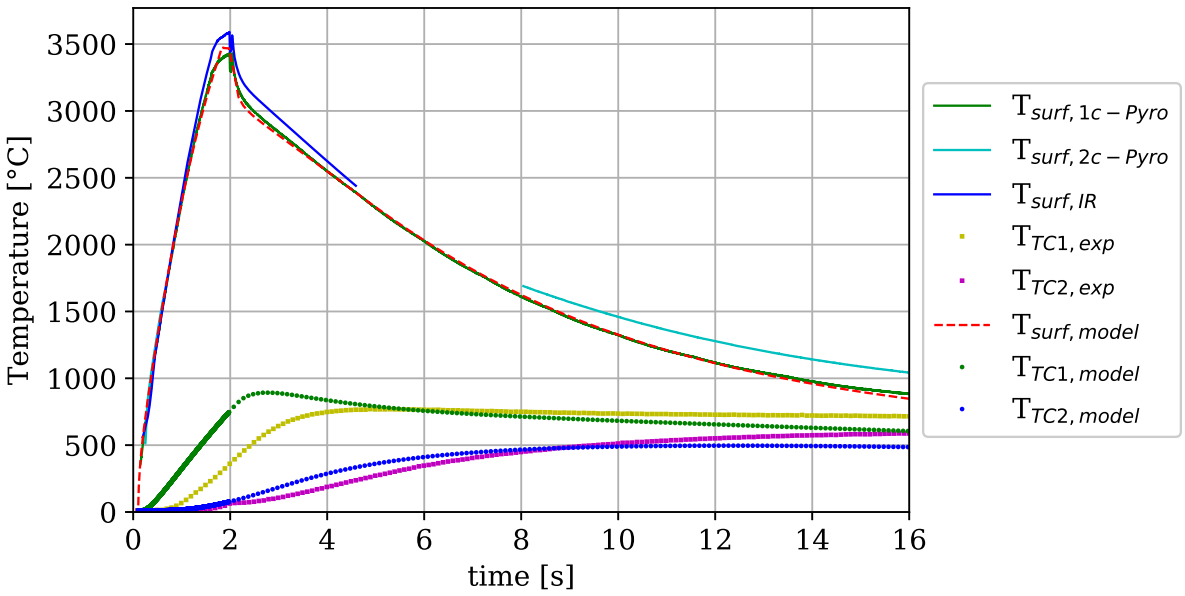

Fig. 5.26: W–1: Experimental VS modelled temperature evolutions.

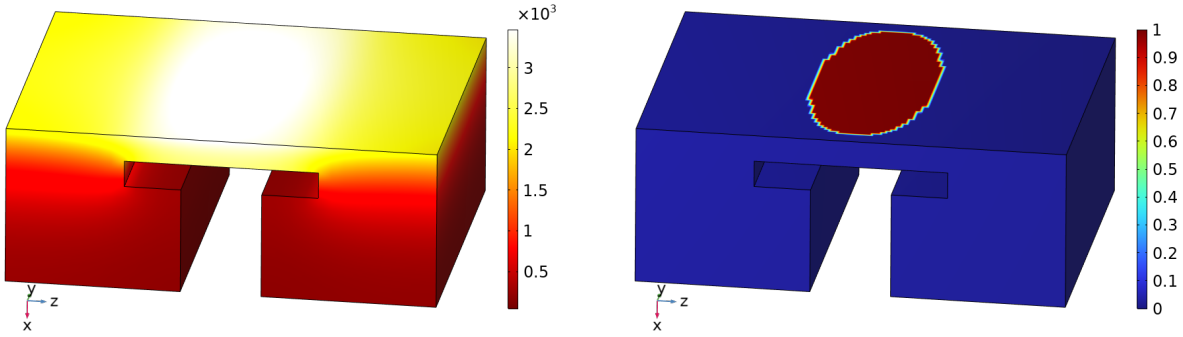

(a) Temperature field [°C]. (b) Melt pool (Ω_2).

Fig. 5.27: W–1 contour plots at the end of the heating time.

	W–1				
	EXP		**TARTIFL&TTE**	**Δ**	
	1c–Pyro	IR			
t_m [s]	1.48	1.49	1.69	14%	14%
T_m [°C]	3422	3422	3422	–	–
T_0 [°C]	12	12	12	–	–
HF_{max} [MW m^{-2}]	30	30	30	–	–
Δt [s]	1.87	1.87	1.87	–	–
$T_{surf,max}$ [°C]	3433	3591	3473	1%	3%
$TC1_{max}$ [°C]	768		893	16%	
$TC2_{max}$ [°C]	598		496	17%	
E_{abs} **[kJ]**	245		244	–	
HTC [W m^{-2} K^{-1}]	2000		2000	–	–
ε_m	–		0.4	–	–
Mass loss [g]	0.09[1]		0.001[2]	–	–
Molten mass [g]	–		3.19	–	–
s(t) [m]	–		2.31E-04	–	–
r(t) [m]	–		1.05E-07	–	–

[1] Mass loss weight.
[2] Evaporative mass loss.

Table 5.7: W–1 quantitative benchmark.

5.5.4 W–2 – temperature data, imaging and computational benchmark

This section is dedicated to the results obtained for the W–2 sample. Fig. 5.28 collects the main IR frames during the pulse, which clearly show the cracking before the tile reaches its melting point, in line with what has been observed for the W–1 sample. Fig. 5.29 shows the tile shape at the end of the experiments.

The modelled maximum surface temperature is plotted in Fig. 5.30, together with the experimental measurements from IR camera, pyros, and TCs.

Fig. 5.31 provides a snapshot of the temperature distribution and melt pool volume contour plots at the end of the heating time, whereas Table 5.8 collects the quantitative benchmark between the maximum measured compared to modelled values of the main parameters of interest.

	W–2				
	EXP		**3D–TARTIFL&TTE**	**Δ**	
	1c–Pyro	IR			
t_m [s]	1.5	1.5	1.69	13%	13%
T_m [°C]	3422	3422	3422	–	–
T_0 [°C]	17		17	–	–
HF_{max} [MW m^{-2}]	30	30	30	–	–
Δt [s]	1.82	1.82	1.82	–	–
$T_{surf,max}$ [°C]	3401	3548	3468	2%	2%
$TC1_{max}$ [°C]	830		870	5%	
$TC2_{max}$ [°C]	628		487	22%	
E_{abs} [kJ]	239		238	–	
HTC [W m^{-2} K^{-1}]	2000		2000	–	–
ε_m	–	–	0.6	–	–
Mass loss [g]	0.13[1]		0.001[2]	–	–
Molten mass [g]	–		2.06	–	–
s(t) [m]	–		2.31E-04	–	–
r(t) [m]	–		7.68E-08	–	–

[1] Mass loss weight.
[2] Evaporative mass loss.

Table 5.8: W–2 quantitative benchmark.

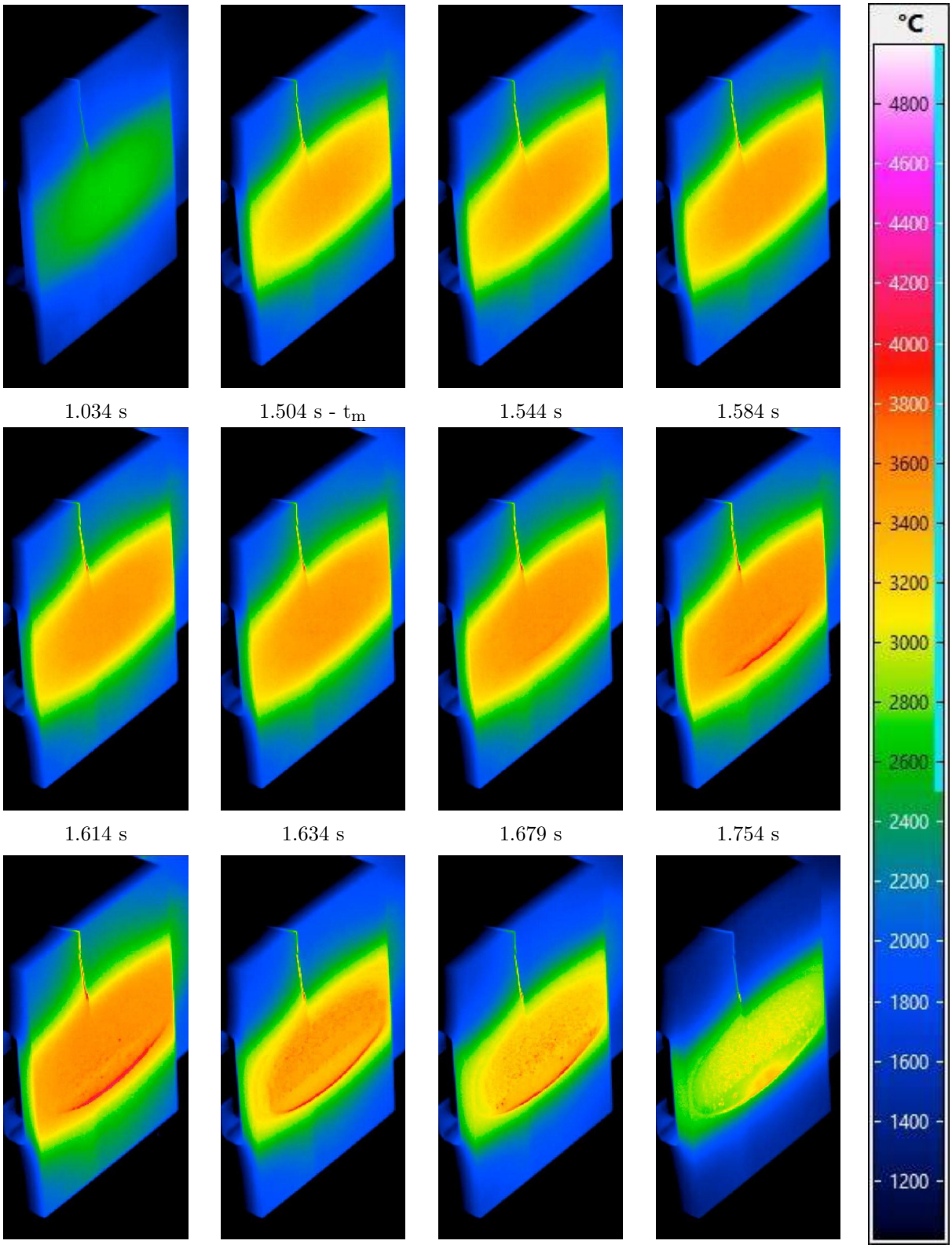

Fig. 5.28: W–2 IR frames.

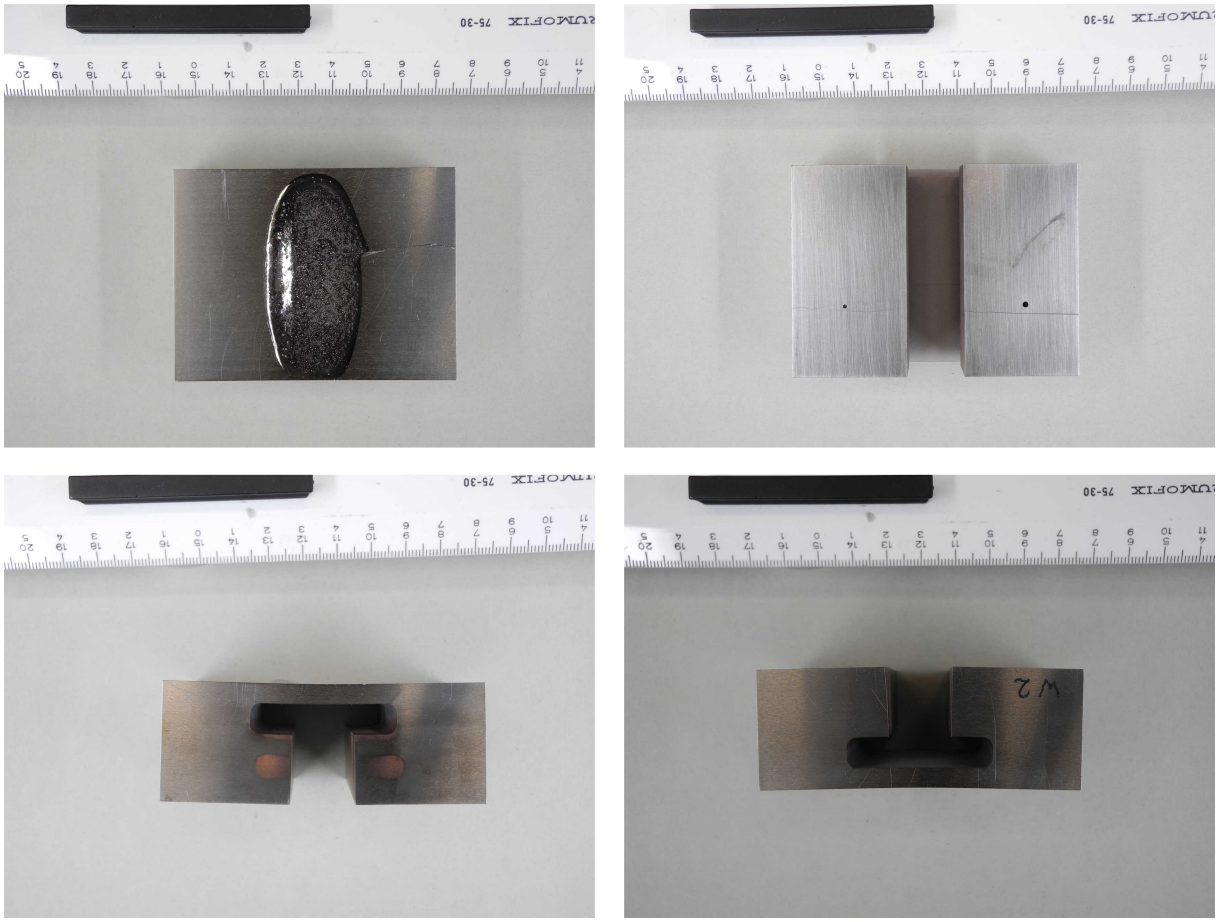

Fig. 5.29: W–2 sample at the end of the experiments.

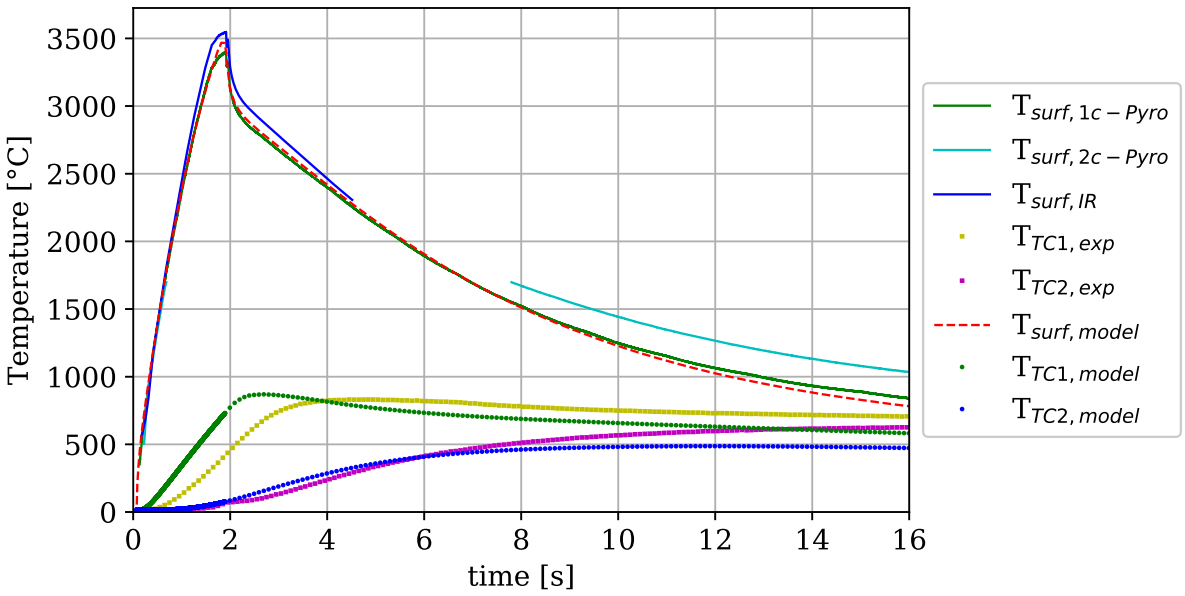

Fig. 5.30: W–2: Experimental VS modelled temperature evolutions.

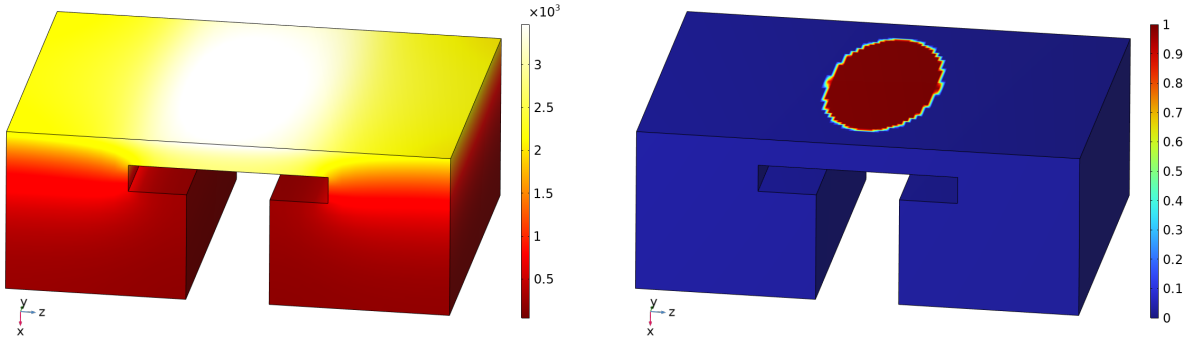

(a) Temperature field [°C]. (b) Melt pool (Ω_2).

Fig. 5.31: W–2 contour plots at the end of the heating time.

5.5.5 SS–1 – temperature data, imaging and computational benchmark

This section reports the results obtained for the SS–1 sample. Fig. 5.32 collects the main frames captured by IR cameras during the pulse, whereas Fig. 5.33 shows the change of the tile shape at the end of the experiments.

Fig. 5.34 shows the benchmark between modelled versus calculated temperature evolutions for the SS–1 sample, whereas the quantitative comparison between their maximum values is reported in Table 5.9. It is noted that the maximum heat flux is increased by 7% to match the experimental absorbed energy. This is valid for both the SS samples. Uncertainty on material properties and emissivity values is likely to affect the heating phase.

Fig. 5.35 provides a snapshot of the temperature distribution and melt pool volume contour plot after the heating time.

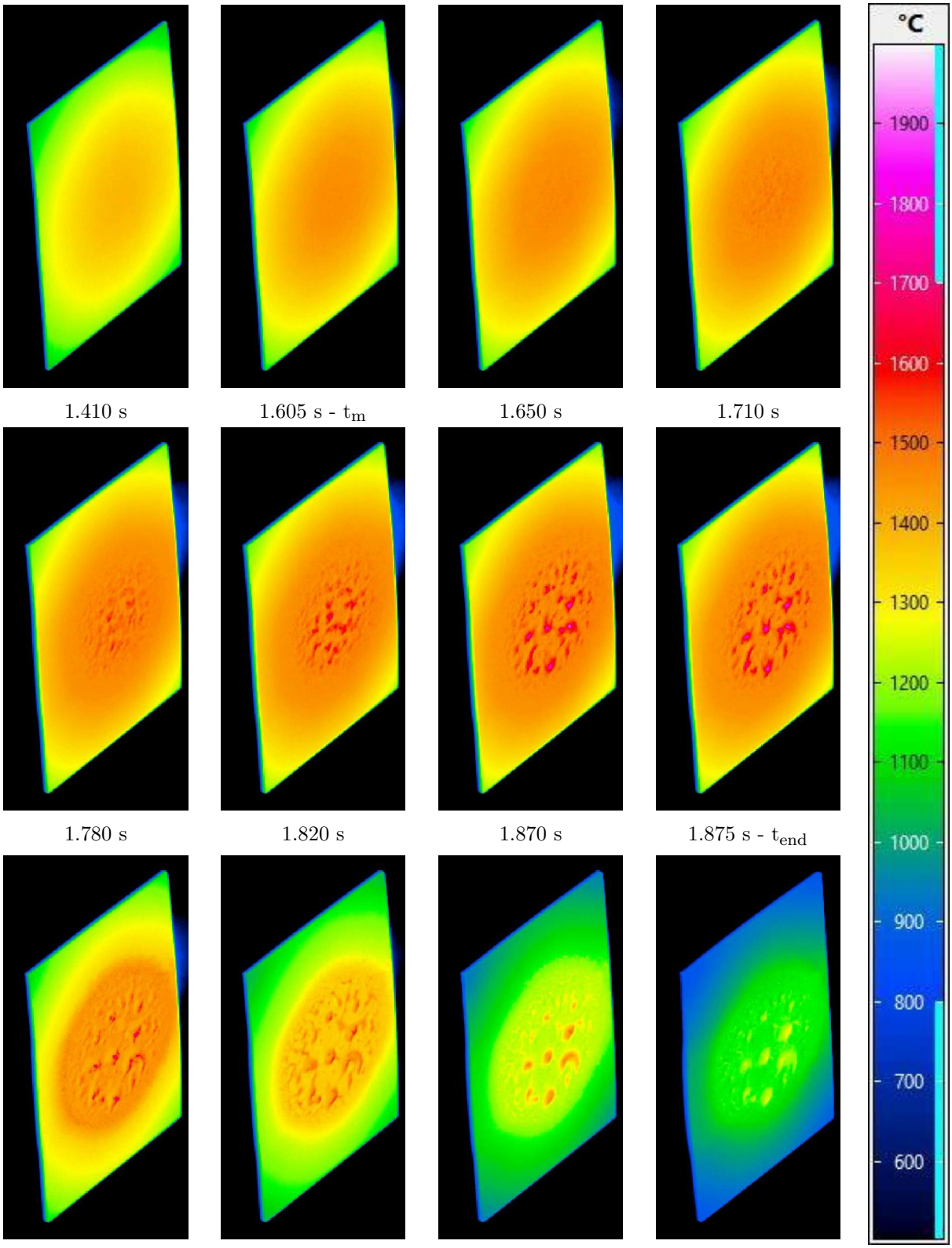

1.410 s | 1.605 s - t_m | 1.650 s | 1.710 s

1.780 s | 1.820 s | 1.870 s | 1.875 s - t_{end}

1.890 s | 1.935 s | 2.045 s | 2.220 s

Fig. 5.32: SS–1 IR frames.

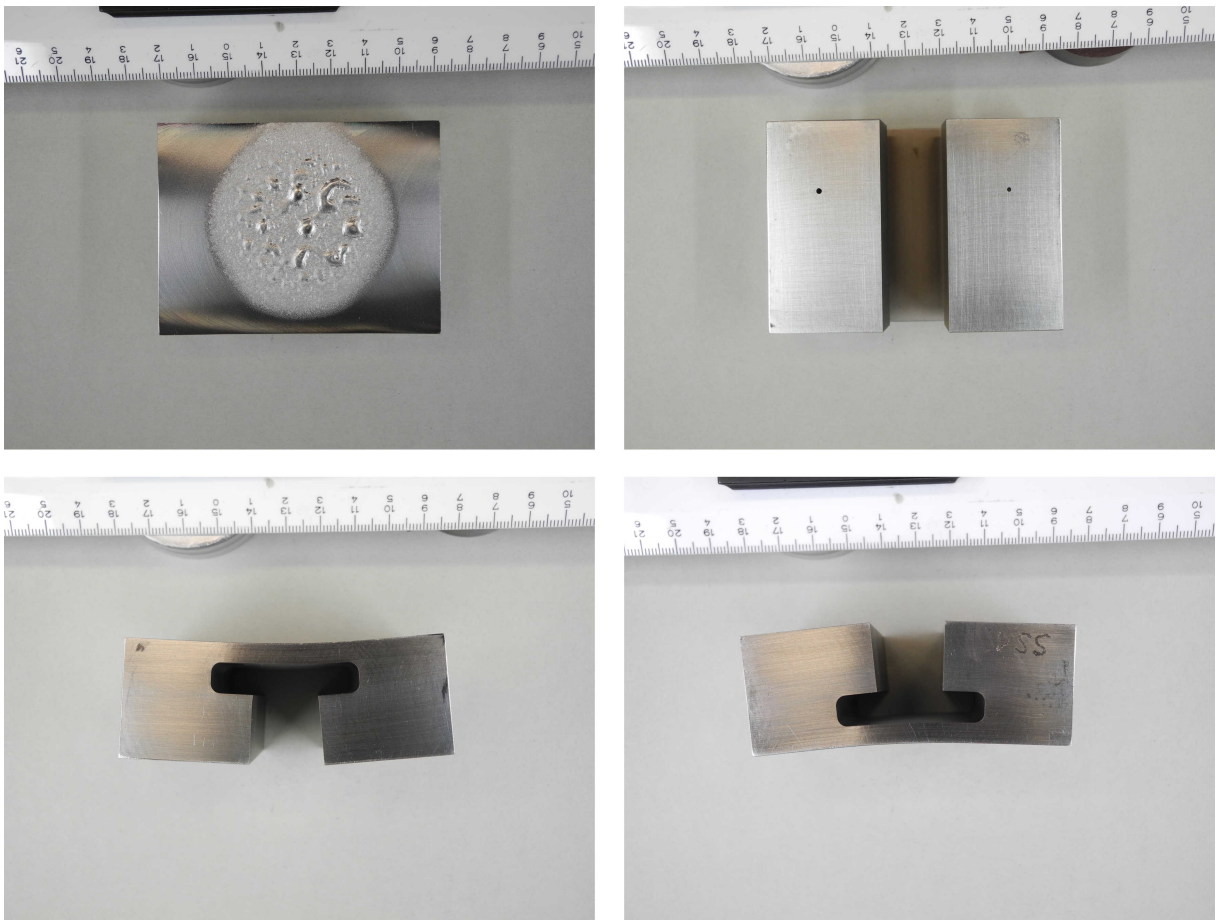

Fig. 5.33: SS–1 sample at the end of the experiments.

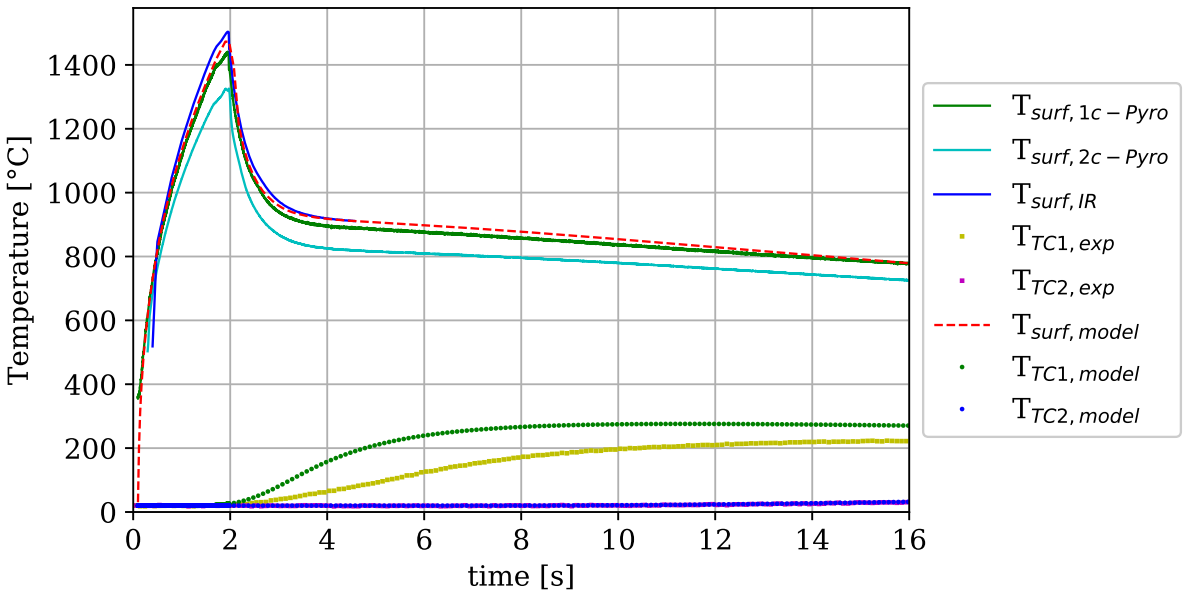

Fig. 5.34: SS–1: Experimental VS modelled temperature evolutions.

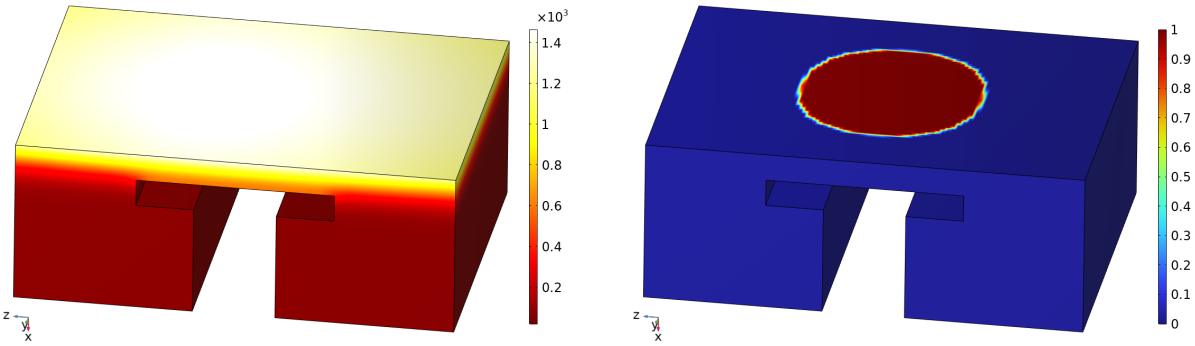

(a) Temperature field [°C]. (b) Melt pool (Ω_2).

Fig. 5.35: SS–1 contour plots at the end of the heating time.

	SS–1				
	EXP		**3D–TARTIFL&TTE**	**Δ**	
	1c–Pyro	IR			
t_m [s]	1.61	1.61	1.64	2%	2%
T_m [°C]	1427	1427	1427	–	–
T_0 [°C]	20	20	20	–	–
HF_{max} [MW m^{-2}]	10	10	10.7	7%	7%
Δt [s]	1.88	1.88	1.88	–	–
$T_{surf,max}$ [°C]	1440	1504	1473	2%	2%
$TC1_{max}$ [°C]	227		275	21%	
$TC2_{max}$ [°C]	66		61	6%	
E_{abs} **[kJ]**	87		87	–	
HTC [W m^{-2} K^{-1}]	2000		2000	–	–
ε_m	–	–	0.8	–	–
Mass loss [g]	0.05[1]		7.10E-04[2]	–	–
Molten mass [g]	–		1.48	–	–
s(t) [m]	–		2.31E-04	–	–
r(t) [m]	–		8.29E-08	–	–

[1] Mass loss weight.
[2] Evaporative mass loss.

Table 5.9: SS–1 quantitative benchmark.

5.5.6 SS–2 – temperature data, imaging and computational benchmark

This section reports the results related to the SS–2 sample. As in the previous sections, the IR frames are collected in Fig. 5.36, whereas Fig. 5.37 shows the tile shape after the experiments. Fig. 5.38 shows the benchmark between modelled versus calculated temperature evolutions for the SS–2 sample, whereas the quantitative comparison between their maximum values is reported in Table 5.10. Fig. 5.39 provides a snapshot of the temperature and melt pool volume contour plot after the heating time.

	SS–2				
	EXP		**3D–TARTIFL&TTE**	**Δ**	
	1c–Pyro	IR			
$\mathbf{t_m}$ **[s]**	1.63	1.60	1.63	0%	2%
$\mathbf{T_m}$ **[°C]**	1427	1427	1427	–	–
$\mathbf{T_0}$ **[°C]**	19	19	19	–	–
$\mathbf{HF_{max}}$ **[MWm^{-2}]**	10	10	10.7	7%	7%
Δt [s]	2.11	2.11	2.11	–	–
$\mathbf{T_{surf,max}}$ **[°C]**	1437	1509	1473	3%	2%
$\mathbf{TC1_{max}}$ **[°C]**	270		304	12%	
$\mathbf{TC2_{max}}$ **[°C]**	43		33	24%	
E_{abs} **[kJ]**	98		98	–	–
HTC [W m^{-2} K^{-1}]	2000		2000	–	–
ε_m	–	–	1	–	–
Mass loss [g]	0.03[1]		1.7E-03[2]	–	–
Molten mass [g]	–		3.5	–	–
s(t) [m]	–		2.78E-04	–	–
r(t) [m]	–		1.64E-05	–	–

[1] Mass loss weight.
[2] Evaporative mass loss.

Table 5.10: SS–2 quantitative benchmark.

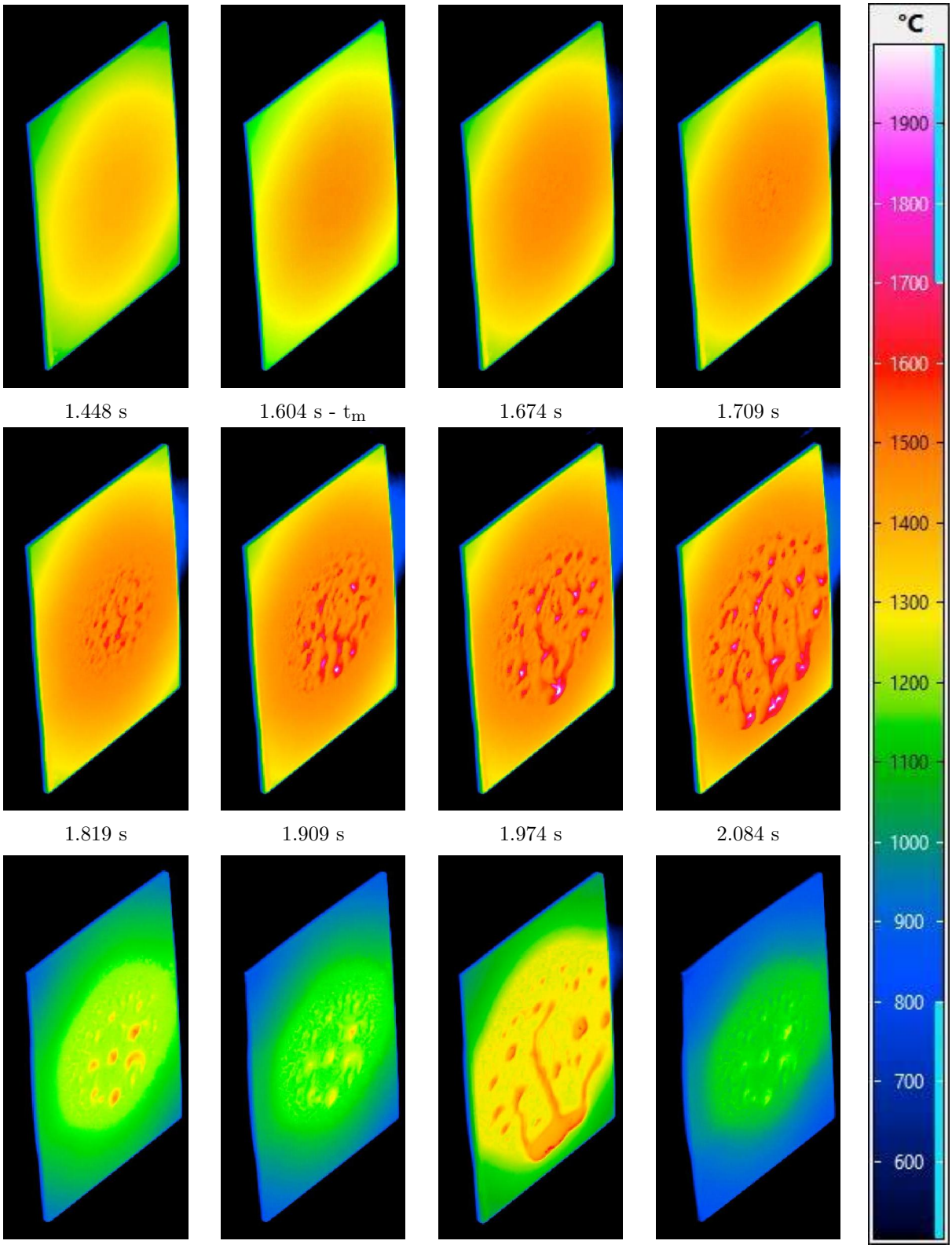

Fig. 5.36: SS–2 IR frames.

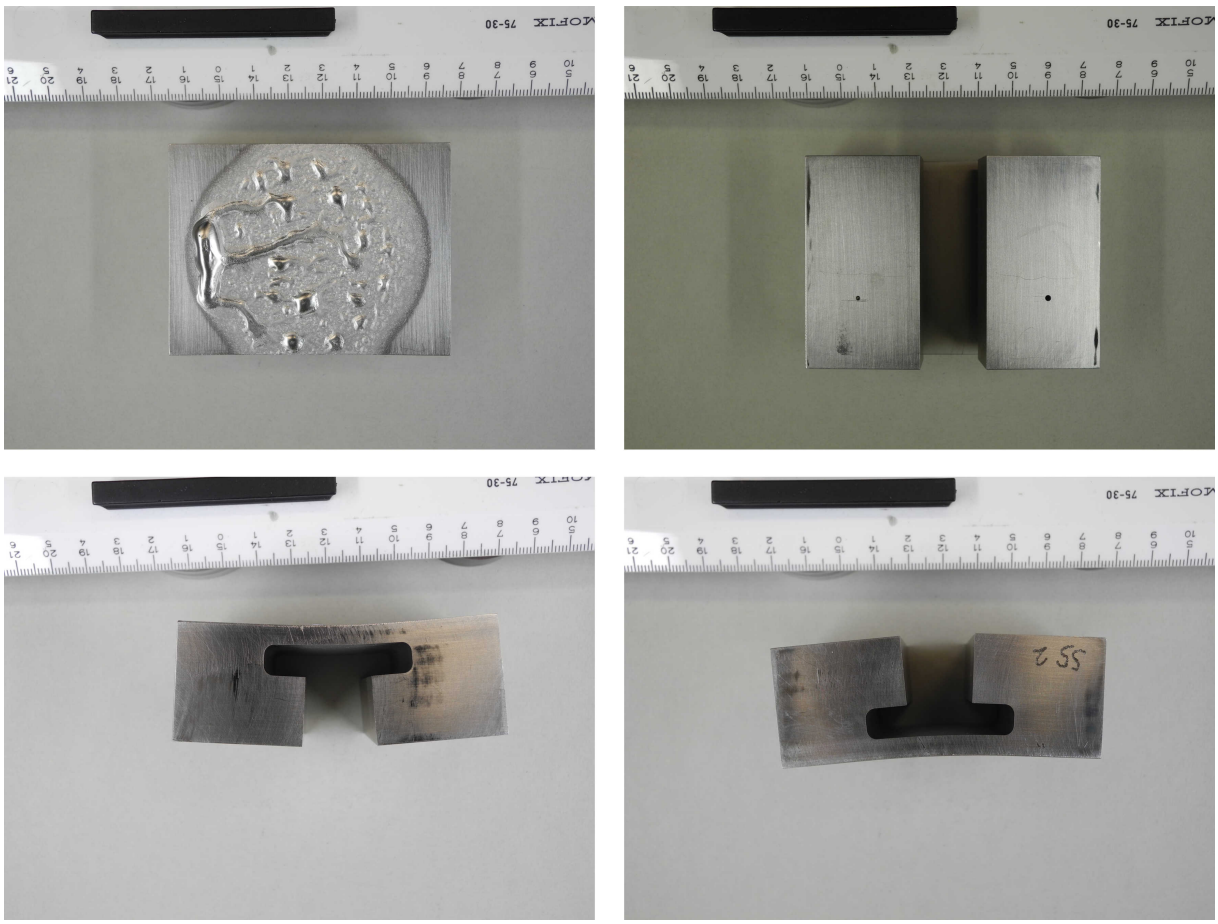

Fig. 5.37: SS–2 sample at the end of the experiments.

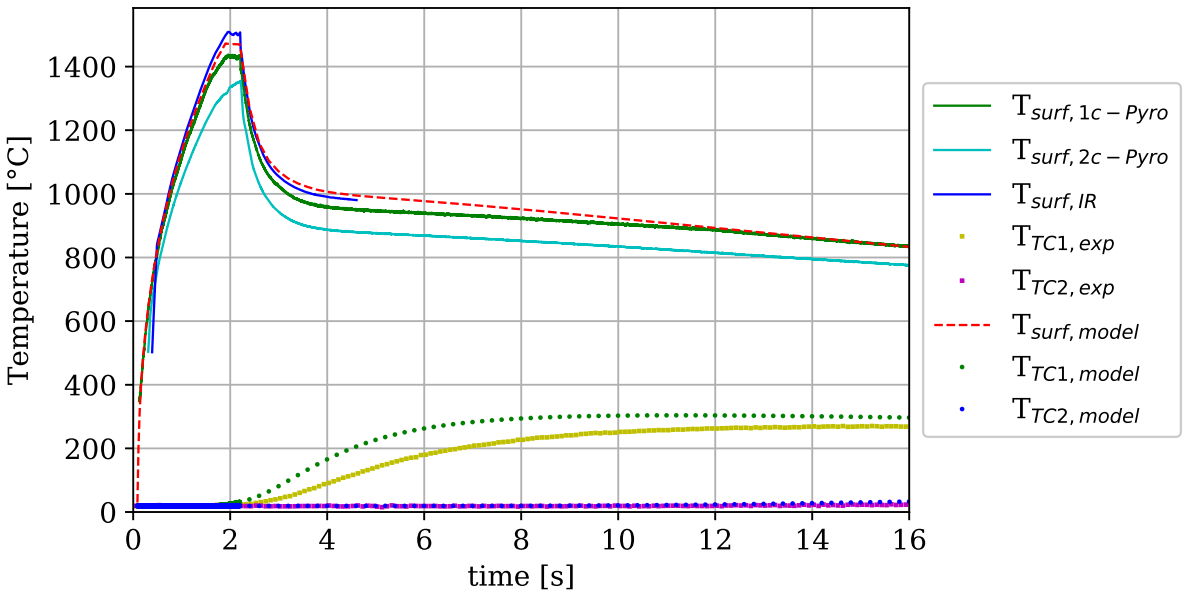

Fig. 5.38: SS–2: Experimental VS modelled temperature evolutions.

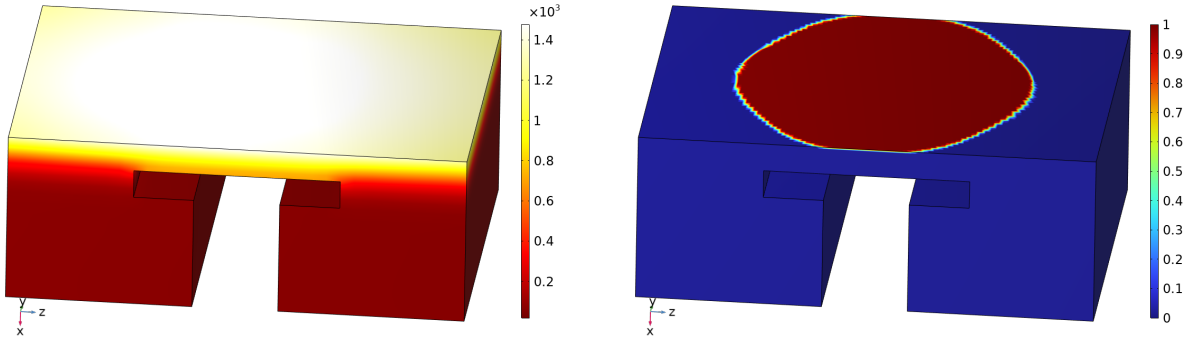

(a) Temperature field [°C]. (b) Melt pool (Ω_2).

Fig. 5.39: SS–2 contour plots at the end of the heating time.

5.6 Uncertainties

This section is dedicated to the identification of the primary sources of uncertainties impacting the maximum temperature value T_{max} of the samples.

Measurement Uncertainties: These uncertainties arise from the diagnostics sensitivity range and conditioning status of the beam source. Due to the complex nature of the exact error estimation, as the beam data also depend on the conditioning status of the heat sources, an average error of 5% is applied to all the experimental data, including operating data and the uncertainties in diagnostics data acquisition.

Material Property Characterization Uncertainties: These uncertainties stem from characterizing the material properties used for calculating temperature values. The quantification of these uncertainties and their propagation to the calculated temperature are here performed on W samples, considered as case study and representative of all the other materials. Uncertainties on the thermophysical properties for pure W can be inferred from [109]. Table 5.11 lists these uncertainties and their effects on the maximum temperature of the W sample, with other properties held constant. The uncertainty propagation is evaluated by means of thermal analyses lasting 0.5 seconds, during which the same model in §5.4 is subjected to a uniform heat flux of 30 MW m^{-2} on its front face. The *reference case* refers to the thermal problem with unaltered material properties, and the uncertainty propagation associated with perturbations imposed on each thermophysical property is assessed by comparing the resulting T_{max} values with the reference one.

Model Discretization Uncertainties: It is noted that uncertainties on mesh size do not

Thermophysical property	Uncertainty [%]	Variation	T_{max} [°C]	ΔT [%]
Reference Case	–	–	1548	–
ρ [kg m^{-3}]	1.5	±1.5	1531/1564	±1
k [W m^{-1} K^{-1}]	5	±0.5	1526/1571	±1
c_p [J kg^{-1} K^{-1}]	4	±0.4	1506/1593	±3

Table 5.11: Uncertainties on W thermophysical properties and their propagation on T_{max}.

affect the maximum temperature value at the front surface, as a 5% increase in element size does not alter the reference T_{max}. However, this consideration does not account for element size variations across the first layers of the sample beneath the heated surface. Mesh sensitivity analysis determines the appropriate element size to ensure accurate capture of smooth variation of the main output parameters, whose main conclusion is described in §5.4.

5.7 Destructive post–processing

A dedicated destructive post–processing follows the experiments for post mortem analyses on the sectioned tiles. The idea is to cut the samples in four parts, as indicated in red in Fig. 5.40a, from which slicing off the two specimens enclosed within the green and red boxes. The additional cut in Fig. 5.40b is beneficial for separating the heated layer from the T–legs of the sample, while preserving the reference surface highlighted in black in Fig. 5.40b for any measurements. The aim is to try and identify, across each specimen's thickness, any alteration in the crystalline morphology caused by the phase change, and correlate the depth of the molten layer with any visible physical interface between different areas with different morphology. The thickness of the molten layer can be retrieved by measuring the thickness of the unmelted material from the reference point up to the top surface, and subtracting it to the original thickness (5 mm) of the loaded volume highlighted in violet in Fig. 5.40b. Where it is not possible to identify any interface, the lowest point measured beneath the footprint is considered as the interface between solid and liquid phases. The maximum depth values are then benchmarked against the computational results from the 3D–TARTIFL&TTE.

Samples are sectioned by the Manufacturing Support Group (MSG), a precision machining workshop based in UKAEA and specialized in Electrical Discharge Machining wire cutting. As

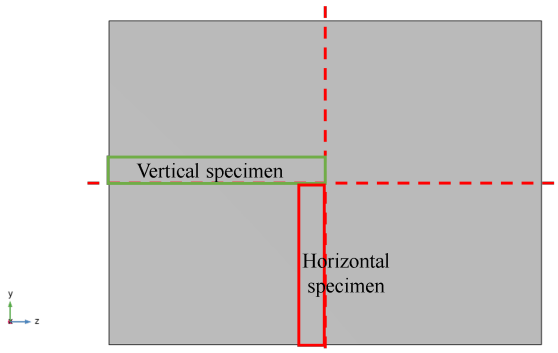

(a) Top view of the sample cut-through.

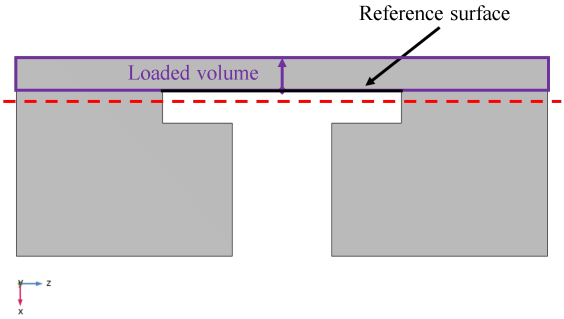

(b) Side view of the sample cut-through.

Fig. 5.40: (a) Top view of the sample sectioning in four parts along the red lines, and highlights on the specimens in violet; (b) Lateral view of the sample sectioning just below the T–shape holder, whose surface is taken as reference for measuring the unmelted layer.

anticipated in Fig. 5.40, samples are cross–sectioned into four parts, from which the vertically–oriented and the horizontally–oriented specimens are extracted from the loaded volume. The vertically and horizontally–oriented specimens are highlighted, respectively, in green and red for the TZM samples (Fig. 5.41), W samples (Fig. 5.42) and SS samples (Fig. 5.43). Unfortunately, both the W–2 specimens and the horizontal SS–2 specimen are excluded from the post–processing, since the additional cut separating the T–legs from the loaded volume occurs above the red line in Fig. 5.40b, not preserving the measurement reference surface.

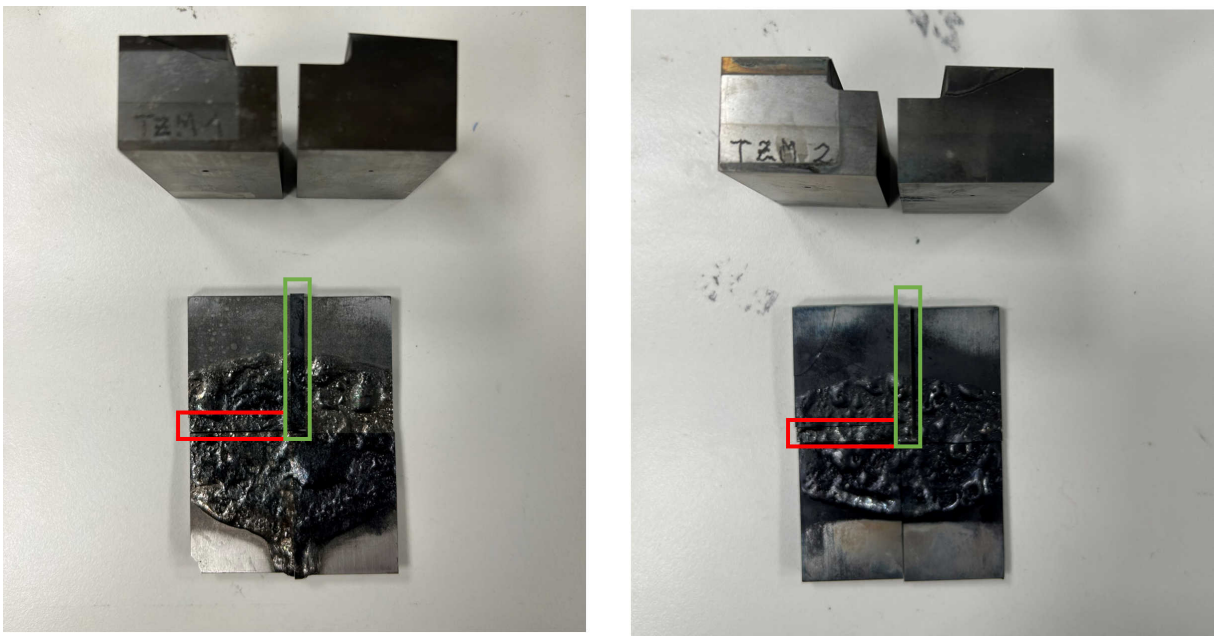

Fig. 5.41: TZM–1 (lhs) and TZM–2 (rhs) sample specimens.

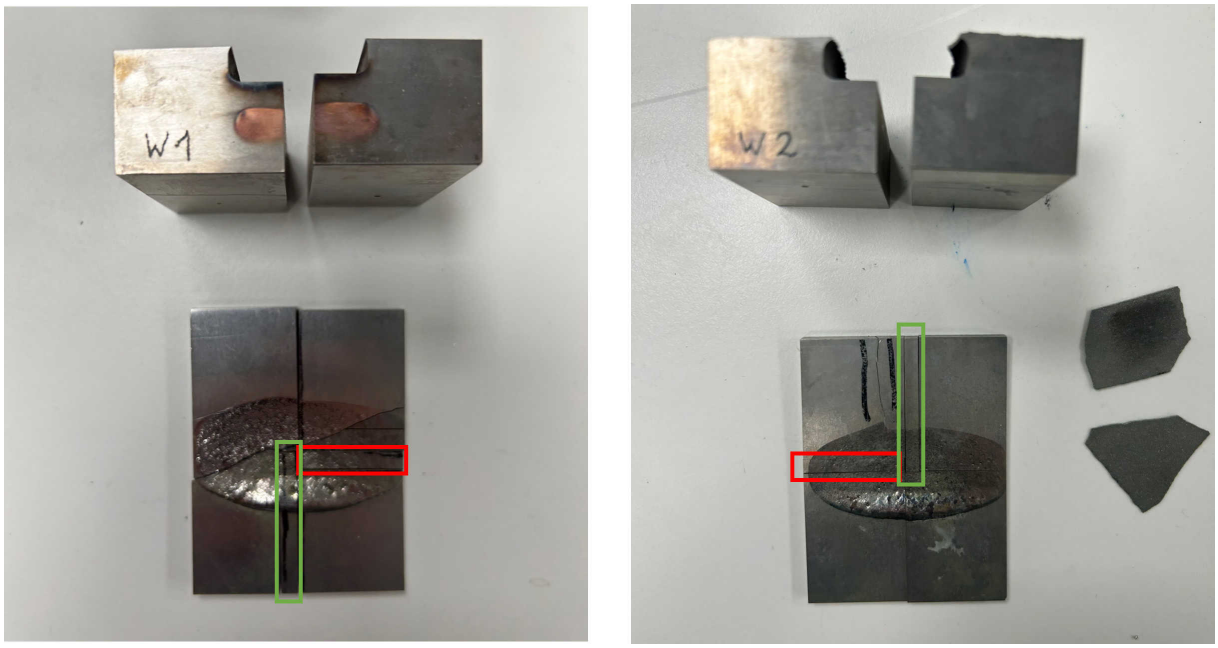

Fig. 5.42: W–1 (lhs) and W–2 (rhs) sample specimens.

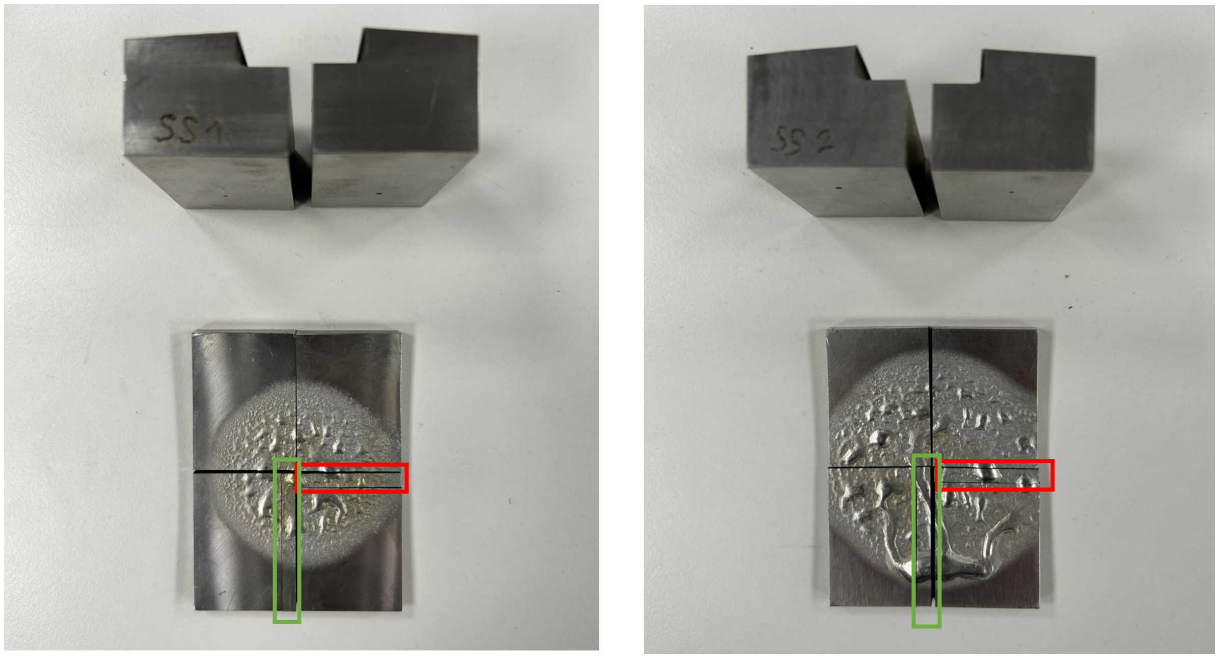

Fig. 5.43: SS–1 (lhs) and SS–2 (rhs) sample specimens.

5.7.1 Sample Preparation

Any optical analysis of the sample microstructure requires the specimens to be polished. For carrying on with the sample preparation, the author is granted access to the Non–Active Sample Preparation (NASP) laboratory of the Materials Research Facility (MRF), hosted by UKAEA.

Due to the specimens' size being bigger than the available polisher holder's size, the author polishes the specimens by hands. This involves using polishing cloths of different fabrics on a rotating wheel and suitable abrasive suspensions, or any other lubricant to prevent overheating and consequent deformation of the surface. Every specimen is suitably labelled and mounted on stubs by using mounting wax, which keeps the specimen in place during the polishing.

Fig. 5.44: Raw specimen mounted on the Al stub by using mounting wax (lhs), and stub screwed into the polishing frame (rhs).

The polishing procedure followed by the author for W, TZM, and SS is taken from [120] (see Table 5.12 and Table 5.13) and adapted to manual polishing for coarse–to–intermediate results (down to 3 μm diamond abrasive suspensions). Each polishing stage, while producing damage itself, must remove the damage from the previous step. Ideally, the final result is the production of a deformation–free surface that is flat, scratch free, and mirror–like under naked eye but showing its microstructure under high magnifications.

The polishing procedure commences by grinding the interested surface with 320 and 400 grit (35-22 μm) abrasive Silicon Carbide (SiC) papers mounted on a rotating wheel. This multi–step process lasts as long as it takes for establishing a plane surface by removing the effects of sample sectioning. The grinding steps are performed under water to prevent any surface overheating and extra damage introduction to both the specimen and the abrasive surface.

The bulk of the deformation created in the grinding process is removed by two subsequent

polishing steps, which use successively finer high removal rate diamond suspensions (MetaDi Supreme), 9 and 3 μm respectively. The surface looks smoother, and grain boundaries can be observed under optical microscope. Fig. 5.45 shows the W–1 specimen surface shape after different polishing stages. The final polishing suspensions used during the chemo-mechanical stage remove the layer of surface deformation often invisible to naked eye. Alumina is used for SS, whereas colloidal silica is deployed for refractory materials (W and TZM). Alumina exerts a pure mechanical abrasive action of material removal and surface finish, whereas colloidal silica adds a soft reaction layer to chemically attach the specimen surface, which is then gently wiped away without scratches. In some cases, the author uses a combined alumina and silica suspension for a better and more effective surface finish. During the last 30 seconds of the final stage, any suspension is replaced with water to flush the cloth surface and rinse the specimen.

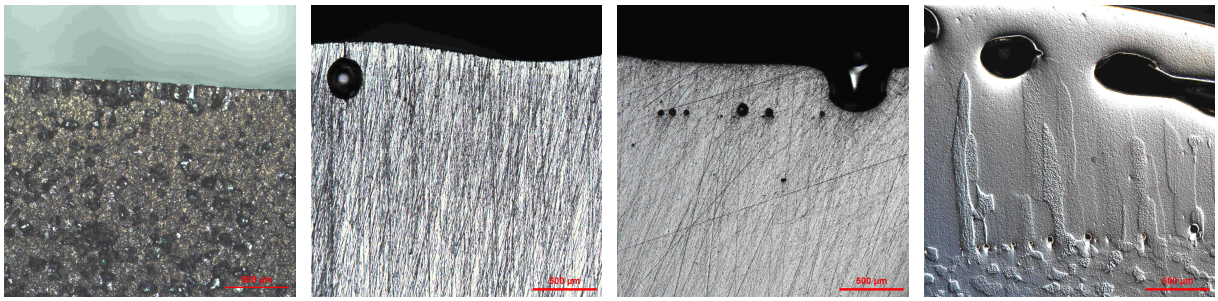

(a) (b) (c) (d)

Fig. 5.45: From left to right: W–1 surface after (a) sectioning; (b) grinding; (c) 9 μm diamond suspension stage; (d) 3 μm diamond suspension and final colloidal silica etching stage.

Due to variable load applied during the manual polishing, the time of each stage is increased to enhance surface relief, which leaves harder grains raised above the surface of the softer matrix. Ultrasonic cleaning of the specimen in deionised water is performed before each step, as it is more efficient at removing impurities and abrasive residuals in between polishing steps.

Surface	Abrasive/Size	time [min:sec]
CarbiMed	320[P400]-400[P800] grit SiC water cooled	until plane
UltraPad	9μm MetaDi Supreme Diamond	10:00
Trident	3μm MetaDi Supreme Diamond	8:00
ChemoMet	0.02-0.06μm Master-Met Colloidal Silica	5:00

Table 5.12: 4-steps polishing for refractory metals.

Surface	Abrasive/Size	time [min:sec]
CarbiMed	320[P400]-400[P800] grit SiC water cooled	until plane
UltraPad	9μm MetaDi Supreme Diamond	5:00
Trident	3μm MetaDi Supreme Diamond	3:00
ChemoMet	0.05μm MasterPrep Alumina	2:00

Table 5.13: 4-steps polishing for Stainless Steels.

5.7.2 Molten layer depth estimate under optical microscope analysis

Metals usually have a polycrystalline structure. It is therefore possible to identify crystallites (or grains) exhibiting a regular atomic structure where atoms form planes with a consistent crystallographic orientation. Grain boundaries define the interface between crystal lattices that have different crystallographic orientation. Every boundary is associated with a free Gibbs energy level, which depends on the extent of the boundary misorientation, composition of the two crystals, and mismatch of the crystal lattices [121]. Therefore, under high temperature treatments, crystals usually try to reduce their total grain boundary area in order to minimize their total free energy, and induce grain growth. In a single–phase material, this translates into thermally–activated nucleation and grain growth towards the hotter side. This process is identified as recrystallization, during which the material releases its stored energy generated from the deformation process when they are heated above a threshold temperature ($0.3T_m \leq T \leq 0.5T_m$) before reaching the melting point [122].

The author carries out optical analysis of the polished specimens in the Oxford Materials Characterization Service based in Begbroke and part of the University of Oxford Materials Department. The author is granted access to the Hirsh Building Laboratory, where she is trained to use the Polyvar Reichert–Jung Optical Microscope. The microscope works with the Leica Application Suite (LAS) software for image acquisition. For analysing the 2D specimen cross–section, a 2D mapping is generated from multiple tiled images captured automatically, with different focus point setups and linear predictive focus as well. In the following, the different specimens are described and analysed.

5.7.2.1 TZM

This section focuses on data retrieved from the destructive post–processing on TZM samples. All the four specimens from the TZM–1 and TZM–2 samples are analysed. Fig. 5.46 and Fig. 5.47 show a tiled image of the TZM–1 horizontally and vertically–oriented specimens, respectively. The TZM–2 horizontally and vertically–oriented specimens are instead shown, respectively, in Fig. 5.48 and Fig. 5.49. From both the horizontal specimens in Fig. 5.46 and Fig. 5.49, it is very difficult discerning between re–solidified molten layer and bulk structure, as the grains have similar size due to recrystallization occurring over the whole material thickness beneath the loaded area (see Fig. 5.50). The grain size is about hundreds of μm all over the area. Since this specimen top face is falling within the footprint area, it is likely that the molten layer is removed under gravity. Therefore, the author assumes that the molten layer is swept away, and the lowest thickness of recrystallized material does not go through any melting, otherwise that amount of material would miss as well. As already anticipated, the TZM–1 sample experiences the biggest loss of molten material during experiments, as Fig. 5.16 shows. This prevents any accumulation of the molten droplet before it solidifies.

Where the elongation is present, grain size can reach up to 500 μm (Fig. 5.51a), then decreases to 200 μm after recrystallization (Fig. 5.51b). The bulk shows 45 μm grain size (Fig. 5.51d).

From the vertical specimens (Fig. 5.47 and Fig. 5.49), it is more evident that the grains immediately below the loaded area are more elongated (up to 500 μm) and less porous that the recrystallized crystals beneath them, and their elongation is consistent with the direction of the heat flux (see Fig. 5.51a). The pink cross marks draw a separation line between solidified molten layer and recrystallized structure characterized by 200 μm grain size (see Fig. 5.51b), whereas the green cross marks identify a second interface which separates this last region from the original bulk structure, characterized by grain size smaller than 50 μm. This is more visible in Fig. 5.51c and Fig. 5.51d, with recrystallized grain size of hundreds of microns against bulk grain size of tens of microns.

For both the horizontally and vertically–oriented specimens of TZM–2 sample, the same conclusions drafted for the TZM–1 specimens stand. The horizontal specimen is mainly characterized by grains of the same size, with no identification of any elongated columnar growth

Fig. 5.46: TZM–1 horizontally–oriented specimen.

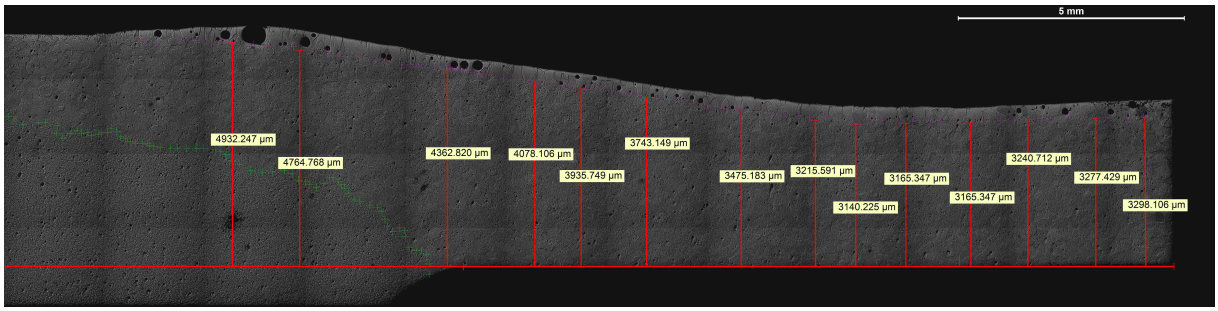

Fig. 5.47: TZM–1 vertically–oriented specimen.

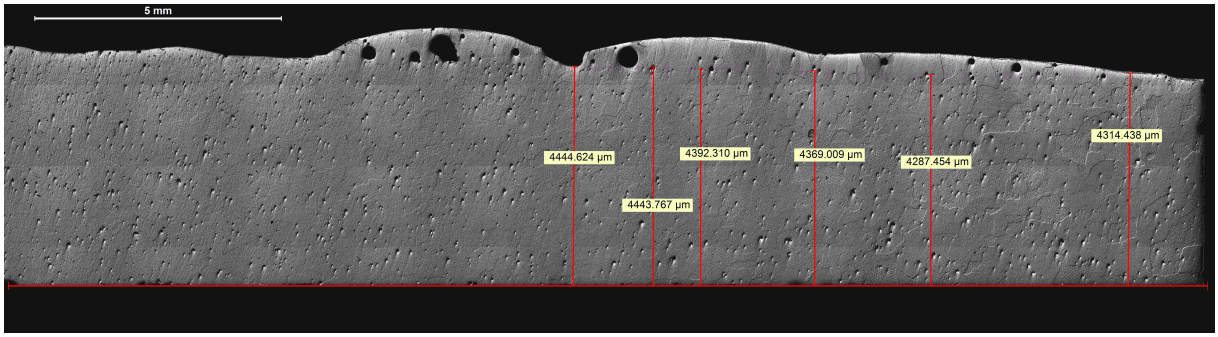

Fig. 5.48: TZM–2 horizontally–oriented specimen.

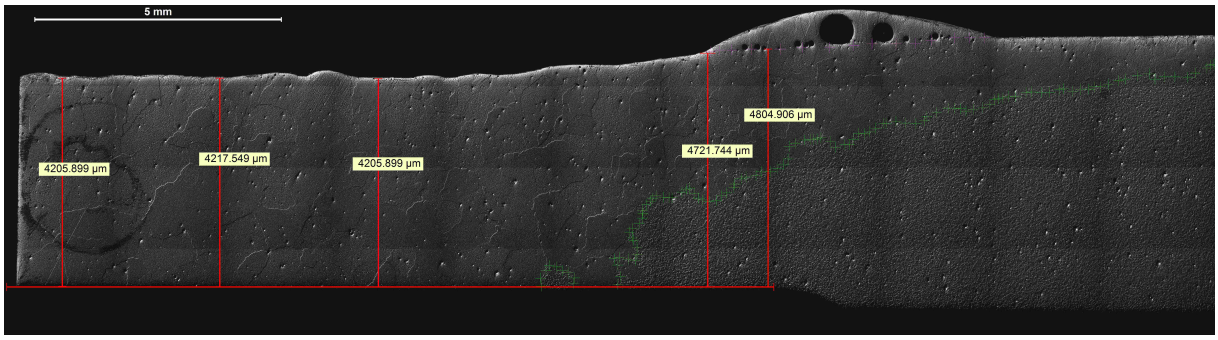

Fig. 5.49: TZM–2 vertically–oriented specimen.

immediately beneath the loaded area. This is visible in Fig. 5.52. The vertical one shows the same features as the TZM–1 vertically–oriented specimen, with a less accentuated grain elongation, apart from the point where the molten droplet accumulates before solidifying. Therefore, for both the specimens, it is likely that the deepest point of the surface corresponds to a physical

interface between the swept molten layer and the solid material beneath it.

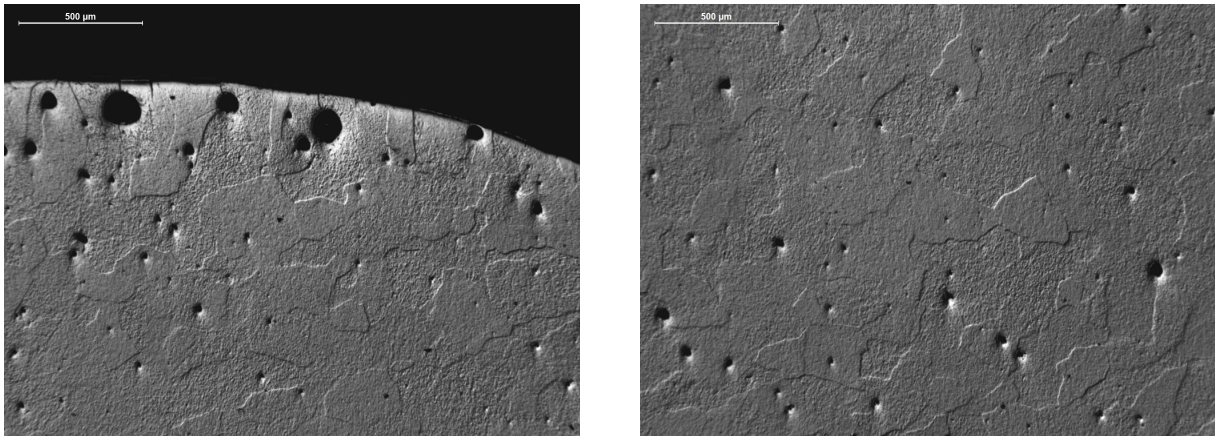

(a) Grain size along the heated boundary. (b) Grain size in the bulk of the specimen.

Fig. 5.50: Melted and bulk microstructure morphology of the horizontally–oriented TZM–1 specimen.

The recrystallization temperature range for TZM found in literature is around 1400°C, ≈ 250°C higher than the Mo recrystallization temperature. This results from the presence of carbides along the grain boundaries, which increases the grain growth, thus increasing the thermal energy required for recrystallization [123]. By plotting the isothermal surfaces between 1300°-1400°C across the thickness of the TZM sample in Fig. 5.53, they are located close to the green interface highlighted in the TZM–1 vertical specimen (Fig. 5.47), whereas the TZM–2 recristallization surface in Fig. 5.49 results at a higher temperature).

Void–like structures can be easily identified in both the horizontally and vertically–oriented TZM specimens. Although the TZM shows a bulk porous structure highlighted in Fig. 5.48 and Fig. 5.49, bigger size voids are trapped closer to the surface, breaking the continuity of the molten layer, where visible. The bigger voids close to the surface may be originated by coalescence of smaller voids, migrating to the surface and bursting under the beam heat flux.

The measurements of the TZM grain size are shown in Appendix (§A.1.1).

In summary, by taking the average of the three lowest measurements, Table 5.14 reports an estimate of the molten layer depth for the analysed TZM specimens.

Fig. 5.54 and Fig. 5.55 plot the solid–to–liquid and the liquid–to–vapour interface tracking computed by 3D–TARTIFL&TTE for the TZM–1 and TZM–2 samples, respectively.

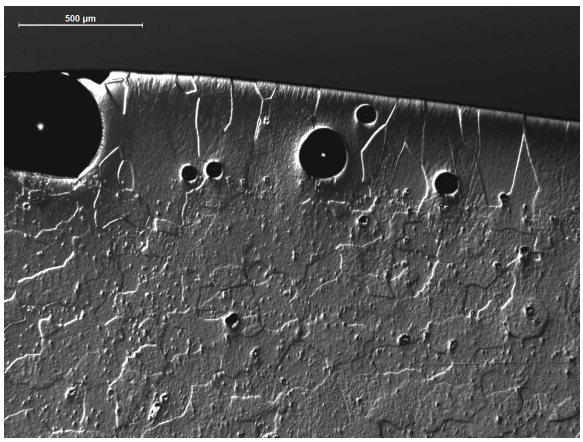

(a) Grain size near the melted area.

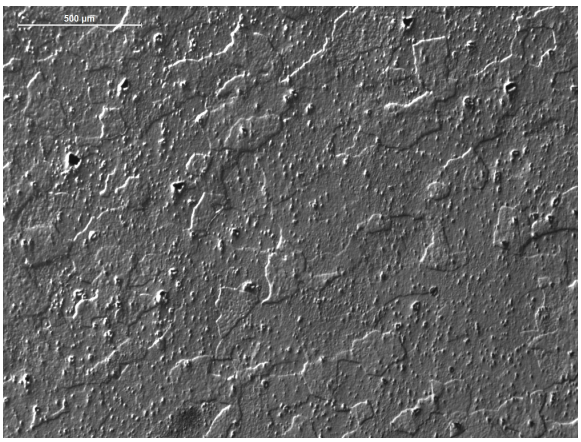

(b) Grain size in the recrystallized area.

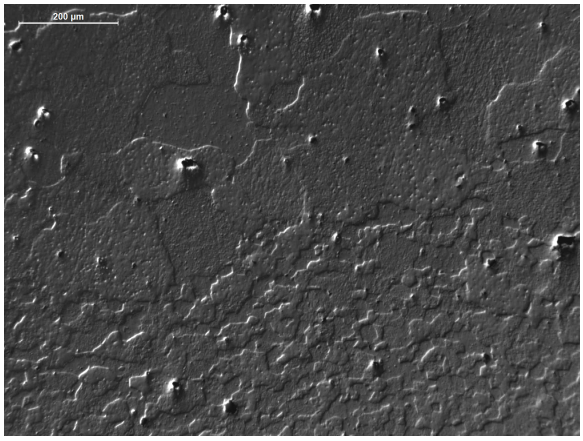

(c) recrystallized and bulk grain interface.

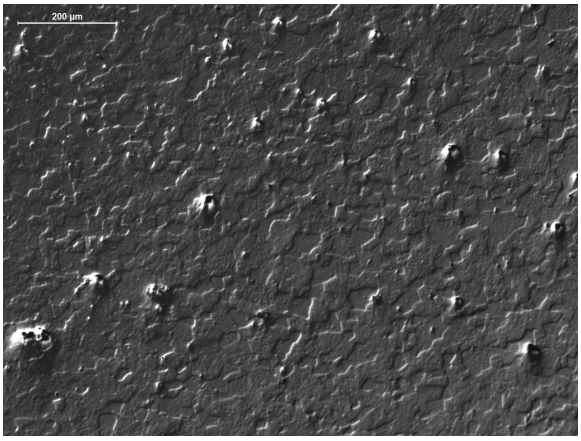

(d) Particular of the bulk grain size.

Fig. 5.51: Melted and bulk microstructure morphology of the vertically–oriented TZM–1 ((a)–(b)) and TZM–2 ((c)–(d)) specimens.

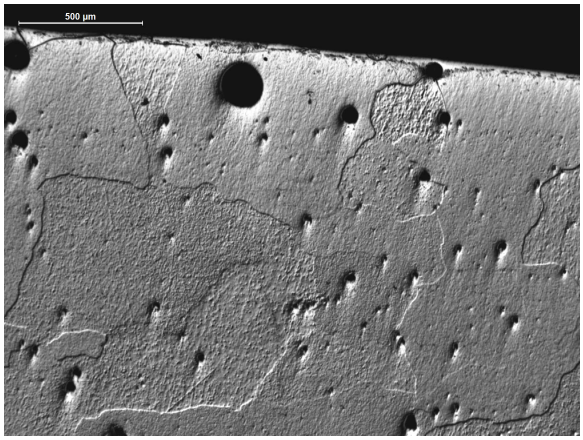

(a) Grain size along the heated boundary.

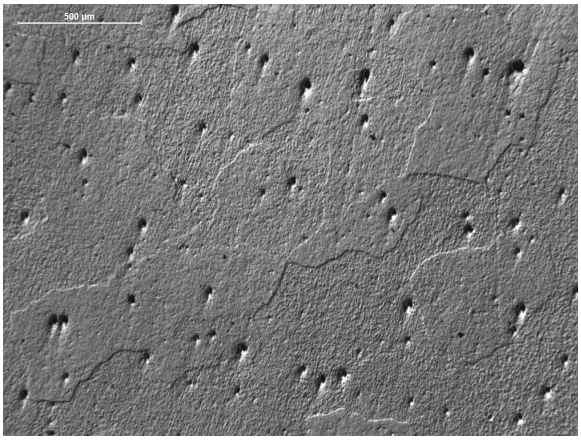

(b) Grain size in the bulk of the specimen.

Fig. 5.52: Melted and bulk microstructure morphology of the horizontally–oriented TZM–2 specimen.

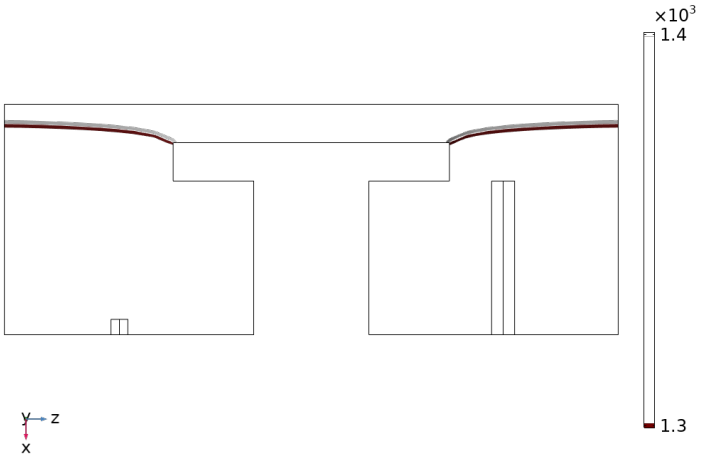

Fig. 5.53: Isothermal surfaces delimiting the TZM recrystallization temperature range [°C].

	TZM–1		TZM–2	
	horizontal	vertical	horizontal	vertical
bulk measurements	3262.193	3260.252	4287.454	4205.889
	3250.542	3282.582	4369.009	4205.889
	3287.752	3245.364	4314.438	4217.549
bulk average	3266.829±16	3262.733±15	4323.634±34	4209.776±5
melted thickness	1733.171±16	1737.267±15	676.366±34	790.224±5
average melted thickness	1735.219±15		733.295±24	

Table 5.14: Molten layer depth estimate [µm] for the TZM–1 and TZM–2 samples.

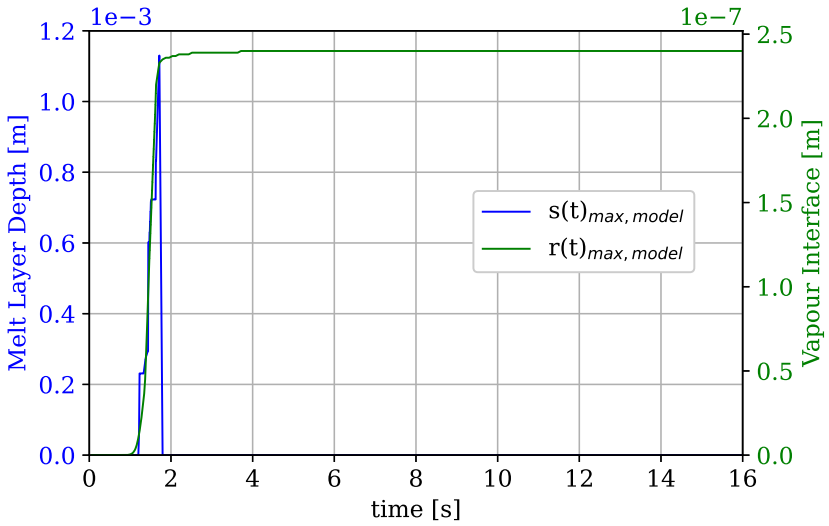

Fig. 5.54: TZM–1: Modelled solid–to–liquid interface (s(t)) and surface recession (r(t)).

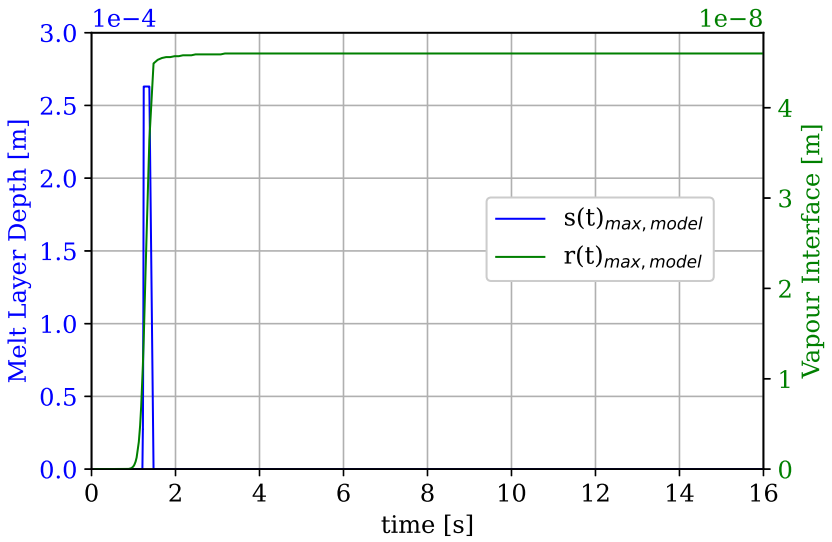

Fig. 5.55: TZM–2: Modelled solid–to–liquid interface (s(t)) and surface recession (r(t)).

5.7.2.2 W

This section focuses on data retrieved from the destructive post–processing on the W–1 sample. Unfortunately, the W–2 sample is discarded from this analysis because the reference point in Fig. 5.40b is lost due to a bad cut slicing off the reference surface. Therefore, only the two specimens from the W–1 sample are analysed and taken as reference for both the samples. Fig. 5.56 and Fig. 5.57 show a tiled image of the W–1 horizontally and vertically–oriented specimens, respectively.

Both the specimens show an elongated crystal growth beneath the heated area, and the direction of this growth is parallel to the beam source that mainly dictates the preferred direction of the heat transfer across the sample during the heating time. This is more visible in Fig. 5.58a and Fig. 5.59a, where the crystal growth can form conglomerates of hundreds of microns from pre–existing grains. The structure below the melted interface has grain size of around 70 µm, according to Fig. 5.58b and Fig. 5.59b, although the vertical specimen shows the existence of a third smaller grain domain (see Fig. 5.58c and Fig. 5.58d), which is likely to be the original structure of W–1 sample characterized by grain size no bigger than 50 µm. The difference in grain size for W–1 enables the author to draw a physical interface between grain growth closer to the heated surface and the pentagonal grain shape throughout the specimen. The bulk of the structure is instead recrystallized under heat treatment, and this prompts the grains to minimise

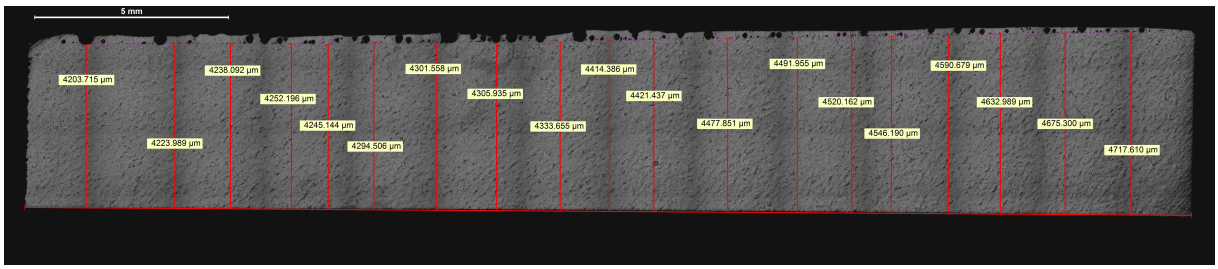

Fig. 5.56: W–1 horizontally–oriented specimen.

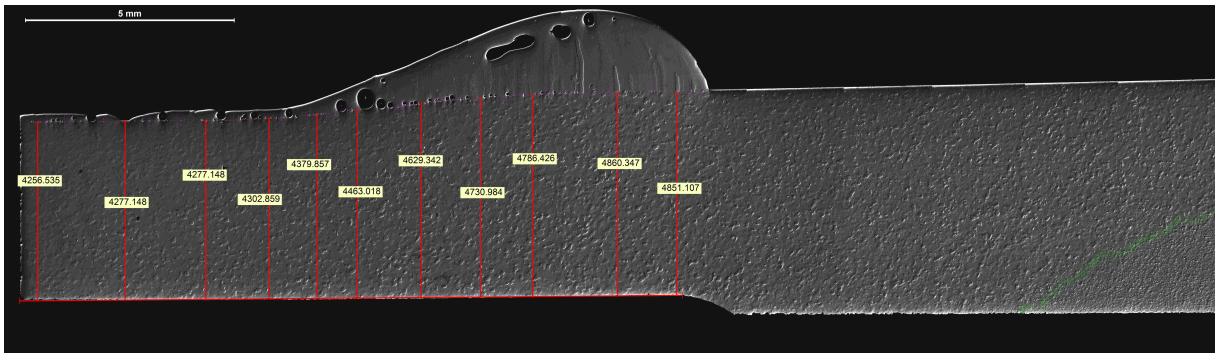

Fig. 5.57: W–1 vertically–oriented specimen.

their exposed area to keep the low energy level at the boundary.

The recrystallization temperature found in literature for W is in the range 1100°-1500°C [124], depending on the level of cold deformation applied during manufacturing. By plotting the isothermal surfaces between 1100°-1600°C across the thickness of the W sample in Fig. 5.60, the green interface highlighted in the W vertical specimen (Fig. 5.57) results closer to the 1300°C iso–T.

In addition to grain growth and recrystallization, it is also important to highlight the void–like structures remarking the interface between the re–solidified and bulk microstructure in Fig. 5.56 and Fig. 5.57. Both the W specimens show smaller lined–up bubble–like structures at the solid–to–liquid interface, which become bigger in size as they approach the melt wobbling surface. The smaller voids probably appear once the melting starts, and coalesce throughout the duration of the shot before any molten layer drifts. Local evaporation and bubble bursting affect the size and shape of these voids, opening up at the surface of the molten layer. The biggest bubble visible within the re–solidified droplet in Fig. 5.57 shows the coalescence of bubbles trapped within the molten layer on their way to the surface. The same bubbly phenomenon is observed in re–solidified molten layers from W samples analyzed in [125, 126, 127], where the

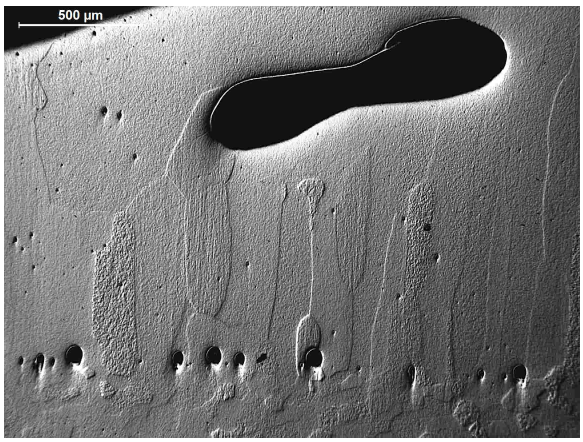

(a) Grain size near the melted area.

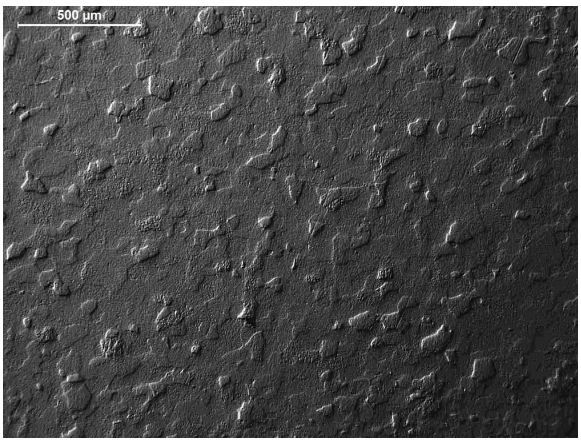

(b) Grain size in the recrystallized area.

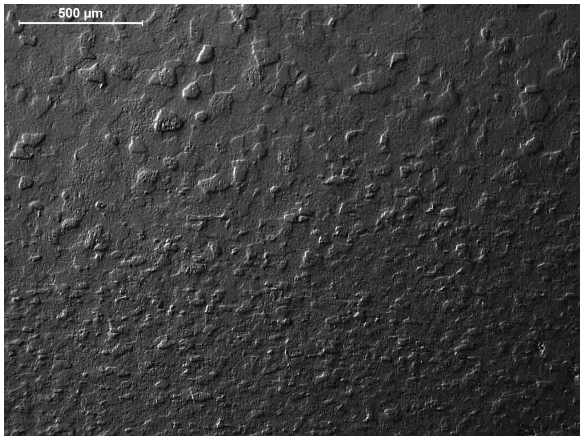

(c) recrystallized and bulk grain interface.

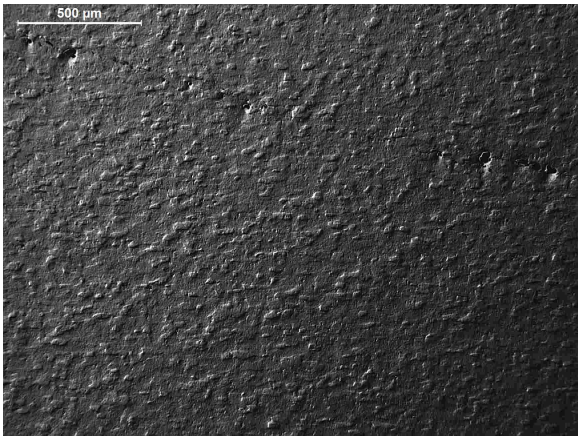

(d) Particular of the bulk grain size.

Fig. 5.58: Melted and bulk microstructure morphology of the vertically–oriented W–1 specimen.

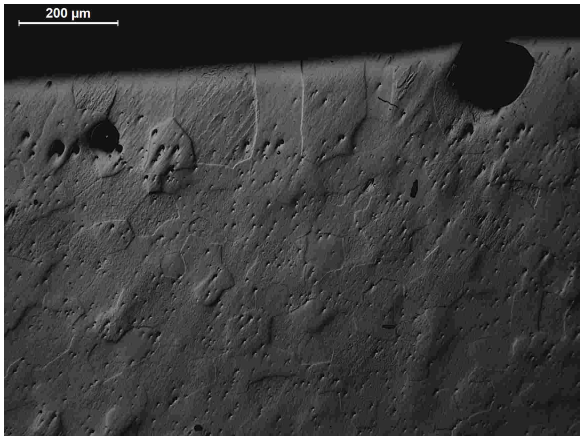

(a) Grain size along the heated boundary.

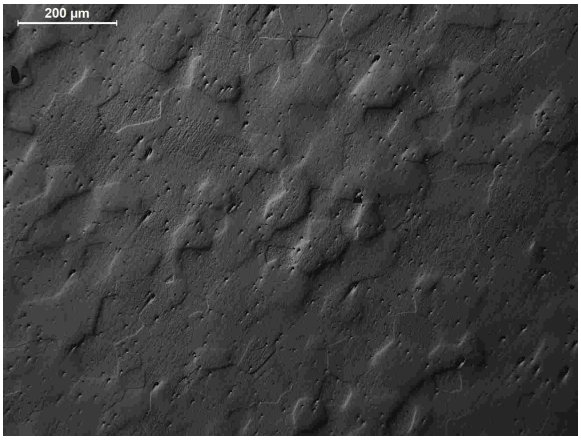

(b) Grain size in the bulk of the specimen.

Fig. 5.59: Melted and bulk microstructure morphology of the horizontally–oriented W–1 specimen.

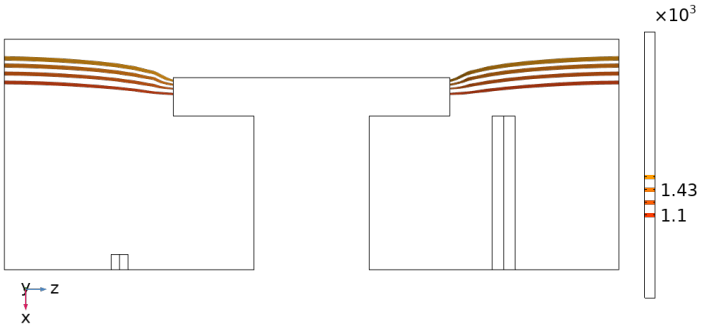

Fig. 5.60: Isothermal surfaces delimiting the W recrystallization temperature range [°C].

authors highlight the same phenomenology after the liquid solidifies, although Fig. 5.61c does not show elongated grains in the re–solidified layer. It cannot be excluded that hydrogen and other gaseous content affects the formation and the growth of the bubbles. Similar to the TZM vertical specimens, the W–1 vertical one shows the solidified melt droplet drifting down under gravity effect.

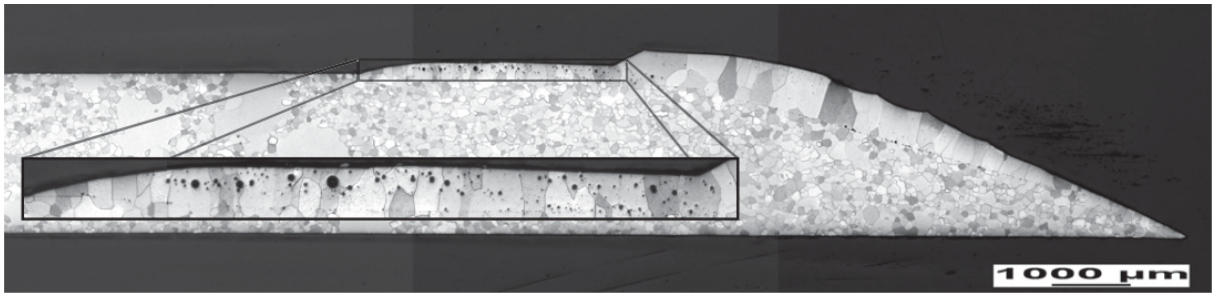

(a) [125]

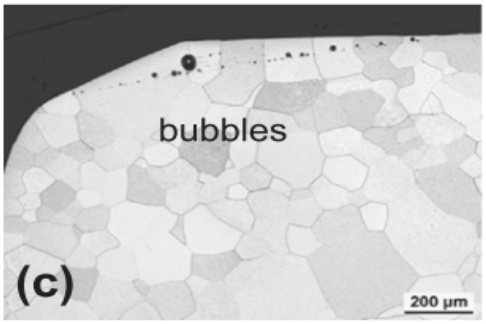

(b) [126]

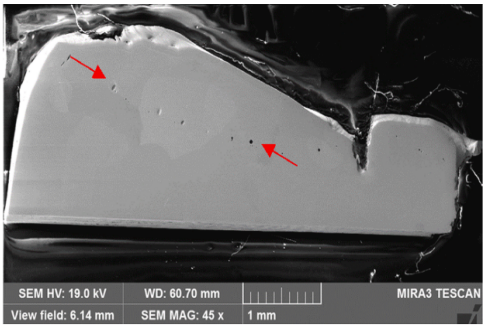

(c) [127]

Fig. 5.61: Void–like structures at the interface between the liquid and solid phases in W tiles undergoing melt experiments in tokamaks like TEXTOR ((a) and(b)) and JET (c).
Figure 5.61a reproduced with permission. ©IOP Publishing. All rights reserved.
Figure 5.61b reprinted from [126], with permission from Elsevier.

The measurements of the W grain size are shown in Appendix (§A.1.2).

In summary, by taking the average of the three lowest measurements, Table 5.15 reports an estimate of the molten layer depth for the analysed W–1 specimen.

	W–1		W–2	
	horizontal	vertical	horizontal	vertical
bulk measurements	4203.715	4277.148	–	–
	4223.989	4256.536	–	–
	4238.092	4277.148	–	–
bulk average	4221.932±14	4270.277±10	–	–
melted thickness	778.068±14	729.723±10	–	–
average melted thickness	753.895±12		–	

Table 5.15: Molten layer depth estimate [µm] for the W–1 sample.

Fig. 5.62 and Fig. 5.63 plot the solid–to–liquid and the liquid–to–vapour interface tracking computed by 3D–TARTIFL&TTE for the W–1 and W–2 samples, respectively.

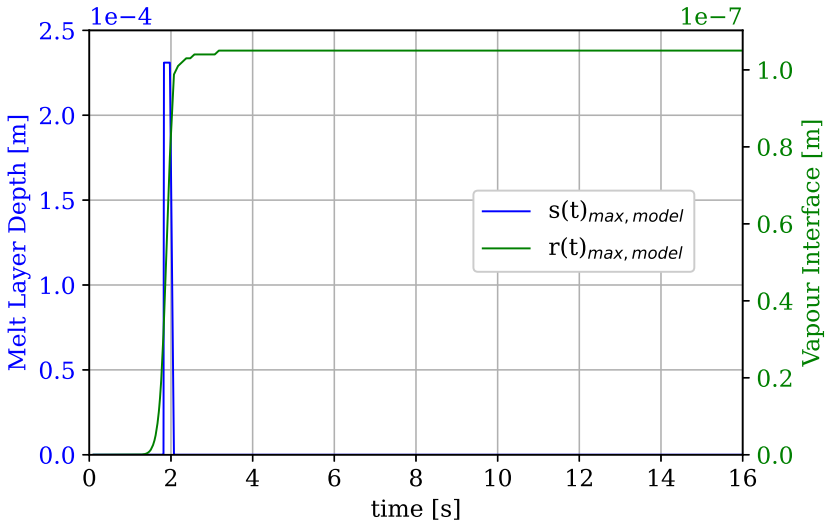

Fig. 5.62: W–1: Modelled solid–to–liquid interface (s(t)) and surface recession (r(t)).

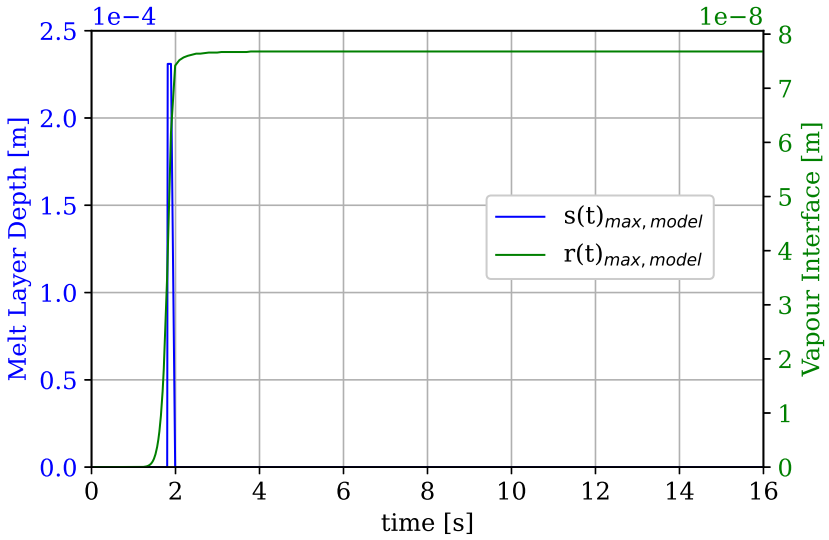

Fig. 5.63: W–2: Modelled solid–to–liquid interface (s(t)) and surface recession (r(t)).

5.7.2.3 SS

This last section focuses on data retrieved from the destructive post–processing on the SS samples. Similar to the W–2 sample, the SS–2 horizontal specimen is discarded because the reference surface in Fig. 5.40b is not preserved during the cross–sectioning. The SS–2 vertically–oriented specimen only partially shows the reference surface, which is mostly sliced off. The reference is partially lost for the SS–1 specimens in some areas as well, since the cut is not straightly executed; however, the author tries to set a new reference point built upon the visible left reference surface at the back of the specimen. The tiled images of the two SS–1 horizontally and vertically–oriented specimens are shown in Fig. 5.64 and Fig. 5.65, respectively. The tiled image of the SS–2 vertically–oriented specimen is instead shown in Fig. 5.66.

All the specimens show a wobbling exposed surface, with bumps characterized by a dendrite structure with thinner elongated grains (see Fig. 5.67a, Fig. 5.68a and Fig. 5.69a) compared to the bulk (see fig. 5.67b, Fig. 5.68b and Fig. 5.69b). The dendrites grow along the beam source beneath the heated area. Being the SS samples the last experimental batch, their loading time is tuned on the previous shots to reach melting and avoid any huge drifting of the molten layer under gravity. This means that, especially for the SS–1 sample, the loading time lasts until the melting is reached, allowing the liquid layer to stay in place and solidify as long as it appears.

Fig. 5.67 shows a comparison of the edge and bulk microstructure of the SS–1 horizontal

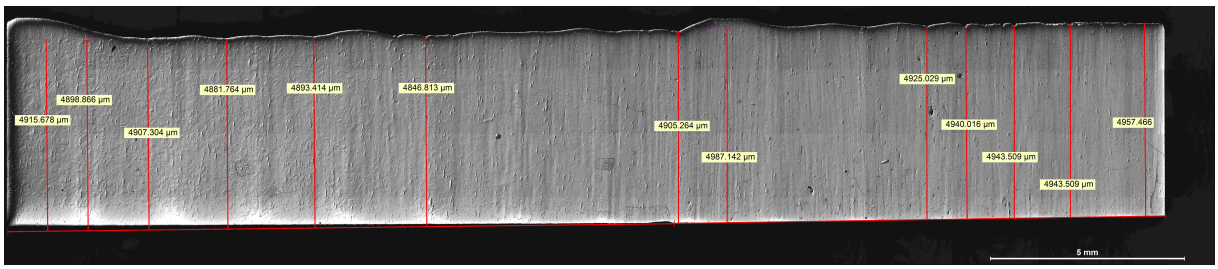

Fig. 5.64: SS–1 horizontally–oriented specimen.

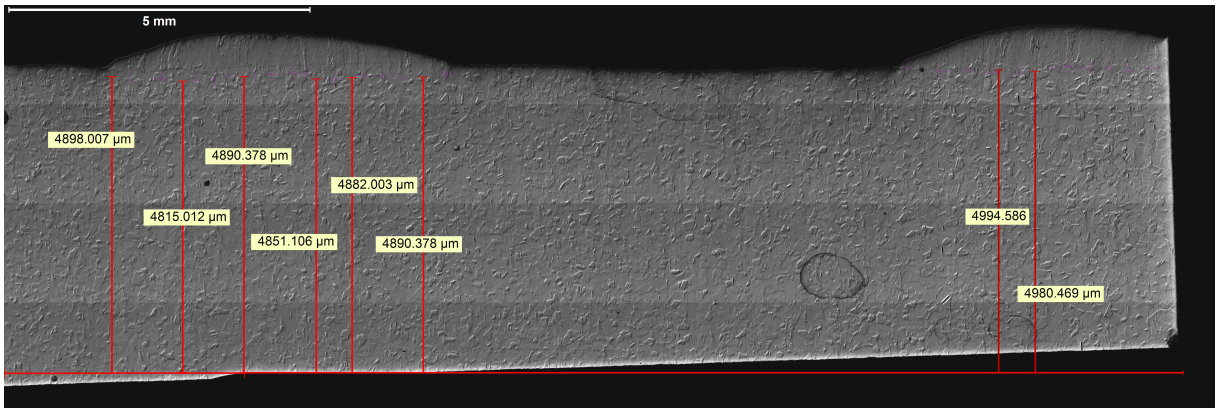

Fig. 5.65: SS–1 vertically–oriented specimen.

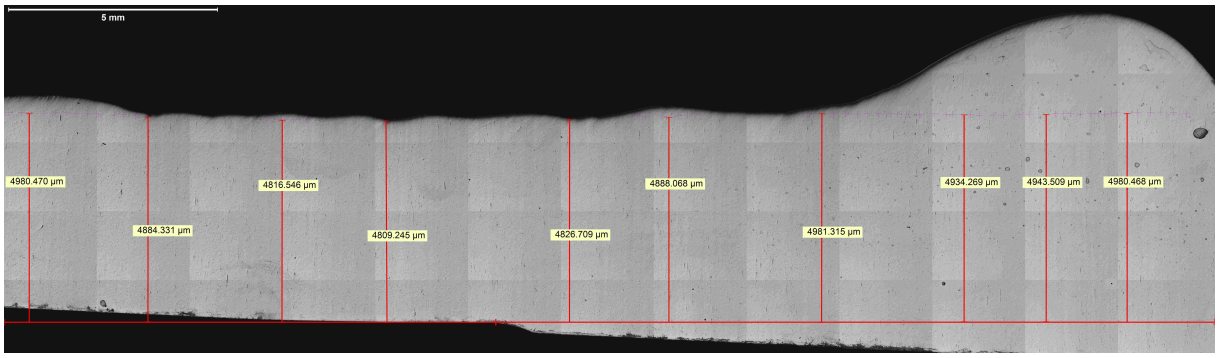

Fig. 5.66: SS–2 vertically–oriented specimen.

sample in Fig. 5.67a and Fig. 5.67b, respectively. The dendrites are clearly visible in Fig. 5.67a, even without etching the final SS polished surface. Since the optical microscope allows the author to distinguish between the different morphological structures, the SS sample preparation does not include further etching stages. A comparison between the non–etched and etched surface of the SS specimen is reported in §A.1.3 (Fig. A.6c and Fig. A.6d), which shows that the interface between different phases is visible before any use of the etchant.

Only the SS–2 vertical specimen shows the solidified melt droplet drifting down under gravity effect, since its heated time is slightly longer than the one set for heating the SS–1 sample. Fig.

5.69a shows a zoom of the 200 μm transition region between the solid and the drifted re–solidified structure.

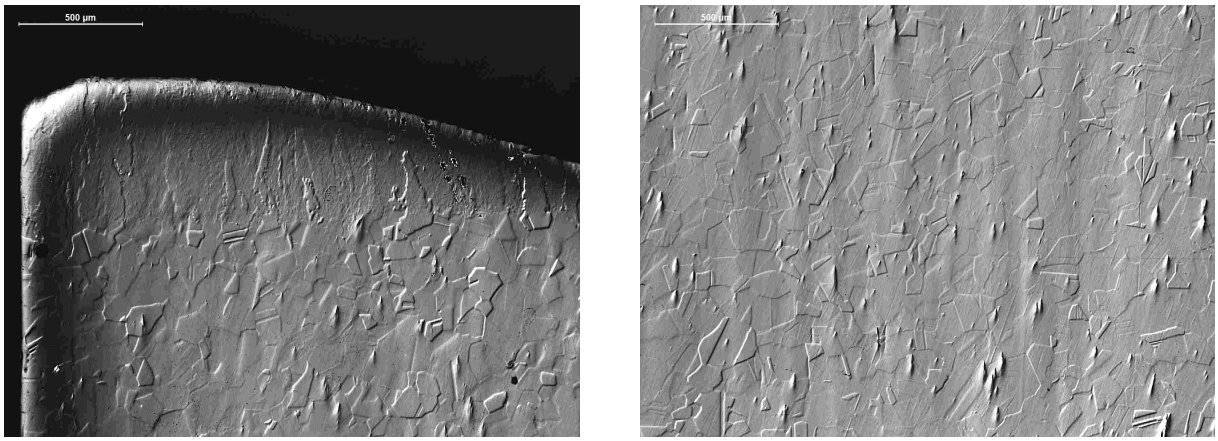

(a) Edge structure after polishing. (b) Bulk structure after polishing.

Fig. 5.67: Melted and bulk microstructure morphology of the horizontally–oriented SS–1 specimen.

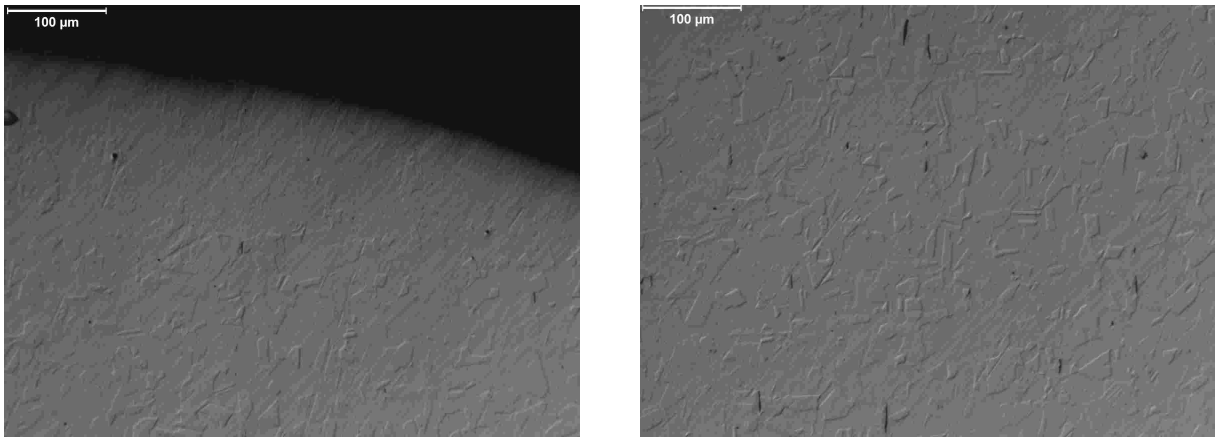

(a) (b)

Fig. 5.68: Melted and bulk microstructure morphology of the vertically–oriented SS–1 specimen.

The author cannot identify any evident recrystallization boundary in the SS specimens, although the recrystallization temperature range found in literature for SS–316 is within 750°-1100°C [128]. In case of austenitic steel, the recrystallization is temperature dependent, and its activation level is strongly dependent on the manufacture treatment for improving their mechanical properties. Nonetheless, the isothermal surfaces within the recrystallization temperature interval are plotted across the thickness of the SS sample in Fig. 5.70, supporting the consideration that the unmelted SS specimen thickness is all recrystallized.

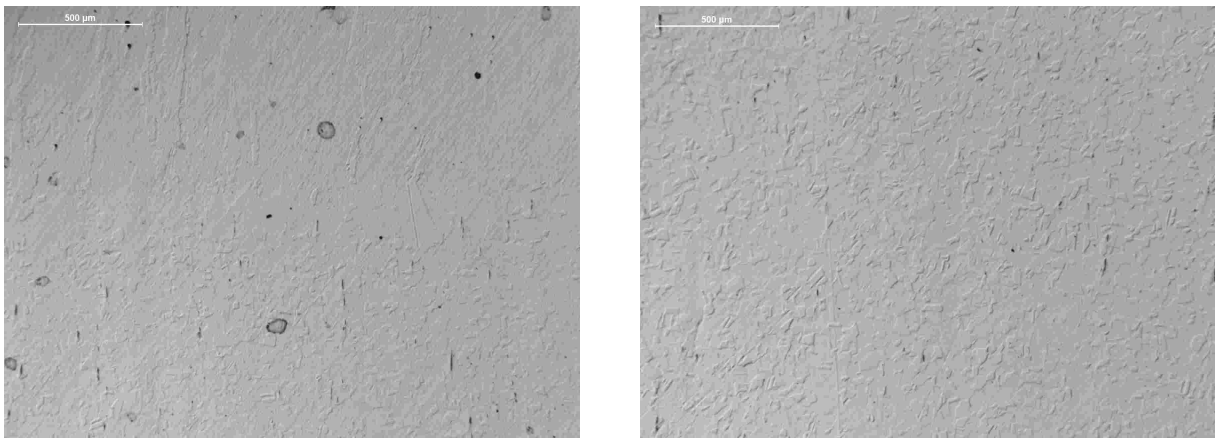

(a) (b)

Fig. 5.69: Melted and bulk microstructure morphology of the vertically–oriented SS–2 specimen.

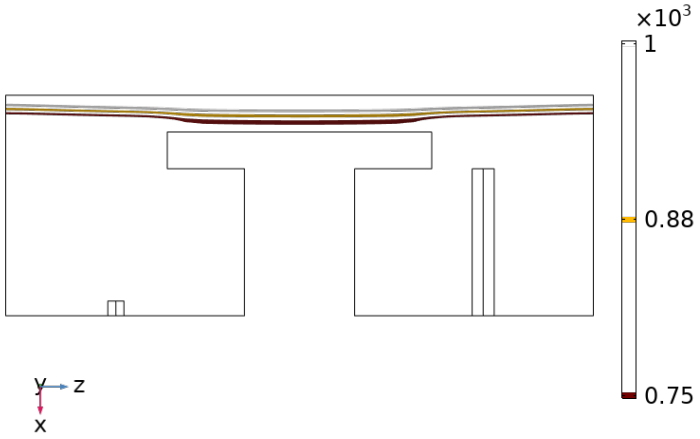

Fig. 5.70: Isothermal surfaces within the SS recrystallization temperature range [°C].

Further measurements of the SS grain size are reported in Appendix (§A.1.3).

In summary, by taking the average of the three lowest measurements, Table 5.16 reports an estimate of the molten layer depth for the analysed SS–1 specimen. Table 5.71 and Table 5.72 plot the solid–to–liquid and the liquid–to–vapour interface tracking computed by 3D–TARTIFL&TTE for the SS–1 and SS–2 samples, respectively.

	SS–1		SS–2	
	horizontal	vertical	horizontal	vertical
bulk measurements	4846.813	4815.012	–	4816.546
	4893.414	4882.003	–	4809.245
	4881.764	4851.106	–	4826.709
bulk average	4873.997±19	4849.374±27	–	4817.500±7
melted thickness	126.003±19	150.626±27	–	182.500±7
average melted thickness	138.315±24		182.500±7	

Table 5.16: Molten layer depth estimate [µm] for the SS–1 and SS–2 samples.

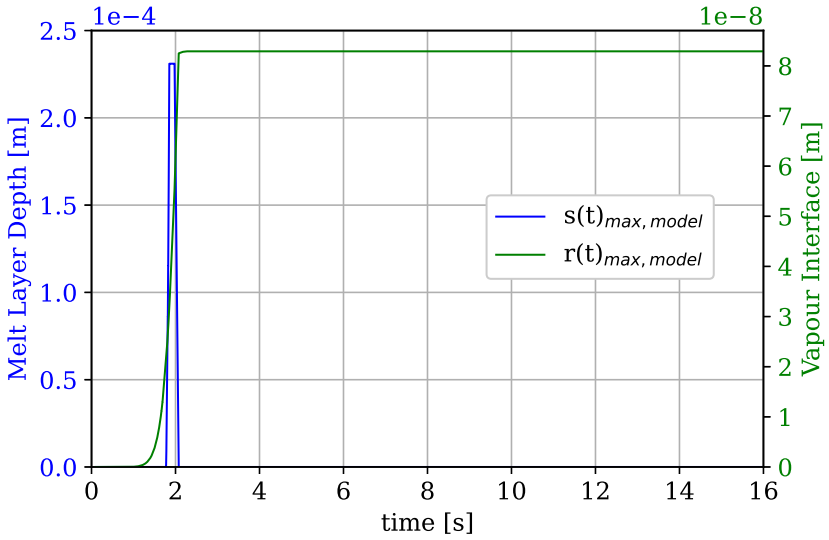

Fig. 5.71: SS–1: Modelled solid–to–liquid interface (s(t)) and surface recession (r(t)).

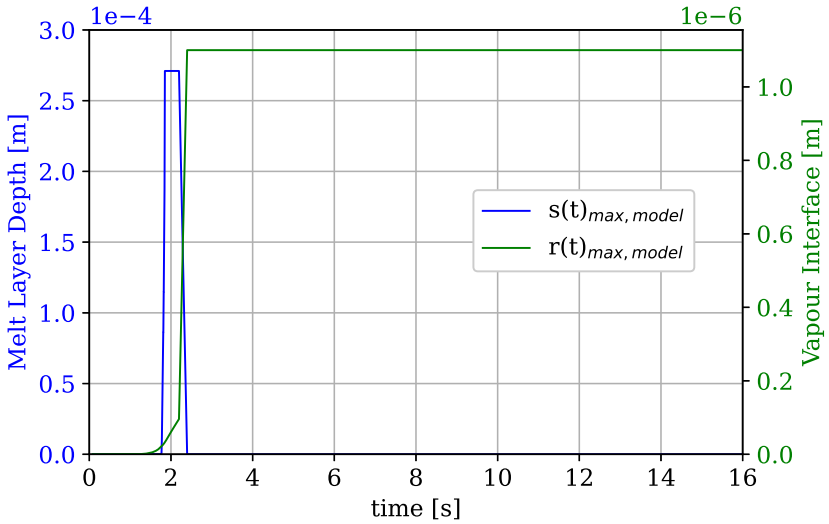

Fig. 5.72: SS–2: Modelled solid–to–liquid interface (s(t)) and surface recession (r(t)).

5.8 Result discussion

The main results derived from the quantitative benchmarks of all the cases analyzed in §5.5 are summarized in Table 5.17.

		TZM–1/TZM–2			**W–1/W–2**			**SS–1/SS–2**		
		Exp	Model	Δ[%]	Exp	Model	Δ [%]	Exp	Model	Δ [%]
HF_{max} [MW m^{-2}]		30		–	30		–	10	10.7	7%
Δt [s]		1.57/1.30		–	1.87/1.82		–	1.88/2.11		–
E_{abs} [kJ m^{-2}]		206/171	205/170	0%/0%	245/239	244/238	0%/0%	87/98	87/98	0%/0%
T_0 [°C]		12/13		–	12/17		–	20/19		–
t_m [s]	**IR**	0.96/0.95	1.11	16%/17%	1.49/1.5	1.68	14%/13%	1.61/1.60	1.64	2%/2%
	1c–Pyro	0.96/0.95		16%/17%	1.48/1.5		14%/13%	1.61/1.63		2%/0%
T_{max} [°C]	**IR**	3024/3120	2911/2680	4%/14%	3591/3548	3473/3468	3%/2%	1504/1509	1473/1473	2%/2%
	1c–Pyro	2859/2631		2%/2%	3433/3401		1%/2%	1440/1437		2%/3%
	TC1	731/627	700/603	4%/4%	768/830	893/870	16%/5%	227/270	275/303	21%/12%
	TC2	570/NA	277/334	50%/NA	598/628	496/487	17%/22%	66/43	61/32	6%/24%

Table 5.17: Thermal benchmark result summary.

The benchmark allows the author to draw some general conclusions. Starting from the integrated energy density, both model and experiments agree very well, except for the SS samples where an increase of 7% in the maximum heat flux is necessary to match the experimental absorbed energy. Problems of sample assembly and cooling are of minor significance as the short pulse loading is adiabatic. The deviation of the SS samples could be explained with difficulties of optical temperature measurements on steel surfaces at low emissivity, combined with uncertainties in the SS–316 thermophysical properties. Considering the 7% heat flux increase for SS samples, it follows a good prediction of the maximum surface temperature collected by the 1c–Pyro for all the samples, whose agreement is well within 1%-3%. IR temperature values are higher than the ones captured by pyros, therefore the discrepancy between the IR values and the modelled T_{max} is within 2%-14%.

The melting phase is triggered by 3D–TARTIFL&TTE a fraction of seconds after the melting time detected by the diagnostics, with a 12%-18% delay with respect to the experimental data. To some extent, this depends on the T_m value triggering the melting phase, and therefore related to the uncertainty in the material properties. Furthermore, 3D–TARTIFL&TTE predicts the maximum temperature value measured by TC1 within 21%, whereas the agreement with the TC2 data is within 25% for all the shots apart from the TZM–1 one. In this case, the maximum modelled temperature is half the experimental value. It cannot be excluded that the TC2 gets damaged during the first TZM–1 shot, as the same TC fails during the TZM–2 shot. It is difficult to accurately explain this mismatch, besides that the 3D–TARTIFL&TTE models the

TC measurements through a probe located in place of the TC holes with no contact resistance nor other factors affecting the experimental TC measurements to be considered.

The big uncertainty lies in the prediction of the mass loss. This is highlighted by the tabulated data on mass in §4.3 reporting both the evaporative mass flux and the total amount of liquid mass, and the dedicated §5.7.2 section. As explained in §4, the only mass lost from the computational domain is due to the evaporative mass flux. Fig. 5.16 shows mass loss due to gravity, and potential splashes of liquid droplets under the beam action. By assuming as reference the experimental mass losses calculated in Table 5.4, there is no match with neither the mass loss due to evaporation, nor the maximum amount of molten mass calculated by 3D–TARTIFL&TTE, although the computed TZM–1 molten mass agrees within 15% with the experimental data, under the hypothesis that all the molten mass is removed once formed. This last case allows the author to state that the TZM–1 sample loses almost all the molten mass, whose little remainder solidifies on the surface. The other shots are instead characterized by a partial loss of molten mass, which is difficult to accurately quantify. Broadly speaking, apart from gravity which gives a consistent contribution to the mass downward drifting due to the GLADIS experimental setup, splashes and liquid droplet ejections arising far below the boiling point should be accounted for computing the melt mass loss. These mechanisms might be due to some instabilities arising under the beam impact (i.e. during the interaction between fluids at different density) or to local impurities which contribute to lower down the melting point of the solid material. Further investigation is required for quantifying their contribution that, once understood, can be implemented in the 3D–TARTIFL&TTE as an additional source causing the recession of the condensed phase surface, together with the evaporative mass flux.

As far as the molten thickness estimate is concerned, the data included in §5.7.2 are summarized in Table 5.18. This first comparison shows that both the experimental measurements and the 3D–TARTIFL&TTE estimates of molten thickness target the same order of magnitude, despite the difference in modules.

As far as TZM and W are concerned, the melt pool thickness estimated by 3D–TARTIFL&TTE is lower than the experimental one, and the closest prediction achieved for the TZM–1 is within 36%. This difference increases up to 70% for the other samples. A different conclusion can be stated for the SS samples, for which 3D–TARTIFL&TTE predicts a bigger depth of the melt

	Exp [m]	3D–TARTIFL&TTE [m]	Δ
TZM–1	1.74E-03±1.5E-05	1.00E-03	35%
TZM–2	7.33E-04±2.4E-05	2.62E-04	66%
W–1	7.54E-04±1.2E-05	2.31E-04	69%
W–2	7.54E-04±1.2E-05	2.31E-04	69%
SS–1	1.38E-04±2.4E-05	2.31E-04	67%
SS–2	1.83E-04±7E-06	2.71E-04	48%

Table 5.18: Molten thickness estimate benchmark summary.

pool. This is likely caused by the increase in the heat flux peak for matching the absorbed energy value.

The main achievement of this comparison is matching the predicted melt pool depth in its order of magnitude. The comparison suggests that the methodology works, despite the module discrepancies. This might strongly depend on the uncertainties affecting the experimental process, which start from a more accurate metrology assessment of the samples before and after running the experiments. The post mortem analyses require more accurate cross–sectioning of the samples, for which it is important to preserve any reference surface unaltered during any sectioning.

5.9 Conclusion

The results of the TARTIFL&TTE benchmark against dedicated melting experiment data support the author's approach phase change modelling. The following points are highlighted:

- Good agreement on surface temperature and energy absorbed.
- Good agreement on molten layer thickness under the TARTIFL&TTE assumptions and the experimental uncertainties and discrepancies under gravity action.

Chapter 6

EU–DEMO Upper Limiter integrated engineering design

"The true meaning of a term is to be found by observing what a man does with it, not by what he says about it."

Percy Williams Bridgman

This chapter describes the rationale driving the integrated design of the Upper Limiter. Starting from its plasma–facing wall, the TARTIFL&TTE model is applied to this study to establish the minimum safest thickness of the W armour against off–normal transient event energy release. The design of the shield block supporting the plasma–facing armour is instead based on considerations related to the minimization of the electro–magnetic loads induced in the EUROFER steel block. A new attachment system between shield block and vacuum vessel is proposed as well. Volumetric nuclear heating drives the design of the cooling system layout.

Although the design concept and assessment workflow are conceived by the author, since early 2022 the assessment workflow has been handed over to a group of researchers led by the author, who has been appointed as EU–DEMO Limiter System Design Lead. Therefore, the author acknowledges the contribution of other researchers in helping perform the assessment workflow in support of the author's conceptual design choices. Two of the assessment contributions' highlights, i.e. the neutronic and the electro–magnetic ones, are summarized in §6.1.2 and §6.3.1, respectively.

The UL design concept, together with the assessment workflow supporting the design choices,

will be published in a joint paper entitled "The integrated Engineering Design Concept of the Upper Limiter within the EU–DEMO LIMITER System", led by the author and co–authored with A. Cardella (Supervisor), A. Cufar (Neutronics expert), A. Froio (Thermal–Hydraulics expert), P. Ireland (author's supervisor), I. Maione (Electro–magnetism expert), G. Pautasso (Plasma disruption expert), A. Martin Ramos (Cad Designer), G.A. Spagnuolo (Coordinator), F. Vigano (Structural assessment expert), and Z. Vizvary (author's supervisor). It is cited in [18].

6.1 UL integrated engineering design overview

Plasma disruptions are certainly challenging for IVCs. On one hand, they are responsible for releasing energy into the struck component and, on the other hand, for inducing electro–mechanical loads due to the interaction between currents induced in the conductive structure and $\vec{B}$. Although sacrificial limiters are primarily designed for facing the energy released by a limited plasma during transients, their design should safely withstand a combination of loads relevant to IVCs during steady–state. They are not meant to breed tritium, nor to provide plasma stability. However, sitting in place of blanket portions, they should ensure an adequate shielding function to VV and magnets while withstanding both their dead weight and the above–mentioned electro–mechanical loads.

As already anticipated in §1.3.1, the integrated design of the limiter system is made of two actively water–cooled sub–components: the PFC, directly exposed to the plasma and made of refractory material; the SB, made of a mixture of water and steel and devoted to hold the PFC while providing neutronic shielding. The general concept of the limiter system is sketched in Fig. 6.1.

The PFC design is driven by disruptive heat loads mainly during the TQ, which precedes the CQ phase. During the latter, the plasma current decay induces toroidal and poloidal currents in conducting structures, which experience significant electromagnetic loads. The design of the SB is indeed driven by electro–magnetic loads, nuclear heating under neutronic irradiation, and neutronic shielding requirements for VV (by limiting the displacement per atom – dpa), and magnets (by limiting the deposited energy).

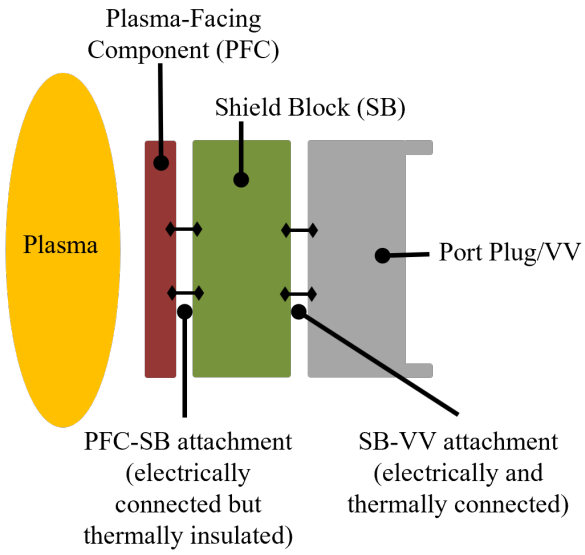

Fig. 6.1: Schematics of the integrated design of the limiter system.

Among the four limiters described in §2.1.1, the UL (see Fig. 6.2) is the one considered in the following. Since it is expected to be replaced more often than the other IVCs, the UL is installed and handled through the upper port, which enables it to be maintained independently from the rest of the IVCs.

The UL design workflow and assessment results from a close and iterative synergy among different fields. Static–structural and energy balance hand calculations based on preliminary electro–magnetic and neutronic load estimates are used, respectively, for evaluating the main dimensions of the attachment system mechanical elements (see §6.3) and the thermal–hydraulic parameters for both PFC (§6.2) and SB (§6.3). The UL integrated design performance is then verified against electro–magnetic, neutronic, thermal–hydraulic, and structural assessment under the above–mentioned load combination. The outcome will be taken as reference for future limiter engineering designs.

The UL integrated design overview is shown in Fig. 6.3. The SB is composed of 32 steel plates, electrically separated at the front but joined together at their back. The PFC is made of 64 units running poloidally, and attached to the SB plates (see Fig. 6.4). Every plate supports two PFC units. The two sub–components will be deeply discussed in §6.3 and §6.2, respectively.

This chapter is organized as follows. After explaining the requirements behind the choice of the temperature levels for the limiter cooling systems in §6.1.1, it follows the description of

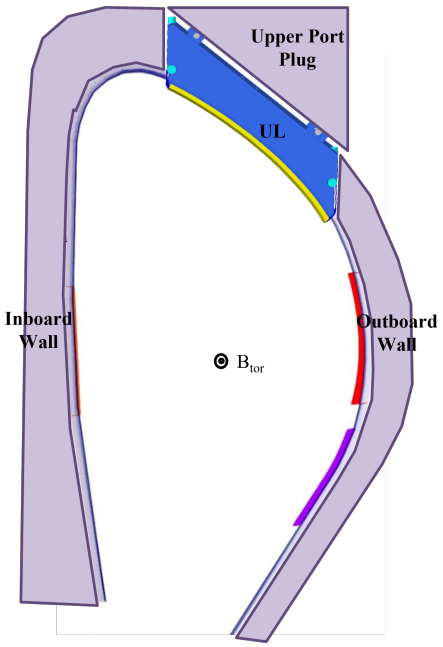

Fig. 6.2: Poloidal location of the UL.

the volumetric power deposited by neutrons within the limiter domain (§6.1.2). This volumetric power source drives the design of the cooling system layout during normal operation. The UL integrated design introduced in here is further broken down and explained in the two sections §6.2 and §6.3 specifically focused on, respectively, PFC and SB design drivers. Furthermore, the design of the SB–VV attachment system is presented.

6.1.1 Cooling system temperature level requirements

For reducing the numbers of different inlet parameters feeding all the IVC cooling systems in DEMO, it is sensible to align the inlet values of the coolant pressure and temperature for limiter and divertor systems, since they share several features highlighted below:

- Both are non–tritium breeding IVCs subjected to neutron flux during operation.
- Both adopt a refractory armour directly copying with the plasma heat loads.
- Both are subjected to high heat flux, despite the different intensity and duration.

Furthermore, this also limits the water chemistry to just the ones devoted to the sub-components directly facing the plasma thermal loads (Cu alloys), and the structural ones made of steel.

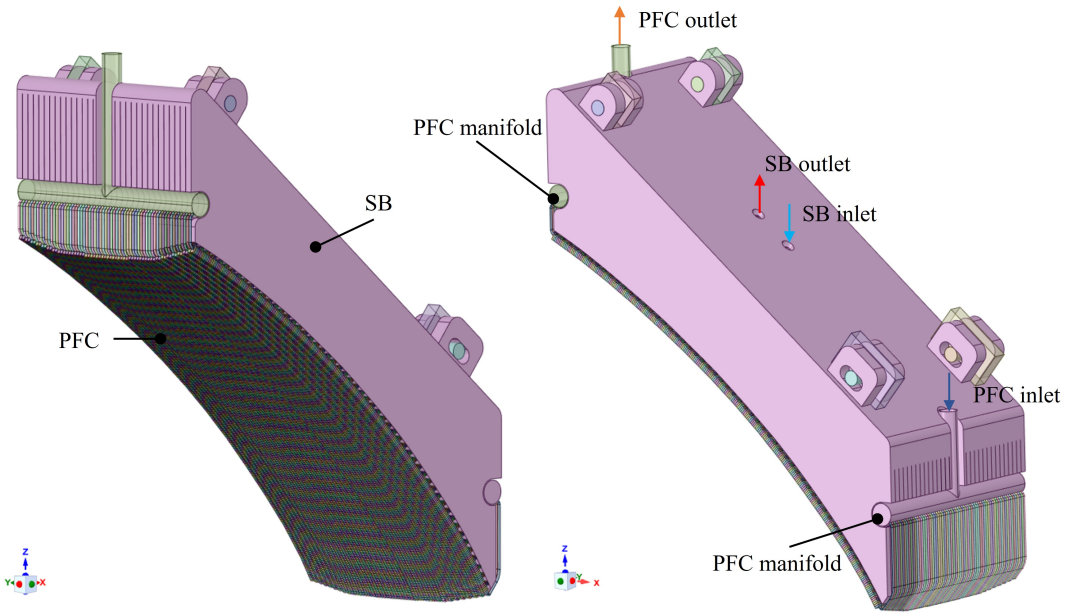

Fig. 6.3: UL integrated design overview.

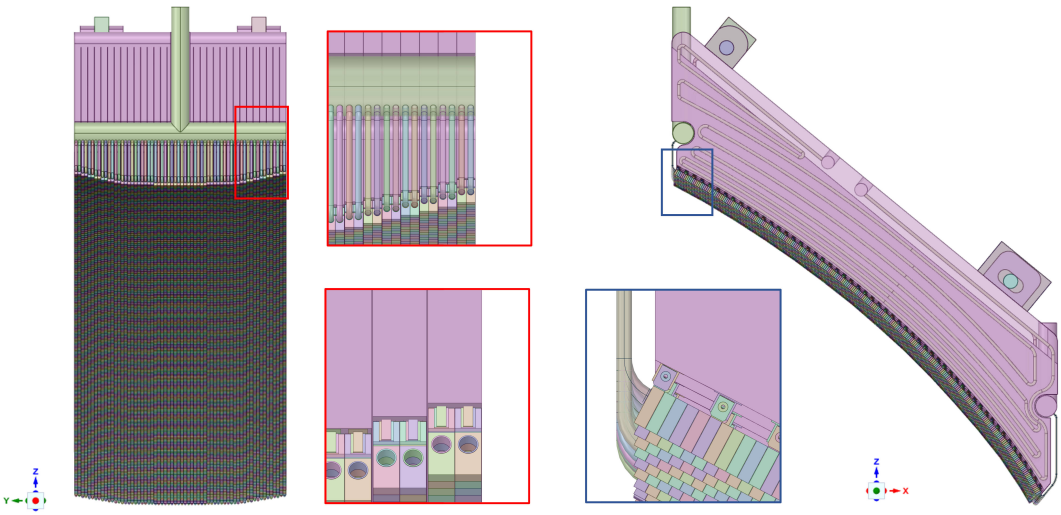

Fig. 6.4: Particular of the PFC–SB interface.

As far as the PFC is concerned, due to the most stringent normal operation conditions faced by the divertor, the inlet parameters of the PFC cooling systems are assumed within the range highlighted below, provided that the verification of their performance under both transient and steady–state heat loads satisfies the limiter requirements.

- $T_{in,PFC}$ = 70 - 140 °C
- $P_{in,PFC}$ = 5.0 - 6.5 MPa

As far as the SB is concerned, the working temperature of EUROFER should ensure sufficient ductile behaviour under neutron irradiation during both operation and maintenance. Therefore, Pressurized Water Reactors (PWR) cooling conditions listed below help EUROFER work within good safety margins against embrittlement, over a temperature range where the DBTT is mainly independent from damage (dpa). This also makes the extension of the SB lifetime and its re–use after annealing possible.

- $T_{in,SB}$ = 280 - 295 °C
- $P_{in,SB}$ = 14.0 - 16.0 MPa

The author bases the UL first design point on the inlet cooling parameters in Table 6.1.

Component	T_{in} [°C]	P_{in} [MPa]	$\langle v \rangle$ [m s^{-1}]
PFC	130	5	$\approx$ 12 (imposed - §6.2)
SB	295	15.5	$\approx$ 3 (calculated - §6.3)

Table 6.1: Inlet temperature and pressure values of the PFC and SB cooling systems.

6.1.2 Nuclear heating

The 14 MeV–peaked energy distribution neutrons escape from the magnetic confinement and any Coulombian action among charged particles, hence directly interacting with the lattice nuclei of the surrounding structure. As a result of these interactions, nuclei can be either scattered or sputtered from their original locations (dpa) or absorbed by transmutating the original nuclei into unstable radioactive isotopes, which releases the excess of energy either splitting into lighter nuclei or emitting gammas. The design of IVCs must be carried out by reducing the level of neutron irradiation to the most critical components like VV and magnets to a minimum, to limit the degradation of their structural performance, since those components are not meant to be replaced during the DEMO lifetime [129].

The main factors enhancing the shielding function are the radial distance from the plasma and the material composition of the component the neutrons interact with. It is known that water is a good moderator for neutrons, whose interaction can very effectively slow down energetic neutrons due to the comparable mass between H nuclei and neutrons. Slowing down the neutrons

is important because low energy neutrons have significantly higher absorption cross sections for steels compared to the fast ones. On the other hand, due to their higher mass nuclei, steels can either absorb or inelastically scatter the neutrons but are less efficient at slowing them down. Therefore, a trade–off between steel–water composition exists for enhancing the SB shielding performance. As far as the neutron–induced nuclear loads are concerned, requirements on the IVC design are imposed, which translate in the toroidal field coils (TFCs) and VV design limits summarized in Table 6.2.

	Nuclear heating	**dpa**
TFC	50 W m^{-3}	–
VV	–	2.75 dpa/reactor lifetime

Table 6.2: TFCs and VV design upper limits for relevant nuclear loads [129].

The UL geometry is relatively simplistic at this stage, as the resulting nuclear loads, in turn, aid the definition of the UL design, which will be upgraded iteratively. Fig. 6.5 shows the UL geometry on the lhs and the related nuclear heating distribution on the rhs. The current one consists of three layered PFC, a single homogenised layer for the SB, a 3 cm gap, and an additional homogenised shielding layer referred to as port plug, located behind the SB.

The material composition of these components is indicated in Table 6.3. Three different concepts of SB with different volumetric percentages of water and steel are studied. The first concept involves a "box" design of the SB, foreseeing a EUROFER box filled with water, as opposed to the "plate" design whose shield consists of EUROFER plates cooled with water channels. This last concept is analysed by considering two different water densities (Cases (b) and (c) in Table 6.3). This reflect the choice of using two separate cooling systems, and, hence, two different coolant parameters, between PFC and SB (Case (c) in Table 6.3), since the probability of neutron–atom interaction depends on the target volumetric particle density, which is affected by the temperature. This preliminary stage is aimed at providing a first sketch of the UL limiter design baseline, which will go through an iterative work and upgrade, if needed.

To test and compare the performance of the three different UL SB options, the monitored parameters are the nuclear heating across the UL as a function of position (see Fig. 6.6), and the toroidal field coil nuclear heating and the VV dpa (see Fig. 6.7). Among the three SB concepts, the Case b) and c) show lower volumetric power deposited by neutrons compared to

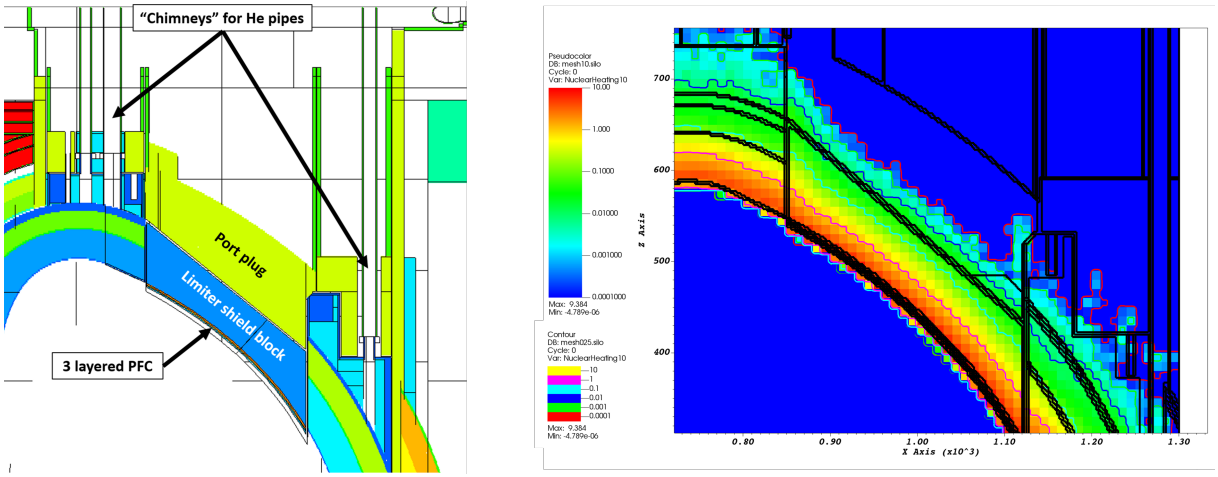

Fig. 6.5: Lhs: Simplified model used for neutronic calculations. Rhs: Volumetric power distribution across the UL [130].

Layer	Material composition (%vol)
PFC1–W armour	100% W
PFC2–tube	39.5% W, 17% CuCrZr, 13.5% Cu, 30% H_2O
PFC3–W layer	39.5% EUROFER, 21% W, void
Case a: SB *box*	53% EUROFER, 47% H_2O ($\rho_{150°C}$=920 kg m^{-3})
Case b: SB *plate*	87.5% EUROFER, 7.4% H_2O ($\rho_{150°C}$=920 kg m^{-3}), void
Case c: SB *alter plate*	87.5% EUROFER, 7.4% H_2O ($\rho_{315°C}$=700 kg m^{-3}), void
Port plug	60% SS316L(N)-IG, 40% H2O ($\rho_{150°C}$=920 kg m^{-3})

Table 6.3: Material composition of the UL neutronic models [130].

Case a), whereas all the three configurations have comparable shielding performances towards TFC and VV. Fig. 6.7 shows that HF_{max}=20 W m^{-3} on magnets, whereas the maximum dpa value over 6FPY experienced by the VV is well below its design limit in Table 6.2.

The integrated power deposited in both PFC and SB is reported in Table 6.4, which drives the design of the cooling system layout and the estimate of the related thermal-hydraulic parameters.

	Total deposited power
PFC	3.90 MW
SB	4.50 MW

Table 6.4: Integrated power deposited by neutrons on limiter sub–components [130].

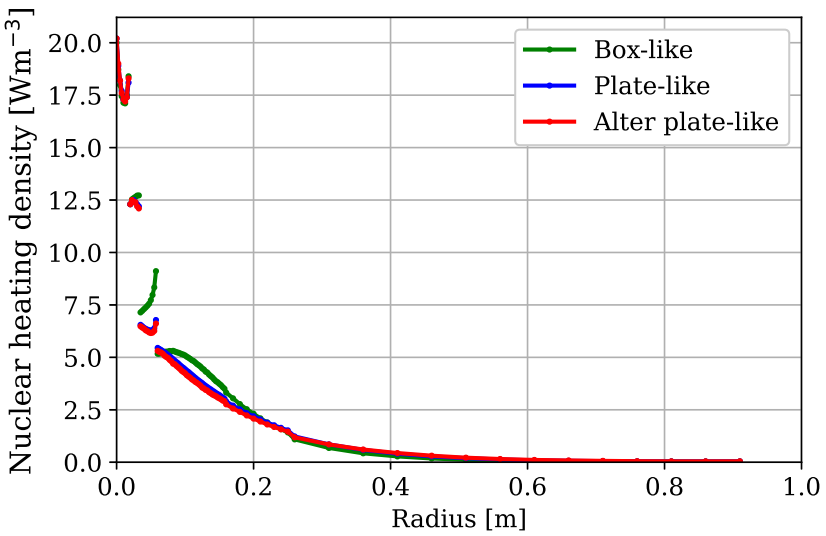

Fig. 6.6: Average radial distribution of the power deposited by neutrons (nuclear heating) under neutron fluence for different volume concentration of steel/water. The chosen configuration is the option c) with a 7%water-3%AlO_2-9%EUROFER SB and two separate cooling system between PFC and SB [130].

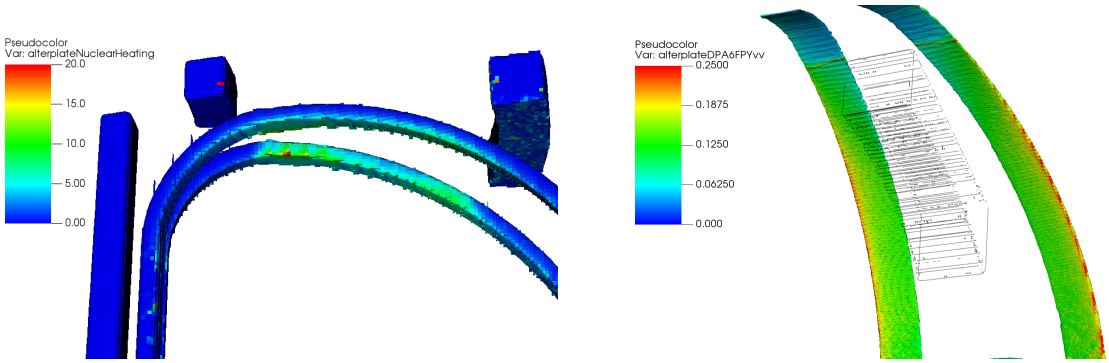

(a) Neutronic volumetric power density [W m^{-3}] on toroidal field coils behind the UL.

(b) VV dpa [dpa/6FPY] reached after 6 Full Power Years calculated by using the SB "alter–plate" concept.

Fig. 6.7: Fulfilment of neutronic load constraints in magnets and VV. Although the results are here shown only for the SB "alter–plate" concept, the outcome is valid for the three analysed SB concepts [130].

6.2 UL PFC design under disruptive heat loads

3D–TARTIFL&TTE is used to study the behaviour of EU–DEMO divertor W monoblocks [131] with different armour thickness L – highlighted in Fig. 6.8 – under a heat load history typical of a UVDE. The foreseen heat sink is water flowing within CuCrZr pipes, thermally coupled with the W monoblock by a Cu interlayer.

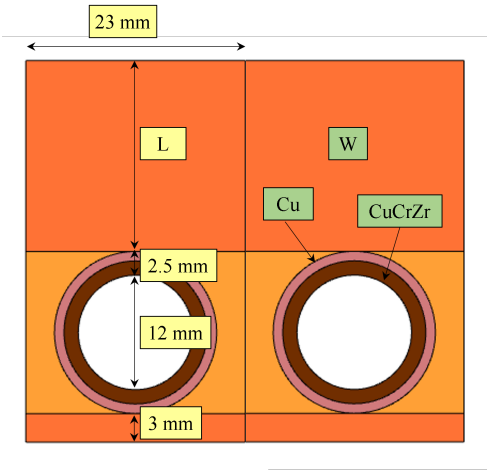

Fig. 6.8: 3D monoblock model used in the present work. It consists of W armour, CuCrZr pipe (D_{in}=0.012 m) and a 1 mm Cu inter–layer (D_{out}=0.017 m).

Starting from the thermal equilibrium reached during normal operation (SOF, see Table 6.5), the monoblock experiences a sudden increase in heat flux following a VDE. Hence, the heat flux goes up to 64 GW m^{-2} during the TQ phase, then decreases to 2.5 MW m^{-2} during the CQ in the following 200 ms, in line with what is foreseen for a UVDE in [31].

Table 6.5 lists the complete set of values of loads and boundary conditions used for the present work.

	Loads and BCs during UVDE		
	SOF	**TQ**	**CQ**
Δt [ms]	2.0E+04 [ms][1]	Δt=4E+00 [ms]	Δt=2E+02 [ms]
$HF_{SOF,TQ,CQ}$ [MWm^{-2}]	8.0E-01	6.4E+04	2.5E+00
$T_{bulk,water}$ [°C]/P [MPa]	138/5		
HTC	5.7E+04 (see Table 6.6)		
T_{rad} [°C]	500		
Volumetric power [MWm^{-3}]	Radial profile in Fig. 6.6: 20 (max) – 8 (min)		

[1] time to reach the thermal equilibrium.

Table 6.5: Loads and boundary conditions used for the W monoblock thermal transient study under UVDE.

Considerations based on energy conservation principle allow the estimate of the bulk temperature of the coolant (water) and its HTC to be fed back into the convective boundary conditions applied at the inner surface of the pipes. The total power deposited by both neutrons and

alpha particles on the PFC is 5.4 MW. By assuming this is uniformly deposited into the 64 units, this translates into 0.084 MW per PFC unit. The mass flow rate required by every PFC unit to remove it is estimated by imposing a maximum fluid velocity of 12 m s^{-1}, once the geometry is fixed (see Fig. 6.8). The mass flow rate required by every PFC unit is calculated as $\dot{m} = \rho(T_{ave})vA = 1.3$ kg m^{-2} s^{-1}, where $T_{ave} = \frac{T_{in}+T_{out}}{2}$. The HTC is derived from the dimensionless numbers reported in Table 6.6. Having imposed the cross–section area of the pipes and the fluid velocity (§6.1.1, Table 6.1), it follows that $T_{out} = 146°C$ and, hence, $\Delta T = T_{out} - T_{in} = 16°C$.

Re	Pr	Nu	HTC [$Wm^{-2}K^{-1}$]
6.4E+05	9.0E-01	1.1E+03	5.7E+04

Table 6.6: PFC thermal–hydraulic parameters.

An estimate of the PFC cooling system total pressure loss is obtained by summing up the distributed (Darcy–Weisbach, ΔP_{DW}) and localized pressure drops (ΔP_{loc}) as in Eq. 6.1 [132]. The Haaland equation (Eq. 6.2) is used for estimating the Darcy friction factor (f_D) affecting the distributed pressure losses, whereas the values of the coefficient k_{loc} determining the local pressure losses and depending on the nature of local resistances (change in curvature, inlets, outlets) are taken from [132]. For the pipe's inner surface roughness (ε), a typical value for steel pipes is assumed. Its value is reported in Table 6.7, which collects all the relevant calculated parameters.

$$\Delta P_{DW} = f_D L \frac{\rho}{2} \frac{\langle v \rangle^2}{D} + k_{loc} \frac{\rho \langle v \rangle^2}{2} \tag{6.1}$$

$$\frac{1}{\sqrt{f_D}} = -1.8 \log \left[\left(\frac{\varepsilon/D}{3.7} \right)^{1.11} + \frac{6.9}{Re} \right] \tag{6.2}$$

ε [m]	f_D	L [m]	ΔP_{DW} [MPa]	ΔP_{loc} [MPa]	ΔP [MPa]
5.0E-06	1.6E-02	4.5	4.3E-01	0.2E+00	6.3E-01

Table 6.7: PFC cooling system pressure loss parameters.

The inlet and outlet feeding pipe's cross–sections have an internal diameter of 0.01 m, cal-

culated by imposing $v_{in} = 8$ m s^{-1}. Inlet and outlet manifolds of the PFC cooling system are sized by increasing the sum of the cross–section areas of every PFC unit pipe departing from it by 50% (see Eq. 6.3). The PFC manifolds have an internal diameter equal to 0.15 m.

$$D_{manifold} = \sqrt{\left(\sum_i A_i + 0.5 \sum_i A_i\right) \cdot \frac{4}{\pi}} \tag{6.3}$$

The power radiated by the PFC towards an ambient at 500°C is estimated by considering that the limiter is in view of the BB segments, whose surface temperature should not exceed 500°C [34]. Nuclear heating in §6.1.2 is also imposed as volumetric power generation across the W monoblock.

As far as the material properties are concerned, temperature–dependent values for ρ, c_p, k, and ε used throughout the work are taken from [116].

Four values of armour thickness are spanned: 8 mm, 10 mm, 15 mm, and 20 mm. The results are reported in Table 6.8 in terms of maximum surface temperature, melting depth and recession of the loaded surface, together with temperature and heat flux values computed at the inner surface of the pipe. Fig. 6.9 shows the time evolution of the temperature at the plasma–facing surface, and the related melt interface position during the transient, whereas Fig. 6.10 reports the time evolution of the temperature monitored at the inner pipe wall before and after the UVDE. Although the CQ is meant to last 200 ms, the runs are stopped only after the thermal equilibrium is reached under CQ–induced heat flux. The parameters at the inner surface of the pipe are the ones to be monitored for understanding if the temperature increase experienced by the pipe is high enough to enhance onset of nucleate boiling or, equivalently, departure from nucleate boiling. The temperature limit is driven by the saturation temperature at the lowest value of the operational coolant pressure, which can be predicted through the Bergles–Rohsenow correlation [133], but it is in this case close to $T_{sat}(5\text{ MPa}) = 264$°C. The heat flux should be limited to its critical heat flux value calculated at the inner wall of the pipe (CHF_w), which is estimated by using the Tong-75 correlation [134] in Eq. 6.4.

$$CHF_w = 0.23 f\dot{m} H_v \left(1 + 0.00216 \left(\frac{P}{P_{crit}}\right)^{1.8} Re^{0.5} Ja\right) C_f \tag{6.4}$$

Eq. 6.4 is used for the water–cooled ITER divertor design, and directly correlates the CHF at

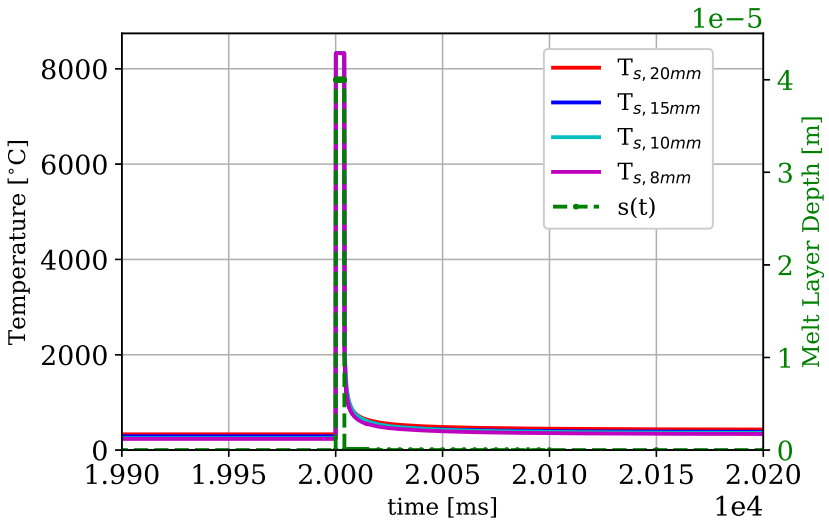

Fig. 6.9: Time evolution of the surface temperature and the melt interface under the heat load history foreseen during Upward VDEs.

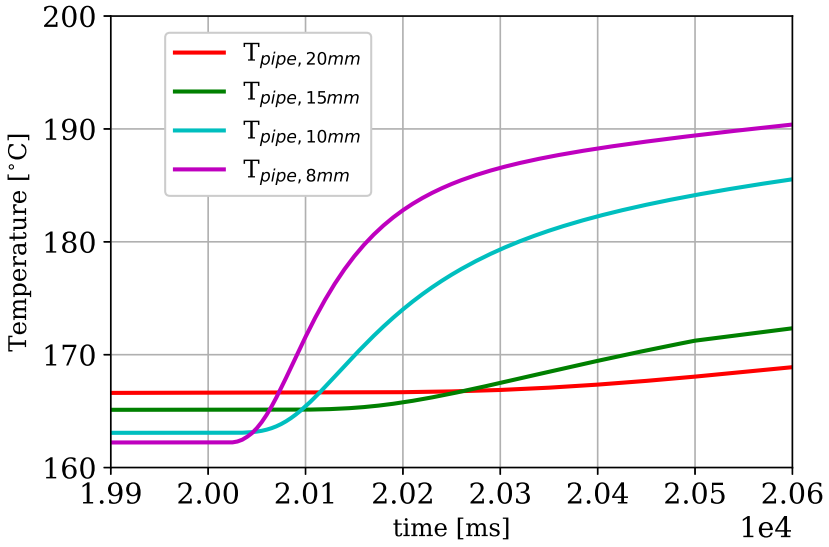

Fig. 6.10: Time evolution of the inner pipe wall temperature under the heat load history foreseen during Upward VDEs.

the wall of smooth pipes to the mass flow rate $\dot{m}$, Reynolds number, coolant pressure compared to its critical value ($P_{crit} = 22.1$ MPa), latent heat of vaporization (H_v), and Jakob number (Eq. 6.5), through a friction factor f (Eq. 6.6) depending on the ratio between the hydraulic diameter (d_h) and a reference diameter ($d_0 = 12.7 \cdot 10^{-3}$ m [134]), and the C_f factor accounting

for channel configuration and dimension. For smooth channels, $C_f \approx 1.2$.

$$Ja = \frac{\rho_l}{\rho_v}\left(\frac{c_p(T_{sat} - T)}{H_V}\right) \tag{6.5}$$

$$f = 8Re^{-0.6}\left(\frac{d_h}{d_0}\right)^{0.32} \tag{6.6}$$

By using a first estimate of the coolant outlet pressure value (P = 4.3 MPa) and an average coolant bulk temperature (T_{ave} = 138°C) for computing the Ja number, the resulting critical heat flux at the inner surface of the smooth pipes results to be $CHF_w \approx 27$ MW m^{-2}.

		Armour Thickness (L)			
		8 [mm]	**10 [mm]**	**15 [mm]**	**20 [mm]**
Monoblock Surface	$\mathbf{T_{SOF}}$[°C]	235	250	289	331
	$\mathbf{T_{TQ}}$[°C]	∼8300	∼8300	∼8300	∼8300
	$\mathbf{T_{CQ}}$[°C]	328	351	390	432
	Melt layer [mm]	∼0.04			
	Deformation [mm]	∼2.5			
Inner Pipe Surface	$\mathbf{T_{max,SOF}}$[°C]	∼162	∼163	∼165	∼167
	$\mathbf{T_{max,TQ}}$[°C]	162	163	165	167
	$\mathbf{T_{max,CQ}}$ [°C]	181	173	167	167
	$\mathbf{HF_{max,CQ}}$ [MW m^{-2}]	∼2.5	∼2	∼1.6	∼1.6

Table 6.8: Armour thickness parametric thermal transient analysis results.

As far as the 3D–TARTIFL&TTE application to a 3D W monoblock is concerned, the results in Table 6.8 show that during the transient event only the refractory armour withstands the plasma impact by means of its thermal inertia. During normal operation, the W monoblock experiences a surface temperature below 350°C, which increases up to ≈8300°C during the TQ phase, no matter how thick the armour is, provided that there is enough material to withstand the heat wave. The sudden rise of the TQ thermal load leads the armour to instantaneously melt and intensively vaporize. Due to the short duration of the TQ, the intense vaporization prevents the molten layer from expanding further against the solid domain, by immediately reaching its "steady–state" value. The phase change lasts for the entire duration of the TQ, after which

the melt layer solidifies under the deformed configuration left by the vapour removal. The boiling temperature at the front face of the monoblock is not constrained to any value, since it depends on the saturation pressure and on the evaporative heat flux leaving the surface, as explained in Ch 4. The same sharp and sudden temperature increase is experienced by the armour at the beginning and at the end of the TQ phase, and only under the CQ thermal loading the temperature of the inner surface of the pipe starts increasing, respectively, ≈300 ms and ≈50 ms after the TQ extinguishes with a 15 mm-and-20 mm-thick and 8 mm-and-10 mm-thick armours.

The coolant is not simulated as a domain but it is instead replaced by a convective condition imposed at the inner surface of the pipe walls, whose temperature is not affected by such a disruptive event until the disruption is actually extinguished. However, data in Table 6.8 shows that the thinner the armour thickness, the higher the temperature at the inner surface of the pipe, where both maximum temperature and incoming heat flux are monitored.

Although both temperature and heat flux at the inner wall of the pipe are well below their critical values, applications with the worst values of outlet coolant pressure and temperature must verify that this condition is never reached for the whole duration of the transient event. Therefore, among the investigated thicknesses, so far the first conservative choice of the armour "space reservation" is 20 mm for facing such transients, to be checked under pressure and temperature values calculated at the cooling system outlet.

6.3 UL SB conceptual design under EM loads

During a VDE, the plasma current decay induces both toroidal and poloidal eddy currents in conducting structure and halo currents flowing between the plasma and the grounded structures. The magnitude and distribution of these currents depend on VV and IVCs designs, electrical connectivity, and plasma conditions (e.g. halo temperature and width), which are difficult to quantify. Such events produce a structural response highly depending on the relative time constants of the conducting components, and plasma motion and current decay times. Disruption–induced electro–magnetic loads are therefore design–driving for IVCs, meaning that the design details (i.e. geometry, electrical connections, attachment system) affect the electro-

magnetic loads acting on it, which, in turn, are affected by the dynamic mechanical response of the system. Both VV and IVCs must withstand load combination due to gravity, internal and external pressure, temperature gradient, earthquakes, and plasma disruptions, which produce a complex loading pattern with multiple force peaks. These load patterns are not always easy to identify.

The limiter SB design is mainly driven by electro–magnetic (EM) loads acting on it during disruptive events, when the time variation of $\vec{B}_\vartheta$ induces eddy currents in the conductive structures trying to oppose this variation. The interaction between these currents and the static $\vec{B}_\varphi$ can generate large EM loads. Fig. 6.11 sketches the EM forces and moments acting on a metallic structure generated by eddy currents induced by magnetic field time variations. The magnitude of the Lorentz forces ($\vec{I} \times \vec{B}$) can be reduced by cutting down the eddy current paths, since the static $\vec{B}$ is given. To reduce the magnitude of the Lorentz forces acting on the ferromagnetic

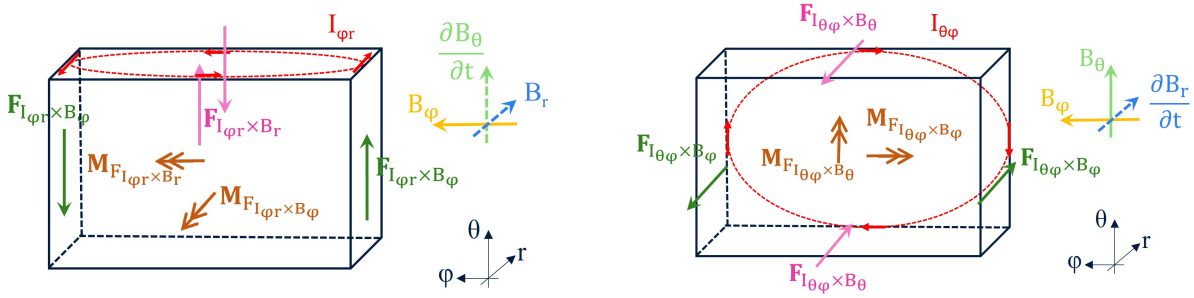

(a) Variation of B_ϑ.

(b) Variation of B_r.

Fig. 6.11: Sketch of the eddy current loop and EM loads acting on a conductive structure due to the time variation of the magnetic field. The total moments the structure undergoes are highlighted in orange.

SB, the proposed SB design is composed of 32 poloidally–oriented 0.05 m–thick EUROFER97 plates, electrically insulated by a 1 mm–thick gap filled with an electrical insulator (like Al_2O_3), which is going to radially extend for almost the entire depth of the limiter. In addition to it, the strong magnetic field magnetizes the structures made of EUROFER97, withstanding ferromagnetic forces acting on it during all the operational scenarios. Those ferromagnetic effects must also be accounted for.

At the back, the plates are bonded for creating a stiffer back–supporting structure on which designing the attachment system to the VV. Every plate is actively water–cooled by coils running in parallel, and having common inlet and outlet manifolds, which are embedded in the SB. The

PFC assembly is fastened to the front of each plate by joints which are not part of the present study and for which the same solution adopted for the divertor system is considered (see Fig. 6.12) [131].

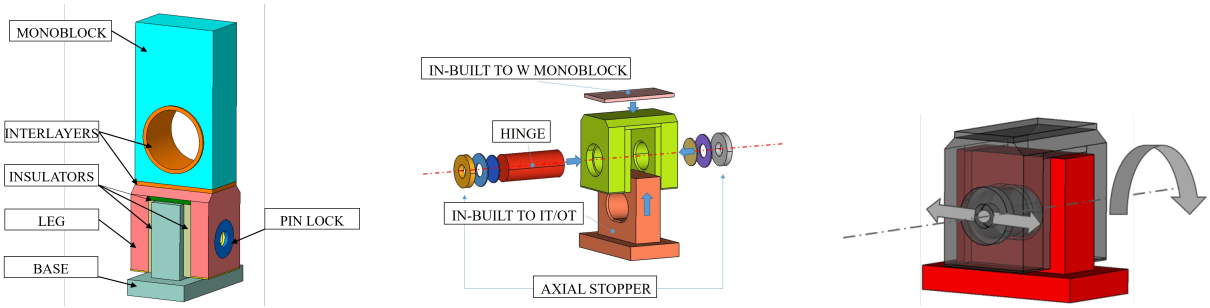

(a) PFC–SB attachment. (b) Exploded view. (c) Degrees of freedom.

Fig. 6.12: W monoblock attachment system and its degrees of freedom [131].

The SB–VV attachment system is required to accomplish the following functions:

- Holding the limiter against its dead weight;
- Reliably reacting against EM forces and moments;
- Allowing the limiter to thermally expand;
- Easy to assemble and to dismantle in the maintenance facility;
- No interference with the SB central feeding pipes.

A preliminary EM study in [135] estimated Lorentz and ferromagnetic loads acting on a simplified UL geometry (sketched as an empty box) under UVDE, whose peak values of forces (F) and moments (M) acting along each direction are listed in Table 6.9. These values are taken as first design point and drive the design of the UL attachment system to the VV.

F_x [MN]	F_y [MN]	F_z [MN]	M_x [MNm]	M_y [MNm]	M_z [MNm]
-3.2	0.2	-1.2	-1.1	0.125	1.1

Table 6.9: Peak values of EM forces and moments acting on the UL during a UVDE.

The attachment system proposed by the author is based on pin connections at the four corners of the SB back–supporting structure. In its simple sketch, a single attachment point foresees a pin reacting to loads that act perpendicularly to its axis, and supported by lugs with

circular holes through which the pin is inserted. The increased distance between each connection point minimizes the reaction force magnitude due to EM moments. The bottom SB lugs foresee a slotted hole allowing the limiter to freely expand poloidally without additional constraints. In fact, considering that the limiter goes from 40° to its averaged operating temperature 350° (from Fig. 6.18), the poloidal thermal expansion is bigger than the toroidal one ($L_{\vartheta,0} \approx 3.5$ m, $L_{\varphi,0} \approx 1.48$ m) and, hence, $\Delta L_{\varphi} << \Delta L_{\vartheta}$. Considering the thermal expansion coefficient for EUROFER to be $\alpha = 1.175\text{E}{-5}\ ^{\circ}\text{C}^{-1}$, the toroidal and poloidal elongations are calculated below.

$$\Delta L_{\varphi} = L_{\varphi,0}\alpha\Delta T \approx 0.006 \text{ m} \tag{6.7}$$

$$\Delta L_{\vartheta} = L_{\vartheta,0}\alpha\Delta T \approx 0.01 \text{ m} \tag{6.8}$$

A detailed view of the SB attachment system is reported in Fig. 6.13, with particular focus on the upper SB lugs in Fig. 6.13a and on the slotted holes in Fig. 6.13b. For such an attachment

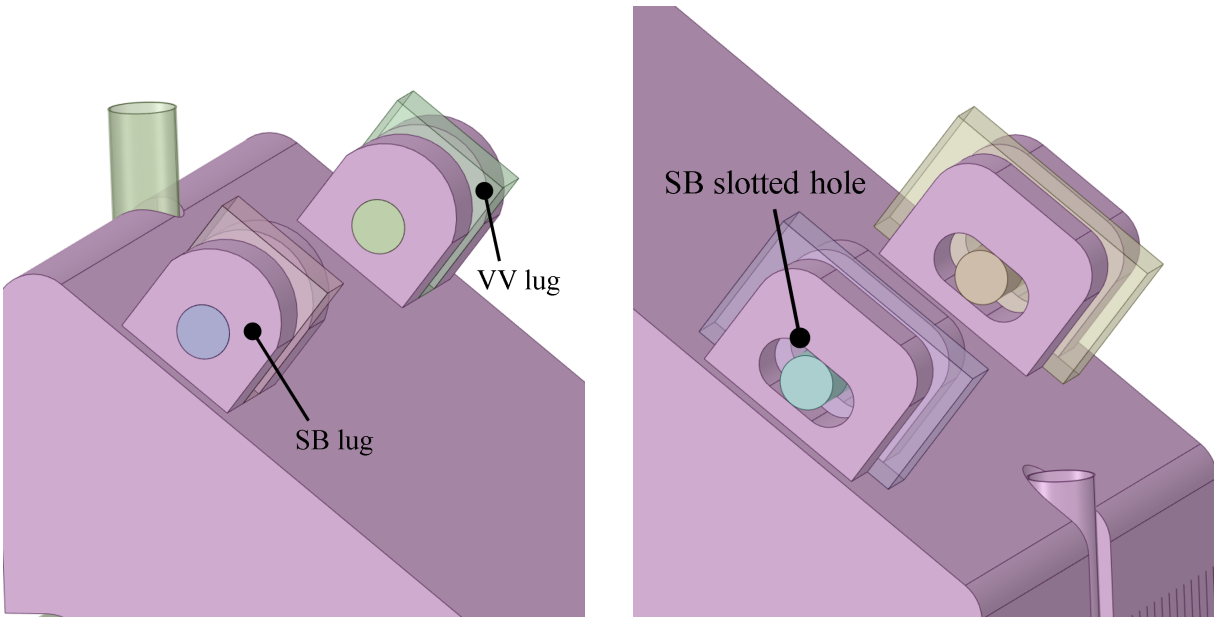

(a) SB upper pin connections. (b) SB lower slotted hole pin connections.

Fig. 6.13: Particular of the SB attachment system.

system layout, the breakdown of concentrated forces and moments is highlighted in the drawn load path in Fig. 6.14, whose expected reacting components are identified in Table 6.10.

The concentrated forces in Fig. 6.14 are estimated as follows, by assuming the attachment points are distant $L_{\varphi} = 1.08$ m toroidally and $L_{\vartheta} = 2.65$ m poloidally, respectively. F_{xy}, F_{yz},

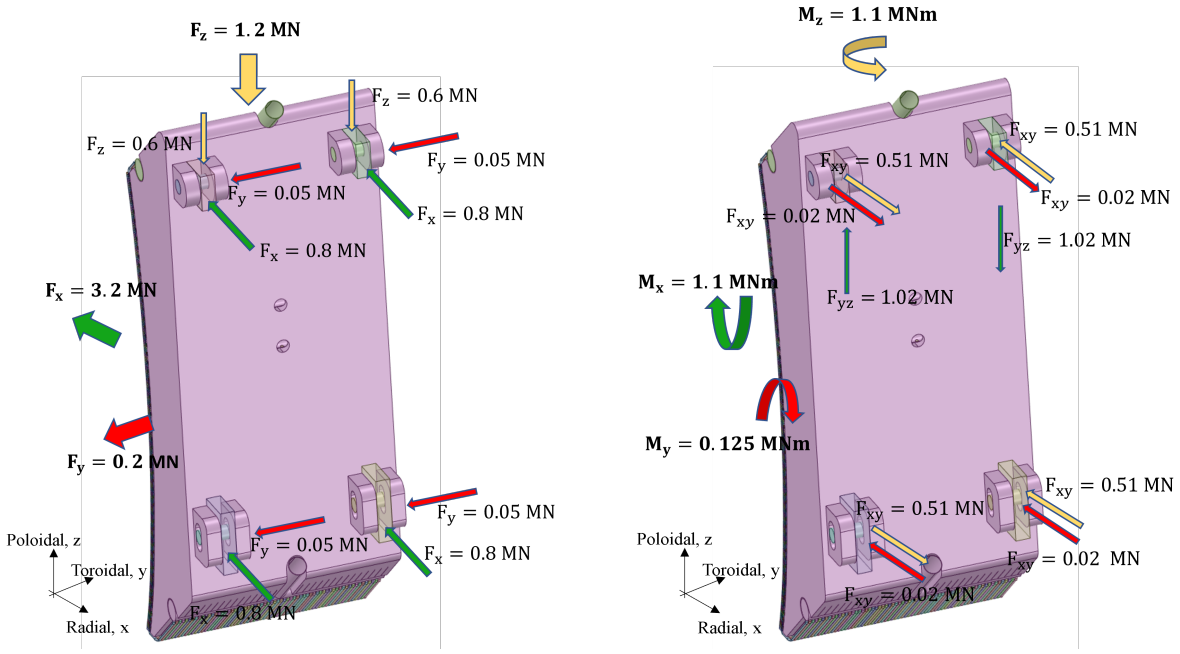

(a) Superposition of EM forces.

(b) Superposition of EM moments.

Fig. 6.14: EM load path for the limiter SB – VV attachment design.

	Expected reaction forces			
	Pin_{up}	Pin_{down}	$Lugs_{up}$	$Lugs_{down}$
F_x	x	x		
F_y			x	x
F_z	x			
M_x	x		x	x
M_y	x	x		
M_z	x	x		

Table 6.10: Components reacting to the directional EM loads in Fig. 6.14.

and F_{xy} represent the force couples generating the related M_z, M_x, and M_y moments, whereas F_x, F_y, and F_z represent the concentrated forces acting along each direction.

- Moments

$$F_{xy} = \frac{|M_z|}{2 \cdot L_\varphi} = 0.51 \text{ MN} \tag{6.9}$$

$$F_{yz} = \frac{|M_x|}{1 \cdot L_\varphi} = 1.02 \text{ MN} \tag{6.10}$$

$$F_{xy} = \frac{|M_y|}{2 \cdot L_\vartheta} = 0.02 \text{ MN} \tag{6.11}$$

- Forces

$$F_x = \frac{|F_x|}{4} = 0.8 \text{ MN} \tag{6.12}$$

$$F_y = \frac{|F_y|}{4} = 0.05 \text{ MN} \tag{6.13}$$

$$F_z = \frac{|F_z|}{2} = 0.6 \text{ MN} \tag{6.14}$$

The pin works in shear. Therefore, the first design iteration is based on shear and bending stress calculations across its section [136]. From Fig. 6.14, the reference force used for sizing the pins (F_{pin}) is calculated as in Eq. 6.15, which considers both the force and moment contributions along the radial direction.

$$F_{pin} = \frac{|F_x|}{4} + \frac{|M_y|}{2 \cdot L_\vartheta} + \frac{|M_z|}{2 \cdot L_\varphi} = 1.33 \text{ MN} \tag{6.15}$$

Fig. 6.15 highlights the geometrical features of the pinned connection cross–section. Ideally, the pin is screwed to the VV lug, and therefore it can be considered bonded to the central lug. Fig. 6.15c is taken as reference for computing the shear and bending stresses on the pin cross–section. The diameter of the pin is indicated with d, whereas the thickness of the SB and VV lugs are indicated, respectively, as L_1 and L_2. The pin diameter is determined by limiting the maximum

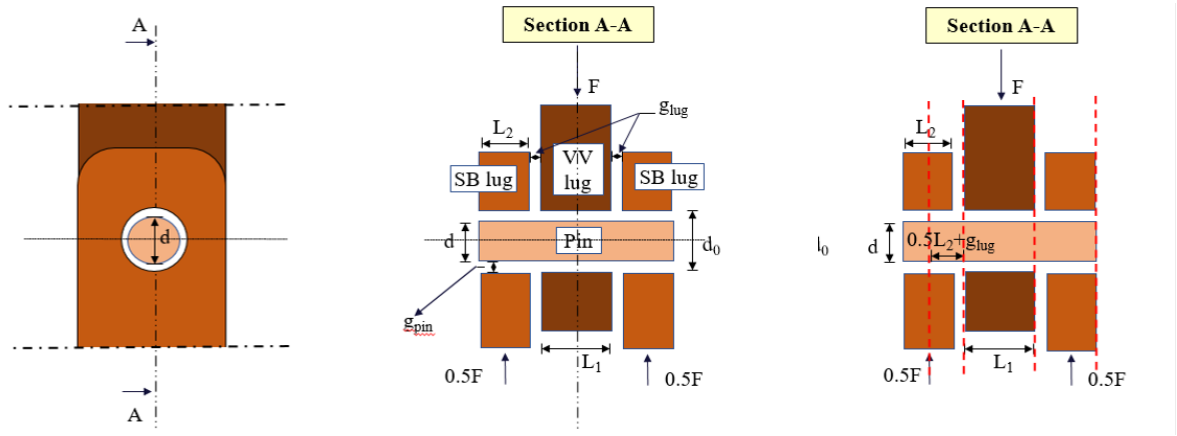

(a) Overview of the pinned connection.

(b) Cross–section of the pinned connection.

(c) Geometrical distances for force and moment balance.

Fig. 6.15: Geometrical features of the pinned constraint.

value of the shear stress (τ_{shear}) on its cross–section to the allowable normal stress S_m (Eq. 6.16),

which is calculated as the lower between the yield stress $\frac{2}{3}S_y$ and the ultimate tensile strength $\frac{1}{3}S_{UTS}$ of the material at the expected temperature. Since the pins are made of EUROFER, its allowable normal stress at T = 350 °C is S_m = 182 MPa, with its related S_{UTS} = 490 MPa [137]. The maximum bending stress value ($\sigma_{bending}$) acting on its cross section is also verified (Eq. 6.17), where $x = 0.5L_2 + g_{lug}$ (Fig. 6.15c). g_{lug} and g_{pin} indicate, respectively, the gaps between pin and hole and between VV and SB lugs.

$$\tau_{shear}[136] = \frac{16}{3}\frac{0.5F}{\pi\, D^2} \leq \tau_{lim} = \frac{S_m}{\sqrt{3}} \Rightarrow D \approx 0.12 \text{ m} \tag{6.16}$$

$$\sigma_{bending}[136] = \frac{32\ 0.5F\ x}{\pi\, D^3} = 254 \text{ MPa} \leq 1.5\ S_m \tag{6.17}$$

For designing the SB lugs, the author follows the guidelines in the "Eurocode 3: Design of steel structures – Part 1-8: Design of joints (EN 1993-1-8)" [138], which also gives recommendations on pinned constraints in presence of slotted holes. The lugs are sized according to Fig. 6.16 – Type B, whereas the design of the lug including the slotted hole is carried according to Fig. 6.17.

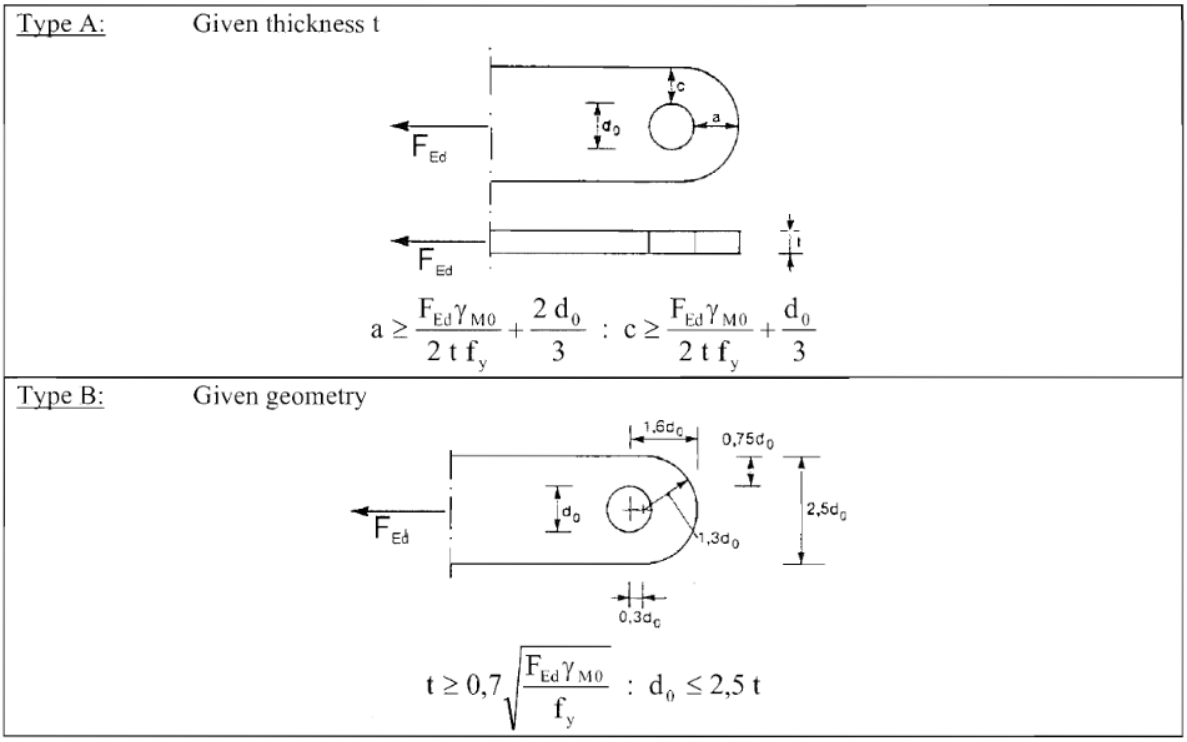

Fig. 6.16: Geometrical requirements for pin ended members – front [138].

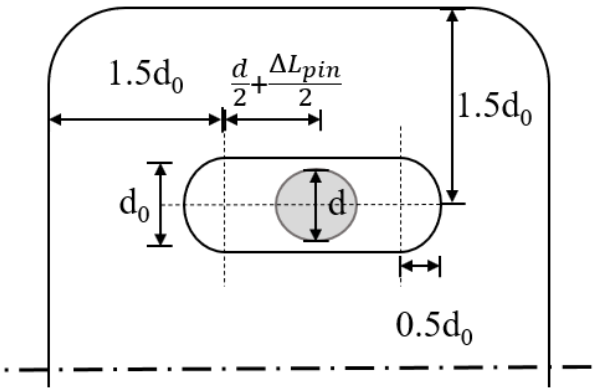

Fig. 6.17: Geometrical requirements adopted for lugs with slotted holes.

Gaps between mechanical parts are defined by taking into account the thermal expansion of the components. The pin radial gap is calculated based on the radial thermal expansion of the pin (Eq. 6.18). Similarly, the gap between SB and VV lugs are about 0.004 m each, calculated by considering an average toroidal distance of L = 1.1 m (see Eq. 6.19).

$$d_0 = d(1 + \alpha\Delta T) = 0.1104 \text{ m} \Rightarrow \frac{d_0 - d}{2} \approx 0.0005 \text{ m} \tag{6.18}$$

$$g_{lug} \approx L \cdot \alpha\Delta T = 0.004 \text{ m} \tag{6.19}$$

The length of the pin is now calculated by summing up the thicknesses of the related plugs. The final values of the attachment system geometrical parameters are summarized in Table 6.11.

d [m]	d_0 [m]	L_{pin} [m]	L_1 [m]	L_2 [m]	g_{pin} [m]	g_{lug} [m]
0.11	0.111	0.3	0.1	0.1	0.1	0.004

Table 6.11: Geometrical parameter values of the attachment system.

The above–mentioned preliminary calculations helps the first draft of the design, whose model can now be used for further analyses and assessment.

The design of the SB internals is described as follows. From Table 6.4, the power density deposited in the SB volume is 4.5 MW. By assuming this is uniformly deposited over the 32 plates, and imposing an inlet and outlet temperatures of, respectively, $T_{in} = 295°C$ and $T_{out} = 328°C$, the calculated mass flow rate needed for cooling down the SB is $\dot{m} \approx 23$ kg m^{-2} s^{-1},

which means $\dot{m} = 0.7$ kg m^{-2} s^{-1} per single plate. By choosing the internal diameter of the cooling coils equal to 0.02 m, the calculated average coolant velocity is equal to v = 3 m s^{-1}. The dimensionless numbers in Table 6.12 give an estimated average of the HTC at the pipe's inner wall, with an average bulk temperature equal to $T_{ave} = \frac{T_{in}+T_{out}}{2} = 312°C$.

Re	Pr	Nu	HTC [W m^{-2} K^{-1}]
5.6E+05	9.0E-01	8.7E+02	2.3E+04

Table 6.12: SB cooling system parameters.

The radial distribution of the coils within every plate is calculated by imposing the "alter plate" nuclear heating radial profile in Fig. 6.6 into a 2D model representative of the plate's cross–section (Fig. 6.18). The cooldown is implemented as convective boundary condition at the pipe's inner wall, by considering the above–calculated constant values of HTC and T_{ave}. Coils are radially spaced for keeping the EUROFER operational temperature within the interval 350°-550°C. The radial distance found in Fig. 6.18 keeps the SB plate average temperature to 350°C.

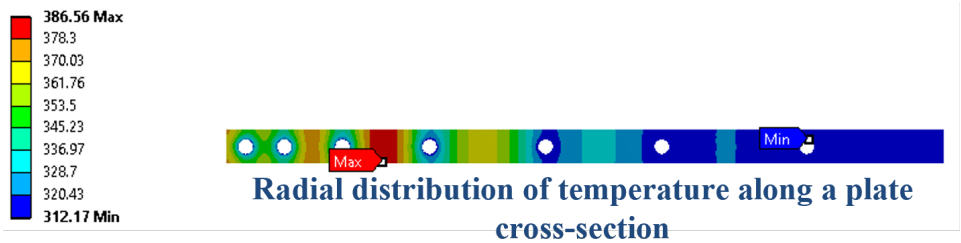

Fig. 6.18: Radial distribution of the cooling coil on a cross–section of a representative plate.

Following the same procedure adopted for the PFC, an estimate of the SB cooling system total pressure loss is calculated according to Eq. 6.1, with a Darcy–Weisbach factor computed through Eq. 6.2. All the SB hydraulic parameters are calculated in Table 6.13.

ε [m]	f_D	L [m]	ΔP_{DW} [MPa]	ΔP_{loc} [MPa]	ΔP [MPa]
5.0E-06	1.6E-02	28	8.3E-02	1.1E-02	9.5E-02

Table 6.13: SB cooling system pressure loss parameters.

The inlet and outlet feeding pipe's cross–sections have an internal diameter of 0.07 m, calculated by imposing $\langle v \rangle_{in} = 8$ m s^{-1}. Inlet and outlet manifolds of the SB are calculated by

following Eq. 6.3. Their calculated internal diameter is 0.09 m.

6.3.1 EM assessment of the sliced SB design concept

The UL integrated design equipped with a sliced SB concept is assessed from the EM standpoint under UVDE triggered by a vertical instability during flat top, which makes the plasma touch the wall and shrink. This is followed by the plasma TQ after 1 s, leading to complete loss of thermal energy in 4 ms. The subsequent slow CQ decreases the I_p to zero in 400 ms (slow UVDE), with halo currents flowing into the halo region around the LCFS. Although the complete assessment is still in progress and will be published in the joint paper [18], the first preliminary results are reported in the following.

The EM assessment primary aim is to prove that the sliced SB design concept works in reducing the magnitude of the EM loads, therefore justifying the benefit of a more complex design. Hence, the UL design concept equipped with a sliced SB is analysed and compared with an equivalent UL design equipped with a full steel box SB. The simplified EM model of a full SB design is adapted to the sliced SB concept through a change in material properties, by increasing the electrical resistivity along the toroidal direction such that no toroidal current path is enhanced.

During TQ, EM loads are due to the plasma toroidal flux increase. Currents are thus mainly induced in the passive structures in the poloidal direction. Given the UL attachment system with electrical connections both on the bottom and on the top of the UL structure, poloidal currents during the TQ mainly flow in the PFC, which is the closest electrical loop to the plasma region. The interaction of these currents with the high toroidal magnetic field produces strong radial and vertical forces. In addition to it, there is a superposition of another current loop generated by the magnetic flux variation due to the plasma upward movement. These loops close toroidally into the structures. During the TQ, both the configurations experience a poloidal current loop going from the upper to the lower manifold of the PFC, and a similar current density distribution in both the SB concepts. The differences in distribution are due to the presence of the slices that force the current to close toroidally in the continuous back–supporting structure of the sliced SB.

EM loads during the CQ are mainly driven by the plasma movement and the decrease of its

toroidal current. The induced currents are thus generated by the variation of the poloidal magnetic flux and they mainly flow through the UL cross–section. These currents loops, interacting with the strong toroidal magnetic field, generate moments mainly about the radial and vertical axes. The current loops during CQ are greatly reduced in the sliced SB since no current can flow toroidally. On the other hand, quite similar current distribution happens during CQ on PFC. Since there is a current loop, couples of vertical and radial forces act on the PFC, generating moment in radial and vertical directions. The time evolution of forces and moments generated in both the integrated UL design with full and sliced SB are shown in Fig. 6.19. Fig. 6.19a and Fig. 6.19b show total forces and moments acting on the UL equipped with a full SB, whereas Fig. 6.19c and Fig. 6.19d refer to the UL equipped with a sliced SB concept.

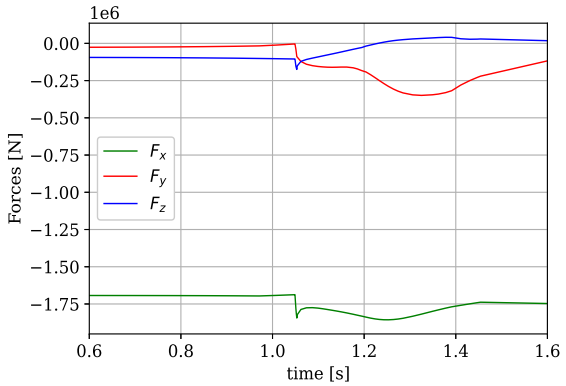

(a) EM forces acting on the UL equipped with a full SB.

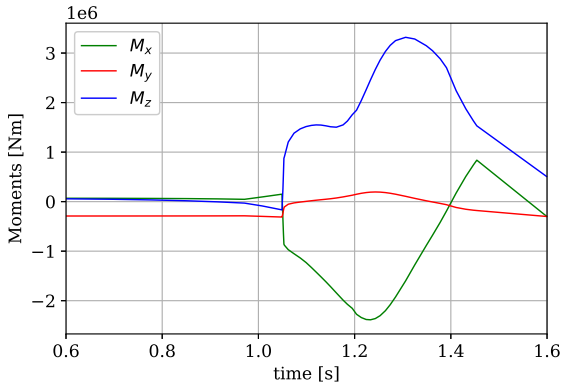

(b) EM moments acting on the UL equipped with a full SB.

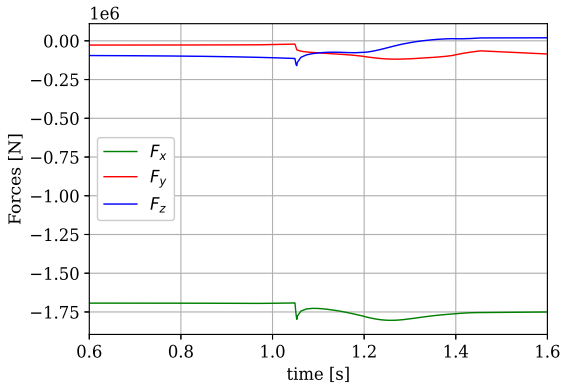

(c) EM forces acting on the UL equipped with a sliced SB.

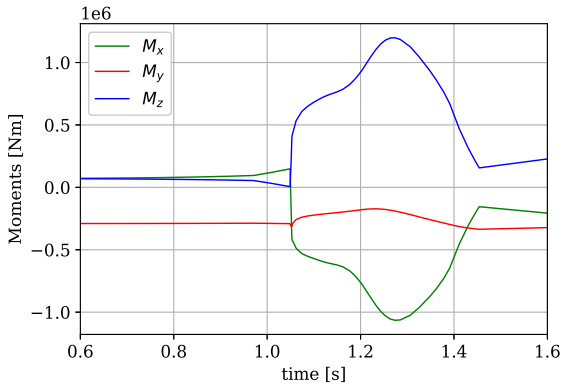

(d) EM moments acting on the UL equipped with a sliced SB.

Fig. 6.19: Lorentz and ferromagnetic forces and moments on UL configurations during a UVDE [139].

Fig. 6.20 gives a summary of the comparison between the two design concepts. During the

TQ, the main load contribution is given by the radial and vertical forces due to the interaction of a net poloidal current with the toroidal magnetic field. Since the sliced SB configuration only introduces minimal effects on the poloidal current path, the forces for both configurations are quite similar. On the other side, moments are low (if compared with that produced during the CQ) due to the lower plasma poloidal flux variation (with respect to the toroidal one). Even if not of particular importance, it is worth noting that moments are higher for the sliced SB configuration. Indeed, the presence of the slices does not allow the toroidal current flow to make bigger loops into the structure. This generates couples of forces responsible of the torque around the vertical and radial axes of the UL.

During the CQ, a general reduction of loads, mainly the moment, is experienced in the sliced configuration. In this time range, the loads are due to poloidal magnetic flux variation, that generates current loops into the SB structures. In sliced SB configuration, the loops are cut due to the presence of the gaps between the slices. This reduces the moment by 50-60%.

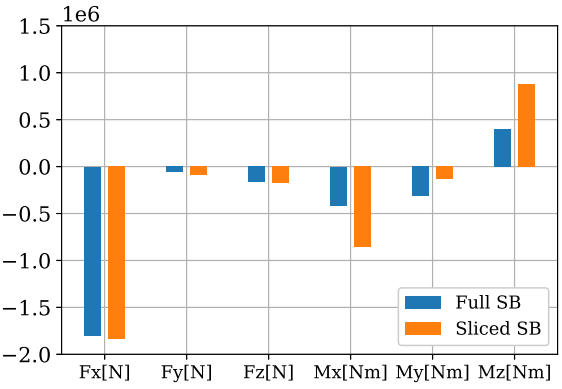

(a) EM loads during TQ phase.

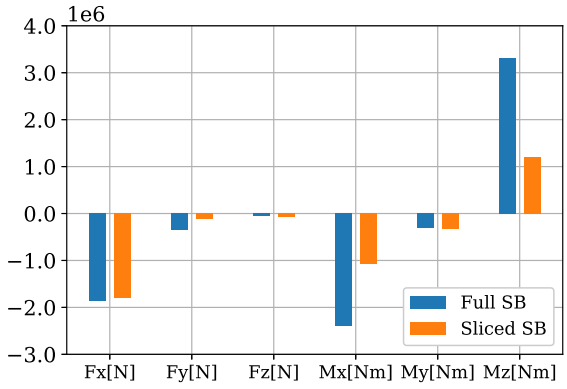

(b) EM loads during CQ phase.

Fig. 6.20: Peak values of force and moment components upper limiter in sliced and full SB configurations [139].

The EM loads in Fig. 6.20a and Fig. 6.20b will be used as input for the UL design and assessment workflow, in order to verifying the structural integrity of the UL design under UVDE.

6.3.2 Considerations on halo current–induced effects on UL

For completeness, the author gives an estimate of the halo current–induced effects in this section, despite the subject complexity due to uncertainties on how to estimate halo current magnitude, paths and related electro–mechanical loads due to their interaction with the static

$\vec{B}_\varphi$. During the UVDE CQ, while the plasma is shrinking and cooling down, a colder resistive region surrounds the plasma core, whose amplitude (w_h) and current distribution (I_h) depends on plasma temperature and density. This is depicted in Fig. 6.23, where the author assumes that the plasma touches the UL and its current goes from the halo region to the UL and then back to the halo region. With all the simplifications highlighted in Fig. 6.23, and neglecting all the 3D effects, the force acting on the UL is calculated as in Eq. 6.20.

$$F_h = L \cdot \vec{I}_h \times \vec{B}_\varphi \tag{6.20}$$

In reality, F_h is not so straightforward to estimate, since it is affected by uncertainties coming from the main variables it depends on, which are mainly related to asymmetries introduced by both the geometry and the plasma physics.

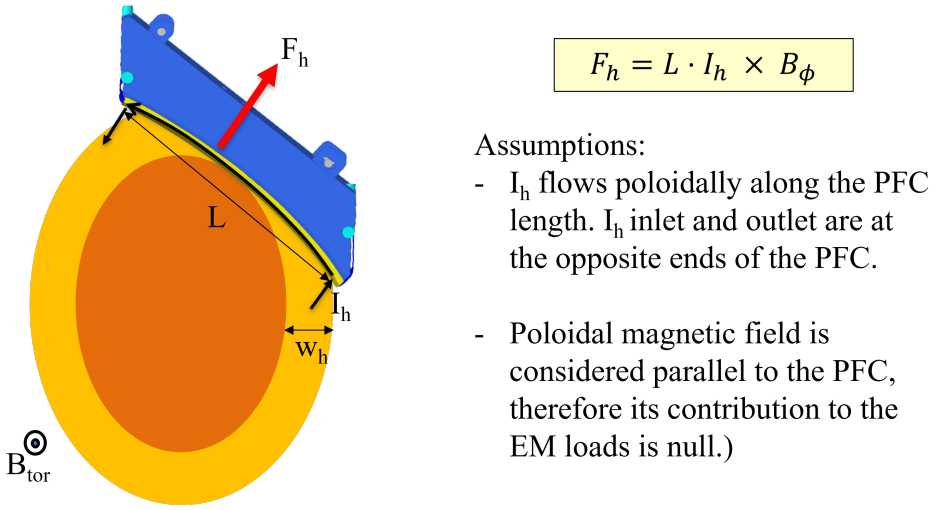

Fig. 6.21: Force estimate due to halo currents.

The first complexity to be introduced comes from the consideration that limiters protect the FW from energy deposition but not from EM effects due to plasma movements, which is also valid for halo currents affecting all the IVCs. Table 6.14 lists the identified scenarios assumed for halo current estimates. Among those, the most realistic one foresees that the halo current spreads among all the IVCs, whose UL contribution is increased through two peaking factors when taking into account their protrusion from the main wall (Π_ϑ), as well as asymmetries in plasma behaviour (Π_φ).

More specifically, F_h can be written as a function of four variables (Eq. 6.21), which are in

Case	Description	#IVC	Comments
1	I_h only distributed among ULs.	8	Unrealistic
2	I_h uniformly distributed among ULs and BB segments.	48	Likely
3	I_h distributed among ULs and segments. I_h increase by Π_ϑ=30% on ULs due to their protrusion.	48	More realistic
4	Same as Case 3. Further increase of I_h on ULs by Π_φ=50% considering toroidal plasma asymmetries.	48	Most realistic

Table 6.14: Analysis of different disruptive scenarios with different assumptions on I_h distribution.

turn affected by uncertainties.

$$F_h = L \cdot \Pi \cdot \vec{I_h} \times \vec{B_\varphi} \tag{6.21}$$

In fact, $L \propto w_h$ depends on plasma temperature and density. The peaking factor Π depends on the plasma being non axisymmetric and other geometric asymmetries introduced by limiters and toroidal cutouts ($\Pi \propto \Pi_\vartheta \cdot \Pi_\varphi$), whereas $I_h \propto I_p$. Therefore, F_h can be more appropriately expressed as the distribution function in Eq. 6.22.

$$\Delta F_h = B_\varphi(\Delta L \cdot \Pi \cdot I_h + L \cdot \Delta\Pi \cdot I_h + L \cdot \Pi \cdot \Delta I_h) \tag{6.22}$$

Fig. 6.22 gives an indication on halo width values with respect to the plasma minor radius. For DEMO, $a/R_{major} \approx 0.15$, $R_{major} = 9$ m, $I_p = 19.1$ MA, $|\vec{B}_\varphi| = 4.89$ T. By choosing three values of w_h/R, i.e. $w_h/R = 0.15$ as the most probable one, as well as $w_h/R = 0.1$ and $w_h/R = 0.2$, the most probable values of F_h are highlighted in magenta in Table 6.15.

	Case 1			Case 2			Case 3			Case 4		
	I_h			I_h			I_h			I_h		
w_h/R	$0.2I_p$	$0.3I_p$	$0.4I_p$	$0.2I_p$	$0.3I_p$	$0.4I_p$	$0.2I_p$	$0.3I_p$	$0.4I_p$	$0.2I_p$	$0.3I_p$	$0.4I_p$
0.1	1.7E+06	2.6E+06	3.4E+06	2.9E+05	4.3E+05	5.7E+05	3.7E+05	5.6E+05	7.4E+05	5.6E+05	8.3E+05	1.1E+06
0.15	4.1E-01	3.8E+06	5.1E+06	4.3E+05	6.4E+05	8.6E+05	3.7E+05	8.3E+05	1.1E+06	8.3E+05	1.3E+06	1.7E+06
0.2	7.2E-01	5.1E+06	6.8E+06	5.7E+05	8.6E+05	1.1E+06	3.7E+05	1.1E+06	1.5E+06	1.1E+06	1.7E+06	2.2E+06

Table 6.15: Most probable values of F_h calculated through Eq. 6.21.

Another uncertainty to the F_h estimate is related to the plasma touching point, which is crucial in estimating the I_h path through the UL. The halo current always tries to close its loop into the plasma, by following the least resistive paths through the structure. Grounded

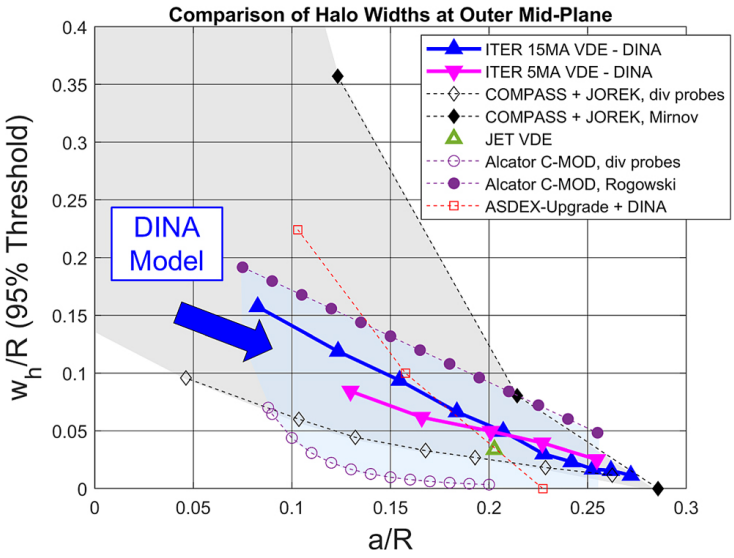

Fig. 6.22: Estimates of w_h as a function of the plasma minor radius, normalized to the major radius of the device. The graph gathers both experimental and computational data [140].

points and electrical connections deeply affect the I_h loop. For the UL, a first guess is assuming that the I_h is spread towards both the grounded VV and the inboard wall where it closes the voltage loop into the plasma itself. A simple sketch is highlighted in Fig. 6.23, whereas Fig. 6.24 highlights three different plasma–limiter touching points and, hence, three different I_h inlet cases into the UL.

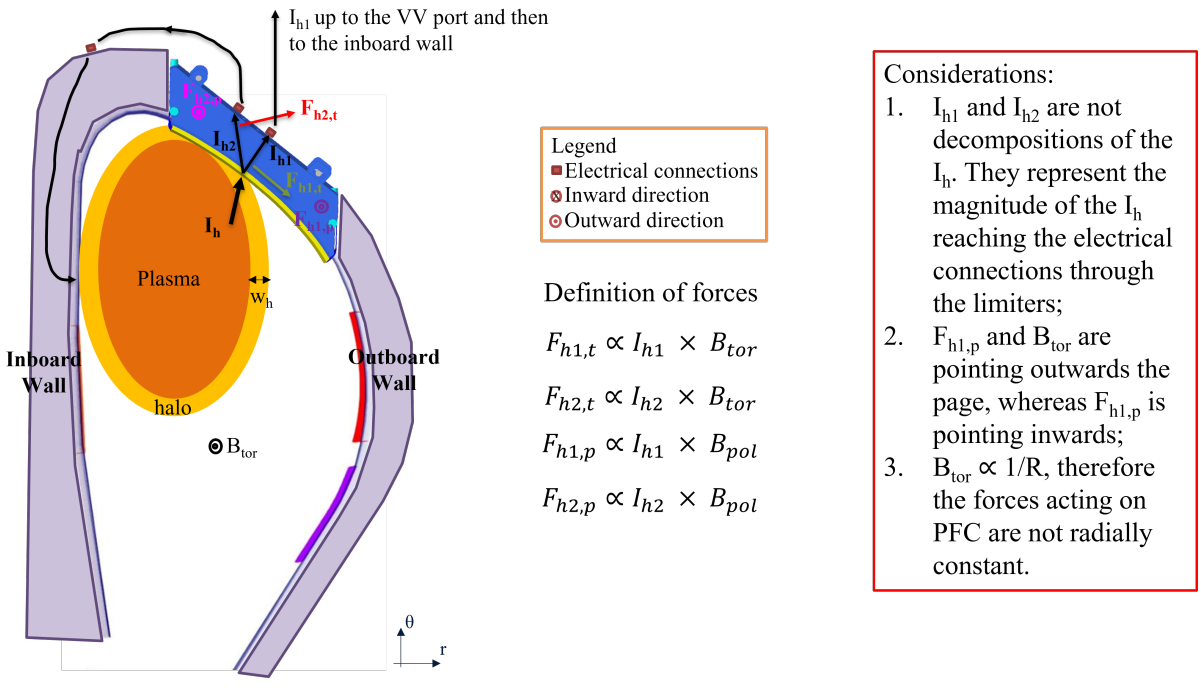

Fig. 6.23: Simplified sketch of the halo current-induced forces on UL.

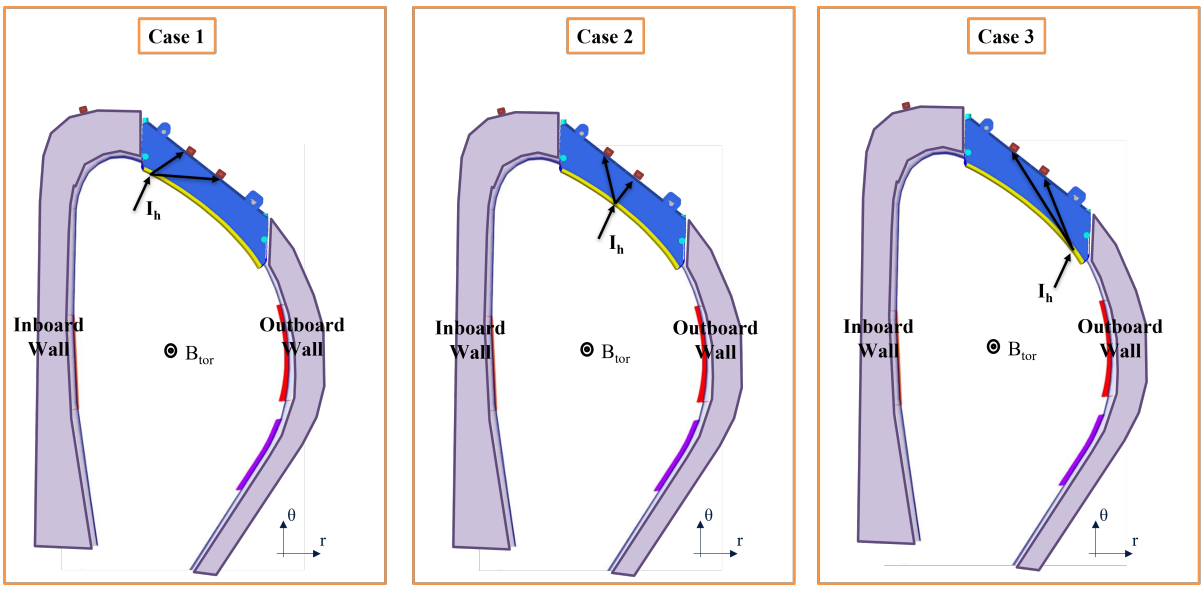

Fig. 6.24: Halo current inlet point cases.

In conclusion, the interactions between halo and the surroundings are very complex to predict, especially by hand calculations. Despite the complexity of predicting paths and plasma–wall interactions within such a complex 3D model, the engineering design of the limiter should always shorten the I_h path in the structure to minimize the related loads. This can be achieved by studying the different effects of electrical connection points between UL and VV. This study will be supported by software EM calculations.

6.4 UL Structural assessment

The structural assessment of the UL supports the conceptual design of the UL component under the simultaneous action of dead weight, EM loads, heat loads, coolant pressure, and nuclear heating, while highlighting the weak design points to be strengthened. It requires a finite element model preparation based on the UL geometry, whose design is driven by hand calculations supported by simplified finite element analyses of the different sub–systems. Furthermore, it also requires the quantification of all the loads acting on a 3D global UL model, which come from a more accurate neutronic analysis calculating the volumetric heat deposited within the UL domain to be used as input for a 3D thermal–hydraulic assessment. The ultimate result will be a 3D temperature mapping used as thermal load on the UL mechanical analyses, which also

collect the EM load contributions and estimate the stress level on the different UL sub–systems.

This assessment has now become part of a broader design activity carried on within the EUROfusion DEMO limiter system, as it requires the synergic cooperation among different domain expertise groups, coordinated by the author. The UL integrated design concept supported by the results from the EM, thermal–hydraulic and thermal–mechanical assessments, will be published in [18].

The finite element model of the integrated UL design concept is in progress. The stress field resulting from the structural assessment will be eventually verified against code and standard integrity rules. In general, components deployed in nuclear devices should comply with essential safety requirements dictated by the hosting country. This compliance is ensured by a set of consistent rules in design assessment and stress analysis considering the safety classification of the component itself, the behaviour of the structural material (EUROFER in this specific case), and the operating conditions inside the nuclear environment. With its harsh neutronic irradiation, DEMO nuclear environment poses new challenges for structural materials, whose performance under any relevant load combination should be verified to prevent failure resulting from specific damage modes over the entire working lifetime.

Currently, the reference design criteria to be used for DEMO are still under development, since they need to address both the effects of neutron irradiation on EUROFER97, CuCrZr and W, as well as specific manufacturing techniques. Therefore, preliminary assessments are performed by following the design criteria of the French RCC–MRx code. It embeds both high temperature operation and irradiated material design rules, integrated with some irradiated EUROFER97 material properties. The RCC–MRx is the upgraded version of the French RCC–MR code developed for high temperature reactors, with the inclusion of the RCC–MX rules for irradiated materials. Besides changes in the mechanical properties, the neutron irradiation–induced creeping and swelling must be considered, either in the form of new design rules or by increasing the safety factors used in calculations.

Following the nuclear industry common practise, the RCC-MRx foresees a classification of the operating conditions, and related loading conditions, into four categories based on the probability of occurrence and the consequence of failure: *Normal*, *Upset*, *Emergency* and *Faulted*. Rules and limits are associated to each category (see Table 6.16). These loading classifications

Loading Category	Category Condition (Damage Limits)	Criteria Level
I. Operational Loading	*Normal*	A
II. Likely Loading	*Upset*	A
III. Unlikely Loading	*Emergency*	C
IV. Extremely Unlikely	*Faulted*	D

Table 6.16: RCC–MRx category conditions and related criteria levels.

are associated with criteria levels used to categorize allowable stress limits against which to compare the stress field resulting from the structural assessment.

Category I and II include all the normal operation loads the component must withstand during its specified service function without any damage requiring repair. Normal category condition includes operational transients like RU and RD, whereas upset category includes incidents of moderate frequency that do not compromise the component functionality (plasma disruptions, operator error, loss of power, control malfunctions).

Category III include accidental events damaging the component with lower probability to occur. The system may need to be shut down to remove the component for inspection or repair.

Category IV include accidental events with the lowest probability to occur, after which the entire system cannot be able to operate again. However, the assessment of the design under this conditions should ensure that the integrity of the safety barriers is retained, even though the system will not be able to operate again.

The assessment under the Level A criteria is the most conservative and comprehensive of all the damage modes, as the allowables used for the criteria level C and D are derived by the criteria level A using lower safety factors. An assessment under Level A criteria will be foreseen for the assessment of the UL global model, based on the following description.

Loads acting on structures can generate different types of internal stresses:

- Primary stresses: any stress field balancing the volumetric forces and the loads applied on the surface and which does not disappear after small permanent deformations (i.e. no evident geometrical deformations nor notable elongation). Primary stresses are due to external and internal coolant pressure, dead weight, EM loads which cause additional volumetric source of primary stresses. These stresses are not self–limiting, but increase as the applied load increases.

- Secondary stresses: stress field that can disappear as a result of small permanent deformations. These stresses are mainly due to inhomogeneous temperature field causing differential deformation in the component. Secondary stresses are therefore self–limiting.

- Peak stresses: increment of stress which is additive to the primary–plus–secondary stresses near local geometrical discontinuities, which can cause crack propagation.

The complex internal stress pattern arising across the thickness of the structure can be linearized into the components highlighted below, regardless of its primary and secondary nature. Within the elastic analysis domain, the design criteria of C&S require the following constituent parts of the breakdown of stresses.

- Membrane stress component: mean value of the total stress along the linearized path.

- Bending stress component: linear component of the total stress along the linearized path and which, when integrated along the supporting line segment, has the same bending moment as the total stress.

- Non–linear component: it is the remainder of the total stress when subtracting the sum of the linear stress components, i.e. bending plus membrane.

Internal stresses cause damage that can ultimately lead to the component failure. Damage modes are attributed to different ways the loads act on the structure, and therefore they are classified in:

- Monotonic damage (P–type), when resulting from the application to a structure of a steadily and regularly increasing loading or a constant loading. Pressure and self–weight loading can cause this damage;

- Cyclic damage (C–type), when resulting from repeated application of loads. Thermally–induced stresses due to pulsed plasma operational mode are related to cyclic damage modes.

However, the failure modes can be affected by in–service environmental conditions, as a result of material property changes under neutron irradiation, coolant impurities and huge temperature gradients.

By assuming an elastic behaviour of the structure, the aim of Level A is to protect the component against the following P–type failure modes:

- Ductile damage modes, relevant for unirradiated materials preserving the original ductility.
  - Immediate plastic collapse and immediate plastic instability are two failure modes caused when the applied primary stress intensity overcomes the yielding of the material. In this case the structure can fail as a result of plastic deformations, which causes the collapse of the structure either because of excessive deformations or necking. The criteria to prevent failure against ductile damage modes limit the primary stresses to the material allowable S_m. They rely on a sufficient amount of material ductility to withstand secondary loads, which are self–limiting and cannot lead to the structure failure.
  - Creep, which is an excessive plastic deformation failure mode similar to the previous ones but occurring at high temperatures. The component must withstand the same loading conditions for a sufficiently long time to deform it over time.
- Non–ductile damage modes, relevant for irradiated (or low ductility) materials with high probability of developing fracture modes with little or no plastic deformations.
  - Immediate plastic flow localization (related to the loss of uniform elongation) and local fracture due to exhaustion of ductility (related to low total elongation) are the two considered failure modes for reduced–ductility materials. In this case, it is necessary to ensure that the strain due to both primary and secondary stresses does not exceed the remaining material elongation. This failure mode is limited by a coefficient depending on S_{UTS}, Temperature, neutron damage and elongation to rupture.
  - Fast fracture, not preceded by any appreciable deformation. It can develop under both constant or cyclic loading conditions as a result of propagation of defects in materials.

For completeness, the C–type damage resulting from a repeated application of the loading condition include:

- Ratcheting, which is an accumulation of increasing progressive inelastic deformations due to the combined action of constant primary loads and a secondary cyclic loading in the plastic regime. The structure changes its original shape, therefore it should be limited. If the structure subjected to cyclic loading experiences permanent deformation, which remain constant after a few cycles, and have no further progressive permanent deformations, elasto–plastic shakedown is achieved.

- Time–independent fatigue, happening if a cyclic load has a sufficiently large number of cycles and amplitude, which cause the material to crack. The crack may grow, eventually leading to fracture. Time–dependent fatigue can happen with sufficiently high temperatures, under which creep deformation may occur during each cycle, accelerating the appearance of cracks by creep–fatigue interaction.

Chapter 7

Conclusions

"I am who I am today because of the choices I made yesterday."

Eleanor Roosevelt

This chapter summarizes the main accomplishments of the research completed by the author and potential future work. The overarching achievement is the development of a design workflow for EU–DEMO limiters under extremely high heat flux. This encompasses the design, thermal modelling (through the development of the TARTIFL&TTE code), and validation by experiment under phase change conditions. The success of the code validation and the promising integrated design of the Upper Limiter proposed by the author, has ensured that the workflow is likely to be used in future limiter design.

7.1 Main research contributions

The development of a design workflow for fusion applications and beyond includes the following author's research contributions.

1. A functional limiter PFC design under relevant plasma scenarios (Ch. 3), which follows the rationale of uniformly spreading the energy deposited by the plasma over as large a surface as possible. The PFC design is then used for heat load estimates through field line tracing codes to confirm the boundary conditions;

2. Integration of the 3D–TARTIFL&TTE code into COMSOL to model the multi–phase

moving boundary problem on a solid armour. The code simulates melting, vaporization, mass removal and re–solidification on 3D geometries subjected to non–uniform heat flux. The code predicts the position of the interface between solid and liquid phases, which drives the predictive position of the cooling system complying with the constraint of protecting its integrity under any circumstances (Ch. 4). The feasibility of the approach permits any other physical effect that decreases the incoming heat flux to be implemented as boundary condition. The approach also permits the deformed geometry to be used for subsequent structural assessments;

3. High heat flux experiments in GLADIS, performed for producing melting events used to validate the 3D–TARTIFL&TTE under melt phase conditions. The destructive post–processing of samples leads to the testing of a novel methodology for melt layer thickness measurements (Ch. 5);

4. The above research is applied to produce the first example of an integrated design for a limiter equipped with a new concept of the shield block, which aims at reducing EM loads acting on ferromagnetic structure during disruptive events (Ch. 6);

7.2 Future work

The research work carried out during the DPhil enables the author to identify future research opportunities. The following three themes are discussed:

1. Improvement on the predictive capability of the COMSOL–implemented TARTIFL&TTE through further melting experiments, aiming at addressing the following issues:

   - Uncertainties in mass losses. These should be quantified through dedicated experiments, designed with a sample layout permitting to discern between losses due to gravity and losses caused by other physical phenomena. An experimental layout foreseeing a horizontally–oriented sample thermally loaded by a vertically–oriented beam would help minimize the effect of gravity;
   - The addition of boundary conditions that model the liquid droplet splashes. Additional understanding of the physics behind mass losses and how to model this process

as boundary conditions into the TARTIFL&TTE code would improve its predictive capability for mass loss, to be added to the already implemented evaporative mass loss;

- Representation of the intense vaporization phenomena. It needs to be adequately understood through dedicated experiments, and eventually implemented in TARTIFL&TTE by means of boundary conditions reducing the incoming heat flux. There are not such adequately powerful heat source facilities available worldwide at present, and there are not sensitive diagnostics to capture surface temperature realistically beyond refractory materials' melting point. Hence, the need to:
  - Rely on the measurement of other surface variables (like surface deformation) over the shot duration, to be correlated with intense vaporization;
  - Seek for facilities providing high heat flux in presence of magnetic field, for understanding the shielding effectiveness of intense vaporization in presence of magnetic field lines;

2. Improvement of the experimental pre and post–processing activities, aiming at reducing uncertainties on the final measurements. The destructive post–processing needs the sectioning to be carefully planned and executed, as well as a more refined polishing and measurement methodology. These improvements can be achieved by:
   - Sample sectioning defined on drawings and performed accordingly;
   - Weight measurements performed with a more sensitive scale and under the same conditions, before and after the experiments;
   - Smaller samples to load under different mechanical constrains would be easier to handle, especially during the post–processing phase;
   - Mechanical polishing with edge retainers is preferred over the hand polishing procedure;
3. Cooling system experiments under non–uniform heat flux should be performed for a damaged armour for testing the capability of the estimated armour thickness to effectively protect the pipes beneath it, as well as the 3D–TARTIFL&TTE reliability of modelling realistic temperature values at the pipe inner surface.

Appendices

Appendix A

Material morphology

A.1 Grain size measurement

A.1.1 TZM specimens

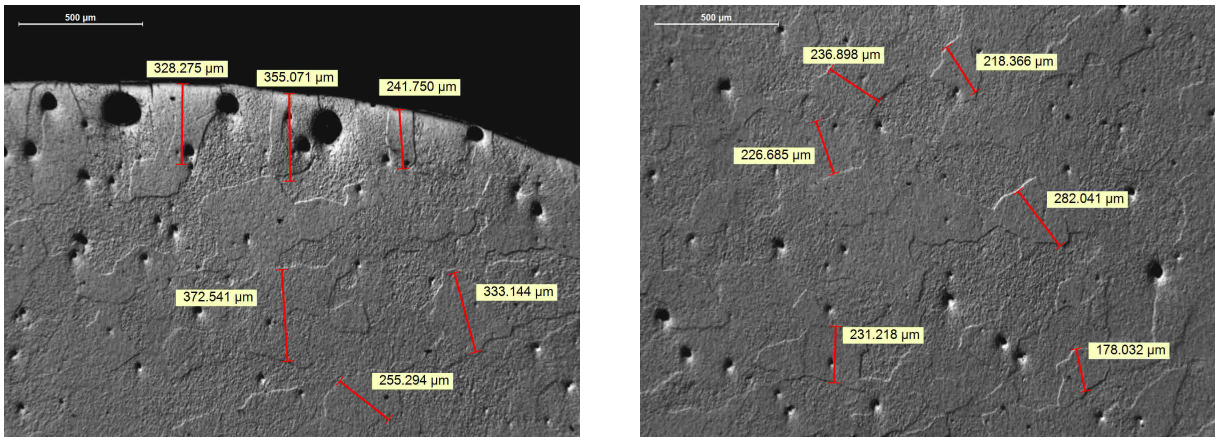

(a) Grain size along the heated boundary.

(b) Grain size in the bulk of the specimen.

Fig. A.1: Microstructure morphology of the horizontally–oriented TZM–1 specimen.

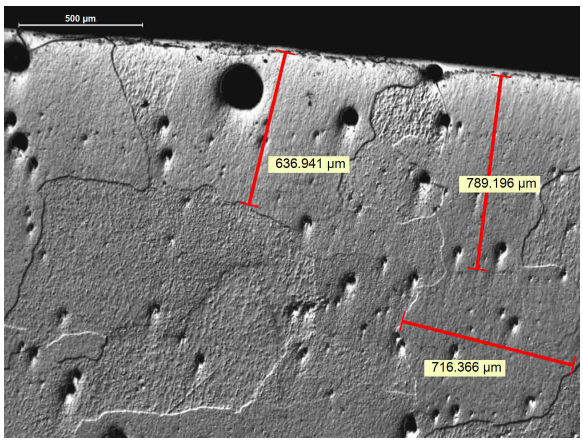

(a) Grain size along the heated boundary.

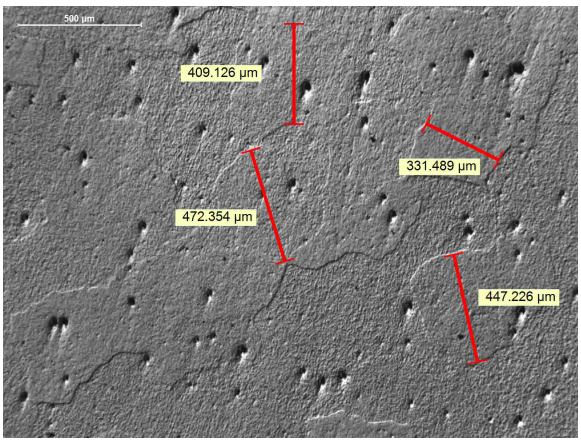

(b) Grain size in the bulk of the specimen.

Fig. A.2: Microstructure morphology of the horizontally–oriented TZM–2 specimen.

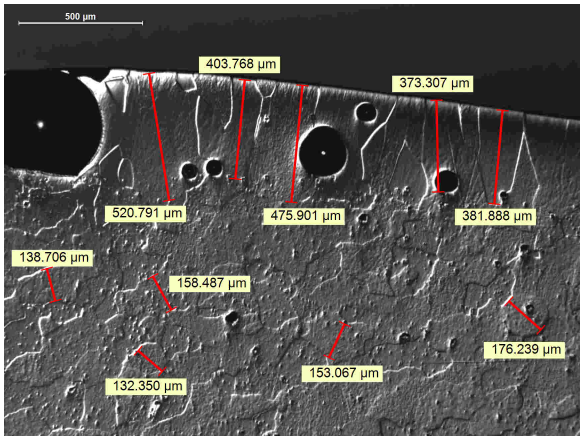

(a) Grain size near the melted area.

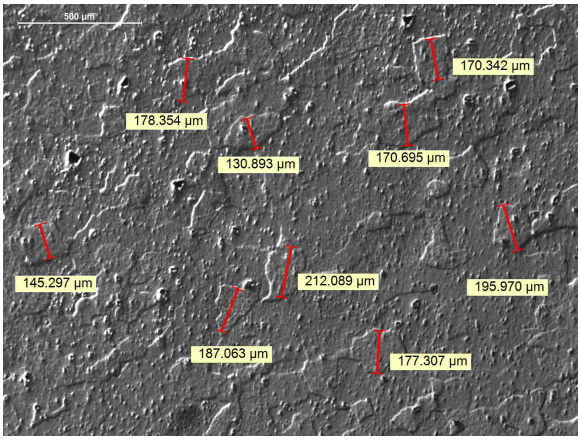

(b) Grain size in the recrystallized area.

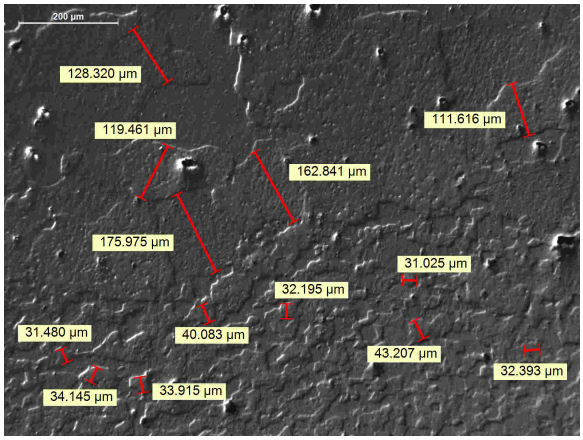

(c) Recrystallized and bulk grain interface.

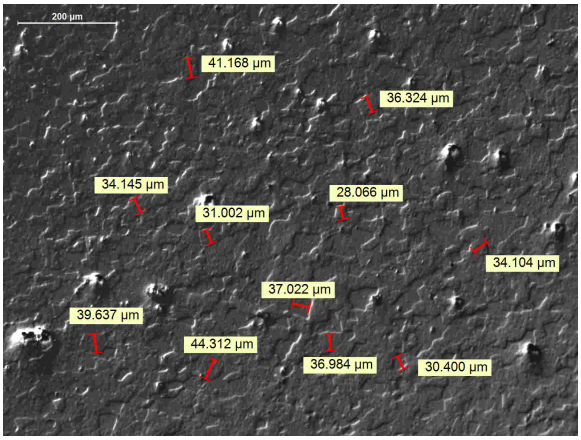

(d) Particular of the bulk grain size.

Fig. A.3: Melted and bulk morphology of the vertically–oriented TZM–1 ((a)–(b)) and TZM–2 ((c)–(d)) specimens.

A.1.2 W specimens

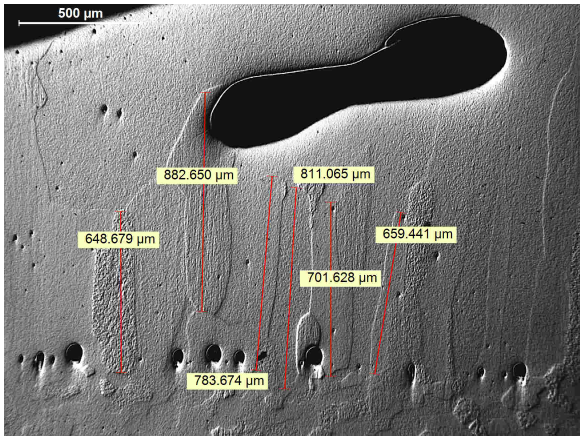

(a) Grain size near the melted area.

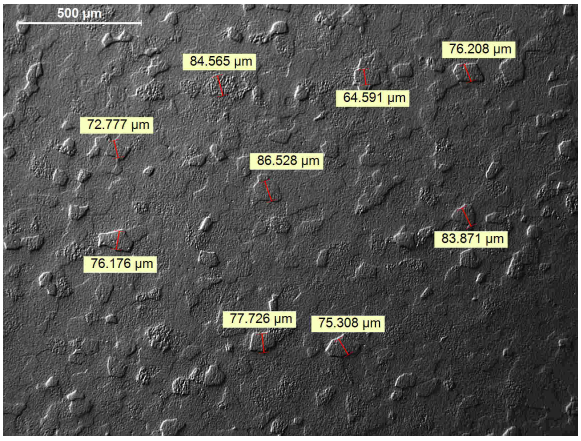

(b) Grain size in the recrystallized area.

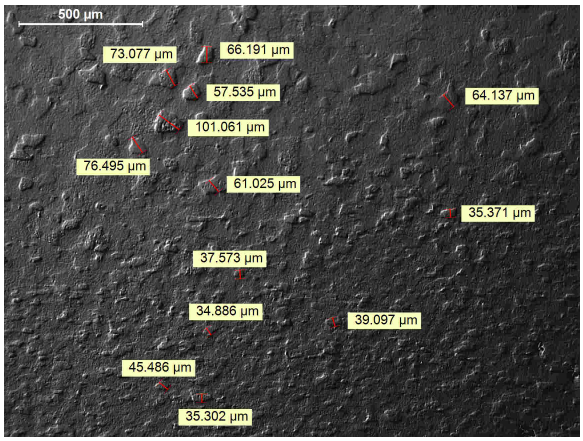

(c) Recrystallized and bulk grain interface.

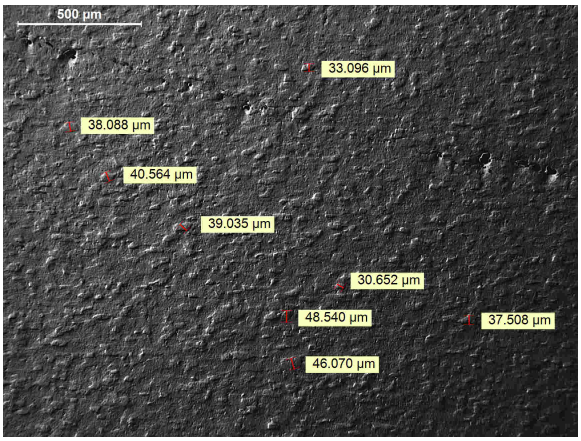

(d) Particular of the bulk grain size.

Fig. A.4: Melted and bulk morphology of the vertically–oriented W–1 specimen.

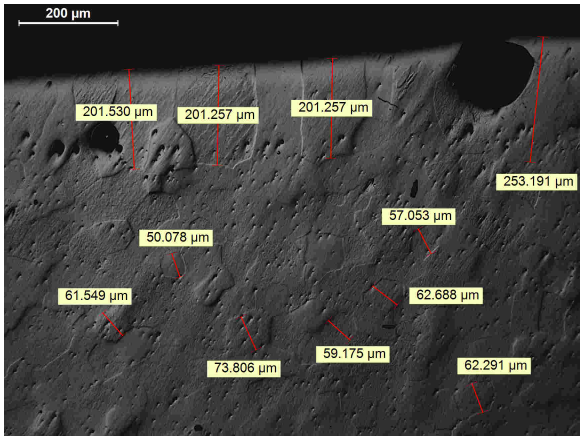

(a) Grain size along the heated boundary.

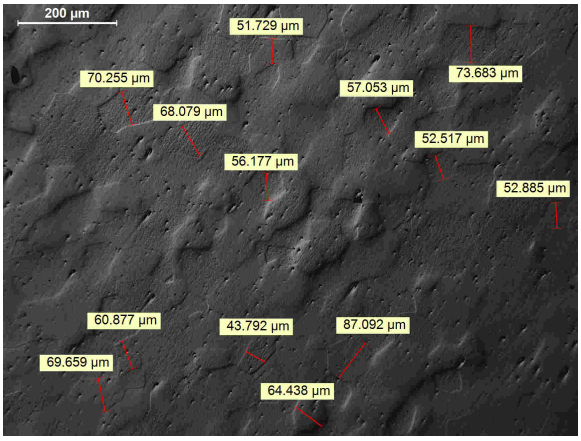

(b) Grain size in the bulk of the specimen.

Fig. A.5: Melted and bulk morphology of the horizontally–oriented W–1 specimen.

A.1.3 SS specimens

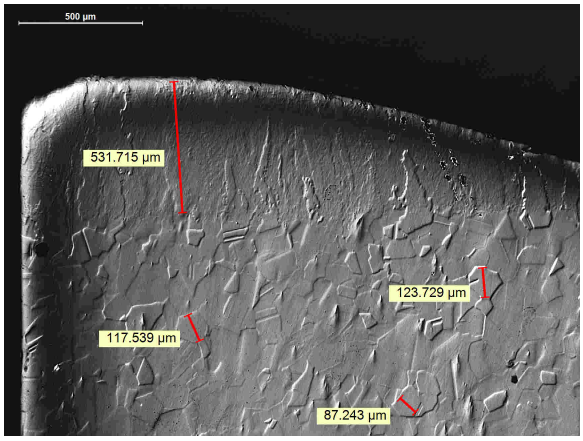

(a) Edge structure after polishing.

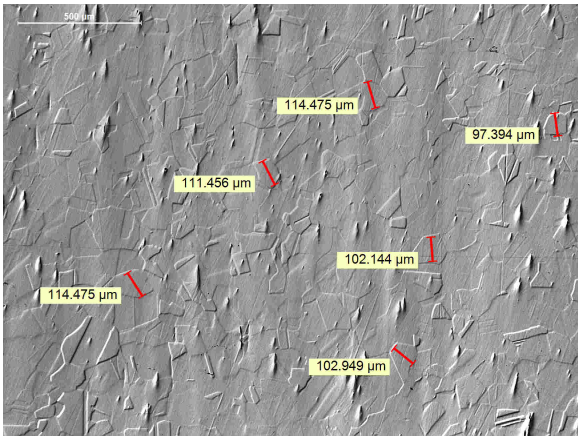

(b) Bulk structure after polishing.

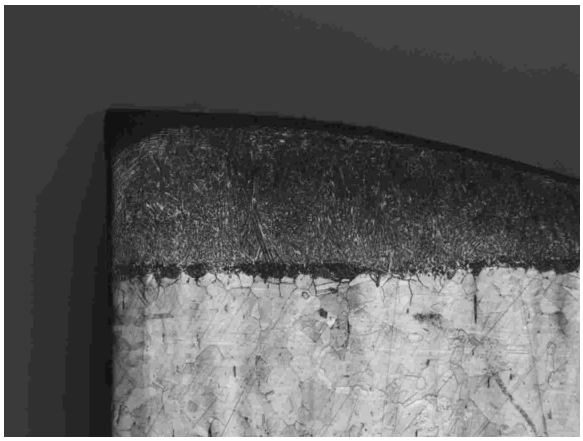

(c) Edge structure after etching.

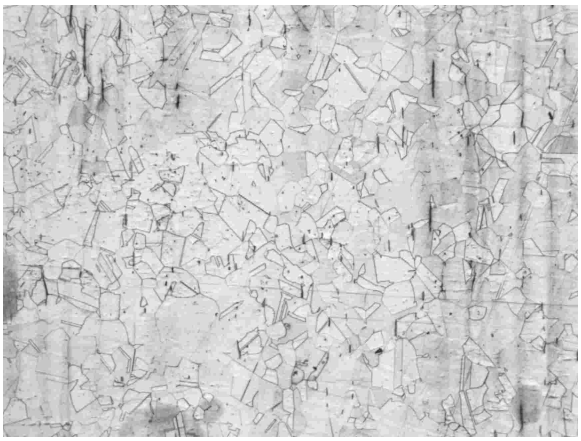

(d) Bulk structure after etching.

Fig. A.6: Melted and bulk morphology of the horizontally–oriented SS–1 specimen, before etching ((a)–(b)) and after etching ((c)–(d)) them.

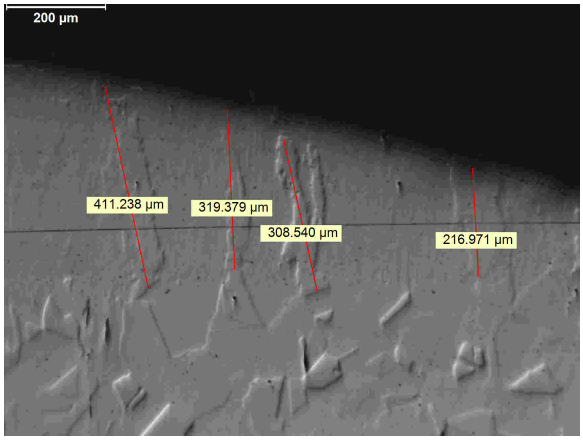

(a) Dendrites below the heated footprint.

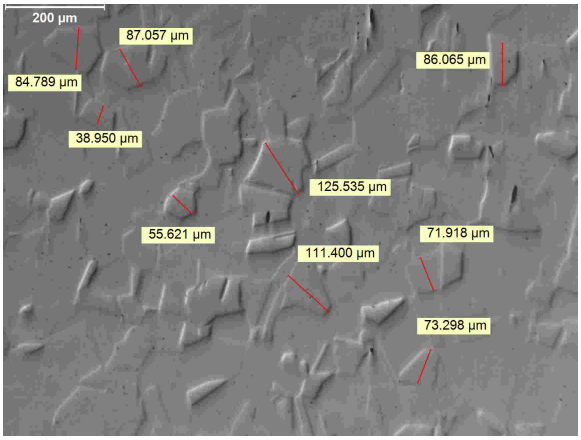

(b) Bulk structure.

Fig. A.7: Melted and bulk morphology of the vertically–oriented SS–1 specimen.

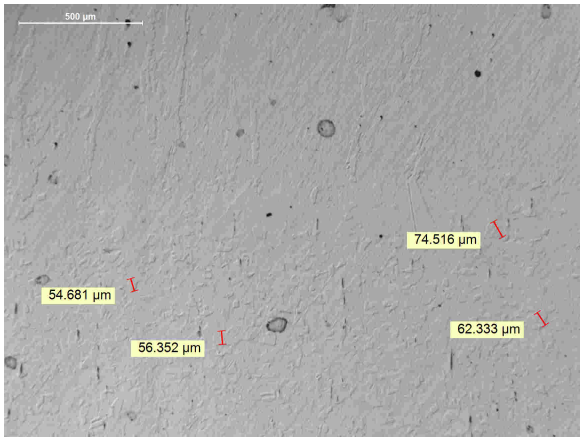

(a) Dendrites below the heated footprint.

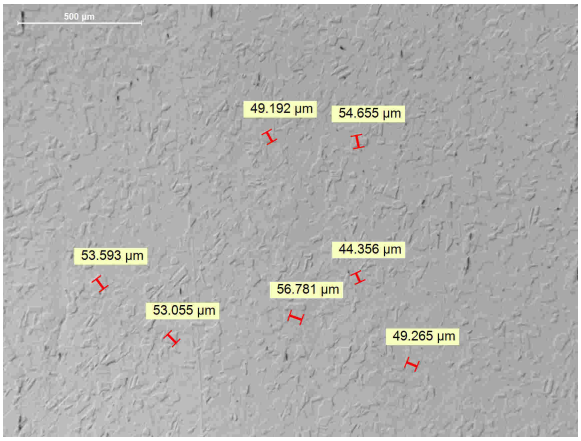

(b) Bulk structure

Fig. A.8: Melted and bulk morphology of the vertically–oriented SS–2 specimen.

Bibliography

[1] International Atomic Energy Authority, P.K. Kaw, and I. Bandyopadhyay. *The case for fusion*. Fusion Physics, Non–serial Publications, IAEA, Vienna, 2012.

[2] J. Raeder, K. Borraß, R. Bünde, W. Dänner, R. Klingelhöfer, L. Lengyel, F. Leuterer, and M. Söll. *Kontrollierte Kernfusion: Grundlagen ihrer Nutzung zur Energieversorgung*. Vieweg+Teubner Verlag, Wiesbaden, 1981.

[3] J. Wesson. *Tokamaks*. Oxford University Press, Oxford, third edition, 2004.

[4] S. Takeda and R. Pearson. Nuclear Fusion Power Plants. Power Plant in the Industry. IntechOpen, 2018.

[5] Y. Xu. A general comparison between tokamak and stellarator plasmas. *Matter and Radiation at Extremes*, 1(4):192–200, 2016.

[6] T. Donné. European Research Roadmap to the Realisation of Fusion Energy. *EUROfusion*, 2018.

[7] P.C. Stangeby. *The Plasma Boundary of Magnetic Fusion Devices*. CRC Press, 1st edition, 2000.

[8] University of York. Scrape Off Layer and Divertor Physics. `https://www.york.ac.uk/physics-engineering-technology/ypi/research/mcf/divphys/`.

[9] J. Friedberg. *Plasma physics and fusion energy*. Cambridge University Press, 2007.

[10] Y.R. Martin, T. Takizuka, and the ITPA CDBM H-mode Threshold Database Working Group. Power requirement for accessing the H–mode in ITER. *Journal of Physics: Conference Series*, 123(1):012033, 2008.

[11] M. Keilhacker, A. Gibson, C. Gormezano, and P.H. Rebut. The scientific success of JET. *Nuclear Fusion*, 41(12):1925–1966, 2001.

[12] J. Mlynář. Focus On : JET. *European centre of fusion research*, 2007.

[13] B.D. Wirth, K. Nordlund, D.G. Whyte, and D. Xu. Fusion materials modeling: challenges and opportunities. *MRS Bull.*, 36(3):216–222, 2011.

[14] JET viewing system. `https://users.euro-fusion.org/openwiki/index.php/JET_viewing_systems`.

[15] M.L. Richiusa, P. Ireland, J. Nicholas, and Z. Vizvary. Rationale Behind EU–DEMO Limiter's Plasma–Facing Component Design Under Material Phase Change. *IEEE Transactions on Plasma Science*, pages 1–7, 2022.

[16] M.L. Richiusa, P. Ireland, F. Maviglia, J. Nicholas, and Z. Vizvary. Advances in material phase change modelling approach for EU–DEMO limiter's plasma-facing components. *Fusion Engineering and Design*, 189:113477, 2023.

[17] M.L. Richiusa, H. Greuner, B. Boswirth, P. Ireland, and Z. Vizvary. High heat flux tests in support of the 3D computational modelling of melting for the EU–DEMO first wall limiters. *IEEE Transactions on Plasma Science*, 2023.

[18] M.L. Richiusa, A. Cardella, A. Čufar, A. Froio, P. Haghdoust, P. Ireland, I. Maione, I. Pagani, G. Pautasso, A. Martin Ramos, G.A. Spagnuolo, F. Vigano, and Z. Vizvary. The integrated Engineering Design Concept of the Upper Limiter within the EU–DEMO LIMITER System. *Fusion Engineering and Design*, 202:114329, 2024.

[19] F. Maviglia, R. Albanese, R. Ambrosino, W. Arter, C. Bachmann, T. Barrett, G. Federici, M. Firdaous, J. Gerardin, M. Kovari, V. Loschiavo, M. Mattei, F. Villone, and R. Wenninger. Wall protection strategies for DEMO plasma transients. *Fusion Engineering and Design*, 136:410–414, 2018.

[20] G. Federici, L. Boccaccini, F. Cismondi, M. Gasparotto, Y. Poitevin, and I. Ricapito. An overview of the EU breeding blanket design strategy as an integral part of the DEMO design effort. *Fusion Engineering and Design*, 141:30–42, 2019.

[21] L.V. Boccaccini, G. Aiello, J. Aubert, C. Bachmann, T. Barrett, A. Del Nevo, D. Demange, L. Forest, F. Hernandez, P. Norajitra, G. Porempovic, D. Rapisarda, P Sardain, M Utili, and L Vala. Objectives and status of EUROfusion DEMO blanket studies. *Fusion Engineering and Design*, 109-111:1199–1206, 2016.

[22] M. Siccinio, J.P. Graves, R. Kembleton, H. Lux, F. Maviglia, A.W. Morris, J. Morris, and H. Zohm. Development of the plasma scenario for EU–DEMO: Status and plans. *Fusion Engineering and Design*, 176:113047, 2022.

[23] R. Kembleton, J. Morris, M. Siccinio, and F. Maviglia. EU–DEMO design space exploration and design drivers. *Fusion Engineering and Design*, 178:113080, 2022.

[24] Christian Vorpahl, Rocco Mozzillo, Christian Bachmann, and Giuseppe Di Gironimo. Initial configuration studies of the upper vertical port of the European DEMO. *Fusion Engineering and Design*, 146:2469–2473, 2019.

[25] R. Wenninger, R. Albanese, R. Ambrosino, F. Arbeiter, J. Aubert, C. Bachmann, L. Barbato, T. Barrett, M. Beckers, W. Biel, L. Boccaccini, D. Carralero, D. Coster, T. Eich, A. Fasoli, G. Federici, M. Firdaouss, J. Graves, J. Horacek, M. Kovari, S. Lanthaler, V. Loschiavo, C. Lowry, H. Lux, G. Maddaluno, F. Maviglia, R. Mitteau, R. Neu, D. Pfefferle, K. Schmid, M. Siccinio, B. Sieglin, C. Silva, A. Snicker, F. Subba, J. Varje, and H. Zohm. The DEMO wall load challenge. *Nuclear Fusion*, 57(4), 2017.

[26] EUROfusion. 22.5 DEMO Sector. `https://idm.euro-fusion.org/?uid=2NSXNG`.

[27] F. Maviglia, M. Siccinio, C. Bachmann, W. Biel, M. Cavedon, E. Fable, G. Federici, M. Firdaouss, J. Gerardin, V. Hauer, I. Ivanova-Stanik, F. Janky, R. Kembleton, F. Militello, F. Subba, S. Varoutis, and C. Vorpahl. Impact of plasma–wall interaction and exhaust on the EU–DEMO design. *Nuclear Materials and Energy*, 26:100897, 2021.

[28] D. A. Humphreys and A. G. Kellman. Analytic modeling of axisymmetric disruption halo currents. *Physics of Plasmas*, 6:2742–2756, 1999.

[29] M.L. Richiusa, W. Arter, D. Calleja, M. Firdaouss, J. Gerardin, M. Kovari, F. Maviglia, and Z. Vizvary. Bare and limiter DEMO single module segment concept first Wall misalignment study by 3D field line tracing. *Fusion Engineering and Design*, 160, 2020.

[30] F. Maviglia, C. Bachmann, G. Federici, T. Franke, M. Siccinio, C.n Vorpahl, R. Albanese, R. Ambrosino, E. Fable, M. Firdaouss, J. Gerardin, V.P. Loschiavo, M. Mattei, F. Palermo, M.L. Richiusa, F. Villone, and Z. Vizvary. Impact of plasma thermal transients on the design of the EU DEMO first wall protection. *Fusion Engineering and Design*, 158(April):111713, 2020.

[31] F. Maviglia, C. Bachmann, G. Federici, T. Franke, M. Siccinio, R. Albanese, R. Ambrosino, W. Arter, R. Bonifetto, G. Calabrò, R. De Luca, L.E. Di Grazia, E. Fable, P. Fanelli, A. Fanni, M. Firdaouss, J. Gerardin, R. Lombroni, M. Mattei, M. Moscheni, W. Morris, G. Pautasso, S. Pestchanyi, G. Ramogida, M.L. Richiusa, G. Sias, F. Subba, F. Villone, J.H. You, and Z. Vizvary. Integrated design strategy for EU–DEMO first wall protection from plasma transients. *Fusion Engineering and Design*, 177, 2022.

[32] L. Tan, Y. Katoh, A.F. Tavassoli, J. Henry, M. Rieth, H. Sakasegawa, H. Tanigawa, and Q. Huang. Recent status and improvement of reduced–activation ferritic–martensitic steels for high–temperature service. *Journal of Nuclear Materials*, 479:515–523, 2016.

[33] J.H. You, G. Mazzone, E. Visca, C. Bachmann, E. Autissier, T. Barrett, V. Cocilovo, F. Crescenzi, P.K. Domalapally, D. Dongiovanni, S. Entler, G. Federici, P. Frosi, M. Fursdon, H. Greuner, D. Hancock, D. Marzullo, S. McIntosh, A.V. Müller, M.T. Porfiri, G. Ramogida, J. Reiser, M. Richou, M. Rieth, A. Rydzy, R. Villari, and V. Widak. Conceptual design studies for the European DEMO divertor: Rationale and first results. *Fusion Engineering and Design*, 109-111:1598–1603, 2016.

[34] D. Stork, P. Agostini, J.L. Boutard, D. Buckthorpe, E. Diegele, S. L. Dudarev, C. English, G. Federici, M.R. Gilbert, S. Gonzalez, A. Ibarra, Ch Linsmeier, A. Li Puma, G. Marbach, P.F. Morris, L.W. Packer, B. Raj, M. Rieth, M.Q. Tran, D.J. Ward, and S.J. Zinkle. Developing structural, high–heat flux and plasma facing materials for a near–term DEMO fusion power plant: The EU assessment. *Journal of Nuclear Materials*, 455(1-3):277–291, 2014.

[35] M. Gasparotto, R. Andreani, L.V. Boccaccini, A. Cardella, G. Federici, L. Giancarli, G. Le Marois, D. Maisonnier, S. Malang, A. Moeslang, Y. Poitevin, B. Van der Schaaf,

and M. Victoria. Survey of in–vessel candidate materials for fusion power plants – The European materials R&D programme. *Fusion Engineering and Design*, 66-68:129–137, 2003.

[36] J.N. Brooks, L. El-Guebaly, A. Hassanein, and T. Sizyuk. Plasma–facing material alternatives to tungsten. *Nuclear Fusion*, 55(4), 2015.

[37] A.M. Hassanein, G.L. Kulcinski, and W.G. Wolfer. Vaporization and melting of materials in fusion devices. *Journal of Nuclear Materials*, 103:321–326, 1981.

[38] A.M. Hassanein and D. Ehst. Dynamic modeling of plasma–vapor interactions during plasma disruptions. *Journal of Nuclear Materials*, 198:680–685, 1992.

[39] T. Eich, B. Sieglin, A. Scarabosio, W. Fundamenski, R. J. Goldston, and A. Herrmann. Inter–ELM Power Decay Length for JET and ASDEX Upgrade: Measurement and Comparison with Heuristic Drift–Based Model. *Phys. Rev. Lett.*, 107:215001, 2011.

[40] W. Arter, V. Riccardo, and G. Fishpool. A CAD–based tool for calculating power deposition on tokamak plasma–facing components. *IEEE Transactions on Plasma Science*, 42(7):1932–1942, 2014.

[41] M. Firdaouss, V. Riccardo, V. Martin, G. Arnoux, C. Reux, and Jet-efda Contributors. Modelling of power deposition on the JET ITER like wall using the code PFCFLux. *Journal of Nuclear Materials*, 438:S536–S539, 2013.

[42] J. Gerardin, M. Firdaouss, F. Maviglia, W. Arter, T. Barrett, and M. Kovari. Simplified heat load modeling for design of DEMO discrete limiter. *Nuclear Materials and Energy*, 20(July):100568, 2019.

[43] H.S. Carslaw and J.C. Jaeger. *Conduction of Heat in Solids*. Oxford science publications. Clarendon Press, 1986.

[44] J. Crank. *Free and Moving Boundary Problems*. Oxford science publications. Clarendon Press, 1987.

[45] H. Hu and S.A. Argyropoulos. Mathematical modelling of solidification and melting: a review. *Modelling and Simulation in Materials Science and Engineering*, 4(4):371–396, 1996.

[46] V. Alexiades. *Mathematical Modeling Of Melting And Freezing Processes*. Taylor & Francis, 1992.

[47] T.G. Myers, M.G. Hennessy, and M. Calvo-Schwarzwälder. The stefan problem with variable thermophysical properties and phase change temperature. *International Journal of Heat and Mass Transfer*, 149:118975, 2020.

[48] T.R. Goodman and J.J. Shea. The Melting of Finite Slabs. *Journal of Applied Mechanics*, 27(1):16–24, 1960.

[49] H.G. Landau. Heat conduction in a melting solid. *Quarterly of Applied Mathematics*, 8(1):81–94, 1950.

[50] W.D. Murray and F. Landis. Numerical and Machine Solutions of Transient Heat–Conduction Problems Involving Melting or Freezing: Part I–Method of Analysis and Sample Solutions. *Journal of Heat Transfer*, 81(2):106–112, 1959.

[51] T.C. Illingworth and I.O. Golosnoy. Numerical solutions of diffusion–controlled moving boundary problems which conserve solute. *Journal of Computational Physics*, 209(1):207–225, 2005.

[52] A. Vande Wouwer, P. Saucez, and C. Vilas. *Simulation of ODE/PDE Models with MATLAB®, OCTAVE and SCILAB*. Springer International Publishing, Cham, 2014.

[53] COMSOL Multiphysics®. *Comsol Multiphysics Reference Manual: Version 6.0*.

[54] J. Donea, A. Huerta, J.-Ph. Ponthot, and A. Rodriguez-Ferran. Arbitrary Lagrangian-Eulerian Methods. In *Encyclopedia of Computational Mechanics*. John Wiley & Sons Ltd, 2004.

[55] H. Hertz. Ueber die Verdunstung der Flüssigkeiten, insbesondere des Quecksilbers, im luftleeren Raume. *Annalen der Physik*, 253(10):177–193, 1882.

[56] M. Knudsen. Die maximale Verdampfungsgeschwindigkeit des Quecksilbers. *Annalen der Physik*, 352(13):697–708, 1915.

[57] I. Langmuir. The condensation and evaporation of gas molecules. *Proceedings of the National Academy of Sciences*, 3(3):141–147, 1917.

[58] I. Langmuir. Vapor pressures, evaporation, condensation and adsorption. *J. Am. Chem. Soc.*, 54(7):2798–2832, 1932.

[59] L.D. Koffman, M.S. Plesset, and L. Lees. Theory of evaporation and condensation. *Physics of Fluids*, 27(4):876–880, 1984.

[60] J. Knaster, T. Kanemura, and K. Kondo. An assessment of the evaporation and condensation phenomena of lithium during the operation of a Li(d,xn) fusion relevant neutron source. *Heliyon*, 2(12):1–23, 2016.

[61] A.H. Persad and C.A. Ward. Expressions for the Evaporation and Condensation Coefficients in the Hertz-Knudsen Relation. *Chem. Rev.*, 116(14):7727–7767, 2016.

[62] A.M. Hassanein. *Thermal Effects and Erosion Rates Resulting from Intense Deposition of Energy in Fusion*. PhD thesis, The University of Wisconsin-Madison, 1982.

[63] T. Ytrehus and S. Østmo. Kinetic theory approach to interphase processes. *International Journal of Multiphase Flow*, 22(1):133–155, 1996.

[64] V.I. Mazhukin, V.V. Nossov, and I. Smurov. Modeling of plasma-controlled evaporation and surface condensation of Al induced by 1.06 and 0.248 μm laser radiations. *Journal of Applied Physics*, 101(2), 2007.

[65] S.M. Yen and T. Ytrehus. Treatment of the nonequilibrium vapor motion near an evaporating interphase boundary. *Chemical Engineering Communications*, 10(6):357–367, 1981.

[66] S. Anisimov and A. Rakhmatulina. The dynamics of the expansion of a vapor when evaporated into a vacuum. *Soviet Journal of Experimental and Theoretical Physics*, 37:441, 1973.

[67] C.J. Knight. Theoretical modeling of rapid surface vaporization with back pressure. *AIAA Journal*, 17(5):519–523, 1979.

[68] Y.A. Mayi, M. Dal, P. Peyre, M. Bellet, C. Metton, C. Moriconi, and R. Fabbro. Laser-induced plume investigated by finite element modelling and scaling of particle entrainment in laser powder bed fusion. *J. Phys. D. Appl. Phys.*, 53(7), 2020.

[69] Y.A. Mayi, M. Dal, P. Peyre, M. Bellet, C. Metton, C. Moriconi, and R. Fabbro. Two-Phase Flow Modelling of Metal Vaporisation under Static Laser Shot using a Double Domain ALE Method-A Feasibility Study. *Proceedings of the 2018 COMSOL Conference*, 7, 2018.

[70] S.I. Anisimov. *Vaporization of metal absorbing laser radiation*, volume 27, pages 14–15. World Scientific, 1996.

[71] K. Hirano, R. Fabbro, and M. Muller. Study on temperature dependence of recoil pressure near the boiling temperature – Towards better modeling and simulation. *ICALEO 2012 - 31st Int. Congr. Appl. Lasers Electro-Optics*, 678(2012):678–684, 2012.

[72] Y.A. Mayi, M. Dal, P. Peyre, M. Bellet, C. Metton, C. Moriconi, and R. Fabbro. Transient dynamics and stability of keyhole at threshold in laser powder bed fusion regime investigated by finite element modeling. *Journal of Laser Applications*, 33(1):012024, 2021.

[73] C.J. Knight. Transient Vaporization from a Surface into Vacuum. *AIAA J.*, 20(7):950–954, 1982.

[74] J. Safarian and T.A. Engh. Vacuum evaporation of pure metals. *Metallurgical and Materials Transactions A: Physical Metallurgy and Materials Science*, 44(2):747–753, 2013.

[75] G. Schiller, S. Jaesch and M. Neumann. High rate electron beam evaporation. *Thin Solid Films*, 110(2):149–164, 1983.

[76] S. Schiller, U. Heisig, and S. Panzer. *Electron beam technology.* Wiley, New York, 1982.

[77] K.W. Westerberg, M.A. McClelland, and B.A. Finlayson. Finite element analysis of flow, heat transfer, and free interfaces in an electron-beam vaporization system for metals. *International Journal for Numerical Methods in Fluids*, 26(6):637–655, 1998.

[78] K.W. Westerberg, T.C. Meier, M.A. Mcclelland, D.G. Braun, L.V. Berzins, T.M. Anklam, and J. Storer. Analysis of the E–Beam Evaporation Titanium and Ti-6Al-4V. *Electron Beam Melting Refin. State Art 1997 Conf.*, 1997.

[79] K.W. Westerberg, M.A. McClelland, and B.A. Finlayson. The interaction of flow, heat transfer, and free interfaces in an electron–beam vaporization system for metals. 1994.

[80] A. Hassanein. Prediction of material erosion and lifetime during major plasma instabilities in tokamak devices. *Fusion Engineering and Design*, 60(4):527–546, 2002.

[81] J. Horacek, R. Dejarnac, J. Cecrdle, D. Tskhakaya, A. Vertkov, J. Cavalier, P. Vondracek, M. Jerab, P. Barton, G. van Oost, M. Hron, V. Weinzettl, D. Sestak, S. Lukes, J. Adamek, A. Prishvitsin, M. Iafratti, Y. Gasparyan, Y. Vasina, D. Naydenkova, J. Seidl, E. Gauthier, G. Mazzitelli, M. Komm, J. Gerardin, J. Varju, M. Tomes, S. Entler, J. Hromadka, and R. Panek. Modeling of COMPASS tokamak divertor liquid metal experiments. *Nucl. Mater. Energy*, 25:100860, 2020.

[82] S. Pestchanyi and F. Maviglia. Simulation of the first wall shielding during upward VDE in DEMO. *Nucl. Mater. Energy*, 24:100767, 2020.

[83] B.I. Khripunov, V.M. Gureev, L.S. Danelyan, V.V. Zatekin, V.S. Koidan, V.S. Kulikauskas, S.T. Latushkin, V.B. Petrov, A.I. Ryazanov, and V.N. Unezhev. Analysis of a tungsten surface irradiated by fast ions and deuterium plasma. *Journal of Surface Investigation. X-ray, Synchrotron and Neutron Techniques*, 8:229–233, 2014.

[84] D.I. Skovorodin, A.A. Pshenov, A.S. Arakcheev, E.A. Eksaeva, E.D. Marenkov, and S.I. Krasheninnikov. Vapor shielding models and the energy absorbed by divertor targets during transient events. *Physics of Plasmas*, 23:022501, 2016.

[85] A.A. Pshenov, A.A. Eksaeva, S.I. Krasheninnikov, and E.D. Marenkov. Vapor Shielding of Solid Targets Exposed to High Heat Flux. *Physics Procedia*, 71:14–19, 2015.

[86] S.I. Krasheninnikov, A.Y. Pigarov, and W. Lee. Physics of the edge plasma and first wall in fusion devices: synergistic effects. *Plasma Physics and Controlled Fusion*, 57:044009, 2015.

[87] V.M. Safronov, N.I. Arkhipov, I.S. Landman, S.E. Pestchanyi, D.A. Toporkov, and A.M. Zhitlukhin. Evaporation and vapor shielding of CFC targets exposed to plasma heat fluxes relevant to ITER ELMs. *Journal of Nuclear Materials*, 386-388:744–746, 2009.

[88] G.F. Matthews, B. Bazylev, A. Baron-Wiechec, J. Coenen, K. Heinola, V. Kiptily, H. Maier, C. Reux, V. Riccardo, F. Rimini, G. Sergienko, V. Thompson, and A. Widdowson. Melt damage to the JET ITER–like Wall and divertor. *Physica Scripta*, T167:014070, 2016.

[89] G. Sergienko, G. Arnoux, S. Devaux, G.F. Matthews, I. Nunes, V. Riccardo, A. Sirinelli, A. Huber, S. Brezinsek, J.W. Coenen, P. Mertens, V. Philipps, and U. Samm. Movement of liquid beryllium during melt events in JET with ITER–like wall. *Physica Scripta*, T159:014041, 2014.

[90] J.W. Coenen, G.F. Matthews, K. Krieger, D. Iglesias, P. Bunting, Y. Corre, S. Silburn, I. Balboa, B. Bazylev, N. Conway, I. Coffey, R. Dejarnac, E. Gauthier, J. Gaspar, S. Jachmich, I. Jepu, C. Makepeace, R. Scannell, M. Stamp, P. Petersson, R.A. Pitts, S. Wiesen, A. Widdowson, K. Heinola, and A. Baron-Wiechec. Transient induced tungsten melting at the Joint European Torus (JET). *Physica Scripta*, T170:014013, 2017.

[91] U. Samm, P. Bogen, H. Hartwig, E. Hintz, K. Höthker, Y.T. Lie, A. Pospieszczyk, D. Rusbüldt, B. Schweer, and Y.J. Yu. Plasma edge physics in the textor tokamak with poloidal and toroidal limiters. *Journal of Nuclear Materials*, 162-164:24–37, 1989.

[92] G. Sergienko, B. Bazylev, T. Hirai, A. Huber, A. Kreter, P. Mertens, A. Nedospasov, V. Philipps, A. Pospieszczyk, M. Rubel, U. Samm, B. Schweer, P. Sundelin, M. Tokar, and E. Wessel. Experience with bulk tungsten test–limiters under high heat loads: melting and melt layer propagation. *Physica Scripta*, T128:81–86, 2007.

[93] P.C. Stangeby. The strong effect of gaps on the required shaping of the ITER first wall. *Nuclear Fusion*, 51(3), 2011.

[94] P.C. Stangeby and R. Mitteau. Analysis for shaping the ITER first wall. *Journal of Nuclear Materials*, 390-391(1):963–966, 2009.

[95] Lao. G EQDSK Format, 1997.

[96] P. Barabaschi. The MAXFEA code. *Proceedings of Plasma Control Technical Meeting*, 1993.

[97] MathWorks®. Solving Partial Differential Equations – MATLAB & Simulink – MathWorks United Kingdom. `https://uk.mathworks.com/help/matlab/math/partial-differential-equations.html`.

[98] A. Vande Wouwer, P. Saucez, and W.E. Schiesser. Simulation of Distributed Parameter Systems Using a Matlab-Based Method of Lines Toolbox: Chemical Engineering Applications. *Industrial & Engineering Chemistry Research*, 43(14):3469–3477, 2004.

[99] M. Zerroukat. A Boundary Element Method for Multiple Moving Boundary Problems. 519:501–519, 1997.

[100] M. Zerroukat and C.R. Chatwin. *Computational Moving Boundary Problems*, volume 310. 2007.

[101] COMSOL Multiphysics®. Heat Transfer Module Users Guide. `https://doc.comsol.com/5.4/doc/com.comsol.help.heat/HeatTransferModuleUsersGuide.pdf`.

[102] V.I. Tereshin. Quasi–stationary plasma accelerators (QSPA) and their applications. *Plasma Physics and Controlled Fusion*, 37(11A), 1995.

[103] A.I. Morozov, O.A. Shchurov, O.S. Pavlichenko, V.I. Tereshin, V.V. Chebotarev, Ya.F. Volkov, V.I. Kovalenko, Kulik. N.V., V.S. Manojlo, V.V. Marinin, D.G. Solyakov, V.V. Stal'tsov, Yu.I. Tashchev, and B.Yu. Tsupko. QSPA Kh-50 full–scale high–power asistationary plasma accelerator. *Plasma Devices and Operations*, 2(2):155–165, 1992.

[104] V.I. Tereshin, I.E. Garkusha, A.N. Bandura, O.V. Byrka, V.V. Chebotarev, V.A. Makhlaj, D.G. Solyakov, and H. Wuerz. Influence of plasma pressure gradient on melt layer macroscopic erosion of metal targets in disruption simulation experiments. *Journal of Nuclear Materials*, 313-316:685–689, 2003.

[105] I.E. Garkusha, A.N. Bandura, O.V. Byrka, V.V. Chebotarev, I. Landman, V.A. Makhlaj, S. Pestchanyi, and V.I. Tereshin. Damage to preheated tungsten targets after multiple

plasma impacts simulating ITER ELMs. *Journal of Nuclear Materials*, 386-388(C):127–131, 2009.

[106] S. Pestchanyi and H. Würz. Brittle destruction of carbon based materials under off–normal ITER–FEAT conditions. *Physica Scripta*, T91:84–89, 2001.

[107] S. Pestchanyi, I. Garkusha, V. Makhlaj, and I. Landman. Estimation of the dust production rate from the tungsten armour after repetitive ELM–like heat loads. *Physica Scripta*, T145:014062, 2011.

[108] V.I. Tereshin, A.N. Bandura, O.V. Byrka, V.V. Chebotarev, I.E. Garkusha, I. Landman, V.A. Makhlaj, D.G. Solyakov, and A.V. Tsarenko. Repetitive plasma loads typical for ITER type-I ELMS: Simulation in QSPA Kh-50. *AIP Conference Proceedings*, 812:128–135, 2006.

[109] P. Tolias. Analytical expressions for thermophysical properties of solid and liquid tungsten relevant for fusion applications. *Nuclear Materials and Energy*, 13:42–57, 2017.

[110] Plansee. tungsten. `https://www.plansee.com/en/materials/tungsten.html`.

[111] H. Greuner, H. Bolt, B. Böswirth, T. Franke, P. McNeely, S. Obermayer, N. Rust, and R. Süß. Design, performance and construction of a 2 MW ion beam test facility for plasma facing components. *Fusion Engineering and Design*, 75-79:345–350, 2005.

[112] H. Greuner, B. Boeswirth, J. Boscary, and P. McNeely. High heat flux facility GLADIS:. Operational characteristics and results of W7-X pre-series target tests. *Journal of Nuclear Materials*, 367-370 B:1444–1448, 2007.

[113] H. Shinno, M. Kitajima, and M. Okada. Thermal stress analysis of high heat flux materials. *Journal of Nuclear Materials*, 155-157:290–294, 1988.

[114] K. Thurnay. Thermal Properties of Transition Metals. *Forschungszentrum Karlsruhe, Technik und Umwelt, Wissenschaftliche Berichte FZKA 6095*, page 126, 1998.

[115] M. Portelli. *Numerical Modelling of Advanced Materials Subjected to High–Energy Particle Beam Impacts*. PhD thesis, 2021.

[116] ITER Organization. ITER Material Property Handbook. Technical report, ITER Organization, https://user.iter.org/Portal/Pages/ContentView.aspx?uid=2239QQ, 2017.

[117] M. Bober and J. Singer. High Temperature Vapor Pressures of Stainless Type 1.4970 and of some other Pure Metals from Laser Evaporation. Technical report, 1984.

[118] C.S. Kim. *Thermophysical Properties of Stainless Steels*, volume 75. 1975.

[119] T.S. Hunnewell, K.L. Walton, S. Sharma, T.K. Ghosh, R.V. Tompson, D.S. Viswanath, and S.K. Loyalka. Total hemispherical emissivity of SS 316L with simulated very high temperature reactor surface conditions. *Nuclear Technology*, 198(3):293–305, 2017.

[120] Buehler. *A Guide to Materials Preparation & Analysis*. Fourth edi edition.

[121] J.C. Anderson, K.D. Leaver, R.D. Rawlings, and P.S. Leevers. *Materials Science for Engineers*. 2004.

[122] K.K. Alaneme and E.A. Okotete. Recrystallization mechanisms and microstructure development in emerging metallic materials: A review. *Journal of Science: Advanced Materials and Devices*, 4(1):19–33, 2019.

[123] S. Islam, G.J. Seo, Md.R.U. Ahsan, H. Villarraga-Gómez, H.J. Lee, and D. Bong Kim. Investigation of microstructures, defects, and mechanical properties of titanium-zirconium-molybdenum alloy manufactured by wire arc additive manufacturing. *International Journal of Refractory Metals and Hard Materials*, 110, 2023.

[124] X.X. Zhang, Q.Z. Yan, C.T. Yang, T.N. Wang, M. Xia, and C.C. Ge. Recrystallization temperature of tungsten with different deformation degrees. *Rare Metals*, 35:566–570, 2016.

[125] J.W. Coenen, V. Philipps, S. Brezinsek, G. Pintsuk, T. Tanabe, Y. Ueda, and U. Samm. Analysis of structural changes and high–heat–flux tests on pre–damaged tungsten from tokamak melt experiments. *Physica Scripta*, T145:014066, dec 2011.

[126] J.W. Coenen, B. Bazylev, S. Brezinsek, V. Philipps, T. Hirai, A. Kreter, J. Linke, G. Sergienko, A. Pospieszczyk, T. Tanabe, Y. Ueda, and U. Samm. Tungsten melt layer

motion and splashing on castellated tungsten surfaces at the tokamak TEXTOR. *Journal of Nuclear Materials*, 415:S78–S82, 2011.

[127] R. Kerr, Y. Zayachuk, A. Widdowson, E. Alves, N. Catarino, S. Lozano-Perez, and D.E.J. Armstrong. Mechanical and microstructural analysis of tungsten exposed in JET deuterium plasmas. *Nuclear Materials and Energy*, 35:101420, 2023.

[128] S. Kheiri, H. Mirzadeh, and M. Naghizadeh. Tailoring the microstructure and mechanical properties of AISI 316L austenitic stainless steel via cold rolling and reversion annealing. *Materials Science and Engineering A*, 759:90–96, 2019.

[129] C. Bachmann, S. Ciattaglia, F. Cismondi, T. Eade, G. Federici, U. Fischer, T. Franke, C. Gliss, F. Hernandez, J. Keep, M. Loughlin, F. Maviglia, F. Moro, J. Morris, P. Pereslavtsev, N. Taylor, Z. Vizvary, and R. Wenninger. Overview over DEMO design integration challenges and their impact on component design concepts. *Fusion Engineering and Design*, 136:87–95, 2018.

[130] A. Cufar. Radial profile of nuclear heating in upper port limiter. Technical report, EUROfusion IDM, `https://idm.euro-fusion.org/?uid=2P9L5K&action=get_document`, 2022.

[131] J.H. You, G. Mazzone, E. Visca, H. Greuner, M. Fursdon, Y. Addab, C. Bachmann, T. Barrett, U. Bonavolontà, B. Böswirth, F.M. Castrovinci, C. Carelli, D. Coccorese, R. Coppola, F. Crescenzi, G. Di Gironimo, P.A. Di Maio, G. Di Mambro, F. Domptail, D. Dongiovanni, G. Dose, D. Flammini, L. Forest, P. Frosi, F. Gallay, B.E. Ghidersa, C. Harrington, K. Hunger, V. Imbriani, M. Li, A. Lukenskas, A. Maffucci, N. Mantel, D. Marzullo, T. Minniti, A.V. Müller, S. Noce, M.T. Porfiri, A. Quartararo, M. Richou, S. Roccella, D. Terentyev, A. Tincani, E. Vallone, S. Ventre, R. Villari, F. Villone, C. Vorpahl, and K. Zhang. Divertor of the European DEMO: Engineering and technologies for power exhaust. *Fusion Engineering and Design*, 175:113010, 2022.

[132] I.E. Idelchik. *Handbook of hydraulic resistance, 4th Edition Revised and Augmented.* 2007.

[133] N.E. Todreas and M.S. Kazimi. *Nuclear Systems Volume I: Thermal Hydraulic Fundamentals, Third Edition.* CRC Press, 2021.

[134] A.R. Raffray, J. Schlosser, M. Akiba, M. Araki, S. Chiocchio, D. Driemeyer, F. Escourbiac, S. Grigoriev, M. Merola, R. Tivey, G. Vieider, and D. Youchison. Critical heat flux analysis and R&D for the design of the ITER divertor. *Fusion Engineering and Design*, 45(4):377–407, 1999.

[135] F. Lucca and M. Roccella. EM DEMO model (Baseline 2017) including ferromagnetic effects of HCPB blanket modules–model with limiters. Technical report, EUROfusion IDM, `https://idm.euro-fusion.org/?uid=2MCH97&version=v1.1&action=get_document`, 2019.

[136] R.G. Budynas and J.K. Nisbett. *Shigley's Mechanical Engineering Design, 11th edition.* 2019.

[137] EUROfusion. EU–DEMO Material Property Handbook 4th release (EFDA_D_2MYQDV v1.1). Technical report, EUROfusion IDM, `http://idm.euro-fusion.org/?uid=2MYQDV`, 2020.

[138] European Committee for Standardization. EN 1993-1-8:2005. Eurocode 3: Design of steel structures - Part 1-8: Design of joints. In *EUROCODE*, volume 1. 2011.

[139] I. Pagani. EM analysis on Upper Limiter. Technical report, EUROfusion IDM, `https://idm.euro-fusion.org/?uid=2QCW7J`, 2022.

[140] J. Coburn, M. Lehnen, R.A. Pitts, G. Simic, F.J. Artola, E. Thorén, S. Ratynskaia, K. Ibano, M. Brank, L. Kos, R. Khayrutdinov, V.E. Lukash, B. Stein-Lubrano, E. Matveeva, and G. Pautasso. Energy deposition and melt deformation on the iter first wall due to disruptions and vertical displacement events. *Nuclear Fusion*, 62(1):016001, 2021.